Numéro d'ordre NNT: 2016LYSEC38 Année: 2016

L'UNIVERSITÉ DE LYON
OPÉRÉE AU SEIN DE L'ÉCOLE CENTRALE DE LYON

ÉCOLE DOCTORALE MEGA
Mécanique, Enegétique, Génie civil et Acoustique

THESIS

Optimization of Dynamic Behavior of Assembled Structures Based on Generalized Modal Synthesis

defended on November 21, 2016 by

Xing-Rong HUANG

to obtain the title of

Doctor of École Centrale de Lyon

Specialty : MECHANICS

Jury members:

Reviewers :	Pierre LEMERLE	-	Researcher, HDR, INRS
	Pierre ARGOUL	-	Associate Professor, HDR, ENPC
Advisor :	Louis JÉZÉQUEL	-	Professor, ECL
Co-advisors :	Lin LI	-	Professor, Beihang University
	Sébastien BESSET	-	Associate Professor, HDR, ECL
Examinators :	Denis AUBRY	-	Professor, MSSMat, ECP
	Olivier SAUVAGE	-	PhD, Engineer PSA Group

To my mother Ai-Xin Pan, my father Wen-Ping Huang, my sister Yi-Ting Huang,
and my boy friend Zeng-Lin Liu.

Acknowlegements

I would like to express my sincere gratefulness to my thesis advisor Prof. Louis Jézéquel for proposing this thesis and showing me the power of modal synthesis, for his generous sharing of incessant new ideas, patient guidance, consistent encouragement and all the concerns. In the meanwhile, I would like to thanks Dr Sébastien Besset, for his patient explanation of modal synthesis, precise instructions, active feedbacks, consistent interventions and precious advices for the publications and this dissertation. As well, I would like to address my gratitude to Prof. Lin Li for the insight discussions on nonlinear modal synthesis, the forward looking in the thesis subject and the sharing of life experience. I would also want to thank Dr Olivier Sauvage for following this work and precious industrial remarks. Many thanks should also be delivered to other jury members of the thesis defense: Prof. Denis Aubry for being the president of jury and many open questions; Dr Pierre Lemerle and Dr Pierre Argoul for taking time to review this work and precious advices on the dissertation. I gratefully acknowledge Chinese Scholarship Council (CSC) for the financial support of this thesis.

I want to show my thankfulness to Mme Isabelle Tixier for managing all the administrative procedures and instructions in daily life. I am also grateful to Mme Cheng Sun for her guidance in Chinese language teaching and concerns in daily life. Many thanks to kind hearted and experienced researchers in the team: Dr Jean-Pierre Lainé for being the mechanical encyclopedia; Dr Claude Gibert for the valuable instructions on nonlinear modal synthesis; Dr Olivier Dessombz for the technical support of fundamental basis for simulation. I also appreciate the scientific discussions with the doctoral students in the laboratory. Among the Chinese colleges: Yu Fan for the daily scientific discussion, patient guidance in research and polishing of the publications; Changwei Zhou for the selfless sharing of thesis experience, companionship and precious advices for the publications; Jiuzhou Liu for the valuable exchange and discussion about nonlinear problems; Kai Zhang for the instructions on control policy. Among the French colleges: Kevin Soobbarayen for the precise guidance in Structural Dynamic Toolbox; Régis Boukadia for the discussions on mathematic and your friendship; Jean-Loup Christen for the instructions of matlab and the corrections in French language; Christophe Droz for the discussions on carrier planning; Colas Joannin for the discussions about harmonic balance method.

The wonderful experience in Ecole Centrale de Lyon and the enthusiastic reception of LTDS would brand me for life: the jogging, the badminton, the dance, the ski, the gastronomy, the wine and the most important of all: the friendship (There are so many persons concerned in this single word that names are not listed herein).

Last but not the least, I would like to give my deepest gratitude to my mother, my father, my sister and my boy friend for your unconditional love and support, and the success of this thesis is the fruit of your love.

Abstract

Noise and vibration are important topics in the automotive industry for several reasons, including passenger comfort and structural integrity. The main objective of this thesis is to propose a series of appropriate methods to optimize structural system characteristics, so that the vibration and noise can be reduced. To achieve this goal, interface control strategies are employed, including bonding viscoelastic layers onto the most heavily deformed zones and introducing frictional damping devices calibrated on certain resonance frequencies. Such built-up structural systems are numerically investigated via a generalized modal synthesis approach that incorporates several groups of modes.

The employed modal synthesis approach consists of several levels of condensation. The first one is on the internal degrees of freedoms (DOFs) of each substructure, and the second condensation is on the branch modes so as to reduce the boundary DOFs among substructures. For coupled fluid-structural systems, a third condensation on the fluid DOFs is suggested. With these condensation techniques, the system dimension can be significantly reduced. The method allows us to obtain the forced response of the structures as well as the pressure variation of the fluids.

Additionally, modal parameters characterizing vibration and noise transmission paths can be deduced as mid-stage results. We show that these modal parameters can be used as optimization objective during the interface configuration design. The Pareto front of the optimal design is achieved by employing Kriging approximations followed with an elitist multi-objective genetic algorithm. Another advantage of the modal approach is that a modal overview on the system characteristics is provided by analyzing the natural frequencies, modal damping ratios and the aforementioned modal parameters.

The modal synthesis approach is further extended to study nonlinear systems. The basic assumption is that the nonlinear modes are weakly coupled. Nonlinear modal parameters, such as modal frequency and modal damping ratio, contain the essential nonlinear information and depend on modal amplitude. The main idea is to compute nonlinear normal modes according to their modal amplitude and superimpose the response of several nonlinear modes to obtain the overall forced response. The method is applied to systems involving Duffing and dry friction nonlinearities. In the case of dry friction, a generalized Masing model is considered to capture the dry friction nature. Both complex modes and real modes are used in the modal synthesis, leading to different frictional damping terms. We show that the nonlinear modal synthesis combined with the generalized Masing model yields a simple, fast and efficient numerical method to describe nonlinear performance of structures with dry friction.

Keywords: Modal synthesis, interface control, model reduction, fluid-structural coupling, multi-objective optimization, nonlinear mode

Résumé

Dans le processus de conception des véhicules, la vibration et le bruit sont des sujets d'étude très importants. En effet, les vibrations sont susceptibles d'affecter le comportement dynamique des structures et le bruit dégrade le confort acoustique des passagers. L'objectif principal de la thèse est de proposer un ensemble de méthodes pour l'optimisation du comportement dynamique des systèmes complexes afin de réduire les vibrations des structures et le bruit dans l'habitacle. À cet effet, on s'intéresse à des stratégies de contrôle des interfaces, comme le collage de couches viscoélastiques sur les zones les plus déformées, ou l'introduction de dispositifs frottants calibrés pour ajouter de l'amortissement à certaines fréquences de résonance. Les structures assemblées résultantes sont étudiées numériquement par une méthode de synthèse modale généralisée.

La méthode de synthèse modale proposée contient plusieurs niveaux de condensation. Le premier concerne les degrés de libertés (DDL) internes de chaque sous-structure. La deuxième condensation s'effectue sur les modes de branches, de sorte à réduire le nombre de DDL aux interfaces entre les sous-structures. Pour les systèmes couplés fluide/structure, une troisième condensation portant sur les DDL du fluide est proposée. Suite à ces condensations, la dimension du système est fortement réduite. Cette méthode permet alors d'obtenir aussi bien la réponse forcée de la structure que les fluctuations du champ de pression dans le fluide.

Les chemins de transmission acoustiques et vibratoires peuvent également être déduits des contributions modales intermédiaires. On montre que ces paramètres modaux peuvent être utilisés comme fonctions objectif pour une démarche d'optimisation des interfaces. Le front de Pareto des conceptions optimales est obtenu avec un algorithme génétique multi-objectif élitiste, appliqué à une approximation par krigeage de la fonction objectif.

Cette approche modale est étendue à l'étude de systèmes non-linéaires. L'hypothèse fondamentale est que les modes non-linéaires sont faiblement couplés. Les paramètres modaux non-linéaires (fréquences propres, amortissements...), dépendent des amplitudes modales. L'idée est alors de calculer des modes normaux non-linéaires en fonction de leur amplitude et de superposer leurs réponses pour obtenir celle de la structure. La méthode est appliquée à des systèmes incorporant des non-linéarités de type Duffing et de frottement sec. Le cas particulier du frottement sec est considéré à travers un modèle de Masing généralisé. Deux approches modales sont développées : l'une basée sur les modes complexes, et l'autre basée sur les modes réels. L'utilisation de modes complexes ou réels dans la synthèse modale conduit à des termes d'amortissement par frottement différents. On montre que la synthèse modale non-linéaire combinée au modèle de Masing généralisé aboutit à une méthode numérique simple, rapide et efficace pour décrire le comportement non-linéaire de structures soumise à du frottement sec.

Mots-clés: Synthèse modale, contrôle d'interfaces, réduction de modèle, interaction fluide-structure, optimisation multi-objectif, mode non-linéaire

Contents

General introduction **xxvii**
- Industrial Background . . . xxvii
- Motivation of the work . . . xxviii
- Organization of the dissertation . . . xxix

I Optimization of passive interfaces for vibration control of linear systems **1**

Part 1: Introduction **5**

1 Optimization strategy based on double modal synthesis **11**
- 1.1 Finite element formulation of the assembled systems . . . 11
- 1.2 Theory of double modal synthesis . . . 13
- 1.3 Modal parameters characterizing vibration transmission . . . 15
  - 1.3.1 Study of plate 2 . . . 19
  - 1.3.2 Study of the junction . . . 20
  - 1.3.3 Study of the plate 1 . . . 23
  - 1.3.4 Study of the vibration transmission paths . . . 24

2 Outlines of the numerical tools in triple modal synthesis **27**
- 2.1 Mechanical model with fluid-structure interaction . . . 27
- 2.2 Theory of triple modal synthesis . . . 31
- 2.3 Criteria characterizing acoustic comfort . . . 33
- 2.4 Modal parameters characterizing noise transmission . . . 34

3 Case study – linear systems **41**
- 3.1 Numerical schemes for system optimization . . . 41
- 3.2 Assembled plates . . . 45
  - 3.2.1 Reduced model . . . 48
  - 3.2.2 A modal overview based on Modal-based criteria . . . 50
  - 3.2.3 Meta-models and Pareto optimal . . . 53
  - 3.2.4 Conclusions . . . 59
- 3.3 An assembled box filled with air . . . 60
  - 3.3.1 Reduced model . . . 62
  - 3.3.2 Modal-based criteria and sensitivity analysis . . . 64
  - 3.3.3 Meta-models and Pareto optimal . . . 69
  - 3.3.4 Conclusions . . . 75

Part 1: Conclusions **77**

II Optimization of passive interfaces for vibration control of nonlinear systems 79

Part 2: Introduction 83

4 Extensions of nonlinear modal synthesis 87
4.1 Introduction . . . 87
4.2 Reference numerical method – Runge-Kutta . . . 88
4.3 Theoretical basis of nonlinear modal analysis . . . 89
4.3.1 Nonlinear normal modes . . . 89
4.3.2 Nonlinear modal parameters . . . 91
4.3.3 Modal synthesis of forced responses . . . 92
4.4 Reduced nonlinear modal synthesis . . . 92
4.5 Case study of an assembled structure . . . 96
4.5.1 Truncation effects of higher-order nonlinear normal modes . . 98
4.5.2 Truncation effects of internal modes and branch modes . . . 98
4.5.3 Analysis of nonlinear phenomena from a modal overview . . . 107

5 Structures involving dry friction 113
5.1 Friction models . . . 113
5.1.1 Static friction models . . . 114
5.1.2 Dynamic friction models . . . 115
5.1.3 Masing models by the use of restoring force . . . 117
5.2 Generalized Masing model . . . 119
5.3 Reference numerical methods . . . 124
5.3.1 Theory of Newmark-β method . . . 124
5.3.2 Theory of Harmonic Balance method . . . 127
5.4 Theory of nonlinear modal analysis . . . 129
5.4.1 Frictional damping by using real modal synthesis . . . 130
5.4.2 Frictional damping by using complex modal synthesis . . . 132
5.5 Case study of 2 DOFs mass-stiffness model . . . 133
5.5.1 Time history of responses by using Newmark-β method . . . 134
5.5.2 Steady-state responses by using nonlinear modal synthesis method . . . 137
5.5.3 Modal overview based on nonlinear modal synthesis method . 140
5.6 Case study of a cantilever beam . . . 144
5.6.1 Time history of responses by using Newmark-β method . . . 144
5.6.2 Analysis based on nonlinear modal synthesis method . . . 145
5.7 Case study of the assembled plates . . . 148
5.7.1 Time responses by using Newmark-β method . . . 149
5.7.2 Analysis based on nonlinear modal synthesis method . . . 151

Part 2: Conclusions 155

Conclusions and perspectives 157

Publications during the thesis **161**

A Kriging approximations **163**

B An elitist multi-objective genetic algorithm **167**

C Discussion on nonlinear branch modal synthesis **169**

D Analysis of nonlinear modal damping ratio **173**

Bibliography **177**

List of Figures

1 Assembled vehicle structural system 8

1.1 Illustration of assembled system with rubber layer interface 11
1.2 Vibration transmission in the assembled structures 16
1.3 Physical illustration of evaluation criteria 17
1.4 Physical illustration of modal parameters attached to plate 2 19
1.5 Physical illustration of modal parameters attached to the junction . 21
1.6 Physical illustration of modal parameters attached to plate 1 23
1.7 Vibration transmission path: E-Plate 2 24
1.8 Vibration transmission path: E-Junction-Plate 2 25
1.9 Vibration transmission path E-Plate 1-Junction-Plate 2 25

2.1 Vehicle Model 28
2.2 Academic model used for simulation 28
2.3 Simple drawing of fluid-structure coupling 29
2.4 Pairing procedure when structural and fluid meshes do not match at boundaries 29
2.5 Noise transmission in the model 34
2.6 Physical illustration of evaluation criteria 35

3.1 Flow diagram of NSGA-II 44
3.2 Process flow chart 45
3.3 The assembled plates model with its physical dimensions 46
3.4 Detail geometry of plate and rubber layer 46
3.5 Comparison of normal modes frequencies of the full FE model and the reduced model 49
3.6 Comparison of forced responses of the full FE and reduced model . . 50
3.7 $\mathbf{C}_{ej}$ at 45.5 Hz for different interface configurations. 51
3.8 $\mathbf{C}_{ji_1}$ at 45.5 Hz for different interface configurations. 52
3.9 $\mathbf{C}_{ji_2}$ at 45.5 Hz for different interface configurations. 52
3.10 $\mathbf{C}_{i_2j}$ at 45.5 Hz for different interface configurations. 53
3.11 Comparison of modal parameters for excitation frequency at 45.5 Hz - Arbitrary design site: $l = 5.3\ mm, \theta = 0.8\ mm$. 54
3.12 Comparison of modal parameters for excitation frequency at 45.5 Hz - Arbitrary design site: $l = 7\ mm, \theta = 6.1\ mm$. 54
3.13 Kriging model of $\mathbf{C}_{je}$ in θ and l at 45.5 Hz 55
3.14 Kriging model of $\mathbf{C}_{ji_1}$ in θ and l at 45.5 Hz 55
3.15 Kriging model of $\mathbf{C}_{ji_2}$ in θ and l at 45.5 Hz 56
3.16 Kriging model of $\mathbf{C}_{i_2j}$ in θ and l at 45.5 Hz 56
3.17 Distribution of each modal parameter on the 4D Pareto front for $\mathbf{C}_{je}$, $\mathbf{C}_{ji_1}$, $\mathbf{C}_{ji_2}$ and $\mathbf{C}_{i_2j}$ in function of rubber characteristics at at 45.5 Hz 57

3.18 Distribution of θ and l on 4D Pareto front at 45.5 Hz 58
3.19 Distribution surface of the average amplitude of plate 2 in function of θ and l 58
3.20 Surrogate model of the average amplitude of plate 2 in function of θ and l 59
3.21 Comparison of average amplitude for excitation frequency around 45 Hz with different interface configuration- Arbitrary design site: $l = 5\ mm, \theta = 6\ mm$ and $l = 1.1\ mm, \theta = 1.1\ mm$(upper), Optimal design site: $l = 2.1\ mm, \theta = 8\ mm$ and $l = 1.6\ mm, \theta = 2.4\ mm$(lower). The right figure is an amplification of the left figure around 45.5 Hz . 60
3.22 FE model with all DOFs retained 61
3.23 Comparison of normal modes frequencies of the full FE model and the reduced model 62
3.24 Normal mode frequency distribution of the reduced model with $\theta =\ 1mm$ and $l = 1\ mm$. f_{FS}: natural frequency of coupled fluid-structure model, f_{F_1} and f_{F_2}: natural frequency of S_1 and S_2 fixed-interface modes, f_B: natural frequency of branch modes, f_a: natural frequency of acoustic modes 63
3.25 Distribution of branch modes in function of θ and l 64
3.26 Pressure variations induced by the vibration of structure components 65
3.27 S_1 displacements induced by the displacements of the excitation nodes 66
3.28 Interface displacements induced by the displacements of S_1 nodes . . 66
3.29 S_2 displacements induced by the displacements of the interface nodes 67
3.30 Value of $\mathbf{C}_{aj}$ in function of θ and l 67
3.31 Value of $\mathbf{C}_{ji_1}$ in function of θ and l 68
3.32 Value of $\mathbf{C}_{i_2j}$ in function of θ and l 68
3.33 Kriging model of $\mathbf{C}_{aj}$ in θ and l at 250 Hz 70
3.34 Kriging model of $\mathbf{C}_{ji_1}$ in θ and l at 250 Hz 70
3.35 Kriging model of $\mathbf{C}_{i_2j}$ in θ and l at 250 Hz 71
3.36 2D view of 3D Pareto front for $\mathbf{C}_{ji_1}$ and $\mathbf{C}_{i_2j}$ in function of rubber characteristics 71
3.37 2D view of 3D Pareto front for $\mathbf{C}_{aj}$ and $\mathbf{C}_{i_2j}$ in function of rubber characteristics 72
3.38 2D view of 3D Pareto front for $\mathbf{C}_{aj}$ and $\mathbf{C}_{ji_1}$ in function of rubber characteristics 72
3.39 Distribution of θ and l in 3D Pareto front 73
3.40 Distribution surface of the average pressure variations in function of θ and l 73
3.41 Comparison of modal parameters for an excitation frequency of 250 Hz - Arbitrary design site: $l = 3\ mm, \theta = 5\ mm$(upper), Optimal design site: $l = 8\ mm, \theta = 3\ mm$(lower). 74
3.42 2D Pareto front for $\mathbf{C}_{aj}$ and $\mathbf{C}_{ji_1}$ 75
3.43 Distribution of θ and l in 2D Pareto front for $\mathbf{C}_{aj}$ and $\mathbf{C}_{ji_1}$ 76

4.1 Substructures with nonlinear interfaces 88
4.2 Assembled system composed of Kirchoff plates and nonlinear rubber layer interface 97
4.3 Rubber layer model 97
4.4 Assembled system composed of Kirchoff plates and nonlinear rubber layer interface 97
4.5 Comparison of the forced responses obtained by NLMA method applied on the full FE model, corresponding to different r_c. r_c corresponds to the reduction coefficient on nonlinear modes. Results corresponding to $r_c = 1$, $r_c = 1.5$, $r_c = 2$ and $r_c = 4$ are compared herein. 99
4.6 Comparison of the forced responses obtained by nonlinear modal analysis corresponding to $r_c = 2$ and those obtained by RungeKutta method 99
4.7 Comparison of the forced responses obtained by RNLMS-CI method corresponding to different r_c. r_c corresponds to the reduction coefficient on internal modes. Results corresponding to $r_c = 1$, $r_c = 2$, $r_c = 4$ and $r_c = 6$ are shown herein 101
4.8 Comparison of the forced responses on excitation point obtained by Constraint NLMS method with $r_c = 2$ and by RungeKutta method . 101
4.9 Comparison of the forced responses on an arbitrary point of J obtained by Constraint NLMS method with $r_c = 2$ and by RungeKutta method 102
4.10 Comparison of the forced responses on an arbitrary point of S_1 obtained by Constraint NLMS method with $r_c = 2$ and by RungeKutta method 102
4.11 Comparison of the forced responses on an arbitrary point of S_2 obtained by Constraint NLMS method with $r_c = 2$ and by RungeKutta method 103
4.12 Comparison of the forced responses obtained by RNLMS-BI method corresponding to different r_c. r_c corresponds to the reduction coefficient on branch modes. Results corresponding to $r_c = 1$, $r_c = 2$, $r_c = 4$ and no truncation are shown herein 104
4.13 Comparison of the forced responses obtained by RNLMS-BI method corresponding to different r_c. r_c corresponds to the reduction coefficient on internal modes. Results corresponding to $r_c = 2$, $r_c = 4$, and $r_c = 6$ are shown herein 104
4.14 Comparison of the forced responses on excitation point obtained by Branch NLMS method with $r_c = 2$ for internal modes and with $r_c = 2$ for branch modes and by RungeKutta method 105
4.15 Comparison of the forced responses on an arbitrary point of J obtained by Branch NLMS method with $r_c = 2$ for internal modes and with $r_c = 2$ for branch modes and by RungeKutta method 105

4.16 Comparison of the forced responses on an arbitrary point of S_1 obtained by Branch NLMS method with $r_c = 2$ for internal modes and with $r_c = 2$ for branch modes and by RungeKutta method 106
4.17 Comparison of the forced responses on an arbitrary point of S_2 obtained by Branch NLMS method with $r_c = 2$ for internal modes and with $r_c = 2$ for branch modes and by RungeKutta method 106
4.18 Forced responses of the nine first nonlinear modes 107
4.19 mode 1 around 6 Hz 107
4.20 mode 2 around 6 Hz 107
4.21 mode 7 around 6 Hz 108
4.22 mode 9 around 46 Hz 108
4.23 Nonlinear normal mode frequency variation in function of the modal amplitude for nonlinear modes-$1, 2, 7, 9$ 108
4.24 Damping ratio variation in function of the modal amplitude for nonlinear modes-$1, 2, 7, 9$ 109
4.25 Modal participations of linear normal modes in function of the modal amplitude for nonlinear modes-$1, 2, 7, 9$ 109
4.26 Variation of modal components versus their corresponding modal amplitude for nonlinear modes-$1, 2, 7, 9$ obtained with reduced constraint NLMS strategy 110

5.1 Difference of Coulomb model around zero with $sign(v)$ and $atan(v)$, x axis represents the velocity, y axis represents the dry friction force 118
5.2 lumped-parameter system with dry friction modeled by one damper . 120
5.3 lumped-parameter system with dry friction modeled by one damper . 121
5.4 The hysteresis loop of the bilinear model 121
5.5 lumped-parameter system with dry friction modeled by three dampers in parallel 122
5.6 The hysteresis loop of the three bilinear dampers in parallel 122
5.7 lumped-parameter system with dry friction modeled by an infinity of dampers in parallel 123
5.8 The hysteresis loop of an infinity of dampers in parallel 125
5.9 Illustration of Alternating Frequency Time process [Lin 2016] 128
5.10 Algorithm for the computation of forced responses of mechanical model involving dry friction 131
5.11 2-DOF model with dry friction modeled by one damper 134
5.12 2-DOF model with dry friction modeled by an infinity of dampers in parellel 134
5.13 Time history of m_2 displacement obtained with Newmark-β method when $N = 5\ N$ 135
5.14 Stabilized displacement of m_2 obtained with Newmark-β method when $N = 5\ N$ 135
5.15 Time history of friction force obtained with Newmark-β method when $N = 5\ N$ 135

5.16 Stabilized friction force obtained with Newmark-β method when $N = 5\ N$ . . . 135
5.17 Time history of loading curve obtained with Newmark-β method when $N = 5\ N$ . . . 135
5.18 Stabilized first loading curve obtained with Newmark-β method when $N = 5\ N$ . . . 135
5.19 Bilinear Masing: Stabilized m_2 displacement, frictional force and hysteresis loop obtained with Newmark-β method in case that $N = 5\ N$ 136
5.20 Polynomial Masing: Stabilized m_2 displacement, frictional force and hysteresis loop obtained with Newmark-β method in case that $N = 5\ N$ 136
5.21 Comparison of forced response of m_1 obtained with real modal synthesis, complex modal synthesis, Harmonic balance and Newmark methods for $N = 35\ N$ . . . 137
5.22 Comparison of forced response of m_2 obtained with real modal synthesis, complex modal synthesis, Harmonic balance and Newmark methods for $N = 35\ N$ . . . 138
5.23 Forced response of m_1 corresponding to different normal load level of bilinear model. N denotes the normal load, *e.g.*, $N = 15\ N$ represents that the normal load applied on the dry friction contact point is $15\ N$ 139
5.24 Forced response of m_2 corresponding to different normal load level of bilinear model . . . 139
5.25 Forced response of m_1 corresponding to different normal load level when the 10 bilinear model are set in parallel . . . 139
5.26 Forced response of m_2 corresponding to different normal load level when 10 bilinear model are set in parallel . . . 140
5.27 Forced responses in function of frequency corresponding to different design of polynomial Masing model when $N = 15\ N$ and $x_g = 0.0375\ m$ are constant . . . 141
5.28 Evolution of natural frequency and modal damping factor *vs.* modal amplitude, corresponding to different normal load level, using bilinear model . . . 141
5.29 Evolution of natural frequency and modal damping factor *vs.* modal amplitude, corresponding to different normal load level, using bilinear model . . . 142
5.30 Evolution of natural frequency and modal damping factor *vs.* modal amplitude, corresponding to different normal load level, using generalized Masing model . . . 142
5.31 Evolution of natural frequency and modal damping factor *vs.* modal amplitude, corresponding to different normal load level, using generalized Masing model . . . 143
5.32 Synthesized forced response corresponding to different external loads *vs.* Backbone curve for mode 1 . . . 143
5.33 Synthesized forced response corresponding to different external loads *vs.* Backbone curve for mode 2 . . . 144

5.34 Beam model . . . 144
5.35 Time history of displacement obtained with Newmark-β method when $N = 10\ N$ . . . 145
5.36 Stabilized displacement obtained with Newmark-β method when $N = 10\ N$ . . . 145
5.37 Time history of friction force obtained with Newmark-β method when $N = 10\ N$ . . . 145
5.38 Stabilized friction force obtained with Newmark-β method when $N = 10\ N$ . . . 145
5.39 Time history of loading curve obtained with Newmark-β method when $N = 10\ N$ . . . 146
5.40 Stabilized first loading curve obtained with Newmark-β method when $N = 10\ N$ . . . 146
5.41 Comparison of forced response of excitation point obtained with complex modal synthesis, Harmonic balance and Newmark methods for $N = 10\ N$ . . . 146
5.42 Comparison of forced response of friction point obtained with complex modal synthesis, Harmonic balance and Newmark methods for $N = 10\ N$ . . . 146
5.43 Forced response of excitation point corresponding to different normal load level of bilinear model . . . 147
5.44 Forced response of friction point corresponding to different normal load level of bilinear model . . . 147
5.45 Evolution of natural frequency and modal damping factor *vs.* modal amplitude, corresponding to different normal load level, using bilinear model . . . 148
5.46 FE model of the plate . . . 149
5.47 Stabilized displacement obtained with Newmark-β method ($N = 0.01\ N$) . . . 150
5.48 Stabilized friction force obtained with Newmark-β method ($N = 0.01\ N$) . . . 150
5.49 Stabilized loading curve obtained with Newmark-β method ($N = 0.01\ N$) . . . 151
5.50 Comparison of forced response of excitation point obtained with real modal synthesis, complex modal synthesis, Harmonic balance-3 harmonics, Harmonic balance-1harmonic and Newmark methods for $N = 0.01\ N$ . . . 152
5.51 Forced response of excitation point corresponding to different normal load level of the plate. N denotes the normal load applied on the dry friction contact . . . 152
5.52 Evolution of natural frequency and modal damping factor *vs.* modal amplitude, corresponding to different normal load level, using bilinear model . . . 153

D.1 Rheological model of assembled structures 173
D.2 Equilavent rheological model of assembled structures 174

List of Tables

3.1 Formulation of the optimization problem 43
3.2 Outlines of model geometry and material properties 48
3.3 Comparison of mode number retained in the full and reduced model 49
3.4 CPU time comparison of different reduction techniques 50
3.5 Interface configurations 51
3.6 Model characteristics 61
3.7 Comparison of mode number retained in the full and reduced model 63
3.8 CPU time comparison of different reduction techniques 64
3.9 Sensibility of defined criteria to rubber properties 69
3.10 Comparison of average pressure variations for different configurations 75

4.1 Comparison of natural frequency of the full FE and reduced model . 100
4.2 Comparison of retained modes number and CPU time 111

Nomenclature

α	coefficient of nonlinear damping in Duffing oscillator
$\bar{\mathbf{F}}$	reduced force vector with the reduce basis
$\bar{\mathbf{K}}$	reduced stiffness matrix with the reduce basis
$\bar{\mathbf{M}}$	reduced mass matrix with the reduce basis
δy	mesh width (in direction y) of the rubber layer padding on the interface
λ_n	dominant coefficient of resonance in modal parameter
$\mathbf{\Phi}_j$	linear mode shapes j
$\mathbf{\Phi}_{\mathrm{B}}$	branch modes matrix obtained with double modal synthesis for interface set
$\mathbf{\Phi}_{aa}$	acoustic modes matrix
$\mathbf{\Phi}_{i_s i_s}$	fixed interface modes matrix for substructure-s with excitation set and interface set constrained
$\mathbf{\Psi}_S$	constraint modes matrix of the global structure
$\mathbf{\Psi}_{\mathrm{B}}$	constraint modes matrix obtained with double modal synthesis for interface set
$\mathbf{\Psi}_{\mathrm{CB}}$	constraint modes matrix obtained with Craig&Bampton reduction method for excitation set
$\mathbf{C}$	the coupling term between the compressible, non-weighting fluid and its surrounding structure
$\mathbf{C}_n$	derivable criteria of modal parameters for $n = aj, ji_1, i_2j, ae, ai_1, i_1e, ai_2$
$\mathbf{D}$	damping matrix
$\mathbf{F}$	external load applied to the model
$\mathbf{K}$	the stiffness matrix
$\mathbf{M}$	the mass matrix
$\mathbf{p}$	the pressure variation of the fluid
$\mathbf{q}_{\mathrm{rj}}$	modal coordinates of forced responses of reduced nonlinear mode j
$\mathbf{T}$	reduce basis of the proposed modal synthesis
$\mathbf{u}$	the displacement of the solid part

$\mathbf{u}_\mathrm{j}$	physical coordinates of forced responses of nonlinear mode j
ω	the excitation frequency
θ	thickness (in direction z) of the rubber layer padding on the interface
$\tilde{\lambda}_j$	nonlinear eigenvalue of nonlinear mode j
$\tilde{\beta}_{jk}$	participation coefficient of linear mode k in a single nonlinear mode j
$\tilde{\mathbf{\Phi}}_j$	nonlinear mode shapes j
$\tilde{\mathbf{G}}$	modal participation
$\tilde{\mu}_j$	modal mass of nonlinear mode j
$\tilde{\mu}_{\mathrm{rj}}$	modal mass of reduced nonlinear mode j
$\tilde{\omega}_{\mathrm{rj}}$	natural frequency of reduced nonlinear mode j
$\tilde{\xi}_j$	modal damping factor of nonlinear mode j
$\tilde{d}_j$	modal damping of nonlinear mode j
$\tilde{d}_{\mathrm{rj}}$	modal damping of reduced nonlinear mode j
$\tilde{f}_j$	modal force of mode j
$\tilde{f}_{\mathrm{rj}}$	modal force of reduced nonlinear mode j
ξ	damping ratio
a	the node in the cavity of the model
B	Branch modes
C	Constraint modes
E	Young's modulus
e	thickness (in direction z) of the rubber layer padding on the interface
F	Fixed interface modes or internal modes
G	shear modulus
i_s	the internal node of substructure-s of the solid part
J	Junction
j_s	the node on the interface attached to substructure-s of the solid part
l	length (in direction x) of the rubber layer padding on the interface

N	system dimension
N_a	retained acoustic modes number
N_B	retained branch modes number
N_E	excitation modes number
N_l	number of linear modes employed to represent a single nonlinear mode
$N_{\mathrm{i_s}r}$	number of retained internal modes of substructure-s
$N_{\mathrm{i_s}}$	ddls number of substructure-s
N_{I}	Retained internal modes number
$N_{\mathrm{J}r}$	number of retanied branch modes
N_{J}	Junction DOFs number
N_{J}	ddls number of the interface
N_{S}	Internal DOFs number
N_{i_s}	retained fixed interface mode number for substructure-s
q_j	modal amplitude for mode j
r_c	reduction coefficient
S	the node of the solid part of the model
S_1	Substructure 1
S_2	Substructure 2
Δu	relative displacements

General introduction

Contents

Industrial Background xxvii
Motivation of the work xxviii
Organization of the dissertation xxix

Industrial background

In vehicle design, vibration and noise have always been the hot topics for the automotive industry and vehicle manufacturers. Vibration and noise damage system's performance and degrade user's comfort. The increased competition in vehicle industry market requires vehicle's vibration and noise characteristics to be well optimized.

It should be recognized that there are many trade-offs between Noise&Vibration requirements, weight, cost, development time, *etc.* A compromise must be reached in the development process. The emphasis on lightweight vehicle structures, as imposed by financial and energy cost constraints, has in many cases resulted in a more significant decrease in structural stiffness than the actual mass savings. As such, the resonance frequencies of these streamlined structures have been considerably lowered and often disturb dynamic behavior in the frequency domain when associated with loadings applied on the structure. Moreover, in the process of designing vehicle systems, passengers' acoustic comfort is becoming increasingly important. The human ear is sensitive to air vibrations from about 20 Hz to 20,000 Hz, the most sensitive frequency range is between 100 Hz and 5 kHz, which is also the frequency range of most annoying vibrations of mechanical equipment. Structural and acoustic resonances can amplify the excitation load and degrade severely the acoustic comfort in the carriage. Since one cannot avoid resonances altogether, it is very important to consider the dislocation of resonant frequencies during vehicle design. In order to reduce vehicle development cost and time, an improved vehicle development process should be proposed.

This thesis is ongoing in the context of OpenLab PSA VAT@Lyon. OpenLab is a mixed research structures that pool research teams and experimental resources from the Group and partner laboratories. OpenLabs are the essential elements in the network of the StelLab (Science & Technologies Exploratory Lean LABoratory). StelLab is PSA Group's scientific innovation entity and was founded in 2010. StelLab is established in the context of continuous requirements of successful innovation and technological breakthroughs in the design of the future vehicles. This mission of the StelLab is searching for a broad scope of opportunities to cut development costs, to detect new trends and to reduce the time-to-market. Up to now, StelLab comprises some 100 PSA Peugeot Citroën scientists, 12 OpenLabs and six university chairs in Europe, China and Latin America. This thesis belongs to Lot-Z of OpenLab with the innovation cell located in Lyon.

In this thesis program, research work will focus on a widespread strategy that calls for introducing damping systems into the interfaces between substructures or between two isolated points of the structure. One thesis objective is to propose adapted methods that optimize system characteristics to control vibration levels and improve acoustic comfort of vehicle structures. These suggested methods would be based on a generalized modal synthesis that incorporates both interface modes and excitation modes. Several damping sources will be examined: viscoelastic materials, solid-solid friction along the continuous interfaces. Moreover, active or semi-active devices will be conceived in order to improve performance.

Motivation of the work

The research conducted in this thesis aimes at exploring efficient methods to optimize system performance. The systems considered herein are linear assembled structures, coupled fluid-structure systems, and nonlinear structures. To reduce the vibration level and improve the acoustic comfort in the systems, both passive interface control and dry friction dampers for the optimization object were investigated. The work can be related to five main axes:

1) The generalized modal synthesis methods for assembled structures and coupled fluid-structure systems. The underlying idea is to reduce large-sized structures to smaller size, while maintaining sufficient information to describe the dynamic performance of the system. Physical space is projected to modal space with a transformation matrix by means of acoustic modes, interface modes and excitation modes. Physical DOFs are projected to generalized modal coordinates, which represent a smaller size dimension.

2) The understanding of dynamic performance of the system from a modal overview. Modal parameters can be deduced from the generalized modal synthesis. By analyzing these modal parameters, responsible mode for resonance can be identified. Modal criteria indicating vibration and noise transmission in the system can also be determined based on the modal synthesis. Structural modification can be carried out by examining these modal criteria.

3) Optimization for linear assembled structures and coupled fluid-structure systems were conducted. Kriging approximation is employed to surrogate physical models with mathematical models thanks to its meta-modeling capability. A genetic algorithm is then used to solve the optimization problem with the meta-models constructed with Kriging approximation.

4) Extension to nonlinear modal synthesis is investigated since real industrial cases are of nonlinear nature. Nonlinear mode concept is thus combined with reduction techniques wildly applied in linear cases by using excitation modes, branch

modes and constraint modes. Steady-state responses can be calculated with a smaller-size model. Nonlinear modal parameters depending on modal amplitude are derived from the nonlinear modal synthesis. These nonlinear modal parameters that can evaluate nonlinear phenomena are studied.

5) Passive interface control and dry friction damper are investigated as means to reduce the vibration level of the system. As passive interface control, viscoelastic rubber layers are padded on the interfaces between substructures; an optimized rubber layer configuration is expected in the design process by using the proposed optimization strategy. Dry friction dampers renders the system of nonlinear nature; nonlinear modal synthesis integrating dry friction model is thus required for analyzing systems involving dry friction dampers; an optimized normal force applied on the damper is expected to maximizing structural damping.

Organization of the dissertation

The brief outline of the thesis is listed as follows: the background and the motivation of this work are briefly presented in the general introduction; then according to the nature of investigated structures, linear or nonlinear, the dissertation is divided in two parts: optimization of large systems by means of passive interface control based on hybrid modal synthesis method; the extensions of modal synthesis to analyze nonlinear systems.

In Part I, generalized modal synthesis methods and optimization strategy for linear systems are shown in Chapters 1, 2, and 3.

In the introduction of Part I, the basic theoretical aspects concerned in the part are presented, including: linear modal synthesis, passive control strategies and optimization techniques.

In Chapter 1, the basic theoretical formulation for an assembled structure model, along with the extensive double modal synthesis method by means of interface modes and excitation modes is presented; modal parameters characterizing vibration transmission in the system are derived based on this double modal synthesis;

In Chapter 2, the formulation of a coupled fluid-structure system is introduced; the implementation of a generalized triple modal synthesis by means of acoustic modes, interface modes and excitation modes is presented; and modal parameters indicating noise transmission in the system is proposed based on this triple modal synthesis;

In Chapter 3, interpolations techniques and optimization techniques are outlined; the theoretical basis of Kriging approximation for the construction of surrogate models is presented; and a multi-objective optimization strategy is presented to achieve Pareto optimal; the fundamental concepts and procedures of a multi-objective optimization strategy by means of an elitist genetic optimization algorithm is summarized. Two study cases are performed by using the aforementioned strategies in Chapter 1 and 2, and the simulation results are also discussed. An assembled plates model with an continuous interfaces is analyzed based on double modal synthesis described in Chapter 1; A coupled fluid-structure model is investigated based on triple modal synthesis described in Chapter 2; the optimal rubber layer configuration for these two cases are found out by employing the optimization procedure based on modal parameters presented in Chapter 3.

In Part II, The implementation of an extensive nonlinear modal synthesis by combining nonlinear mode concept and modal synthesis techniques is presented. Nonlinear structures with continuous nonlinear interface are studied in Chapter 4. The dynamic behavior of nonlinear structures involving dry friction is examined in Chapter 5.

In the introduction of Part II, numerical methods for analyzing nonlinear structures are briefly reviewed. The vibration control by introducing dry friction dampers are summarized, along with a brief overview of typical dry friction models.

In Chapter 4, the theoretical basis of the nonlinear modal analysis method is presented; modal parameters are proposed based on the nonlinear modal synthesis; both numerical and analytical methods for calculating forced responses of harmonically excited systems are given; then how reduction techniques are integrated into the nonlinear modal analysis by means of interface modes, excitation modes and constraint modes is depicted; the proposed strategy is then applied to an assembled model composed of plates and nonlinear rubber material interfaces for validation purposes.

In Chapter 5, dry friction models used in the literature are briefly reviewed; the generalized Masing model is presented, which is employed as dry friction model in the following analysis; the implementation of a time integration method Newmark-β is outlined for calculating transient responses; the harmonic balance method is introduced to calculate the periodic responses of nonlinear systems under periodic excitation; nonlinear modal synthesis methods to compute steady state response of the system are depicted; modal parameters are also derived; in relying on these numerical methods, case studies are carried out: one study case of a 2 DOFs model is used to illustrate the proposed method; another study case of cantilever beam is used for validation purpose.

Concluding remarks and discussions concerning the perspective work are synthesized in Chapter 5.7.2.

The first appendix outlines theoretical aspects of Kriging approximations for interpolation purpose used in Chapter 3. The second appendix gives supplementary material of the elitist multi-objective genetic algorithm for optimization purpose used in Chapter 3. The third appendix presents the detailed derivation and discussions of the nonlinear branch modal synthesis, which has been developed in parallel with reduced nonlinear modal synthesis in Chapter 4. The fourth appendix provides supplementary discussions on the frictional damping ratio used in Chapter 5.

Part I

Optimization of passive interfaces for vibration control of linear systems

Abstract: The characteristics of the interfaces between substructures play an important role in controlling the dynamic vibration of large structures. In this part, we have proposed a strategy to obtain an optimal interface configuration for both assembled structures and coupled fluid-structure systems. The assembled structures are analyzed by using excitation modes, interface modes and constraint modes; the coupled fluid-structure systems are studied by employing acoustic modes, excitation modes, interface modes and constraint modes. Based on the proposed modal synthesis approach, the steady-state responses of the investigated systems in the interested frequency band can be evaluated by two strategies: the first consists in calculating the dynamic response by employing an extensive modal synthesis; the second concerns using modal parameters characterizing vibration transmission paths or noise transmission paths between substructures in the system, which can also provide a modal overview of the dynamic behavior. Our objective consists in searching the optimal configuration of the elastic layer padding on the interface to minimize the vibration level and improve the acoustic comfort of a vehicle system. The optimization criteria are substituted by Kriging interpolation models to avoid prohibitive simulation steps during optimization of the complex system. Once the mathematical models of the investigated modal criteria are established and the multi-objective functions for rubber characteristics defined, an approximate optimal solution leading to superior dynamic performance could be obtained based on a genetic algorithm. The analytical results and numerical experiments conducted have also justified the efficiency of our proposed strategy.

Part 1: Introduction

Linear modal synthesis used in analyzing industrial structures

In order to reduce vehicle development cost and time, an improved vehicle development process should be proposed. To analyze the noise and vibration problems, frequency analysis is powerful for identifying noise sources and enables the effectiveness of noise control measures to be assessed. Modal analysis is a mathematical tool that enables engineers to determine characteristic values that describe the resonances and then to build an analytical model from this information. It permits determining the natural mode shapes and frequencies of the structure during free vibration and is independent on the external load. Modes are inherent properties of a structure, and are determined by the material properties and boundary conditions of the structure. If the stiffness of the structure is modified, it will vibrate differently and resonant frequency will be different.

For the convenience of the analytical simulations, great interest has consistently been shown in employing dynamic sub-structuring and component mode synthesis (CMS) to reduce the degrees of freedom (DOFs) of large complex systems since 1960 [Hurty 1960]. A brief review of dynamic sub-structuring can be found in [Klerk 2008]. CMS can be implemented in the system design process for industrial applications, *e.g.* automotive applications [Vermot 2010]. The strategy of CMS is to project the physical space onto the modal space. Instead of confining all physical information to the physical space, only essential modes in the modal space are retained. Using a transformation matrix, the physical space is projected onto the modal space. This step significantly reduces the problem size.

For systems with flexible physical interfaces, a clarification about component mode synthesis methods has been provided in [Ohayon 2014]. Fixed interface modes were first introduced to describe substructures by Hurty [Hurty 1971]. A method combining constraints modes and fixed interface modes was proposed by Craig and Bampton [Craig 1968]; They proposed condensing modes on the interface by retaining the fundamental modes of the structure; The mode shape information includes all boundary modes expressed in physical coordinates, along with truncated elastic modes expressed in modal coordinates. For a further reduction, Gladwell [Gladwell 1964] was one of the first to introduce branch mode analysis, in which each component of a complex continuous vibrating system is replaced by an appropriate lumped mass model. By imposing certain sets of constraints on the system, the principal modes of the constraint system can thus be obtained. It has been proven that accurate results may be found by using a sufficient number of degrees of freedom [Gladwell 1964]. This branch modal synthesis has been further developed by Jézéquel et al. [Jézéquel 1994a, Jezequel 1994b, Besset 2008a, Huang 2016]. Model reduction techniques for structural dynamics were compared in [Besselink 2013].

Double modal synthesis [Besset 2008b, Brizard 2012] is a hybrid approach based on the fixed interface modes, the constraint modes and the branch modes.

Compared to the method proposed by Craig and Bampton, the advantage of this double modal synthesis lies in the fact that the boundary DOFs are also reduced. Moreover, the truncation effect can be mitigated by adding a second-order ω^2 term, as described in [Jézéquel 1994a]. In our study, the double modal synthesis method has been extended by distinguishing excitation sets from boundary sets, *i.e.* excitation modes are presented in physical coordinates while boundary modes are presented in modal coordinates, since excitation modes provide important information yet in most cases are small in size. Reduction techniques in CMS are generally accompanied by a reduction coefficient so as to indicate how many modes are harmonically retained for each substructure. Avitabile has offered a fairly complete analysis of the truncation effect on results when studying the structural dynamic performance in [Avitabile 1990]. Reduction coefficient α is defined as follows: if the frequency band in this study varies from 0 to ω_{max}, then the number of modes retained for each part of the system, corresponding to their natural frequency, extends to $\alpha * \omega_{max}$ during the reduction step.

For a structural-acoustic problem, the fields of interest are the displacement and the pressure field in the internal fluid. In order to calculate the vibration of complex structures and noise level in the fluid, appropriate numerical formulations are required. A proper fluid-structure interaction model should be constructed. In order to reduce structure-borne vibration and noise, changing the system's stiffness to alter the resonance frequencies permits reducing the unwanted vibration in a narrow band of frequency. Most efforts to reduce acoustic sensitivity via body structural modifications have involved increasing body stiffness while damping treatments are often used to reduce the overall vibration and noise levels. It should be noted that mass, stiffness, and damping changes will affect different modes differently. Damping treatments usually help to reduce the vibration response at panel resonances.

When analyzing coupled fluid-structure systems, acoustic modes will be presented and integrated into modal synthesis approach to characterize the fluid behavior. This is the so called triple modal synthesis [Besset 2008a].

Vibration performance of dynamic structures can be featured by modal parameters based on modal synthesis. [Chen 2006] presented methods for determining the modified modal parameters in a structural dynamic modification analysis when the structural modifications are relatively large. As another solution when studying the dynamic characteristics of structures, the structure's modal parameters were introduced in [Lemerle 1994]. These modal parameters are expressed in terms of dynamic flexibility and transmissibility. This strategy was then extended for vibro-acoustic systems in [Besset 2008a]. Since the proposed criteria are small in size, *i.e.* equal to the size of substructures, the computational cost can be considerably reduced if the optimization process is based on these modal parameters. Furthermore, these criteria provide a modal overview of the dynamic phenomena. In this study, the modal criteria are defined so as to describe the noise transmission paths between substructures. Attention is paid to those paths involving interfaces that rely on rubber layer characteristics. An analysis of these criteria enables identifying both the modes and paths responsible for pressure variations in the cavity. A sensitivity study of these criteria has been performed to subsequently sort out the crucial criteria that serve for optimization purposes.

Passive control strategies

In order to mitigate the influence of these resonance modes, the classical approach consists in damping the modes by employing the following strategies: Introduction of damped resonators calibrated on the first resonance frequencies; Bonding of viscoelastic layers onto the most heavily deformed zones. The mechanic energy can be transformed into thermal energy by damping treatment. The use of damping treatment in the automotive and aerospace industries is made possible by the advancements in manufacturing processes. Sometimes the best option for control of unwanted vibration can be adding supplemental dampers, which permits dislocations of resonant frequencies in the system, which is essentially dominated by the mass matrix and the stiffness matrix of the structures. This is especially useful when the vibration issue occurs for a single frequency, or across a very narrow frequency range.

Complex systems like industrial vehicles are composed of many substructures, which in general are connected by interfaces as shown in Figure 1. Hence, interface characteristics prove to be crucial for the behavior of global systems. The typical focus of studies in structural dynamic modifications include [Avitabile 2003, Cruz 2011, Duhem 1980, Gobbi 2006]: 1) influences of simplistic structural stiffness changes on predicted frequencies and mode shapes; 2) determination of structural characteristic changes to shift a given resonance; and 3) the impacts of adding joints on the modal characteristics of a system. Local modifications applied to interfaces between the substructures investigated in this work belong to the second category.

Viscoelastic material is used for vibration control by applying them to areas that have high vibration amplitudes during resonance, for example interfaces of sheet metals that are under resonance. A typical viscoelastic damper consists in bonding viscoelastic layers to steel plates. When mounted in a structure, shear deformation and hence energy dissipation takes place when the structural vibration induces relative motion between the outer steel flanges and the center plate. Viscoelastic materials are in general polymeric materials, such as plastics, rubbers, acrylics, silicones, vinyl, adhesives, urethanes, epoxies, *etc.*, which have long-chain molecules exhibit viscoelastic behavior. The dynamic properties of linear viscoelastic materials can be represented by their modulus. Thus by properly selecting the modulus of these viscoelastic layers, the structure vibration can be reduced. The basis principle in the design is to apply the viscoelastic material in such a way that it is significantly strained whenever the structure is deformed in the vibration mode under investigation. The dynamic responses of the system can thus be controlled by regulating the resonant frequencies and the associated damping ratio.

Rubber bushings are extensively used to link parts in a vehicle chassis, thus making it possible to filter noise and vibration [Puel 2013]. The control of vibration

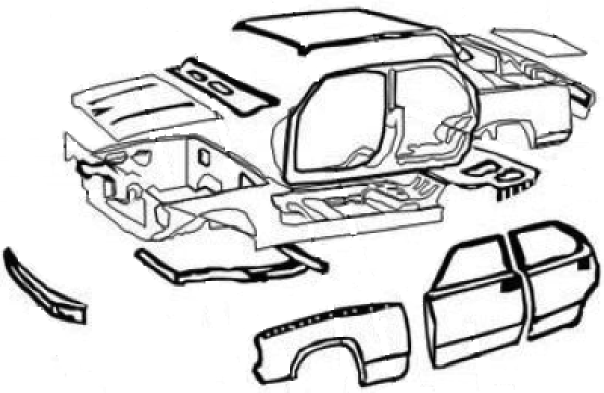

Figure 1: Assembled vehicle structural system

and noise in vehicles have several difficulties, mainly lying in the complexity of the system. Moreover, the design of the viscoelastically damped structures by padding rubber layer is an iterative process: First, an analysis of the structure without added rubber layer should be carried out. Then the required criteria become the primary design objective for adding viscoelastic dampers to the structure; and the characteristics of the viscoelastic material become the design parameters. The design consists in the following steps: a) determine structural properties of the structure and perform structural analysis; b) determine the desired objective function for optimization; c) define design parameters representing damper characteristics; e) perform structural analysis and calculate the objective function using the design parameters. When steps (e) satisfy the desired criteria and the structural performance criteria, the design is complete. Otherwise, new design cycle will be recomputed leading to new damper dimensions and properties. This procedure may continue to update the structural properties after each design cycle. That is why efficient numerical methods are required, especially during the optimization process of large complex systems.

Optimization strategy

An interesting review of optimization in a dynamic environment has been presented in [Cruz 2011]. This review has confirmed that most studies in the given industrial context are conducted based on synthetic problems, where the complexity of the objective function and degree of dynamism are controllable. Even with the most efficient criteria, optimization may be prohibitively expensive. In this context, a simplified mathematical model has been built to save on computational cost. The speed of simulating a pure mathematical model is 10 to $10,000$ times faster than that of an original physical model [Gobbi 2006]. The state-of-the-art for constructing surrogate models and their applications in optimization strategies were reviewed in [Henderson 2006, Forrester 2009]. Various series of techniques exist to perform this approximation, from a simple polynomial interpolation to more accurate representative functions such as radial-based neural networks [Másson 1990] or Kriging models [Ruzika 2005]. All these methods have their advantages and drawbacks, yet no particular method has emerged as the best. The choice of surrogate method depends on many factors, such as problem size, expected complexity, analytical cost, and form of infill strategy. Neural network and Kriging approximation are among the most popular techniques in simulation optimization meta-modeling [Jin 2001]. However, in the work of [Ren 2009], it is revealed that Kriging approximation is in general likely to be preferred thanks to its meta-modeling capability. Various Kriging models, specifically ordinary, universal, co-Kriging and blind Kriging, are available. Ordinary Kriging is recommended for data that do not provide *a priori* knowledge of the trends. An additional feature of Kriging approximations is their impressive predictive power.

Engineering problems very often deal with multi-objective optimization (MOO) [Marler 2004], which simultaneously optimizes a group of objective functions. The predominant concept in defining an optimal point for an MOO problem is Pareto optimal, offering a state within a multi-criteria optimization. In this particular state, it is impossible to make any individual better off without causing at least one individual to become worse off. The Pareto front refers to the set of allocations that are all Pareto efficient for a given system; the Pareto front is especially useful in engineering applications: by yielding all potential optimal solutions, a designer can thus focus on tradeoffs within the constrained parameter set rather than considering the full range of parameters. In this study, Kriging surrogate models of the modal parameters that rely on rubber layer characteristics will be defined as objective functions; the rubber layer characteristics are defined as input variables. A fast, elitist multi-objective genetic algorithm is employed to solve the MOO problem that allows achieving Pareto optimal [Deb 2002].

Chapter 1
Optimization strategy based on double modal synthesis

Contents

1.1 Finite element formulation of the assembled systems 11

1.2 Theory of double modal synthesis 13

1.3 Modal parameters characterizing vibration transmission . . 15

    1.3.1 Study of plate 2 19

    1.3.2 Study of the junction 20

    1.3.3 Study of the plate 1 23

    1.3.4 Study of the vibration transmission paths 24

1.1 Finite element formulation of the assembled systems

The assembled system under consideration is given in Figure 1.1.

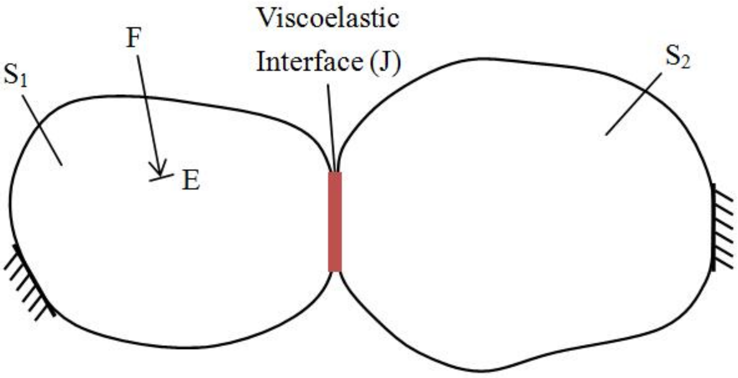

Figure 1.1: Illustration of assembled system with rubber layer interface

The dynamic model can be used to determine the effect of structural changes of mass, damping and stiffness. There are basically three different types of models commonly used for solving structural dynamic problems [Avitabile 2000]: physical model, which is developed from basis physical characteristics describing the system mass, damping and stiffness from a finite element model description; modal space models, which is developed from the modal characteristics describing the frequency, damping and mode shape; response based model, which is developed from characteristics of the system response by measurements.

Finite element (FE) modeling consists in the discretization of the structure into elements that are defined by nodes that describe the elements. Element characteristics are determined from the theory of elasticity and strength of materials. A simple solution to governing equations for each element is formulated and general solution for all elements results in algebraic set of simultaneous equations [W.Kwon 1997]. Classical finite element codes provide mass and stiffness matrices. We propose to explain the principle of the double modal synthesis method using matrices. The governing motion equation of the model is given by:

$$\mathbf{M}\ddot{\mathbf{U}} + \mathbf{K}\mathbf{U} = \mathbf{F} \tag{1.1}$$

where $\mathbf{M}$ is the mass matrix, $\mathbf{K}$ the stiffness matrix, $\mathbf{U}$ the unknown array, $\ddot{\mathbf{U}}$ the second time derivative of the $\mathbf{U}$. $\mathbf{F}$ is the force vector applied on the system.

To represent the free-vibration and eigensolutions of the structure, harmonic motion is assumed so that $\ddot{\mathbf{u}}$ is taken to equal $\lambda\mathbf{u}$, where λ is the eigenvalue and $\mathbf{u}$ is the amplitude of the following characteristic equation:

$$(-\lambda\mathbf{M} + \mathbf{K})\mathbf{u} = \mathbf{0} \tag{1.2}$$

The damping matrix is assumed to be proportional to the mass and/or stiffness matrix since it is often difficult to identify the actual damping. Two types of proportional damping operators are considered in our work: Rayleigh damping and hysteretic damping [Millard 2006]. Rayleigh damping is the viscous damping, which is a combination of mass and stiffness matrix and depends on the excitation frequency.

$$\mathbf{C} = \alpha_c\mathbf{M} + \beta_c\mathbf{K} \tag{1.3}$$

where α_c, β_c are the Rayleigh damping ratios related to the mass and stiffness matrix, respectively. Hysteretic damping represents dissipation by giving a loss factor at the element level. It is related to dynamic stiffness matrix and does not depend on the frequency:

$$\mathbf{C} = h\mathbf{K} \tag{1.4}$$

where h is the hysteretic damping ratio.

For the sake of simplicity and coherence, the matrix in the governing equation is reoriented in order of excitation set (E), junction set (J), substructure 1 (S_1) and substructure 2 (S_2), respectively. The mass matrix and stiffness matrix reads:

$$\mathbf{M} = \begin{bmatrix} \mathbf{M}_E & \mathbf{0} & \mathbf{M}_{ES_1} & \mathbf{0} \\ \mathbf{0} & \mathbf{M}_J & \mathbf{M}_{JS_1} & \mathbf{M}_{JS_2} \\ \mathbf{M}_{S_1E} & \mathbf{M}_{S_1J} & \mathbf{M}_{S_1} & \mathbf{0} \\ \mathbf{M}_{S_2E} & \mathbf{M}_{S_2J} & \mathbf{0} & \mathbf{M}_{S_2} \end{bmatrix} \quad \mathbf{K} = \begin{bmatrix} \mathbf{K}_E & \mathbf{0} & \mathbf{K}_{ES_1} & \mathbf{0} \\ \mathbf{0} & \mathbf{K}_J & \mathbf{K}_{JS_1} & \mathbf{K}_{JS_2} \\ \mathbf{K}_{S_1E} & \mathbf{K}_{S_1J} & \mathbf{K}_{S_1} & \mathbf{0} \\ \mathbf{0} & \mathbf{K}_{S_2J} & \mathbf{0} & \mathbf{K}_{S_2} \end{bmatrix} \tag{1.5}$$

1.2 Theory of double modal synthesis

The dimension of built-up systems is generally very large and the computational cost is expensive in analyzing this kind of system. The modal analysis based on the Ritz-Galerkin projection using appropriate Ritz vectors, allow us to construct reduced models expressed in terms of physical displacement vector field $\mathbf{u}$ in the structure. This is accomplished by approximating $\mathbf{u}$ by a linear combination of normal modes ϕ_k and generalized modal coordinates q_k.

$$\mathbf{U} = \sum_{k=1}^{N_r} \phi_k q_k \tag{1.6}$$

The matrix form of this representation is given as follows: the physical coordinates $\mathbf{U}$ are thus replaced by the generalized modal coordinates $\mathbf{q}$.

$$\mathbf{U} = \left[\begin{array}{cccc} \phi_1 & \phi_2 & \dots & \phi_{N_r} \end{array} \right] \left[\begin{array}{c} q_1 \\ q_2 \\ \dots \\ q_{N_r} \end{array} \right] \tag{1.7}$$

In accordance with the rearrangement of DOFs in the system, the physical space can thus be projected on modal space by the use of a modal basis by using a modal transformation matrix $\mathbf{T}$ of dimension $(N * N_r)$, where N is the total number of DOFs in the FE model, and N_r is the number of retained mode number.:

$$\left[\begin{array}{c} \mathbf{U}_E \\ \mathbf{U}_J \\ \mathbf{U}_{S_1} \\ \mathbf{U}_{S_2} \end{array} \right] = \mathbf{T} \left[\begin{array}{c} \mathbf{q}_E \\ \mathbf{q}_J \\ \mathbf{q}_{S_1} \\ \mathbf{q}_{S_2} \end{array} \right] = \left[\begin{array}{cccc} \mathbf{I}_E & \mathbf{0} & \mathbf{0} & \mathbf{0} \\ \mathbf{0} & \mathbf{\Phi}_B & \mathbf{0} & \mathbf{0} \\ \mathbf{\Psi}_{S_1E} & \mathbf{\Psi}_{S_1J}\mathbf{\Phi}_B & \mathbf{\Phi}_{S_1} & \mathbf{0} \\ \mathbf{0} & \mathbf{\Psi}_{S_2J}\mathbf{\Phi}_B & \mathbf{0} & \mathbf{\Phi}_{S_2} \end{array} \right] \left[\begin{array}{c} \mathbf{q}_E \\ \mathbf{q}_J \\ \mathbf{q}_{S_1} \\ \mathbf{q}_{S_2} \end{array} \right] \tag{1.8}$$

The transformation matrix or the reduction basis is constructed based on a hybrid modal synthesis method by the use of fixed interface modes, constraint modes and branch modes. The reduction technique developed in this chapter is an extension of the work found in [Jézéquel 1994a]. While herein we propose to treat the excitation set and interface set of the structured part differently with two distinct reduction techniques: All modes have been retained for the excitation set; it is not necessary to reduce its size, since the number of DOFs of the excitation set is generally limited. While the interface set is treated using double modal synthesis, a certain number of boundary modes are retained; these modes are also known as branch modes [Jézéquel 1994a]; it is required to reduce the interface mode number when a large number of DOFs are involved. The notion herein is to retain the dominant modes in the targeted frequency band rather than all boundary modes. This approach makes it possible to correctly study the structure's performance with fewer modes, which may significantly lower the computational cost. In order to obtain the reduction basis: fixed interface modes for both substructures are first reduced; a second reduction is then applied on the interface set; no reduction is performed for excitation set. That is why this method is called double modal synthesis.

According to fixed interface modal synthesis theory, which is also known as the Craig & Bampton reduction method [Craig 1966], the displacements of the substructure $\mathbf{u}_{i_s e}$ induced by displacements of the excitation set $\mathbf{u}_e$ are expressed in Equation (1.9) by employing static constraint modes $\mathbf{\Psi}_{\mathrm{CB}_{i_s e}}$, *i.e.* all the N_{E} excitation modes are retained among the total number of N_{E}:

$$\begin{aligned}\mathbf{u}_{i_s e} &= \mathbf{\Psi}_{\mathrm{CB}_{i_s e}} \mathbf{u}_e \\ &= -\mathbf{K}_{i_s i_s}{}^{-1} \mathbf{K}_{i_s e} \mathbf{u}_e \quad s = 1, 2\end{aligned} \tag{1.9}$$

Branch modes represent the performance of the global system. They are introduced herein for the boundary condensation on the interface, which normally includes a large number of DOFs in the model. The branch modes matrix $\mathbf{\Phi}_{\mathrm{B}}$ is formed by $\mathbf{\Phi}_{\mathrm{B}_j}$, which is the eigenvector of Equation (1.10). The eigenvalue matrix $\mathbf{\Lambda}_{\mathrm{B}}$ is a diagonal matrix in which the diagonal elements are λ_{B_j}. Supposing that N_{Jr} branch modes are retained among the total number of N_{J}, the dimension of $\mathbf{\Phi}_{\mathrm{B}}$ is thus $N_{\mathrm{J}} * N_{\mathrm{Jr}}$. This equation is obtained by projecting the physical DOFs onto the constraint modes [Brizard 2012]:

$$\left[-\mathbf{\Lambda}_{\mathrm{B}}\, \mathbf{M}_B + \mathbf{K}_B\right] \mathbf{\Phi}_{\mathrm{B}} = \mathbf{0} \tag{1.10}$$

where $\mathbf{M}_B = {}^t\mathbf{\Psi}_S \mathbf{M} \mathbf{\Psi}_S$ and $\mathbf{K}_B = {}^t\mathbf{\Psi}_S \mathbf{K} \mathbf{\Psi}_S$ are the mass and stiffness matrices of the coupled system condensed on boundaries between substructures. The constraints modes matrix $\mathbf{\Psi}_S$ is expressed as follows:

$$\mathbf{\Psi}_S = \begin{bmatrix} \mathbf{\Psi}_J \\ \mathbf{\Psi}_{S_1 J} \\ \mathbf{\Psi}_{S_2 J} \end{bmatrix} = \begin{bmatrix} \mathbf{I}_j \\ -\mathbf{K}_{i_1 i_1}{}^{-1} \mathbf{K}_{i_1 j} \\ -\mathbf{K}_{i_2 i_2}{}^{-1} \mathbf{K}_{i_2 j} \end{bmatrix} \tag{1.11}$$

The internal displacements of a substructure $\mathbf{u}_{i_s j}$ induced by the interface set displacements $\mathbf{u}_j$ are obtained by projecting branch modes onto the substructure [Brizard 2012]:

$$\mathbf{u}_{i_s j} = \left(-\mathbf{K}_{i_s i_s}{}^{-1} \mathbf{K}_{i_s j}\right) \mathbf{\Phi}_{\mathrm{B}} \mathbf{q}_j \quad s = 1, 2 \tag{1.12}$$

For the construction of reduced models, the static behavior plays an important role. The limit zero-frequency static behavior is taken into account in our boundary value problem. Moreover, the displacements of each substructure imposed by successive unit displacements on the interface, denoted $\mathbf{\Psi}_{i_s j}$, are expressed in Equation (1.13). This expression can be developed as a MacLaurin series, which integrates the influence of the pulsation term ω^2. By controlling the ω^2 development order, it is possible to obtain a more accurate reduced model and lower the truncation error caused by mode condensation on the interface. The purpose of this work however is to improve dynamic behavior by optimizing the interface configuration. A compromise can then be made between the reduced model accuracy and the optimization computation time. The zero-order development has been shown to suffice for the study of dynamic behavior in the low-frequency band [Brizard 2012].

$$\begin{aligned}\boldsymbol{\Psi}_{i_sj} &= -(\mathbf{D}_{i_si_s})^{-1}\mathbf{D}_{i_sj}\boldsymbol{\Psi}_j \\ &= \left(-\omega^2\mathbf{M}_{i_si_s}+\mathbf{K}_{i_si_s}\right)^{-1}\left(-\omega^2\mathbf{M}_{i_sj}+\mathbf{K}_{i_sj}\right)\boldsymbol{\Psi}_j\end{aligned} \tag{1.13}$$

The fixed interface modes matrix of a substructure, denoted $\boldsymbol{\Phi}_{S_s}$, is formed by ϕ_{S_s}, the eigenvector to Equation (1.14), and λ_{S_s} is the associated eigenvalue. Supposing that $N_{\mathrm{i_s r}}$ internal modes are retained among the total number of $N_{\mathrm{i_s}}$, the dimension of $\boldsymbol{\Phi}_{S_s}$ is thus $N_{\mathrm{i_s}} * N_{\mathrm{i_s r}}$.

$$\left(-\lambda_{S_s}\mathbf{M}_{i_si_s}+\mathbf{K}_{i_si_s}\right)\phi_{S_s}=\mathbf{0} \quad s=1,2 \tag{1.14}$$

The dimension of the reduction basis is $N * N_r$, with $N > N_r$, which makes the dimension of the generalized modal array $\mathbf{q}$ smaller than that of the physical array $\mathbf{U}$. $\boldsymbol{\Phi}_{\mathrm{B}}$ is of dimension $N_{\mathrm{J}} * N_{\mathrm{J}r}$, with $N_{\mathrm{J}} > N_{\mathrm{J}r}$, which renders the dimension of $\mathbf{q}_{\mathrm{J}}$ smaller than that of $\mathbf{U}_J$. $\boldsymbol{\Phi}_{S_i}$ is of dimension $N_{\mathrm{i_s}} * N_{\mathrm{i_s r}}$, with $N_{\mathrm{i_s}} > N_{\mathrm{i_s}r}$, which makes the dimension of $\mathbf{q}_{S_s}$ smaller than that of $\mathbf{U}_{S_s}$. Note that $\boldsymbol{\Phi}_{\mathrm{B}}$, $\boldsymbol{\Phi}_{S_1}$ and $\boldsymbol{\Phi}_{S_1}$ are not square matrix, their inverse $\boldsymbol{\Phi}_{\mathrm{B}}^{-1}$, $\boldsymbol{\Phi}_{S_1}^{-1}$ and $\boldsymbol{\Phi}_{S_1}^{-1}$ are in fact Moore-Penrose pseudo-inverse.

The Moore-Penrose pseudo-inverse of the matrix A is the matrix B satisfying four conditions:

$$\begin{aligned}\mathbf{A}*\mathbf{B}*\mathbf{A}&=\mathbf{A}\\ \mathbf{B}*\mathbf{A}*\mathbf{B}&=\mathbf{B}\\ \mathbf{A}*\mathbf{B} &\quad \text{is Hermitian}\\ \mathbf{B}*\mathbf{A} &\quad \text{is Hermitian}\end{aligned} \tag{1.15}$$

The pseudo-inverse is a generalization of the inverse matrix. The matrix B is of the same dimension as the transpose of A and its computation is based on singular value decomposition.

The reduction basis using branch modes is the key point for the fast estimation of dynamic responses of the built-up system. The accuracy of the reduced model depends on the retained modes number during the modal synthesis.

1.3 Modal parameters characterizing vibration transmission

The interface configuration variation is accompanied by the stiffness, damping or mass modification of the system. In this way, the natural frequencies of branch modes are set apart from the natural frequency of other substructures and the excitation frequency. The parameters linked to the interface configuration are thus considered as design variables in optimal design. Vibration level can be calculated directly with the proposed hybrid modal synthesis by the use of excitation modes and branch modes. Based on a proper selection of bounds of the design parameters, sufficient large number of simulations to calculate forced responses is performed for design parameters varying in the chosen bounds. Due to the large size of industrial problems, repeated evaluations of system performance for many design points are not practically affordable. Surrogate mathematical models are constructed based on the previous simulations to predict the system performance of different configurations. A global optimization based on the surrogate model is then conducted to find the optimal interface configuration.

Moreover, we would like to extract modal parameters to analyze the dynamic performance of the system. These modal parameters linked to noise transmission paths between substructures are deduced from dynamic flexibility and transmissibility terms. By analyzing these criteria, one can identify the responsible modes and responsible noise transmissions paths for the high noise level that occurs in the cavity.

From the modal overview, the viscoelastic layer configuration is optimized in order to regulate its fundamental frequency. This brings branch mode frequencies shunning the resonant frequencies of other parts of the structures. To explain from this aspect, modal parameters characterizing vibration transmission paths and depending on the interface configuration are deduced from the above modal analysis. The vibration transmission in the assembled system is illustrated by Figure 1.2.

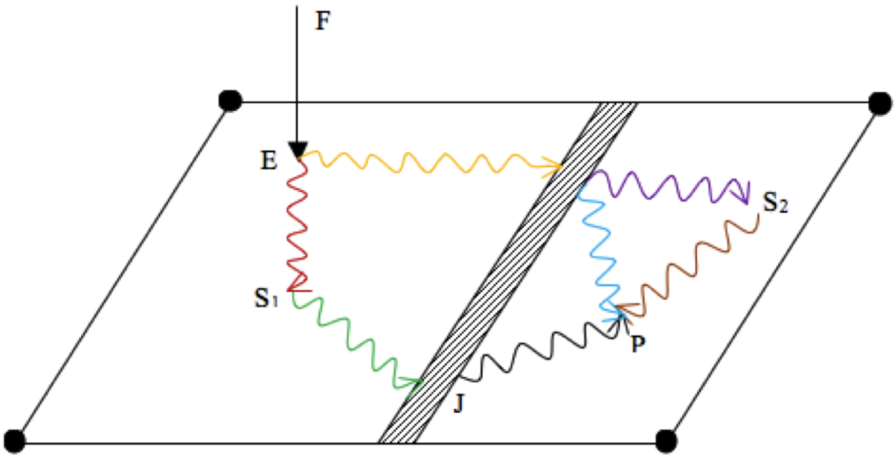

Figure 1.2: Vibration transmission in the assembled structures

The criteria corresponding to various physical meanings can be derived from the explicit motion equation. The five criteria devoted to illustrating vibration transmission paths from the excitation to substructures, as shown in Figure 1.3, have been investigated. Three modal parameters were found to be influenced by the junction. Consequently, they vary with the junction configuration, while the other two modal parameters do not. Another strength of these modal criteria is the realization of a modal overview in order to analyze the influence of a certain mode on vibration transmission.

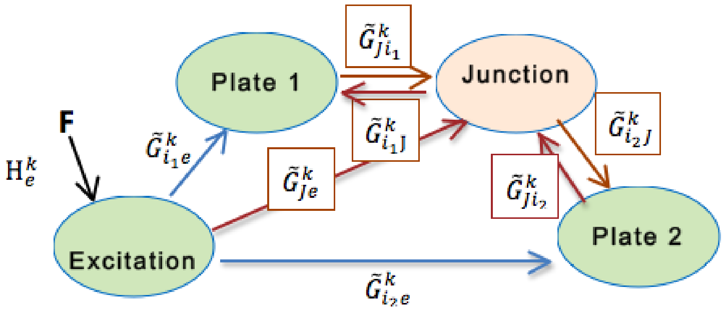

Figure 1.3: Physical illustration of evaluation criteria

From modal coordinates to physical displacements, the relationship is given by:

$$\begin{aligned}
\mathbf{q}_E &= \mathbf{U}_E \\
\mathbf{q}_J &= \mathbf{\Phi}_B^{-1}\mathbf{U}_J \\
\mathbf{q}_{S_1} &= \mathbf{\Phi}_{S_1}^{-1}\left(\mathbf{U}_{S_1} - \mathbf{\Psi}_{S_1E}\mathbf{U}_E - \mathbf{\Psi}_{S_1J}\mathbf{U}_J\right) \\
\mathbf{q}_{S_2} &= \mathbf{\Phi}_{S_2}^{-1}\left(\mathbf{U}_{S_2} - \mathbf{\Psi}_{S_2J}\mathbf{U}_J\right)
\end{aligned} \tag{1.16}$$

The damping matrix is also supposed to be diagonal according to Basile's hypothesis. The reduced governing equation can be written in the following form:

$$\begin{aligned}
&\left(-\omega^2 \begin{bmatrix} \bar{\mathbf{M}}_E & \bar{\mathbf{M}}_{EJ} & \bar{\mathbf{M}}_{ES_1} & \bar{\mathbf{M}}_{ES_2} \\ \bar{\mathbf{M}}_{JE} & \bar{\mathbf{M}}_J & \bar{\mathbf{M}}_{JS_1} & \bar{\mathbf{M}}_{JS_2} \\ \bar{\mathbf{M}}_{S_1E} & \bar{\mathbf{M}}_{S_1J} & \bar{\mathbf{M}}_{S_1} & \mathbf{0} \\ \bar{\mathbf{M}}_{S_2E} & \bar{\mathbf{M}}_{S_2J} & \mathbf{0} & \bar{\mathbf{M}}_{S_2} \end{bmatrix} + i\omega \begin{bmatrix} \bar{\mathbf{C}}_E & \mathbf{0} & \mathbf{0} & \mathbf{0} \\ \mathbf{0} & \bar{\mathbf{C}}_J & \mathbf{0} & \mathbf{0} \\ \mathbf{0} & \mathbf{0} & \bar{\mathbf{C}}_{S_1} & \mathbf{0} \\ \mathbf{0} & \mathbf{0} & \mathbf{0} & \bar{\mathbf{C}}_{S_2} \end{bmatrix} \right. \\
&\qquad \left. + \begin{bmatrix} \bar{\mathbf{K}}_E & \mathbf{0} & \mathbf{0} & \mathbf{0} \\ \mathbf{0} & \bar{\mathbf{K}}_J & \mathbf{0} & \mathbf{0} \\ \mathbf{0} & \mathbf{0} & \bar{\mathbf{K}}_{S_1} & \mathbf{0} \\ \mathbf{0} & \mathbf{0} & \mathbf{0} & \bar{\mathbf{K}}_{S_2} \end{bmatrix} \right) \begin{bmatrix} \mathbf{q}_E \\ \mathbf{q}_J \\ \mathbf{q}_{S_1} \\ \mathbf{q}_{S_2} \end{bmatrix} = \begin{bmatrix} \mathbf{F}_E \\ \mathbf{0} \\ \mathbf{0} \\ \mathbf{0} \end{bmatrix}
\end{aligned} \tag{1.17}$$

The explicit expressions of terms in the reduced motion equation are givens as follows:

$$
\begin{aligned}
\bar{\mathbf{K}}_E &= \mathbf{I}_E \left(\mathbf{M}_E \mathbf{I}_E + \mathbf{M}_{ES_1} \boldsymbol{\Psi}_{S_1 E}\right) + \boldsymbol{\Psi}^t_{S_1 E} \left(\mathbf{M}_{S_1 E} \mathbf{I}_E + \mathbf{M}_{S_1} \boldsymbol{\Psi}_{S_1 E}\right) \\
\bar{\mathbf{M}}_{EJ} &= \mathbf{I}_E \mathbf{M}_{ES_1} \boldsymbol{\Psi}_{S_1 J} \boldsymbol{\Phi}_B + \boldsymbol{\Psi}^t_{S_1 E} \left(\mathbf{M}_{S_1 J} \boldsymbol{\Phi}_B + \mathbf{M}_{S_1} \boldsymbol{\Psi}_{S_1 J} \boldsymbol{\Phi}_B\right) \\
\bar{\mathbf{M}}_{ES_1} &= \mathbf{I}_E \mathbf{M}_{S_1 E} \boldsymbol{\Phi}_{S_1} + \boldsymbol{\Psi}^t_{ES_1} \mathbf{M}_{S_1} \boldsymbol{\Phi}_{S_1} \\
\bar{\mathbf{M}}_{JE} &= \boldsymbol{\Phi}^t_B \mathbf{M}_{JS_1} \boldsymbol{\Psi}_{S_1 E} + \left(\boldsymbol{\Psi}_{S_1 J} \boldsymbol{\Phi}_B\right)^t \left(\mathbf{M}_{S_1 E} \mathbf{I}_E + \mathbf{M}_{S_1} \boldsymbol{\Psi}_{S_1 E}\right) + \left(\boldsymbol{\Psi}_{S_2 J} \boldsymbol{\Phi}_B\right)^t \mathbf{M}_{S_2 E} \mathbf{I}_E \\
\bar{\mathbf{M}}_J &= \boldsymbol{\Phi}^t_B \mathbf{M}_B \boldsymbol{\Phi}_B \\
\bar{\mathbf{M}}_{JS_1} &= \boldsymbol{\Phi}^t_B \mathbf{M}_{JS_1} \boldsymbol{\Phi}_{S_1} + \left(\boldsymbol{\Psi}_{S_1 J} \boldsymbol{\Phi}_B\right)^t \mathbf{M}_{S_1} \boldsymbol{\Phi}_{S_1} \\
\bar{\mathbf{M}}_{JS_2} &= \boldsymbol{\Phi}^t_B \mathbf{M}_{JS_2} \boldsymbol{\Phi}_{S_2} + \left(\boldsymbol{\Psi}_{S_2 J} \boldsymbol{\Phi}_B\right)^t \mathbf{M}_{S_2} \boldsymbol{\Phi}_{S_2} \\
\bar{\mathbf{M}}_{S_1 E} &= \boldsymbol{\Phi}^t_{S_1} \left(\mathbf{M}_{S_1 E} \mathbf{I}_E + \mathbf{M}_{S_1} \boldsymbol{\Psi}_{S_1 E}\right) \\
\bar{\mathbf{M}}_{S_1 J} &= \boldsymbol{\Phi}^t_{S_1} \left(\mathbf{M}_{S_1 J} \boldsymbol{\Phi}_B + \mathbf{M}_{S_1} \boldsymbol{\Psi}_{S_1 J} \boldsymbol{\Phi}_B\right) \\
\bar{\mathbf{M}}_{S_1} &= \boldsymbol{\Phi}^t_{S_1} \mathbf{M}_{S_1} \boldsymbol{\Phi}_{S_1} \\
\bar{\mathbf{M}}_{S_2 E} &= \boldsymbol{\Phi}^t_{S_2} \mathbf{M}_{S_2 E} \mathbf{I}_E \\
\bar{\mathbf{M}}_{S_2 J} &= \boldsymbol{\Phi}^t_{S_2} \left(\mathbf{M}_{S_2 J} \boldsymbol{\Phi}_B + \mathbf{M}_{S_2} \boldsymbol{\Psi}_{S_2 J} \boldsymbol{\Phi}_B\right) \\
\bar{\mathbf{M}}_{S_2} &= \boldsymbol{\Phi}^t_{S_2} \mathbf{M}_{S_2} \boldsymbol{\Phi}_{S_2}
\end{aligned}
\tag{1.18}
$$

The objective is to minimize the effect of external load $\mathbf{F}_E$ on the vibration level of the system. The dynamic amplification of external load is revealed by the coefficient $\mathbf{H}^k_E$ which links $\mathbf{F}_E$ and $\mathbf{U}_E$. In developing the first row of the generalized motion equation – Equation (1.17):

$$
-\omega^2 \left(\bar{\mathbf{m}}^k_E \mathbf{q}_E + \bar{\mathbf{M}}^k_{EJ} \mathbf{q}_J + \bar{\mathbf{M}}^k_{ES_1} \mathbf{q}^k_{S_1}\right) + i\omega \bar{\mathbf{c}}^k_E \mathbf{q}^k_E + \bar{\mathbf{k}}^k_E \mathbf{q}^k_E = \mathbf{F}_E \tag{1.19}
$$

$$
\begin{aligned}
\mathbf{U}_E &= \sum_{k=1}^{N_E} \mathbf{q}^k_E \\
&= \sum_{k=1}^{N_E} \frac{\mathbf{F}_E + \omega^2 \left(\bar{\mathbf{M}}^k_{EJ} \mathbf{q}_J + \bar{\mathbf{M}}^k_{ES_1} \mathbf{q}_{S_1}\right)}{-\omega^2 \bar{\mathbf{m}}^k_E + i\omega \bar{\mathbf{c}}^k_E + \bar{\mathbf{k}}^k_E} \\
&= \sum_{k=1}^{N_E} \frac{1}{1 + 2i\eta^k_E \left(\frac{\omega}{\omega^k_E}\right) - \left(\frac{\omega}{\omega^k_E}\right)^2} \left[\mathbf{F}_E + \left(\frac{\omega}{\omega^k_E}\right)^2 \left(\frac{\bar{\mathbf{M}}^k_{ES_1}}{\bar{\mathbf{m}}^k_E} \mathbf{U}_{S_1} + \frac{\bar{\mathbf{M}}^k_{EJ}}{\bar{\mathbf{m}}^k_E} \boldsymbol{\Phi}^{-1}_B \mathbf{U}_J\right)\right] \\
&= \sum_{k=1}^{N_E} \mathbf{H}^k_E \left[\mathbf{F}_E + \left(\frac{\omega}{\omega^k_E}\right)^2 \left(\frac{\bar{\mathbf{M}}^k_{ES_1}}{\bar{\mathbf{m}}^k_E} \mathbf{U}_{S_1} + \frac{\bar{\mathbf{M}}^k_{EJ}}{\bar{\mathbf{m}}^k_E} \boldsymbol{\Phi}^{-1}_B \mathbf{U}_J\right)\right]
\end{aligned}
\tag{1.20}
$$

where

$$
\omega^k_E = \sqrt{\frac{k^k_E}{m^k_E}}, \quad \lambda^k_E = \frac{\left(\frac{\omega}{\omega^k_E}\right)^2}{1 + 2i\eta^k_E \left(\frac{\omega}{\omega^k_E}\right) - \left(\frac{\omega}{\omega^k_E}\right)^2}, \quad c^k_E = 2\eta^k_E \sqrt{k^k_E m^k_E}
$$

$$
\mathbf{H}^k_E = \frac{1}{1 + 2i\eta^k_E \left(\frac{\omega}{\omega^k_E}\right) - \left(\frac{\omega}{\omega^k_E}\right)^2}
$$

Take the example to minimize the influence of the external load on plate 2 by optimizing interface configuration. The direct and indirect vibration transmission paths starting from the excitation set and finally arriving at plate 2 are investigated. In order to obtain the modal parameters characterizing the transmission paths between substructures, the influence of others parts on one substructure is analyzed in the following. The physical displacements of the substructures can be deduced by using the generalized motion equation Equation (1.16) and the relation between modal coordinates and physical coordinates Equation (1.17). It should be noted herein that the influence of one substructure on another is the modal influence through component modes, which is in accordance with the aforementioned objective to dislocate resonance modes.

1.3.1 Study of plate 2

The modal parameters devoted to characterizing the influence of the other parts on plate 2 are illustrated in Figure 1.4.

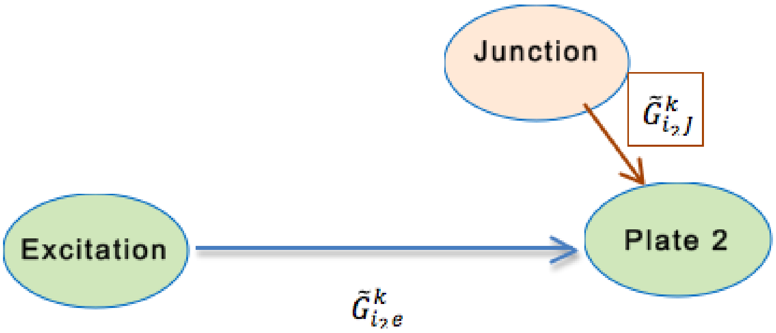

Figure 1.4: Physical illustration of modal parameters attached to plate 2

The physical displacements of plate 2 is written by:

$$\begin{aligned}\mathbf{U}_{S_2} &= \mathbf{\Psi}_{S_2 J}\mathbf{U}_J + \mathbf{\Phi}_{S_2}\mathbf{q}_{S_2} \\ &= \mathbf{\Psi}_{S_2 J}\mathbf{U}_J + \sum_{k=1}^{N_{S_2}} \mathbf{\Phi}^k_{S_2}\mathbf{q}^k_{S_2}\end{aligned} \tag{1.21}$$

The explicit expression of plate 2 displacements require information on $\mathbf{q}^k_{S_2}$. $\mathbf{q}^k_{S_2}$ can be deduced by developing the fourth row of the generalized motion equation – Equation (1.17):

$$-\omega^2\left(\bar{\mathbf{M}}^k_{S_2 E}\mathbf{q}_E + \bar{\mathbf{M}}^k_{S_2 J}\mathbf{q}_J + \bar{\mathbf{m}}^k_{S_2}\mathbf{q}^k_{S_2}\right) + i\omega\bar{\mathbf{c}}^k_{S_2}\mathbf{q}^k_{S_2} + \bar{\mathbf{k}}^k_{S_2}\mathbf{q}^k_{S_2} = \mathbf{0} \tag{1.22}$$

$$\begin{aligned}\mathbf{q}^k_{S_2} &= \frac{\omega^2\left(\bar{\mathbf{M}}^k_{S_2E}\mathbf{q}_E + \bar{\mathbf{M}}^k_{S_2J}\mathbf{q}_J\right)}{-\omega^2\bar{\mathbf{m}}^k_{S_2} + i\omega\bar{\mathbf{c}}^k_{S_2} + \bar{\mathbf{k}}^k_{S_2}} \\ &= \lambda^k_{i_2}\left[\frac{\bar{\mathbf{M}}^k_{S_2E}}{\bar{\mathbf{m}}^k_{S_2}}\mathbf{U}_E + \frac{\bar{\mathbf{M}}^k_{S_2J}}{\bar{\mathbf{m}}^k_{S_2}}\mathbf{\Phi}_B^{-1}\mathbf{U}_J\right]\end{aligned} \tag{1.23}$$

where

$$\omega^k_{i_2} = \sqrt{\frac{k^k_{S_2}}{m^k_{S_2}}}, \quad \lambda^k_{i_2}(\omega) = \frac{\left(\frac{\omega}{\omega^k_{i_2}}\right)^2}{1 + 2i\eta^k_{S_2}\left(\frac{\omega}{\omega^k_{i_2}}\right) - \left(\frac{\omega}{\omega^k_{i_2}}\right)^2}, \quad c^k_{S_2} = 2\eta^k_{S_2}\sqrt{k^k_{S_2}m^k_{S_2}}$$

In replacing Equations (1.23) in Equation (1.21), we have the physical coordinates of nodes on plate 2 written by:

$$\begin{aligned}\mathbf{U}_{S_2} =& \mathbf{\Psi}_{S_2J}\mathbf{\Phi}_B\mathbf{U}_J + \mathbf{\Phi}_{S_2}\mathbf{q}_{S_2} \\ =& \mathbf{\Psi}_{S_2J}\mathbf{U}_J + \sum_{k=1}^{N_{S_2}}\mathbf{\Phi}^k_{S_2}\mathbf{q}^k_{S_2} \\ =& \mathbf{\Psi}_{S_2J}\mathbf{U}_J + \sum_{k=1}^{N_{S_2}}\mathbf{\Phi}^k_{S_2}\lambda^k_{S_2}\frac{\bar{\mathbf{M}}^k_{S_2E}}{\bar{\mathbf{m}}^k_{S_2}}\mathbf{U}_E + \sum_{k=1}^{N_{S_2}}\mathbf{\Phi}^k_{S_2}\lambda^k_{S_2}\frac{\bar{\mathbf{M}}^k_{S_2J}}{\bar{\mathbf{m}}^k_{S_2}}\mathbf{\Phi}_B^{-1}\mathbf{U}_J \\ =& \sum_{k=1}^{N_{S_2}}\lambda^k_{i_2}\bar{\mathbf{G}}^k_{i_2e}\mathbf{U}_E + (\mathbf{\Psi}_{S_2j} + \sum_{k=1}^{N_{S_2}}\lambda^k_{i_2}\bar{\mathbf{G}}^k_{i_2j})\mathbf{U}_J\end{aligned} \tag{1.24}$$

$\mathbf{G}^k_{i_2e}$ is the plate 2 generalized coordiantes induced by excitation for mode-k (a total number of N_{S_2} fixed interface modes of plate 2):

$$\mathbf{G}^k_{i_2e} = \mathbf{\Phi}^k_{S_2}\frac{\bar{\mathbf{M}}^k_{S_2E}}{\bar{\mathbf{m}}^k_{S_2}} \tag{1.25}$$

$\mathbf{G}^k_{i_2j}$ is the plate 2 generalized coordinates induced by interface displacement (a total number of N_{S_2} fixed interface modes of plate 2):

$$\mathbf{G}^k_{i_2j} = \mathbf{\Phi}^k_{S_2}\frac{\bar{\mathbf{M}}^k_{S_2J}}{\bar{\mathbf{m}}^k_{S_2}}\mathbf{\Phi}_B^{-1} \tag{1.26}$$

1.3.2 Study of the junction

When analyzing Equation (1.24), it can be seen that $\mathbf{U}_{S_2}$ depend on $\mathbf{U}_J$. In order to analyze the physical displacement of $\mathbf{U}_J$, the influence of other parts on the junction is analyzed. The modal parameters devoted to characterizing the influence of the other parts on the junction are illustrated in Figure 1.5.

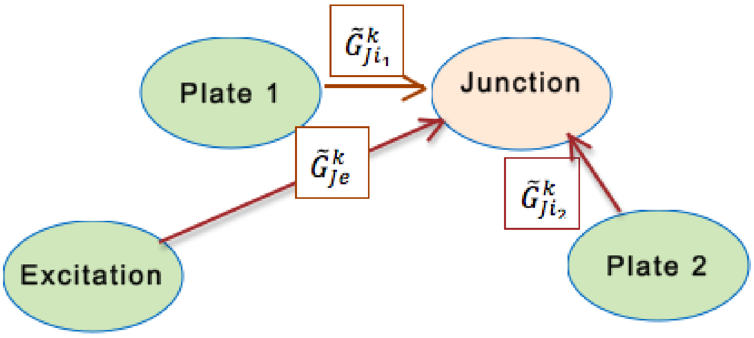

Figure 1.5: Physical illustration of modal parameters attached to the junction

According to the relationship between physical displacements and modal coordinates Equation (1.8), $\mathbf{U}_J$ is written by:

$$\mathbf{U}_J = \sum_{k=1}^{N_J} \mathbf{\Phi}_B^k \mathbf{q}_J^k \tag{1.27}$$

The modal parameters linked to the junction is also derived from the explicit motion equation, and $\mathbf{q}_J^k$ can be obtained by developing the second row of the generalized motion equation– Equation (1.17):

$$-\omega^2 \left(\bar{\mathbf{M}}_{JE}^k \mathbf{q}_E + \bar{\mathbf{m}}_J^k \mathbf{q}_J^k + \bar{\mathbf{M}}_{JS_1}^k \mathbf{q}_{S_1} + \bar{\mathbf{M}}_{JS_2}^k \mathbf{q}_{S_2} \right) + i\omega \bar{\mathbf{c}}_J^k \mathbf{q}_J^k + \bar{\mathbf{k}}_J^k \mathbf{q}_J^k = \mathbf{0} \tag{1.28}$$

$$\begin{aligned} \mathbf{q}_J^k &= \frac{\omega^2 \left(\bar{\mathbf{M}}_{JE}^k \mathbf{q}_E + \bar{\mathbf{M}}_{JS_1}^k \mathbf{q}_{S_1} + \bar{\mathbf{M}}_{JS_2}^k \mathbf{q}_{S_2} \right)}{-\omega^2 \bar{\mathbf{m}}_J^k + i\omega \bar{\mathbf{c}}_J^k + \bar{\mathbf{k}}_J^k} \\ &= \lambda_B^k \left[\frac{\bar{\mathbf{M}}_{JE}^k}{\bar{\mathbf{m}}_J^k} \mathbf{U}_E + \frac{\bar{\mathbf{M}}_{JS_1}^k}{\bar{\mathbf{m}}_J^k} \mathbf{\Phi}_{S_1}^{-1} \left(\mathbf{U}_{S_1} - \mathbf{\Psi}_{S_1 E} \mathbf{U}_E - \mathbf{\Psi}_{S_1 J} \mathbf{U}_J \right) \right. \\ &\left. + \frac{\bar{\mathbf{M}}_{JS_2}^k}{\bar{\mathbf{m}}_J^k} \mathbf{\Phi}_{S_2}^{-1} \left(\mathbf{U}_{S_2} - \mathbf{\Psi}_{S_2 J} \mathbf{U}_J \right) \right] \end{aligned} \tag{1.29}$$

where

$$\omega_B^k = \sqrt{\frac{k_J^k}{m_J^k}}, \quad \lambda_B^k = \frac{\left(\frac{\omega}{\omega_B^k}\right)^2}{1 + 2i\eta_J^k \left(\frac{\omega}{\omega_B^k}\right) - \left(\frac{\omega}{\omega_B^k}\right)^2}, \quad c_J^k = 2\eta_J^k \sqrt{k_J^k m_J^k}$$

In replacing Equation (1.29) in Equation (1.27), we get the physical displacement vector of the boundary:

$$\begin{aligned}
\mathbf{U}_J &= \sum_{k=1}^{N_J} \mathbf{\Phi}_B^k \mathbf{q}_J^k \\
&= \sum_{k=1}^{N_J} \mathbf{\Phi}_B^k \lambda_B^k \left[\frac{\bar{\mathbf{M}}_{JE}^k}{\bar{\mathbf{m}}_J^k} - \frac{\bar{\mathbf{M}}_{JS_1}^k}{\bar{\mathbf{m}}_J^k} \mathbf{\Phi}_{S_1}^{-1} \mathbf{\Psi}_{S_1E} \right] \mathbf{U}_E \\
&+ \sum_{k=1}^{N_J} \mathbf{\Phi}_B^k \lambda_B^k \left[\frac{\bar{\mathbf{M}}_{JS_1}^k}{\bar{\mathbf{m}}_J^k} \mathbf{\Phi}_{S_1}^{-1} \mathbf{U}_{S_1} \right] + \sum_{k=1}^{N_J} \mathbf{\Phi}_B^k \lambda_B^k \left[\frac{\bar{\mathbf{M}}_{JS_2}^k}{\bar{\mathbf{m}}_J^k} \mathbf{\Phi}_{S_2}^{-1} \mathbf{U}_{S_2} \right] \\
&+ \sum_{k=1}^{N_J} \mathbf{\Phi}_B^k \lambda_B^k \left[-\frac{\bar{\mathbf{M}}_{JS_1}^k}{\bar{\mathbf{m}}_J^k} \mathbf{\Phi}_{S_1}^{-1} \mathbf{\Psi}_{S_1J} - \frac{\bar{\mathbf{M}}_{JS_2}^k}{\bar{\mathbf{m}}_J^k} \mathbf{\Phi}_{S_2}^{-1} \mathbf{\Psi}_{S_2J} \right] \mathbf{U}_J \\
&= \sum_{k=1}^{N_J} \lambda_B^k \mathbf{G}_{ji_1}^k \mathbf{U}_{S_1} + \sum_{k=1}^{N_J} \lambda_B^k \mathbf{G}_{ji_2}^k \mathbf{U}_{S_2} + \sum_{k=1}^{N_J} \lambda_B^k \mathbf{G}_{je}^k \mathbf{U}_E - \sum_{k=1}^{N_J} \lambda_B^k \mathbf{G}_{jj}^k \mathbf{U}_J
\end{aligned} \tag{1.30}$$

The decoupled equation of $\mathbf{U}_J$ turns to be:

$$(1 + \sum_{k=1}^{N_J} \lambda_B^k \mathbf{G}_{jj}^k) \mathbf{U}_J = \sum_{k=1}^{N_J} \lambda_B^k \mathbf{G}_{ji_1}^k \mathbf{U}_{S_1} + \sum_{k=1}^{N_J} \lambda_B^k \mathbf{G}_{ji_2}^k \mathbf{U}_{S_2} + \sum_{k=1}^{N_J} \lambda_B^k \mathbf{G}_{je}^k \mathbf{U}_E \tag{1.31}$$

$\mathbf{G}_{je}^k$ gives the generalized boundary coordinates induced by excitation through mode-k (a total number of N_J):

$$\mathbf{G}_{je}^k = \mathbf{\Phi}_B^k \left[\frac{\bar{\mathbf{M}}_{JE}^k}{\bar{\mathbf{m}}_J^k} - \frac{\bar{\mathbf{M}}_{JS_1}^k}{\bar{\mathbf{m}}_J^k} \mathbf{\Phi}_{S_1}^{-1} \mathbf{\Psi}_{S_1E} \right] \tag{1.32}$$

$\mathbf{G}_{ji_1}^k$ indicates the generalized boundary coordinates induced by plate 1 displacements through mode-k (a total number of N_J):

$$\mathbf{G}_{ji_1}^k = \mathbf{\Phi}_B^k \frac{\bar{\mathbf{M}}_{JS_1}^k}{\bar{\mathbf{m}}_J^k} \mathbf{\Phi}_{S_1}^{-1} \tag{1.33}$$

$\mathbf{G}_{ji_2}^k$ represents the generalized boundary coordinates induced by plate 2 through mode-k (a total number of N_J):

$$\mathbf{G}_{ji_2}^k = \mathbf{\Phi}_B^k \frac{\bar{\mathbf{M}}_{JS_2}^k}{\bar{\mathbf{m}}_J^k} \mathbf{\Phi}_{S_2}^{-1} \tag{1.34}$$

$\mathbf{G}_{jj}^k$ shows the influence induced by interface itself through mode-k (a total number of N_J):

$$\mathbf{G}_{jj}^k = \mathbf{\Phi}_B^k \left[\frac{\bar{\mathbf{M}}_{JS_1}^k}{\bar{\mathbf{m}}_J^k} \mathbf{\Phi}_{S_1}^{-1} \mathbf{\Psi}_{S_1J} + \frac{\bar{\mathbf{M}}_{JS_2}^k}{\bar{\mathbf{m}}_J^k} \mathbf{\Phi}_{S_2}^{-1} \mathbf{\Psi}_{S_2J} \right] \tag{1.35}$$

1.3.3 Study of the plate 1

It can be seen from Equation (1.30) that $\mathbf{U}_J$ depend on $\mathbf{U}_{S_1}$. In order to analyze the physical displacement of $\mathbf{U}_{S_1}$, the influence of other parts on plate 1 is analyzed. The modal parameters devoted to characterizing the influence of the other parts on plate 1 are illustrated in Figure 1.6.

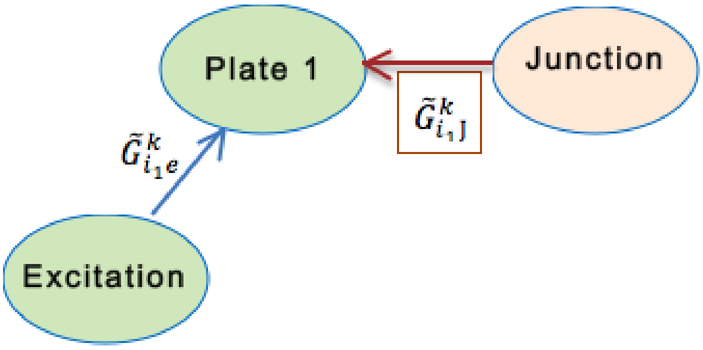

Figure 1.6: Physical illustration of modal parameters attached to plate 1

According to the relationship between physical displacements and modal coordinates Equation (1.8), $\mathbf{U}_{S_1}$ is written by:

$$\mathbf{U}_{S_1} = \mathbf{\Psi}_{S_1E}\mathbf{U}_E + \mathbf{\Psi}_{S_1J}\mathbf{U}_J + \mathbf{\Phi}_{S_1}\mathbf{q}_{S_1} \tag{1.36}$$

By developing the third row of the generalized motion equation Equation (1.17), the modal parameters linked to plate 1 can be derived from the explicit motion equation:

$$-\omega^2\left(\bar{\mathbf{M}}^k_{S_1E}\mathbf{q}_E + \bar{\mathbf{M}}^k_{S_1J}\mathbf{q}_J + \bar{\mathbf{m}}^k_{S_1}\mathbf{q}^k_{S_1}\right) + i\omega\bar{\mathbf{c}}^k_{S_1}\mathbf{q}^k_{S_1} + \bar{\mathbf{k}}^k_{S_1}\mathbf{q}^k_{S_1} = \mathbf{0} \tag{1.37}$$

The generalized coordinates of plate 1 fixed interface mode-k is:

$$\begin{aligned}\mathbf{q}^k_{S_1} &= \frac{\omega^2\left(\bar{\mathbf{M}}^k_{S_1E}\mathbf{q}_E + \bar{\mathbf{M}}^k_{S_1J}\mathbf{q}_J\right)}{-\omega^2\bar{\mathbf{m}}^k_{S_1} + i\omega\bar{\mathbf{c}}^k_{S_1} + \bar{\mathbf{k}}^k_{S_1}} \\ &= \lambda^k_{i_1}\left[\frac{\bar{\mathbf{M}}^k_{S_1E}}{\bar{\mathbf{m}}^k_{S_1}}\mathbf{U}_E + \frac{\bar{\mathbf{M}}^k_{S_1J}}{\bar{\mathbf{m}}^k_{S_1}}\mathbf{\Phi}_B^{-1}\mathbf{U}_J\right]\end{aligned} \tag{1.38}$$

where

$$\omega^k_{i_1} = \sqrt{\frac{k^k_{S_1}}{m^k_{S_1}}}, \quad \lambda^k_{i_1} = \frac{\left(\frac{\omega}{\omega^k_{i_1}}\right)^2}{1 + 2i\eta^k_{i_1}\left(\frac{\omega}{\omega^k_{i_1}}\right) - \left(\frac{\omega}{\omega^k_{i_1}}\right)^2}, \quad c^k_{i_1} = 2\eta^k_{i_1}\sqrt{k^k_{i_1}m^k_{S_1}}$$

In replacing Equation (1.38) in Equation (1.36), the displacement vector of plate 1 is expressed by:

$$\begin{aligned}\mathbf{U}_{S_1} =&\boldsymbol{\Psi}_{S_1E}\mathbf{q}_E + \boldsymbol{\Psi}_{S_1J}\mathbf{U}_J + \boldsymbol{\Phi}_{S_1}\mathbf{q}_{S_1}\\ =&\boldsymbol{\Psi}_{S_1E}\mathbf{U}_E + \boldsymbol{\Psi}_{S_1J}\mathbf{U}_J + \sum_{k=1}^{N_{S_1}}\boldsymbol{\Phi}_{S_1}^k\mathbf{q}_{S_1}^k\\ =&(\boldsymbol{\Psi}_{S_1E} + \sum_{k=1}^{N_{S_1}}\boldsymbol{\Phi}_{S_1}^k\lambda_{i_1}^k\frac{\bar{\mathbf{M}}_{S_1E}^k}{\bar{\mathbf{m}}_{S_1}^k})\mathbf{U}_E + (\boldsymbol{\Psi}_{S_1J} + \sum_{k=1}^{N_{S_1}}\boldsymbol{\Phi}_{S_1}^k\lambda_{i_1}^k\frac{\bar{\mathbf{M}}_{S_1J}^k}{\bar{\mathbf{m}}_{S_1}^k}\boldsymbol{\Phi}_B^{-1})\mathbf{U}_J\end{aligned} \tag{1.39}$$

$\mathbf{G}_{i_1e}^k$ indicates the plate 1 displacements induced by excitation:

$$\mathbf{G}_{i_1e}^k = \sum_{k=1}^{N_{S_1}}\boldsymbol{\Phi}_{S_1}^k\frac{\bar{\mathbf{M}}_{S_1E}^k}{\bar{\mathbf{m}}_{S_1}^k} \tag{1.40}$$

$\mathbf{G}_{i_1j}^k$ represents the influence of boundary displacement on plate 1 through mode-k (a total number of N_{S_1} fixed interface modes of plate 2).

$$\mathbf{G}_{i_1j}^k = \boldsymbol{\Phi}_{S_1}^k\frac{\bar{\mathbf{M}}_{S_1J}^k}{\bar{\mathbf{m}}_{S_1}^k}\boldsymbol{\Phi}_B^{-1} \tag{1.41}$$

1.3.4 Study of the vibration transmission paths

Since the objective is to minimize the influence of external load affected on the vibration level of Plate 2, three transmission paths from the external set to plate 2 are considered and analyzed in the following.

The first is the direct path from the excitation to plate 2 denoted by $\mathbf{U}_{S_2E}$, as shown in Figure 1.7:

$$\begin{aligned}\mathbf{U}_{S_2E} =&\sum_{k=1}^{N_{S_2}}\lambda_{i_2}^k\bar{\mathbf{G}}_{i_2e}^k\mathbf{U}_E\\ =&\sum_{k=1}^{N_{S_2}}\lambda_{i_2}^k\bar{\mathbf{G}}_{i_2e}^k\sum_{k=1}^{N_E}\mathbf{H}_E^k\mathbf{F}_E\end{aligned} \tag{1.42}$$

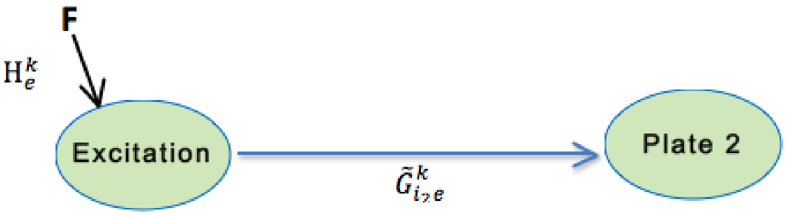

Figure 1.7: Vibration transmission path: E-Plate 2

The second is the path starting from the excitation, going through the interface, and finally arriving at plate 2, denoted by $\mathbf{U}_{S_2JE}$ and shown in Figure 1.8:

$$\mathbf{U}_{S_2JE} = (\mathbf{\Psi}_{S_2J} + \sum_{k=1}^{N_{S_2}} \lambda_{i_2}^k \bar{\mathbf{G}}_{i_2j}^k) \sum_{k=1}^{N_J} \lambda_B^k \mathbf{G}_{je}^k \sum_{k=1}^{N_E} \mathbf{H}_E^k \mathbf{F}_E \tag{1.43}$$

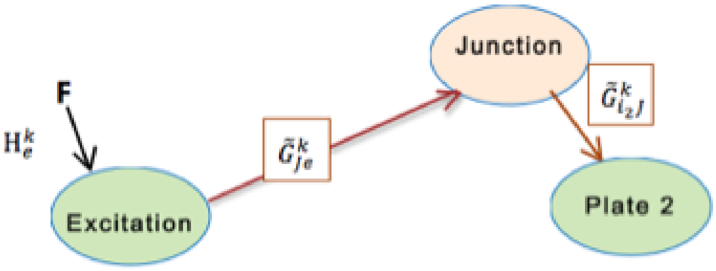
F
H_e^k
Excitation
$\tilde{G}_{je}^k$
Junction
$\tilde{G}_{i_2J}^k$
Plate 2

Figure 1.8: Vibration transmission path: E-Junction-Plate 2

In this vibration transmission path, modal parameters related to the interface configurations are identified: $\mathbf{G}_{je}^k$ characterizing the influence of excitation on the interface by branch modes; $\mathbf{G}_{i_2j}^k$ indicating the influence of the interface on plate 2 by plate 2 fixed interface modes.

The third vibration transmission path starts from the excitation node, passes by plate 1, via the interface and finally arrives at plate 2, denoted by $\mathbf{U}_{S_2JS_1E}$ and shown in Figure 1.9. The influence of $\mathbf{U}_E$ on $\mathbf{U}_{S_2}$ can be described by the following

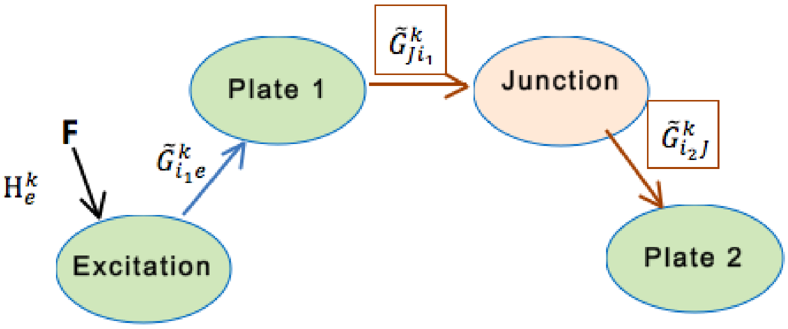
F
H_e^k
Excitation
$\tilde{G}_{i_1e}^k$
Plate 1
$\tilde{G}_{Ji_1}^k$
Junction
$\tilde{G}_{i_2J}^k$
Plate 2

Figure 1.9: Vibration transmission path E-Plate 1-Junction-Plate 2

equation:

$$\mathbf{U}_{S_2JS_1E} = (\boldsymbol{\Psi}_{S_2J} + \sum_{k=1}^{N_{S_2}} \lambda_{i_2}^k \mathbf{G}_{i_2j}^k) \sum_{k=1}^{N_J} \lambda_B^k \mathbf{G}_{ji_1}^k \sum_{k=1}^{N_{S_1}} \lambda_{i_1}^k \mathbf{G}_{i_1e}^k \sum_{k=1}^{N_E} \mathbf{H}_E^k \mathbf{F}_E \tag{1.44}$$

In this vibration transmission path, two modal parameters related to the interface configurations are identified: $\lambda_B^k \mathbf{G}_{ji_1}^k$ characterizing the influence of plate 1 on the interface by branch modes; $\lambda_{i_2}^k \mathbf{G}_{i_2j}^k$ indicating the influence of the interface on plate 2 by plate 2 fixed interface modes.

It should be mentioned that the choice of modal parameters as objective functions in the optimization process is large. Herein four modal parameters depending on the interface configuration are considered to be dominant for indicating the influence of external load on plate 2 vibration: $\lambda_B^k \mathbf{G}_{je}^k$, $\lambda_B^k \mathbf{G}_{ji_1}^k$, $\lambda_B^k \mathbf{G}_{ji_2}^k$ and $\lambda_{i_2}^k \mathbf{G}_{i_2j}^k$.

Chapter 2

Outlines of the numerical tools in triple modal synthesis

Contents

2.1 Mechanical model with fluid-structure interaction 27

2.2 Theory of triple modal synthesis 31

2.3 Criteria characterizing acoustic comfort 33

2.4 Modal parameters characterizing noise transmission 34

2.1 Mechanical model with fluid-structure interaction

The proposed method seeks to demonstrate the influence of interface characteristics on a global system, especially on the pressure variations in the cavity of a vibro-acoustic model.

A simple drawing of vehicle system is shown in Figure 2.1. A simple model, which features a similar geometry to that of a vehicle passenger compartment, is thus employed for simulation purposes. This model consists of a fluid cavity, two substructures formed by Kirchhoff plates and a rubber layer acting as an interface between substructure 1 and 2 (S_1, S_2). These two substructures differ in size so as to avoid symmetric behavior. As boundary conditions, 4 nodes on S_1 are rotationally articulated in three translation directions, as shown in Figure 2.2.

The system considered in this work is structures containing a compressible, non-weighing fluid, with or without a free surface, as shown in Figure 2.3.

Instead of describing the small motion of the fluid by a fluid displacement vector field u_F, which requires an appropriate discretization of the fluid irrotationality constraint curl $u_F = 0$, we will use the pressure scalar field p. The classical formulation describing the harmonic response of a coupled elasto-acoustic system subjected to

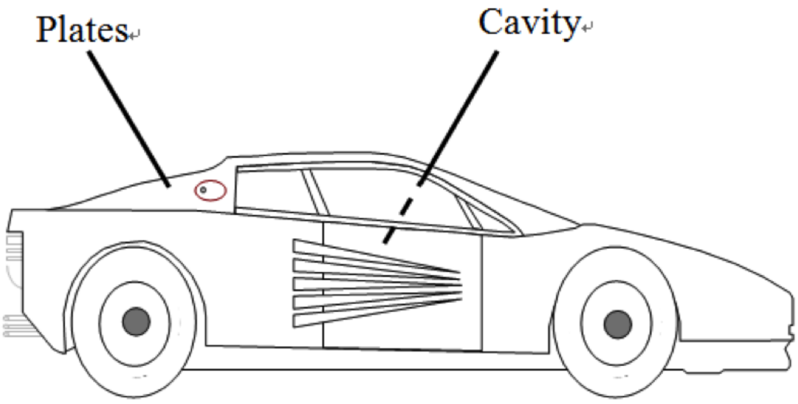
Plates
Cavity

Figure 2.1: Vehicle Model

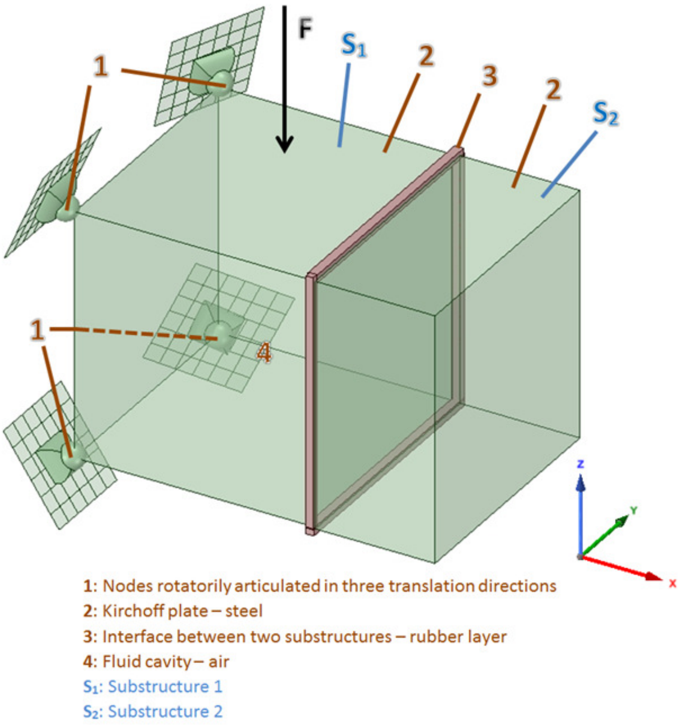
F
S1
1
2
3
2
S2
1
4
z
y
x
1: Nodes rotatorily articulated in three translation directions
2: Kirchoff plate – steel
3: Interface between two substructures – rubber layer
4: Fluid cavity – air
S1: Substructure 1
S2: Substructure 2

Figure 2.2: Academic model used for simulation

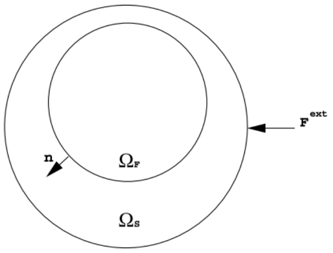

Figure 2.3: Simple drawing of fluid-structure coupling

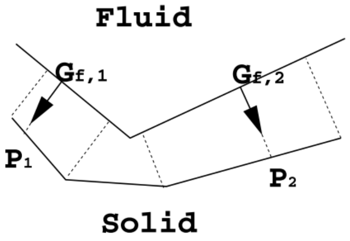

Figure 2.4: Pairing procedure when structural and fluid meshes do not match at boundaries

an external force applied on the structure is written by:

$$\begin{array}{rlll} \sigma_{ij,j}(u) + \omega^2 \rho_S u_i &= 0 & \Omega_S & (a) \\ \sigma_{ij}(u) n_j^S &= F_i^d & \partial\Omega_S \backslash \Sigma & (b) \\ \sigma_{ij}(u) n_j^S &= p n_i & \Sigma & (c) \\ \dfrac{\partial p}{\partial n} &= \omega^2 \rho_F u \cdot n & \Sigma & (d) \\ \Delta p + \dfrac{\omega^2}{c^2} p &= 0 & \Omega_F & (e) \end{array} \tag{2.1}$$

Among which, Equation (2.1).a is the elasto-dynamic motion equation, where σ_{ij} the Cauchy stress tensor; ρ_s is the mass density of the structure; u_i is the displacement of the structure; ω is the studied frequency; the domain occupied by the fluid at rest (which is taken as the equilibrium state) is denoted Ω_F; Equation (2.1).b is the boundary condition describing surficial density of the external force F_i^d applied on the structure, where n_j^S is the unit normal, external to the structure domain; Σ is the fluid-structure interface. Equation (2.1).c describes the relation between the constant static fluid pressure force acting on the structure, with n is the unit normal external to the fluid domain. Equation (2.1).d corresponds to the kinematic condition defined by the wall slipping condition, where $u \cdot n$ is a prescribed arbitrary normal displacement of the fluid-structure interface. Equation (2.1).e is the classical Helmholtz equation expressed in terms of p, where c denotes the (constant) sound speed in the fluid; ρ_F is the (constant) mass density of the fluid at rest.

Then we'll introduce the admissible space $\mathcal{C}_u$ of regular function u defined in Ω_s. In multiplying Equation (2.1).a by an arbitrary test function δu associated to u, then applying Green's formula, and considering Equation (2.1).b and Equation (2.1).c, The weak variational formulation describing the response of the structure to given harmonic forces of amplitude F_d on the external structure boundary, and to fluid pressure field p acting on the internal fluid-structure interface is written as follows:

$$\int_{\Omega_S} \sigma_{ij}(u)\varepsilon_{ij}(\delta u)dx - \omega^2 \int_{\Omega_S} \rho_S u \cdot \delta u dx - \int_{\Sigma} pn \cdot \delta u d\sigma = \int_{\partial\Omega_S \backslash \Sigma} F^d \cdot \delta u d\sigma \quad (2.2)$$

Afterwards, let δp be the test function, associated to p, belonging to the admissible space $\mathcal{C}_p$. By the usual test-function method using Green's formula, the weak variational formulation corresponding to the modal analysis of the structural-acoustic problem is then obtained by setting $F_d = 0$ in Equation (2.5). The eigenvalue structural-acoustic variational formulation is then stated as follows:

$$\frac{1}{\rho_F} \int_{\Omega_F} \nabla p \cdot \nabla \delta p dx - \frac{\omega^2}{\rho_F c^2} \int_{\Omega_F} p \delta p dx - \omega^2 \int_{\Sigma} u \cdot n^F \delta p d\sigma = 0 \quad (2.3)$$

The matrixes corresponding to diverses bilinear forms in the variational formulation are written by:

$$\begin{aligned}
\int_{\Omega_S} \sigma_{ij}(u)\varepsilon_{ij}(\delta u)dx &\Rightarrow \delta \mathbf{U}^T \mathbf{K} \mathbf{U} & (a)\\
\int_{\Omega_S} \rho_S u \cdot \delta u dx &\Rightarrow \delta \mathbf{U}^T \mathbf{M} \mathbf{U} & (b)\\
\frac{1}{\rho_F} \int_{\Omega_F} \nabla p \cdot \nabla \delta p dx &\Rightarrow \delta \mathbf{p}^T \mathbf{K_a} \mathbf{p} & (c)\\
\frac{1}{\rho_F c^2} \int_{\Omega_F} p \delta p dx &\Rightarrow \delta \mathbf{p}^T \mathbf{M}_a \mathbf{p} & (d)\\
\int_{\Sigma} p \delta u \cdot n d\sigma &\Rightarrow \delta \mathbf{U}^T \mathbf{C} \mathbf{p} & (e)\\
\int_{\partial\Omega_S \backslash \Sigma} F^d \cdot \delta u d\sigma &\Rightarrow \delta \mathbf{U}^T \mathbf{F}^d & (f)
\end{aligned} \quad (2.4)$$

where the coupling matrix C is computed using fluid-structure coupling elements in SDTools. The structure element used is $quad4$, and the fluid element is $flui4$. The center of gravity on each element (the center of gravity) is used to evaluate C. However, when structural and fluid meshes do not match at boundaries, pairing of elements needs to be done. For each fluid element F_i, one takes the center of gravity $G_{f,i}$, and searches the solid element S_i which is in front of the center of gravity, in the direction of the normal to the fluid element. The projection of $G_{f,i}$ on the solid element, P_i, belongs to S_i, and one computes the reference coordinate r and s of P_i in S_i. The weights are associated to each node of S_i. The coupling term will associate the DOFs of F_i to the DOFs of S_i with the corresponding weights. (see Figure 2.4). The FE formulation of the coupled fluid-structure model with an external harmonic force can thus be expressed as Equation (2.3) after discretization:

$$\left(-\omega^2 \begin{bmatrix} \mathbf{M}_s & \mathbf{0} \\ {}^t\mathbf{C} & \mathbf{M}_a \end{bmatrix} + \begin{bmatrix} \mathbf{K}_s & -\mathbf{C} \\ \mathbf{0} & \mathbf{K}_a \end{bmatrix} \right) \begin{bmatrix} \mathbf{u} \\ \mathbf{p}_a \end{bmatrix} = \begin{bmatrix} \mathbf{F} \\ \mathbf{0} \end{bmatrix} \quad (2.5)$$

where ω is the excitation frequency of the external harmonic loading $\mathbf{F}$ applied to the model; $\mathbf{M}$ is the mass matrix, $\mathbf{K}$ the stiffness matrix and $\mathbf{C}$ the coupling term between the compressible, non-weighing fluid and its surrounding structures. Subscript s denotes the model's solid part node while subscript a denotes the node in the model cavity; $\mathbf{u}_s$ is the physical displacement of the solid part, and $\mathbf{p}_a$ the physical pressure variation in the fluid. In this model, $\mathbf{u}_s$ has been rearranged in the ordering of: the excitation set ($\mathbf{u}_e$), the interface set ($\mathbf{u}_j$), internal DOFs of S_1 ($\mathbf{u}_{i_1}$), and internal DOFs of S_2 ($\mathbf{u}_{i_2}$). This same approach can be run for $\mathbf{M}$, $\mathbf{K}$, and $\mathbf{F}$:

$$\begin{bmatrix} \mathbf{u} \\ \mathbf{p}_a \end{bmatrix} = \begin{bmatrix} \mathbf{u}_e \\ \mathbf{u}_{j_1} \\ \mathbf{u}_{j_2} \\ \mathbf{u}_{i_1} \\ \mathbf{u}_{i_2} \\ \mathbf{p}_a \end{bmatrix}, \quad \mathbf{M} = \begin{bmatrix} \mathbf{M}_{ee} & \mathbf{0} & \mathbf{0} & \mathbf{M}_{ei_1} & \mathbf{0} & \mathbf{0} \\ \mathbf{0} & \mathbf{M}_{j_1j_1} & \mathbf{0} & \mathbf{M}_{j_1i_1} & \mathbf{0} & \mathbf{0} \\ \mathbf{0} & \mathbf{0} & \mathbf{M}_{j_2j_2} & \mathbf{0} & \mathbf{M}_{j_2i_2} & \mathbf{0} \\ \mathbf{M}_{i_1e} & \mathbf{M}_{i_1j_1} & \mathbf{0} & \mathbf{M}_{i_1i_1} & \mathbf{0} & \mathbf{0} \\ \mathbf{0} & \mathbf{0} & \mathbf{M}_{i_2j_2} & \mathbf{0} & \mathbf{M}_{i_2i_2} & \mathbf{0} \\ \mathbf{M}_{ae} & \mathbf{M}_{aj_1} & \mathbf{M}_{aj_2} & \mathbf{M}_{ai_1} & \mathbf{M}_{ai_2} & \mathbf{M}_{aa} \end{bmatrix}$$

$$\mathbf{F} = \begin{bmatrix} \mathbf{F}_e \\ \mathbf{0} \\ \mathbf{0} \\ \mathbf{0} \\ \mathbf{0} \\ \mathbf{0} \end{bmatrix}, \quad \mathbf{K} = \begin{bmatrix} \mathbf{K}_{ee} & \mathbf{0} & \mathbf{0} & \mathbf{K}_{ei_1} & \mathbf{0} & \mathbf{K}_{ea} \\ \mathbf{0} & \mathbf{K}_{j_1j_1} & \mathbf{K}_{j_1j_2} & \mathbf{K}_{j_1i_1} & \mathbf{0} & \mathbf{K}_{j_1a} \\ \mathbf{0} & \mathbf{K}_{j_2j_1} & \mathbf{K}_{j_2j_2} & \mathbf{0} & \mathbf{K}_{j_2i_2} & \mathbf{K}_{j_2a} \\ \mathbf{K}_{i_1e} & \mathbf{K}_{i_1j_1} & \mathbf{0} & \mathbf{K}_{i_1i_1} & \mathbf{0} & \mathbf{K}_{i_1a} \\ \mathbf{0} & \mathbf{0} & \mathbf{K}_{i_2j_2} & \mathbf{0} & \mathbf{K}_{i_2i_2} & \mathbf{K}_{i_2a} \\ \mathbf{0} & \mathbf{0} & \mathbf{0} & \mathbf{0} & \mathbf{0} & \mathbf{K}_{aa} \end{bmatrix}$$

- the subscript e represents the excitation node of the model
- the subscript i_s ($s = 1, 2$) represents the internal node of substructure-s of the solid part
- the subscript j_s ($s = 1, 2$) represents the node on the interface attached to substructure-s of the solid part
- the subscript a represents the node in the cavity

The zero terms in the matrix indicate that the corresponding parts are not connected to the same element. Since the rubber layer is assumed to contribute no mass but just stiffness, then the term in row 3 and column 2 is zero in the mass matrix and nonzero in the stiffness matrix. The nodes of j_1 and j_2 have been combined as j in the following analysis for the sake of simplicity.

2.2 Theory of triple modal synthesis

The modal analysis based on the Ritz-Galerkin projection using appropriate Ritz vectors, allow us to construct reduced models expressed in terms of physical displacement vector field u in the structure, and pressure variation vector p describing the behavior of the fluid.

The reduction technique developed in this section is an extension of the work found in [Besset 2011]. One improvement is that the excitation set and interface set of the structured part are handled differently with two distinct techniques. A double modal synthesis described in chapter 1.2 is first applied on the structural part, then a third reduction on the cavity modes is applied over the entire fluid domain. Acoustic modes in rigid motionless cavity are introduced as Ritz projection vector basis and plays a fundamental role in the Ritz-Galerkin procedure, including the static solution of the coupled system.

According to [Besset 2011], the cavity modes correspond to the free modes of the fluid. In our cases, nodes in the cavity represent the majority of DOFs. The cavity modes are denoted ϕ_{aa}, which are the solution to the following eigenvalue problem:

$$\left(-\omega^2 \mathbf{M}_{aa} + \mathbf{K}_{aa}\right) \phi_{aa} = \mathbf{0} \tag{2.6}$$

The reduced basis of the entire model is expressed in Equation (2.7) by combining the static constraint modes, branch modes, fixed interface modes and cavity modes:

$$\mathbf{T} = \begin{bmatrix} \mathbf{I}_e & \mathbf{0} & \mathbf{0} & \mathbf{0} & \mathbf{0} \\ \mathbf{0} & \boldsymbol{\Phi}_{\mathrm{B}_j} & \mathbf{0} & \mathbf{0} & \mathbf{0} \\ \boldsymbol{\Psi}_{\mathrm{CB}_{i_1 e}} & \boldsymbol{\Psi}_{\mathrm{B}_{i_1 j}} & \boldsymbol{\Phi}_{i_1 i_1} & \mathbf{0} & \mathbf{0} \\ \boldsymbol{\Psi}_{\mathrm{CB}_{i_2 e}} & \boldsymbol{\Psi}_{\mathrm{B}_{i_2 j}} & \mathbf{0} & \boldsymbol{\Phi}_{i_2 i_2} & \mathbf{0} \\ \mathbf{0} & \mathbf{0} & \mathbf{0} & \mathbf{0} & \boldsymbol{\Phi}_{aa} \end{bmatrix} \tag{2.7}$$

In projecting the modal space onto the physical space with the transformation matrix $\mathbf{T}$, the physical coordinates are thus expressed by the modal coordinates $\mathbf{q}$ as follows:

$$\begin{cases} \mathbf{u}_e = \mathbf{q}_e \\ \mathbf{u}_j = \boldsymbol{\Phi}_{\mathrm{B}_j} \mathbf{q}_j \\ \mathbf{u}_{i_s} = \boldsymbol{\Phi}_{i_s i_s} \mathbf{q}_{i_s} + \boldsymbol{\Psi}_{\mathrm{CB}_{i_s e}} \mathbf{q}_e + \boldsymbol{\Psi}_{\mathrm{B}_{i_s j}} \mathbf{q}_j \\ \mathbf{p}_a = \boldsymbol{\Phi}_{aa} \mathbf{q}_a \end{cases} \tag{2.8}$$

When considering Rayleigh damping in the model, the governing equation of the reduced model becomes:

$$\left(-\omega^2 \bar{\mathbf{M}} + i\omega \bar{\mathbf{D}} + \bar{\mathbf{K}}\right) \mathbf{q} = \bar{\mathbf{F}} \tag{2.9}$$

where

$$\begin{cases} \bar{\mathbf{M}} = {}^t\mathbf{T}\mathbf{M}\mathbf{T}, \quad \bar{\mathbf{K}} = {}^t\mathbf{T}\mathbf{K}\mathbf{T}, \\ \bar{\mathbf{D}} = {}^t\mathbf{T}\mathbf{D}\mathbf{T}, \quad \bar{\mathbf{F}} = {}^t\mathbf{T}\mathbf{F} \end{cases}$$

The stiffness matrix in the reduced motion equation is diagonal, due to the orthogonal properties of the modes used in the modal analysis. Moreover, according to the classical decoupling hypothesis of the damping matrix, also known as Basile's hypothesis [Imbert 1979], the Rayleigh damping matrix is assumed to be diagonal in the new basis. The explicit form of the governing motion equation can thus be expressed as:

$$\left(-\omega^2 \begin{pmatrix} \mathbf{m}_e & \bar{\mathbf{M}}_{ej} & \bar{\mathbf{M}}_{ei_1} & \bar{\mathbf{M}}_{ei_2} & \bar{\mathbf{M}}_{ea} \\ \bar{\mathbf{M}}_{je} & \mathbf{m}_j & \bar{\mathbf{M}}_{ji_1} & \bar{\mathbf{M}}_{ji_2} & \bar{\mathbf{M}}_{ja} \\ \bar{\mathbf{M}}_{i_1e} & \bar{\mathbf{M}}_{i_1j} & \mathbf{m}_{i_1} & \mathbf{0} & \bar{\mathbf{M}}_{i_1a} \\ \bar{\mathbf{M}}_{i_2e} & \bar{\mathbf{M}}_{i_2j} & \mathbf{0} & \mathbf{m}_{i_2} & \bar{\mathbf{M}}_{i_2a} \\ \bar{\mathbf{M}}_{ae} & \bar{\mathbf{M}}_{aj} & \bar{\mathbf{M}}_{ai_1} & \bar{\mathbf{M}}_{ai_2} & \mathbf{m}_a \end{pmatrix} + i\omega \begin{pmatrix} \mathbf{d}_e & \mathbf{0} & \mathbf{0} & \mathbf{0} & \mathbf{0} \\ \mathbf{0} & \mathbf{d}_j & \mathbf{0} & \mathbf{0} & \mathbf{0} \\ \mathbf{0} & \mathbf{0} & \mathbf{d}_{i_1} & \mathbf{0} & \mathbf{0} \\ \mathbf{0} & \mathbf{0} & \mathbf{0} & \mathbf{d}_{i_2} & \mathbf{0} \\ \mathbf{0} & \mathbf{0} & \mathbf{0} & \mathbf{0} & \mathbf{d}_a \end{pmatrix} \right.$$
$$\left. + \begin{pmatrix} \mathbf{k}_e & \bar{\mathbf{K}}_{ej} & \bar{\mathbf{K}}_{ei_1} & \bar{\mathbf{K}}_{ei_2} & \mathbf{0} \\ \bar{\mathbf{K}}_{je} & \mathbf{k}_j & \bar{\mathbf{K}}_{ji_1} & \bar{\mathbf{K}}_{ji_2} & \mathbf{0} \\ \bar{\mathbf{K}}_{i_1e} & \bar{\mathbf{K}}_{i_1j} & \mathbf{k}_{i_1} & \mathbf{0} & \mathbf{0} \\ \bar{\mathbf{K}}_{i_2e} & \bar{\mathbf{K}}_{i_2j} & \mathbf{0} & \mathbf{k}_{i_2} & \mathbf{0} \\ \mathbf{0} & \mathbf{0} & \mathbf{0} & \mathbf{0} & \mathbf{k}_a \end{pmatrix} \right) \begin{pmatrix} \mathbf{u}_e \\ \mathbf{q}_j \\ \mathbf{q}_{i_1} \\ \mathbf{q}_{i_2} \\ \mathbf{q}_a \end{pmatrix} = \begin{pmatrix} \bar{\mathbf{F}}_e \\ \mathbf{0} \\ \mathbf{0} \\ \mathbf{0} \\ \mathbf{0} \end{pmatrix} \tag{2.10}$$

This explicit formulation allows preceding the CMS, which may be very useful when treating assembled structures with local modifications and which serves as the basis to introduce the subsequent evaluation criteria presented in Section 2.4.

2.3 Criteria characterizing acoustic comfort

Various standards exist for the measurement of the sound pressure level, for example A-, B-, C-, D- and Z-weightings according to IEC 61672 standards [Aarts 1992]. Among these standards, C-frequency-weighting and its fitting is mandated to precision sound level meters for testing; D-frequency-weighting was initially designed for the measurement of high level aircraft noise and is now only used for non-bypass engines to military aircrafts; Z-frequency-weighting was introduced to replace the Linear frequency weighting often fitted by manufacturers, while this change was needed as each sound level meter manufacturer could choose their own frequency cut-offs. The most commonly used curve related to the measurement of sound pressure level is A-weighting, which is now mandated for light civilian aircraft measurements, environmental noise measurement and potential hearing damage measurement [Berger 2003].

The A-weighting function that acts on the amplitude spectrum is defined by [Berger 2003]:

$$R_A(f) = \frac{12200^2 \cdot f^4}{(f^2 + 20.6^2)\sqrt{(f^2 + 107.7^2)(f^2 + 737.9^2)}(f^2 + 12200^2)} \tag{2.11}$$

In order to ensure the normalization to 0 dB at 1000 Hz, an offset value of 2 is added to the un-weighted sound level in dB units:

$$A(f) = 2.0 + 20\lg(R_A(f)) \tag{2.12}$$

The pressure variations in the cavity $(P(f))$ is at first converted to $L_p(f)$ with the following equation [Berger 2003]:

$$L_p(f) = 10 \cdot \lg \left(\frac{P}{P_{ref}} \right)^2 \quad P_{ref} = 2 \times 10^{-5} \quad \text{Pa} \tag{2.13}$$

A new criteria reflecting human perception is thus defined:

$$L_a(f) = L_p(f) + A(f) \tag{2.14}$$

2.4 Modal parameters characterizing noise transmission

By analogy with criteria presented in chapter 1.3, rather than calculating pressure variations in the cavity, this section will define the evaluation criteria corresponding to vibration transmission paths in the model. The vibration transmission paths start from an external loading set, extend through components in the model, and finally induce pressure variation in the cavity. Several representative noise transmission paths from the excitation point to the cavity are illustrated in Figure 2.5.

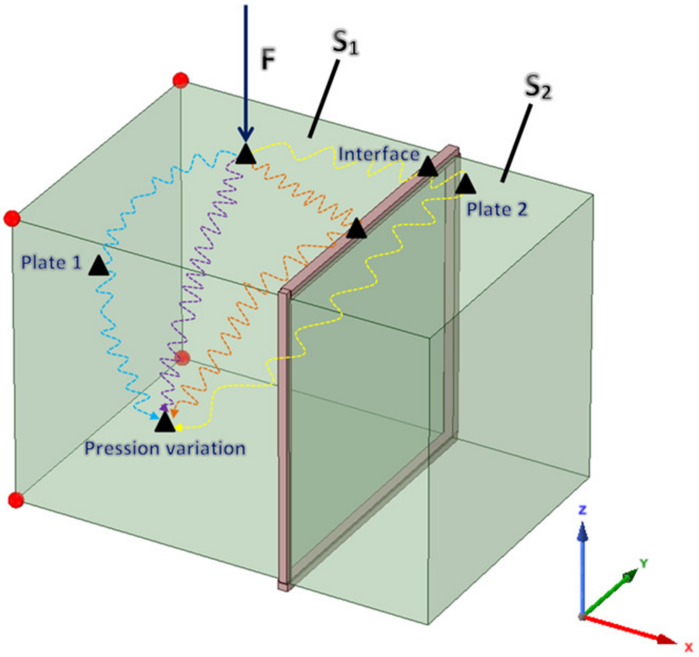

Figure 2.5: Noise transmission in the model

Let's note that the criteria corresponding to various physical meanings may be easily derived from the explicit motion equation. The seven criteria devoted to illustrating noise transmission paths between substructures, as shown in Figure 2.6, have been investigated. Three modal parameters were found to be influenced by the junction. Consequently, they vary with the junction configuration, while the other four modal parameters do not. Another strength of these modal criteria is the realization of a modal overview in order to analyze the influence of a certain mode on noise transmission. For similar models, similar criteria could be employed as well, but the expression would still differ.

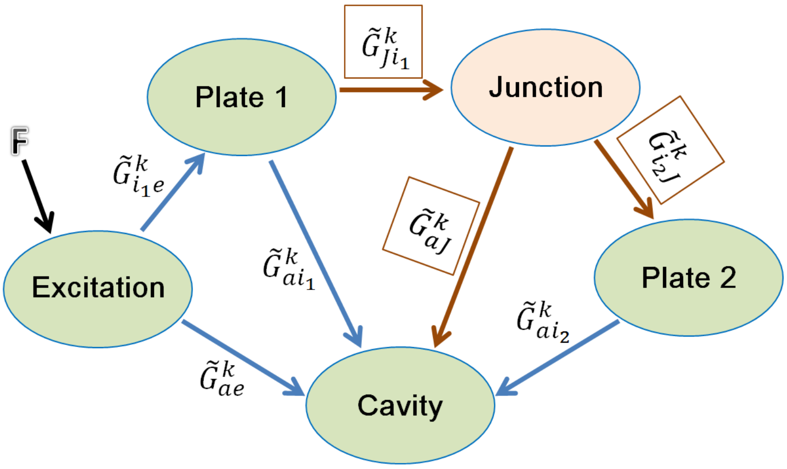

Figure 2.6: Physical illustration of evaluation criteria

By developing the last row of Equation (2.10), the modal coordinate of pressure variations in the cavity is written as:

$$q_a^k = \frac{\omega^2}{-\omega^2 m_a^k + i\omega d_a^k + k_a^k} \left(\bar{\mathbf{M}}^k_{ae}\mathbf{q}_e + \bar{\mathbf{M}}^k_{aj}\mathbf{q}_j + \bar{\mathbf{M}}^k_{ai_1}\mathbf{q}_{i_1} + \bar{\mathbf{M}}^k_{ai_2}\mathbf{q}_{i_2} \right) \tag{2.15}$$

where k indicates the k^{th} row in corresponding matrix or vector, *i.e.*, $\mathbf{M}^k_{ae}$ stands for the k^{th} row of $\mathbf{M}_{ae}$ and q_a^k stands for the k^{th} component of $\mathbf{q}_a$.

In projecting modal coordinates onto physical coordinates, with the transformation matrix described in Equation (2.8) and by retaining N_a acoustic modes, the physical pressure variation is mainly governed by Equation (2.16):

$$\begin{aligned} \mathbf{p}_a &= \sum_{k=1}^{N_a} \mathbf{\Phi}_a^k q_a^k \\ &= \sum_{k=1}^{N_a} \mathbf{u}_e \lambda_a^k \tilde{\mathbf{G}}^k_{ae} + \sum_{k=1}^{N_a} \mathbf{u}_j \lambda_a^k \tilde{\mathbf{G}}^k_{aj} + \sum_{k=1}^{N_a} \mathbf{u}_{i_1} \lambda_a^k \tilde{\mathbf{G}}^k_{ai_1} + \sum_{k=1}^{N_a} \mathbf{u}_{i_2} \lambda_a^k \tilde{\mathbf{G}}^k_{ai_2} \end{aligned} \tag{2.16}$$

where

$$\omega_a^k = \sqrt{\frac{k_a^k}{m_a^k}}, \quad \lambda_a^k(\omega) = \frac{\left(\frac{\omega}{\omega_a^k}\right)^2}{1 - \left(\frac{\omega}{\omega_a^k}\right)^2 + 2i\xi_a^k \left(\frac{\omega}{\omega_a^k}\right)}, \quad d_a^k = 2\xi_a^k \sqrt{k_a^k m_a^k},$$

$$
\begin{aligned}
\tilde{\mathbf{G}}^k_{ae} &= \frac{\mathbf{\Phi}^k_a \left(\bar{\mathbf{M}}^k_{ae} - \bar{\mathbf{M}}^k_{ai_1} \mathbf{\Phi}^{-1}_{i_1 i_1} \mathbf{\Psi}_{\mathrm{CB}_{i_1 e}} - \bar{\mathbf{M}}^k_{ai_2} \mathbf{\Phi}^{-1}_{i_2 i_2} \mathbf{\Psi}_{\mathrm{CB}_{i_2 e}} \right)}{m^k_a} \\
\tilde{\mathbf{G}}^k_{aj} &= \frac{\mathbf{\Phi}^k_a \left(\bar{\mathbf{M}}^k_{aj} - \bar{\mathbf{M}}^k_{ai_1} \mathbf{\Phi}^{-1}_{i_1 i_1} \mathbf{\Psi}_{\mathrm{B}_{i_1 j}} - \bar{\mathbf{M}}^k_{ai_2} \mathbf{\Phi}^{-1}_{i_2 i_2} \mathbf{\Psi}_{\mathrm{B}_{i_2 j}} \right) \mathbf{\Phi}^{-1}_{\mathrm{B}_j}}{m^k_a} \\
\tilde{\mathbf{G}}^k_{ai_1} &= \frac{\mathbf{\Phi}^k_a \left(\bar{\mathbf{M}}^k_{ai_1} \mathbf{\Phi}^{-1}_{i_1 i_1} \right)}{m^k_a} \\
\tilde{\mathbf{G}}^k_{ai_2} &= \frac{\mathbf{\Phi}^k_a \left(\bar{\mathbf{M}}^k_{ai_2} \mathbf{\Phi}^{-1}_{i_2 i_2} \right)}{m^k_a}
\end{aligned}
$$

In addition, let's note that $\mathbf{\Phi}^{-1}_{\mathrm{B}_j} = {}^t\mathbf{\Phi}_{\mathrm{B}_j} {}^t\mathbf{\Psi}_S \mathbf{M} \mathbf{\Psi}_S$, it can be substituted into the above formulations in order to save computational time.

Four modal terms can thus be extracted from Equation (2.16), where $\lambda^k_a \tilde{\mathbf{G}}^k_{ae}$ indicates the pressure variation excited by the excitation set; $\lambda^k_a \tilde{\mathbf{G}}^k_{ai_1}$ reports the pressure variation triggered by the displacement of S_1; $\lambda^k_a \tilde{\mathbf{G}}^k_{aj}$ represents the pressure variation stimulated by junction movement; and lastly $\lambda^k_a \tilde{\mathbf{G}}^k_{ai_2}$ denotes the pressure variation caused by S_2. Let's also note that the explicit expression of $\lambda^k_a \tilde{\mathbf{G}}^k_{aj}$ pertains to branch modes, yet branch modes vary according to interface configuration. $\lambda^k_a \tilde{\mathbf{G}}^k_{aj}$ can therefore be investigated in the optimization process.

By developing the second row of Equation (2.10) and then substituting physical coordinates for the modal coordinates with Equation (2.8) and retaining N_B branch modes, the physical displacements of the interface are obtained:

$$
\begin{aligned}
\mathbf{u}_j =& \sum_{k=1}^{N_B} \mathbf{\Phi}^k_{\mathrm{B}_j} q^k_j \\
=& \sum_{k=1}^{N_B} \lambda^k_B \tilde{\mathbf{G}}^k_{ji_1} \mathbf{u}_{i_1} \\
&+ \sum_{k=1}^{N_B} \frac{\omega^2 \mathbf{\Phi}^k_{\mathrm{B}_j} (\bar{\mathbf{M}}^k_{je} - \bar{\mathbf{M}}^k_{ji_1} \mathbf{\Phi}^{-1}_{F_1} \mathbf{\Psi}_{\mathrm{CB}_{i_1 e}} - \bar{\mathbf{M}}^k_{ji_2} \mathbf{\Phi}^{-1}_{i_2 i_2} \mathbf{\Psi}_{\mathrm{CB}_{i_2 e}}) \mathbf{u}_e}{-\omega^2 m^k_B + i\omega d^k_B + k^k_B} \\
&- \sum_{k=1}^{N_B} \frac{\omega^2 \mathbf{\Phi}^k_{\mathrm{B}_j} (\bar{\mathbf{M}}^k_{ji_1} \mathbf{\Phi}^{-1}_{F_1} \mathbf{\Psi}_{\mathrm{B}_{i_1 j}} \mathbf{\Phi}^{-1}_{\mathrm{B}_j} + \bar{\mathbf{M}}^k_{ji_2} \mathbf{\Phi}^{-1}_{i_2 i_2} + \mathbf{\Psi}_{\mathrm{B}_{i_2 j}} \mathbf{\Phi}^{-1}_{\mathrm{B}_j}) \mathbf{u}_j}{-\omega^2 m^k_B + i\omega d^k_B + k^k_B} \\
&+ \sum_{k=1}^{N_B} \frac{\omega^2 \mathbf{\Phi}^k_{\mathrm{B}j} \bar{\mathbf{M}}^k_{ji_2} \mathbf{\Phi}^{-1}_{i_2 i_2} \mathbf{u}_{i_2}}{-\omega^2 m^k_B + i\omega d^k_B + k^k_B}
\end{aligned}
\tag{2.17}
$$

The decoupled expression of $\mathbf{u}_j$ turns to be:

$$\begin{aligned}
&(1+\sum_{k=1}^{N_B}\frac{\omega^2\boldsymbol{\Phi}_{\mathrm{B}_j}^k(\bar{\mathbf{M}}_{ji_1}^k\boldsymbol{\Phi}_{F_1}^{-1}\boldsymbol{\Psi}_{\mathrm{B}_{i_1j}}\boldsymbol{\Phi}_{\mathrm{B}_j}^{-1}+\bar{\mathbf{M}}_{ji_2}^k\boldsymbol{\Phi}_{i_2i_2}^{-1}+\boldsymbol{\Psi}_{\mathrm{B}_{i_2j}}\boldsymbol{\Phi}_{\mathrm{B}_j}^{-1})}{-\omega^2m_B^k+i\omega d_B^k+k_B^k})\mathbf{u}_j\\
&=\sum_{k=1}^{N_B}\boldsymbol{\Phi}_{\mathrm{B}_j}^k q_j^k\\
&=\sum_{k=1}^{N_B}\lambda_B^k\tilde{\mathbf{G}}_{ji_1}^k\mathbf{u}_{i_1}\\
&+\sum_{k=1}^{N_B}\frac{\omega^2\boldsymbol{\Phi}_{\mathrm{B}_j}^k(\bar{\mathbf{M}}_{je}^k-\bar{\mathbf{M}}_{ji_1}^k\boldsymbol{\Phi}_{F_1}^{-1}\boldsymbol{\Psi}_{\mathrm{CB}_{i_1e}}-\bar{\mathbf{M}}_{ji_2}^k\boldsymbol{\Phi}_{i_2i_2}^{-1}\boldsymbol{\Psi}_{\mathrm{CB}_{i_2e}})\mathbf{u}_e}{-\omega^2m_B^k+i\omega d_B^k+k_B^k}\\
&+\sum_{k=1}^{N_B}\frac{\omega^2\boldsymbol{\Phi}_{\mathrm{B}j}^k\bar{\mathbf{M}}_{ji_2}^k\boldsymbol{\Phi}_{i_2i_2}^{-1}\mathbf{u}_{i_2}}{-\omega^2m_B^k+i\omega d_B^k+k_B^k}
\end{aligned}\tag{2.18}$$

where

$$\omega_B^k=\sqrt{\frac{k_B^k}{m_B^k}},\quad \lambda_B^k\left(\omega\right)=\frac{\left(\frac{\omega}{\omega_B^k}\right)^2}{1-\left(\frac{\omega}{\omega_B^k}\right)^2+2i\xi_B^k\left(\frac{\omega}{\omega_B^k}\right)},\quad d_B^k=2\xi_B^k\sqrt{k_B^km_B^k},$$

$$\tilde{\mathbf{G}}_{ji_1}^k=\frac{\boldsymbol{\Phi}_{\mathrm{B}j}^k\left(\bar{\mathbf{M}}_{ji_1}^k\boldsymbol{\Phi}_{i_1i_1}^{-1}\right)}{m_B^k}$$

The modal parameter extracted from Equation (2.18) is: $\lambda_j^k\tilde{\mathbf{G}}_{ji_1}^k$. It denotes the displacement of the interface stimulated by the displacement of S_1 and moreover corresponds to the transmission path from the S_1 to the interface. In addition, $\tilde{\mathbf{G}}_{ji_1}^k$ varies with interface configuration, which can then be investigated in the optimization process.

By developing the third row of Equation (2.10) and then substituting physical coordinates for modal coordinates using Equation (2.8) while retaining N_{i_1} fixed interface modes of S_1, the physical displacement of S_1 is found to be governed by Equation (2.19):

$$\begin{aligned}
\mathbf{u}_{i_1}=&\boldsymbol{\Phi}_{i_1i_1}\mathbf{q}_{i_1}+\boldsymbol{\Psi}_{\mathrm{B}_{ji_1}}\mathbf{q}_j+\boldsymbol{\Psi}_{\mathrm{CB}_{ei_1}}\mathbf{u}_e\\
=&\left(\sum_{k=1}^{N_{i_1}}\lambda_{i_1}^k\tilde{\mathbf{G}}_{i_1e}^k+\boldsymbol{\Psi}_{\mathrm{CB}_{ei_1}}\right)\mathbf{u}_e\\
&+\sum_{k=1}^{N_{i_1}}\frac{\omega^2\boldsymbol{\Phi}_{i_1i_1}^k\bar{\mathbf{M}}_{i_1j}^k\mathbf{q}_j}{-\omega^2m_{i_1}^k+i\omega d_{i_1}^k+k_{i_1}^k}+\boldsymbol{\Psi}_{\mathrm{B}_{ji_1}}\mathbf{q}_j
\end{aligned}\tag{2.19}$$

where

$$\omega_{i_1}^k=\sqrt{\frac{k_{i_1}^k}{m_{i_1}^k}},\quad \lambda_{i_1}^k\left(\omega\right)=\frac{\left(\frac{\omega}{\omega_{i_1}^k}\right)^2}{1-\left(\frac{\omega}{\omega_{i_1}^k}\right)^2+2i\xi_{i_1}^k\left(\frac{\omega}{\omega_{i_1}^k}\right)},\quad d_{i_1}^k=2\xi_{i_1}^k\sqrt{k_{i_1}^km_{i_1}^k}$$

$$\tilde{\mathbf{G}}^k_{i_1e} = \frac{\mathbf{\Phi}^k_{i_1i_1}\bar{\mathbf{M}}^k_{i_1e}}{m^k_{i_1}}$$

Resonance occurs whenever $\omega = \omega^k_{i_1}$, *i.e.* $\lambda^k_{i_1}$ attain their peaks under this condition. Other terms may be neglected since the resonance is generally the main reason behind large pressure variations. The modal parameter characterizing vibration transmission from excitation set to S_1 is denoted: $\lambda^k_{i_1}\tilde{\mathbf{G}}^k_{i_1e}$.

By developing the fourth row of Equation (2.10) and then substituting physical coordinates for modal coordinates while retaining N_{i_2} fixed interface modes for S_2 and then grouping terms dependent on $\mathbf{u}_j$, the physical displacement of S_2 can be expressed as:

$$\begin{aligned}\mathbf{u}_{i_2} =& \mathbf{\Phi}_{i_2i_2}\mathbf{q}_{i_2} + \mathbf{\Psi}_{\mathrm{B}_{ji_2}}\mathbf{q}_j + \mathbf{\Psi}_{\mathrm{CB}_{ei_2}}\mathbf{q}_e \\ =& \left(\sum_{k=1}^{N_{i_2}} \lambda^k_{i_2}\tilde{\mathbf{G}}^k_{i_2j} + \mathbf{\Psi}_{\mathrm{B}_{ji_2}}\mathbf{\Phi}^{-1}_{\mathrm{B}_j}\right)\mathbf{u}_j \\ &+ \sum_{k=1}^{N_{i_2}} \frac{\omega^2\mathbf{\Phi}^k_{i_2i_2}\bar{\mathbf{M}}^k_{i_2e}\mathbf{u}_e}{-\omega^2 m^k_{i_2} + i\omega d^k_{i_2} + k^k_{i_2}} + \mathbf{\Psi}_{\mathrm{CB}_{ei_2}}\mathbf{u}_e\end{aligned} \tag{2.20}$$

where

$$\omega^k_{i_2} = \sqrt{\frac{k^k_{i_2}}{m^k_{i_2}}}, \quad \lambda^k_{i_2}(\omega) = \frac{\left(\frac{\omega}{\omega^k_{i_2}}\right)^2}{1 - \left(\frac{\omega}{\omega^k_{i_2}}\right)^2 + 2i\xi^k_{i_2}\left(\frac{\omega}{\omega^k_{i_2}}\right)}, \quad d^k_{i_2} = 2\xi^k_{i_2}\sqrt{k^k_{i_2}m^k_{i_2}}$$

$$\tilde{\mathbf{G}}^k_{i_2j} = \frac{\mathbf{\Phi}^k_{i_2i_2}\bar{\mathbf{M}}^k_{i_2j}\mathbf{\Phi}^{-1}_{\mathrm{B}_j}}{m^k_{i_2}}$$

The modal term extracted from Equation (2.20) is $\lambda^k_{i_2}\tilde{\mathbf{G}}^k_{i_2j}$, which reveals the displacement of S_2 stimulated by the interface displacement. This term also represents the transmission path from the interface to S_2. Likewise, $\tilde{\mathbf{G}}^k_{i_2j}$ varies with interface configuration, and this warrants investigation for structural optimization.

Considering the example of the entire noise transmission path starting from the excitation point, passing through S_1, the interface, S_2 and finally arriving at the cavity, the pressure variations caused by this path can be written as:

$$\mathbf{p}_{as_2js_1e} = \sum_{k=1}^{N_a}\lambda^k_a\tilde{\mathbf{G}}^k_{ai_2}\sum_{k=1}^{N_{i_2}}\lambda^k_{i_2}\tilde{\mathbf{G}}^k_{i_2j}\sum_{k=1}^{N_B}\lambda^k_B\tilde{\mathbf{G}}^k_{ji_1}\sum_{k=1}^{N_{i_1}}\lambda^k_{i_1}\tilde{\mathbf{G}}^k_{i_1e}\mathbf{u}_e \tag{2.21}$$

According to the mathematical expression, if λ^k_j and λ^k_a, $\lambda^k_{i_1}$ or $\lambda^k_{i_2}$ reach their peaks at the same time, *i.e.* if the natural frequencies of branch modes equal to that of constraint modes, fixed interface modes or acoustic modes, then the pressure variations in the cavity become violent. In seeking to reduce noise level in the cavity, the coincidence of natural frequencies of the branch modes and the constraint modes, fixed interface modes or acoustic modes should be avoided. By regulating geometric parameters of the rubber layer in the system, this coincident effect can consequently be mitigated by redistributing the natural frequency of branch modes and by adjusting criteria based on the interface configuration. Similarly as the case of assembled plate system, the choice of modal parameters as objective functions in the optimization process is large. Herein three modal parameters depending on the interface configuration are considered to be dominant for indicating the influence of external load on the pressure variations in the cavity: $\lambda_a^k \tilde{\mathbf{G}}_{aj}$, $\lambda_B^k \tilde{\mathbf{G}}_{ji_1}$ and $\lambda_{i_2}^k \tilde{\mathbf{G}}_{i_2 j}$.

Chapter 3

Case study – linear systems

Contents

3.1 Numerical schemes for system optimization 41
3.2 Assembled plates 45
  3.2.1 Reduced model 48
  3.2.2 A modal overview based on Modal-based criteria 50
  3.2.3 Meta-models and Pareto optimal 53
  3.2.4 Conclusions 59
3.3 An assembled box filled with air 60
  3.3.1 Reduced model 62
  3.3.2 Modal-based criteria and sensitivity analysis 64
  3.3.3 Meta-models and Pareto optimal 69
  3.3.4 Conclusions 75

3.1 Numerical schemes for system optimization

Case studies on an assembled plates and a coupled fluid-structure system are performed in this chapter. The aim is to reduce the vibration level for the assembled plates system; and to improve the acoustic comfort in the cavity of the coupled fluid-structure system. To do this, the full FE models of the plates system and the coupled fluid-structure system are reduced by using double modal synthesis presented in Chapter 1 and triple modal synthesis in Chapter 2, respectively.

The optimization problem can be solved either by calculating directly the forced responses or pressure variations with the proposed modal synthesis or by analyzing the proposed modal parameters. For the second case by analyzing the proposed modal parameters, modal criteria characterizing vibration transmission in the system are extracted and defined as objective functions. Meta-models of these objective functions are determined with Kriging interpolation method, and finally the Pareto optimal is deduced by employing a multi-objective optimization algorithm. The optimization strategy is presented in the following.

Kriging approximations

Even though the computation cost of modeling complex systems is reduced with the proposed modal synthesis, the calculation cost of optimization problems nonetheless remains high. It is well known that objective functions need to be evaluated for many iterations during the optimization routine. Even with the most efficient criteria, optimization process appears to be very time-consuming. Once the corresponding Kriging interpolation models are constructed by using DACE toolbox [Lophaven 2002], optimization is achieved by applying a fast, elitist multi-objective genetic algorithm that has been programmed by Seshadri [Seshadri 2006].

The criteria deduced above cannot necessarily be derived with respect to the interface geometry parameters, yet the gradient of parameter evaluations is typically required during the Kriging approximations. To overcome this disadvantage, a new criterion possessing the same extreme as $\lambda_n^k \tilde{\mathbf{G}}_n^k$ is introduced:

$$\mathbf{C}_n = \frac{1}{4} \lg \sum_k \left| \lambda_n^k(\omega) \tilde{\mathbf{G}}_n^k \right|^4 \tag{3.1}$$

where k is the mode number; ω is the excitation frequency; $\lambda_n^k(\omega)\tilde{\mathbf{G}}_n^k$ is the modal terms extracted in Chapter 1.2 and Chapter 2.2; and $n = aj, ji_1, i_2j, ae, ai_1, i_1e, ai_2$.

Kriging is an interpolation method for which the interpolated values are modeled by a stochastic process governed by prior covariance, as opposed to a regression function chosen to optimize smoothness of the fitted values [Krige 1951]. The basic idea of Kriging is to predict the value of a function at a given point by computing a weighted average of the known values of the function in the neighborhood of the point. Under suitable assumptions on the priors, Kriging gives the best linear unbiased prediction of the intermediate values, which is widely used in the domain of computer experiments.

Kriging approximations are obtained by using the software package entitled DACE (Design and Analysis of Computer Experiments), which has been coded by Sondergaard [Lophaven 2002]. The DACE toolbox [Lophaven 2002] provides various regression and correlation models. The numerical steps are briefly presented as follows. A collection of design sites and their responses were first involved in running computer experiments. To ensure that all portions of the vector space are being represented, algorithms with space filling properties should be adopted to set the experimental design sites; the one used herein was the Latin hypercube sampling algorithm. Next, a regression model and stochastic process correlations were combined to establish the mathematical models. The utility of both the regression model and correlation model is: the regression model has been chosen to optimize the smoothness of fitted values, with the correlation model being governed by prior covariance. All surrogate models were carefully verified before serving as objective functions during the optimization. The mean squared error at the untried design sites is selected as the criterion used to evaluate the quality of surrogate models. Its test result is always very small whenever the size of input design sites is sufficiently large. Further details about the Kriging approximation can be found in Annexes A.

For our study cases, 10,000 simulations were carried out as computer experiments in order to construct the surrogate models. The range of design sites θ and l are equally distributed within a rectangular grid by means of applying Latin hypercube sampling. The test conducted on surrogate model that is composed of a ’poly0’ regression model and a Gaussian correlation model, worked quite well for the problem discussed below.

Multi-objective optimization algorithm

The optimization problem consists in determining the optimum thickness and length of the viscoelastic layer to reduce the vibratory phenomenon or vibro-acoustic phenomena in the system. The inequality constraints may result from serviceability requirements (upper and lower bounds for the thickness and length of the viscoelastic layer) and from the condition that the thickness variation law ensures the validity of the Kirchhoff plate theory. The optimization problem is formulated in Table 3.1:

Table 3.1: Formulation of the optimization problem

Design variables	the thickness θ and the length l of the rubber layer
Objective functions	$\mathbf{C}_{je}$, $\mathbf{C}_{ji_1}$, $\mathbf{C}_{ji_2}$, $\mathbf{C}_{i_2j}$ for plates system $\mathbf{C}_{aj}$, $\mathbf{C}_{ji_1}$ and $\mathbf{C}_{i_2j}$ for coupled system
Constraint functions	$\theta \in (0.1\ mm, 10\ mm)$ and $l \in (0.1\ mm, 10\ mm)$

The optimization problem consists in assessing trade-offs between multiples objectives and the problem turns out to be a multi-objective problem. In this case, solution requires a multi-objective algorithm such as Elitist Non-Dominated Sorting Genetic Algorithm version II (NSGA-II) [Deb 2002], in which a ranking selection method emphasizes current non-dominated solutions and a niching method maintains diversity in the population. A tremendous effort has in fact been made by the authors in coding a GA. The NSGA-II toolbox programmed by Seshadri [Seshadri 2006] has ultimately been adopted due to computational complexity, a lack of elitism and the sensitivity to GA parameters.

NSGA-II proceeds according to the steps outlined below: first, the population is initialized into each front based on non-domination, and each individual in each front is assigned a “fitness value". Except for the “fitness value", another parameter called “crowding distance" is also calculated for each individual. The “crowding distance" is a measure of how close an individual is to his neighbors. Second, based on these two parameters, parents are selected from the population by using binary tournament selection. Third, offspring are generated with simulated binary crossover [Deb 1994] and polynomial mutation [Deb 2002] operators. The next-generation individuals are then selected from the offspring and the current population. The process therefore repeats for the subsequent $N_{gen} - 1$ generations, where N_{gen} is the number of generations. Moreover, the best N_{pop} individuals are selected, where N_{pop} is the population size. The NSGA-II toolbox demonstrated its efficiency and good performance. When the generation number and population size are large enough, the Pareto front remains stable. Further details about the fast, elitist multi-objective genetic algorithm can be found in Annexes B. The NSGA-II procedure is illustrated in Figure 3.1.

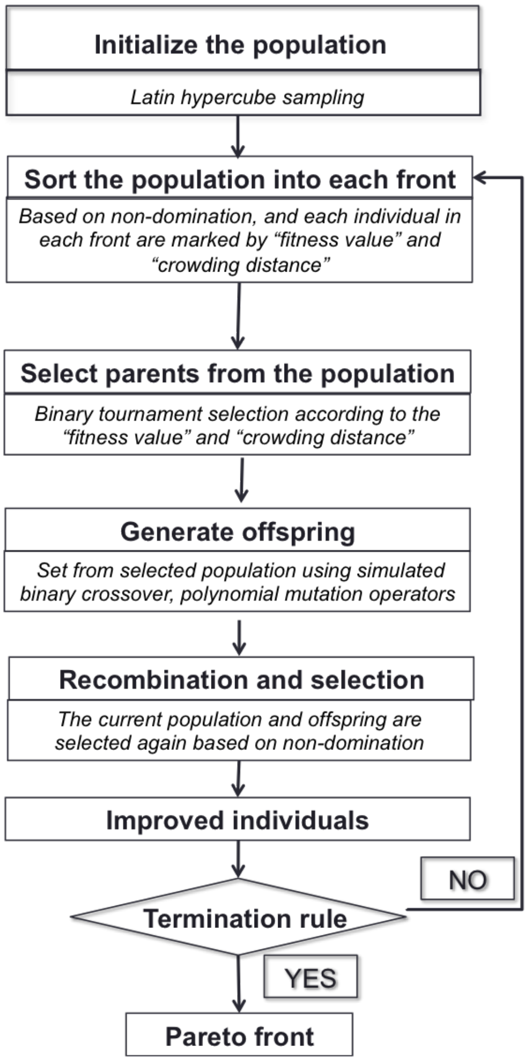
Initialize the population
Latin hypercube sampling
Sort the population into each front
Based on non-domination, and each individual in each front are marked by "fitness value" and "crowding distance"
Select parents from the population
Binary tournament selection according to the "fitness value" and "crowding distance"
Generate offspring
Set from selected population using simulated binary crossover, polynomial mutation operators
Recombination and selection
The current population and offspring are selected again based on non-domination
Improved individuals
NO
Termination rule
YES
Pareto front

Figure 3.1: Flow diagram of NSGA-II

A convergence study of the population number and generation number has also been carried out for our study cases. As a compromise between computational time and accuracy, 500 populations and 150 generations were chosen for this optimization, which permits a stable Pareto front.

For illustration, the primary techniques used during the entire procedure have been outlined in Figure 3.2. Special attention are paid to the 'quality control' in the simulation process: to validate the quality of the reduced model when passing from step 1 to step 2, we used two criteria, namely: the natural frequency, and the modal assurance criterion (MAC) value. For the evaluation of the accuracy of surrogate models when passing from step 3 to step 4, the mean squared error of the modal prediction parameters at untried points are evaluated. To justify a lower noise level with optimal interface configurations obtained in step 5, pressure variations inside the cavity derived from optimal design sites on the Pareto front are compared to those derived from arbitrary design sites by using the full FE model in step 1 (see Figure 3.2).

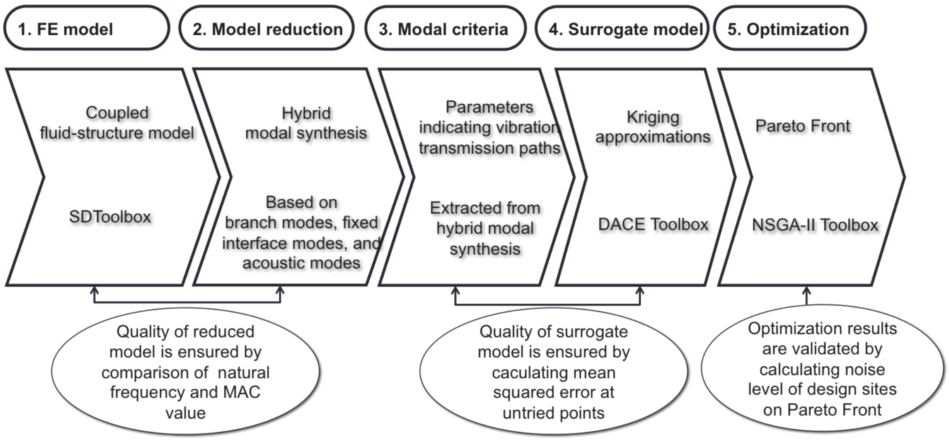
1. FE model
2. Model reduction
3. Modal criteria
4. Surrogate model
5. Optimization
Coupled fluid-structure model
SDToolbox
Hybrid modal synthesis
Based on branch modes, fixed interface modes, and acoustic modes
Parameters indicating vibration transmission paths
Extracted from hybrid modal synthesis
Kriging approximations
DACE Toolbox
Pareto Front
NSGA-II Toolbox
Quality of reduced model is ensured by comparison of natural frequency and MAC value
Quality of surrogate model is ensured by caculating mean squared error at untried points
Optimization results are validated by calculating noise level of design sites on Pareto Front

Figure 3.2: Process flow chart

3.2 Assembled plates

In this case study, we seek to reduce the vibration level of plate 2 of the assembled structural system. It should be mentioned that the choice of modal parameters as objective functions in the optimization process is large. Herein four modal parameters depending on the interface configuration are considered to be dominant for indicating the influence of external load on plate 2 vibration: $\mathbf{C}_{je}$, $\mathbf{C}_{ji_1}$, $\mathbf{C}_{ji_2}$ and $\mathbf{C}_{i_2j}$. Moreover, the analysis of these modal parameters permits identifying the responsible resonant modes. These parameters can then be employed for optimization, which turns out to be a multi-optimization problem since multiple parameters need to be minimized simultaneously.

A simple model, which features a similar geometry to that of an assembled vehicle system, is thus employed for simulation purposes. The system under consideration is two rectangular Kirchhoff plates connected by a viscoelastic layer, with four edge nodes clamped over the three translation and the three rotation directions, and Rayleigh damping in the structures. Compared to the Kirchhoff plates, the mass of the viscoelastic layer is negligible and more elastic. Since the major contribution of the viscoelastic layer for the built-up system is the correction of stiffness matrix in the translation directions, it is modeled by three spring elements to represent the stiffness in three translation directions. The assembled structure is illustrated in Figure 3.3.

A detailed view of how the rubber layer is padded on the plates can be seen in Figure 3.4. The rubber layer is modeled by springs along the interface between

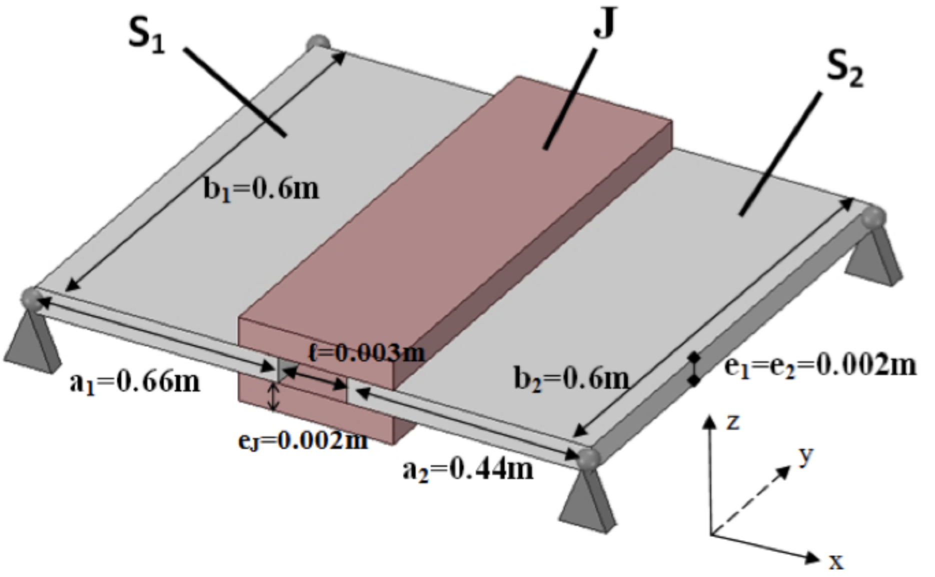
S1
J
S2
b1=0.6m
t=0.003m
a1=0.66m
b2=0.6m
e1=e2=0.002m
eJ=0.002m
a2=0.44m
z
y
x

Figure 3.3: The assembled plates model with its physical dimensions

S_1 and S_2. The proposed rubber layer model is assumed to be viscoelastic, which can be considered as fairly reasonable for describing the stress-strain relationship of this rubber specimen. Since the rubber layer mass is negligible compared to the plate mass and since the rubber layer stiffness is far less than the plate stiffness. θ and l represent respectively the thickness and length of the rubber layer. These parameters are related to the stiffness value of the rubber layer.

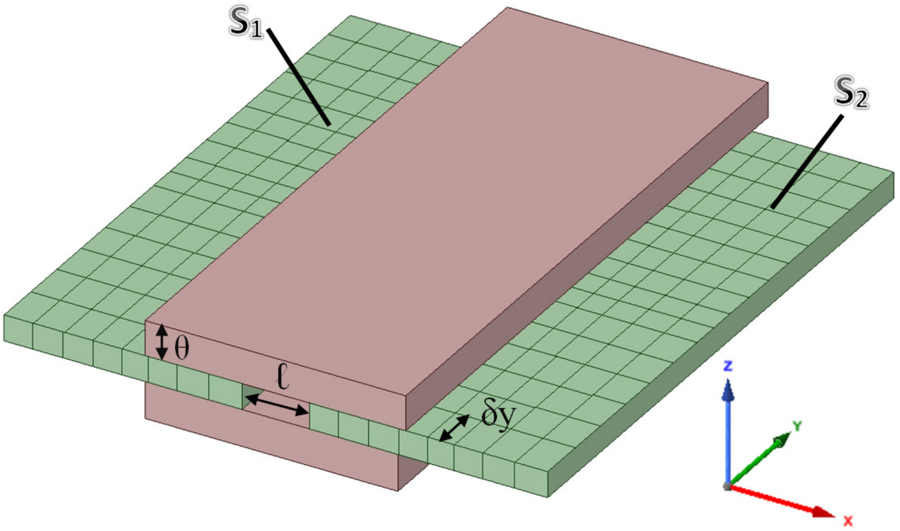
S1
S2
θ
ℓ
δy
z
Y
x

Figure 3.4: Detail geometry of plate and rubber layer

For the sake of simplicity, scalar springs have been introduced to model the rubber layer, which is considered as reasonable for describing the stress-strain relationship of the rubber specimen. Since the rubber layer mass is negligible compared to the plate mass and since the rubber layer stiffness is far less than the plate stiffness. The rubber layer material is assumed to be orthotropic, in considering the Young's modulus value (E) along connection axis x and shear modulus ($G = E/(2(1+\nu))$) along both the y and z axes. This rubber material can be deemed as elastic for small deformations. To ensure the quasi-incompressibility of the rubber material in volume term, a Poisson's ratio value of 0.49 has been adopted. Young's modulus varies with carbon content in the rubber. The Young's modulus value adopted in this study case agrees with that of a real rubber material in order of magnitude [James 1943]. The three equivalent linear element stiffness (*i.e.* k_x, k_y, and k_z) are given in Equation (3.2):

$$\begin{cases} k_x = E\dfrac{\delta y}{l}\theta, \\ k_y = G\dfrac{\delta y}{l}\theta, \\ k_z = G\dfrac{\delta y}{l}\theta. \end{cases} \tag{3.2}$$

where θ is the thickness of the rubber layer, l is the length of the rubber layer and δy is the mesh width. It should be noted that these stiffness terms depend on $\frac{\theta}{l}$, thus the effective variable to be optimized is in fact the ratio of θ and l.

The viscoelastic layer is located at $x = 0.6875m$. Structural hysteresis damping is integrated in the system, with the hysteresis damping coefficient equals to 0.01 on the plates and 0.02 on the interface. The external loading is applied at $a = 0.55m, b = 0.36m$ in form of tire balance $\mathbf{F} = m\omega^2 R\cos\omega t$ at a frequency ω, with $m = 6\ g$. Further details on the geometric dimension and material properties are provided in Table 3.2.

For a plate of thickness e, Young's modulus E and Poisson's ratio ν, the bending rigidity has the form:

$$D = \frac{Ee^3}{12(1-\nu^2)} \tag{3.3}$$

The wavenumber k for an exitation frequency of 100 Hz is:

$$k = \sqrt{\omega}\ (\frac{e\rho}{D})^{\frac{1}{4}} \tag{3.4}$$

where ρ is the mass density.

With a targeted frequency band ranging from 0 to 100 Hz, the minimum value of wavelength is found to be 0.4431 m by using the following relation [FRANK 2007]:

$$\lambda = \frac{2\pi}{k} \tag{3.5}$$

A convergence study on the FE mesh size has been performed, and 4 elements per wavelength are utilized for the mesh size, *i.e.* $\delta_x = 0.1375\ mm$ as element

Table 3.2: Outlines of model geometry and material properties

	Physical quantity	Unit	Value
Plates	material		steel
	length	m	1.1
	width	m	0.6
	thickness	mm	2
	Poisson's ratio		0.285
	density	kg/m^3	7800
	Young's modulus	Pa	2.10E+11
	Shear modulus	Pa	8.17E+11
Joint	thickness	mm	2
	length	mm	3
	Poisson's ratio		0.49
	Young's modulus	Pa	1.0E+08
	Shear modulus	Pa	3.4E+07

length and $\delta_y = 0.12\ mm$ as element width. This provides a good compromise between accuracy and computation time. The system is discretized into a FE model with 18 stiffness elements on the interface, 25 rectangular elements on S_1 and 15 rectangular elements on S_2. The FE model contains 54 nodes and 180 DOFs, in considering translation displacement in x and z direction and rotation in θ_y. As boundary conditions, the four nodes on the edge of the plate are clamped to the ground.

3.2.1 Reduced model

The double modal synthesis presented in Chapter 1.2 is employed to study the dynamic performance of the system, so as to reduce the computational cost.

The reduction coefficient, denoted by r_c, is a common criterion in the mode synthesis method; it is defined as follows: if the maximum frequency of the targeted frequency band is 100 Hz, then the modes less than $r_c * 100$ Hz are all to be selected to describe the model's dynamic behavior. For the determination of reduction coefficient for this plates system, 0.002 m and 0.003 m are respectively set as thickness and length of the rubber layer. The frequency band of interest of the external load is from 0 Hz to 100 Hz. According to a convergence study of the reduction coefficient, $\alpha = 3$ is used for all types of retained modes, *i.e.* the fixed interface modes of each plate and branch modes of the built-up model are retained up to $3 * 100$ Hz.

In order to verify the quality of reduced model, three metrics are used in this part, natural frequency error between the reduced model and the complete FE model, modal assurance criterion between reduced mode shapes and accurate mode shapes, and forced responses error between the reduced model and the complete FE model.

A comparison of system's natural frequency and transfer function is carried out as shown respectively in Figures 3.5 and 3.6. In addition, MAC values have been calculated to compare the reduced mode and exact mode shapes. The MAC values are in fact greater than 0.9 up to 100 Hz, which confirms the quality of the reduced model.

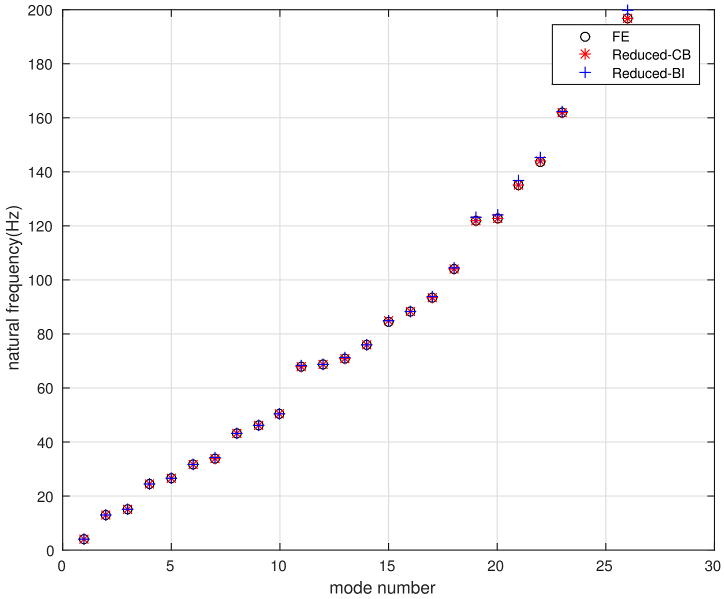

Figure 3.5: Comparison of normal modes frequencies of the full FE model and the reduced model

Table 3.3 compares the retained DOFs of the reduced model and the DOFs of the full FE model. It is shown that 50% of DOFs are truncated by applying the proposed modal synthesis. This finding implies a significant reduction in the simulation time for large-scale systems.

Table 3.3: Comparison of mode number retained in the full and reduced model

Model	Excitation	Branch Mode	S_1: Fixed Interface Mode	S_2: Fixed Interface Mode	Total
FE	1	36	83	48	96
$\alpha = 3$	1	22	21	13	57

Simulations have been conducted on a server containing 32 Xeon (R) processors running at 2.9 GHz. Considering the 5,000 linearly-spaced excitation frequencies from 0 to 350 Hz, the CPU time consumed when calculating average pressure vari-

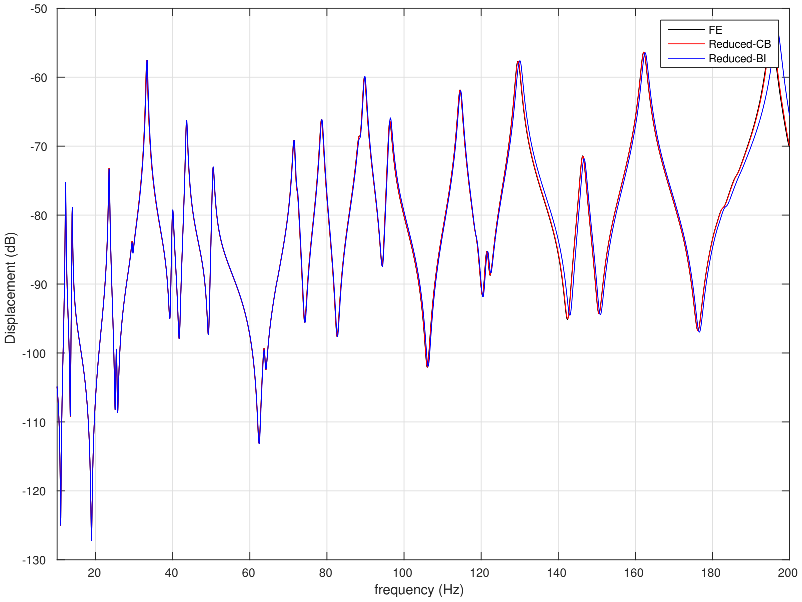

Figure 3.6: Comparison of forced responses of the full FE and reduced model

ations in the cavity over this frequency band is compared for typical models: the full FE model, the reduced model obtained using Craig & Bampton method, the reduced model obtained with the double modal synthesis method, and lastly the reduced model obtained with the proposed modal synthesis method, as presented in Table 3.4. All reduction techniques serve to lower computation time, and several observations are worth discussing. The double modal synthesis consumes less time than the Craig & Bampton method by also condensing interface DOFs. Craig & Bampton, on the other hand, conserves all DOFs on the interface, which may be prohibitive in certain cases. The proposed modal synthesis method consumes a bit more time than the double modal synthesis method; this outcome is reasonable since it conserves all special region modes.

Table 3.4: CPU time comparison of different reduction techniques

Methods	FE (all DOFs retained)	Craig&Bampton Method	Extensive Modal Synthesis
CPU time (s)	5.39	2.35	1.09

3.2.2 A modal overview based on Modal-based criteria

A modal overview is accessible with the modal parameters defined in Chapter 1.2: $\mathbf{C}_{je}$, $\mathbf{C}_{ji_1}$, $\mathbf{C}_{ji_2}$ and $\mathbf{C}_{i_2j}$. The modal criteria are investigated for the following interface configurations, as depicted in Table 3.5:

Table 3.5: Interface configurations

Variables	Group 1	Group 2	Group 3	Group 4	Group 5	Group 6
Length (mm)	5.3	8.5	7	0.1	3	0.9
Thickness (mm)	0.8	6.1	6.1	10	1.9	8.7

On one hand, different interface configurations render the responsible modes for vibration of one certain modal parameter different. In Figure 3.7 for $\mathbf{C}_{ej}$, mode 2 and 5 are the dominant mode for vibration at 45.5 Hz in case of group 1, 2 and 5; while mode 1, 2, 3 and 4 are responsible for the vibration in case of group 3; and mode 3 for group 4 and 6. If we compare $\mathbf{C}_{ej}$ for group 2, 3 and 4 with other configurations, the average level of these modal parameters are lower, *i.e.* the maximum value 2.5 *vs* 3.5. Whereas in Figure 3.8 for $\mathbf{C}_{ji_1}$, mode 2, 4, 5 and 6 are the dominant modes for vibration at 45.5 Hz in case of group 1; while mode 2 is responsible for the vibration in case of group 2, 3 and 5; and mode 2 and 4 in case of group 4 and 6. If we compare $\mathbf{C}_{ji_1}$ for group 1 with other configurations, the average level of these modal parameters are lower. The same analysis can be carried out for $\mathbf{C}_{ji_2}$ and $\mathbf{C}_{i_2j}$ in Figures 3.9 and 3.10.

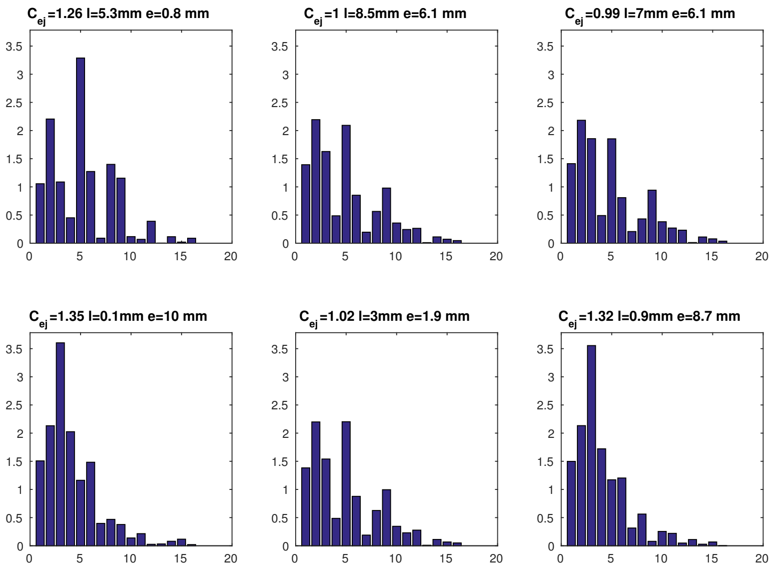

Figure 3.7: $\mathbf{C}_{ej}$ at 45.5 Hz for different interface configurations.

One the other hand, comparative study on modal parameters for one interface are carried out. Take the example of group 1, dominant modes of vibration for the

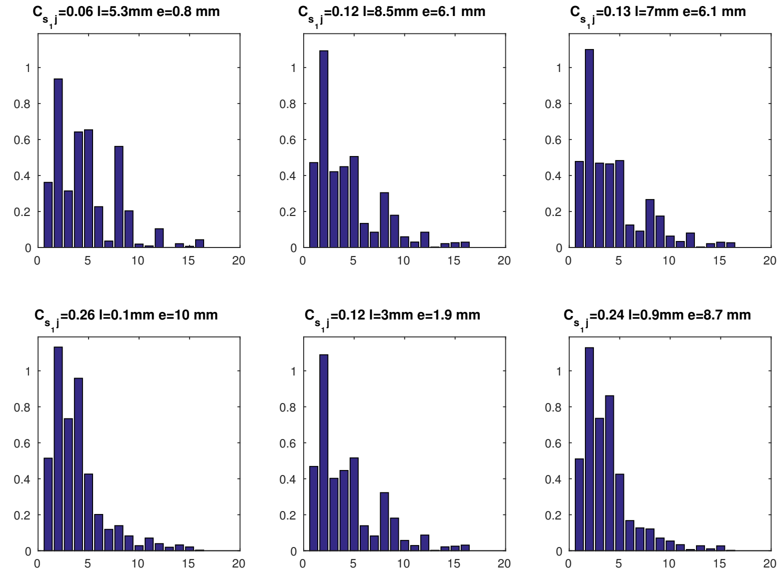

Figure 3.8: $\mathbf{C}_{ji_1}$ at 45.5 Hz for different interface configurations.

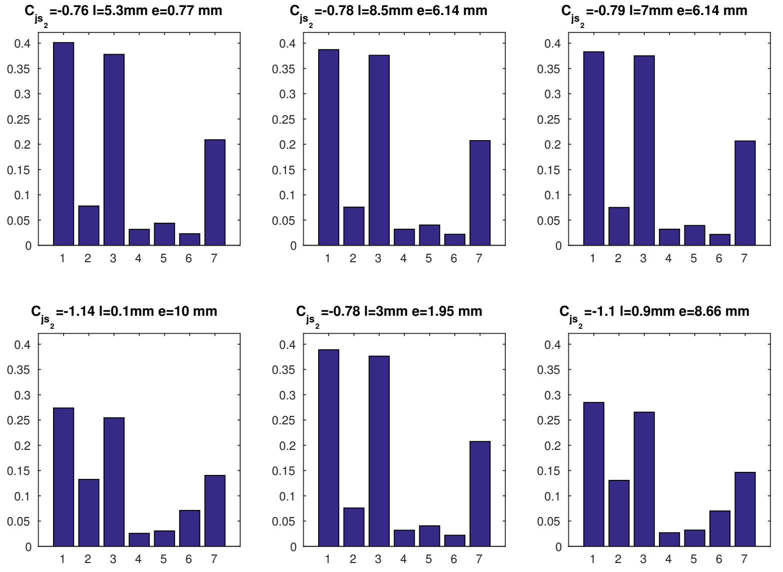

Figure 3.9: $\mathbf{C}_{ji_2}$ at 45.5 Hz for different interface configurations.

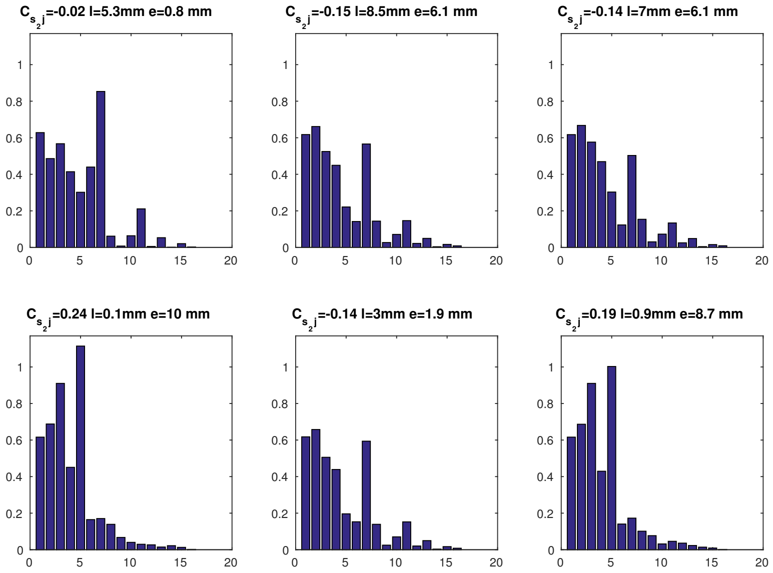

Figure 3.10: $\mathbf{C}_{i_2j}$ at 45.5 Hz for different interface configurations.

same interface configuration are different for all the four modal parameters. The average value of $\mathbf{C}_{ej}$ is larger than the others, and that of $\mathbf{C}_{ji_2}$ is smaller than the others. Moreover, when the configuration change from group 1 to group 3, the average level of the modal parameters are different. In comparing Figures 3.11 and 3.12, it is shown that the average levels of $\mathbf{C}_{i_1j}$, $\mathbf{C}_{ej}$ and $\mathbf{C}_{i_2j}$ in case of group 1 are higher than those for group 3; while the average level of $\mathbf{C}_{i_2j}$ for group 1 is lower than that for group 3.

Moreover, the weighting of each parameter is not evident, multi-optimization shall be performed.

3.2.3 Meta-models and Pareto optimal

The imposed upper and lower bounds of the thickness and length for optimization are 0.1 mm and 10 mm. Before the optimization procedure, surrogate models by Kriging approximations for these modal parameters are computed and depicted in Figures 3.13-3.15. The mean squared error of the prediction from all these surrogate models and the real value is very small, which shows that the quality of the surrogate models is quite good.

Optimizations were then conducted based on these surrogate models. The objective is to achieve Pareto optimal of $\mathbf{C}_{je}$, $\mathbf{C}_{ji_1}$, $\mathbf{C}_{ji_2}$ and $\mathbf{C}_{i_2j}$ with θ and l as the design variables. A convergence study of the population number and generation number has also been carried out. As a compromise between computational time and accuracy, 500 populations and 150 generations were chosen for this optimiza-

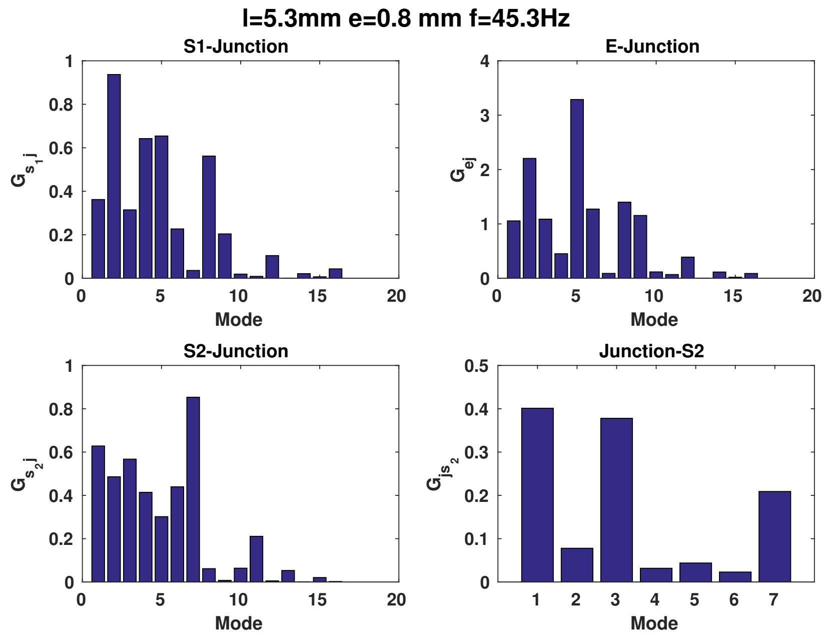

Figure 3.11: Comparison of modal parameters for excitation frequency at 45.5 Hz - Arbitrary design site: $l = 5.3\ mm, \theta = 0.8\ mm$.

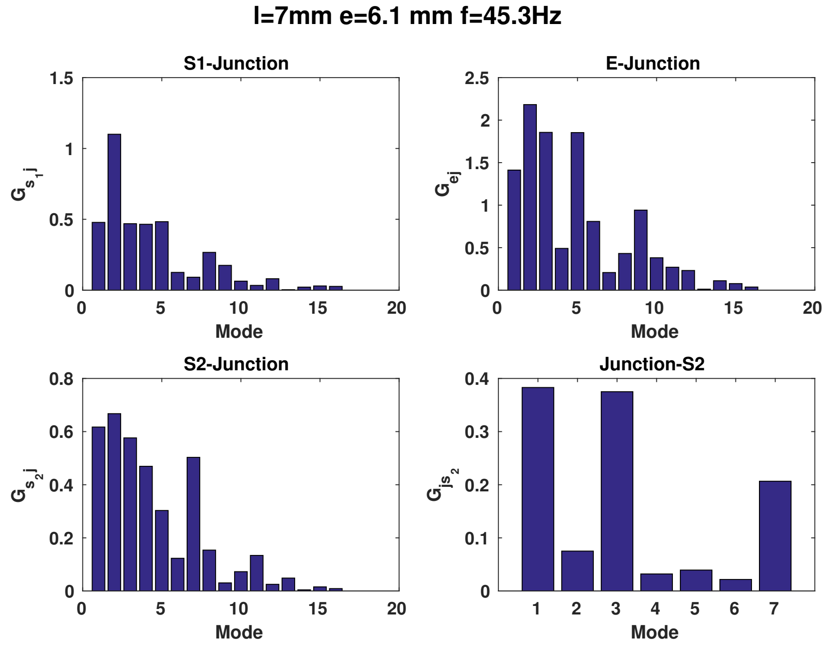

Figure 3.12: Comparison of modal parameters for excitation frequency at 45.5 Hz - Arbitrary design site: $l = 7\ mm, \theta = 6.1\ mm$.

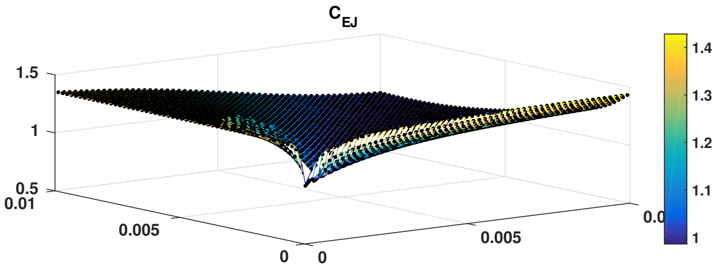

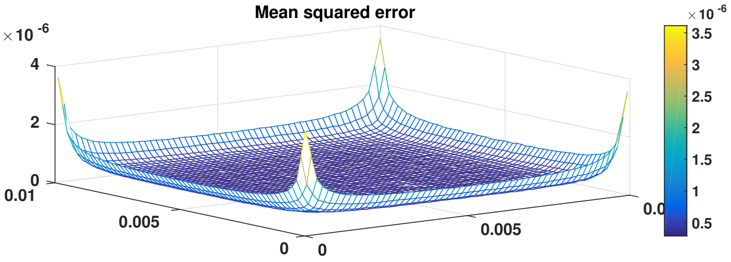

Figure 3.13: Kriging model of $\mathbf{C}_{je}$ in θ and l at 45.5 Hz

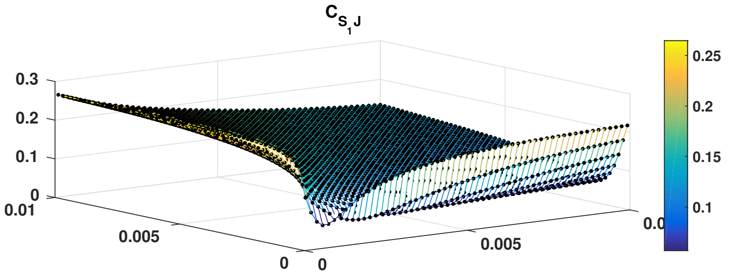

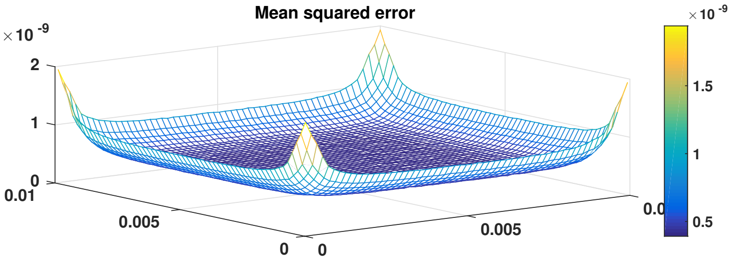

Figure 3.14: Kriging model of $\mathbf{C}_{ji_1}$ in θ and l at 45.5 Hz

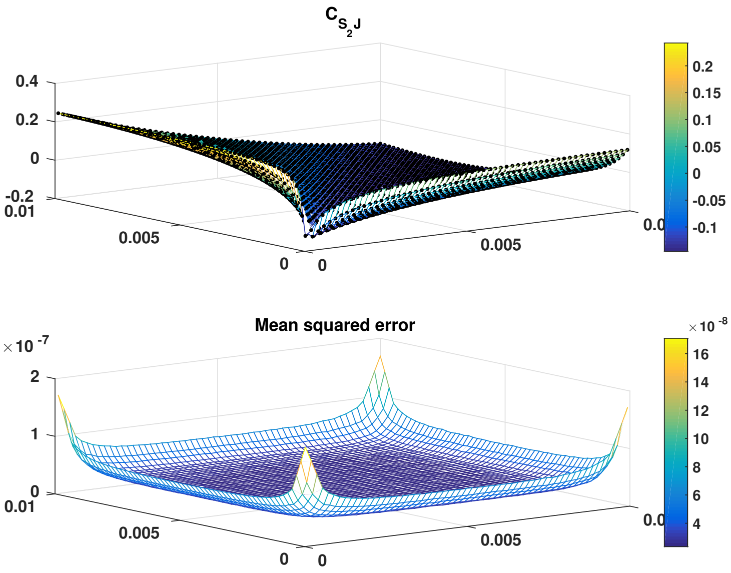

Figure 3.15: Kriging model of $\mathbf{C}_{ji_2}$ in θ and l at 45.5 Hz

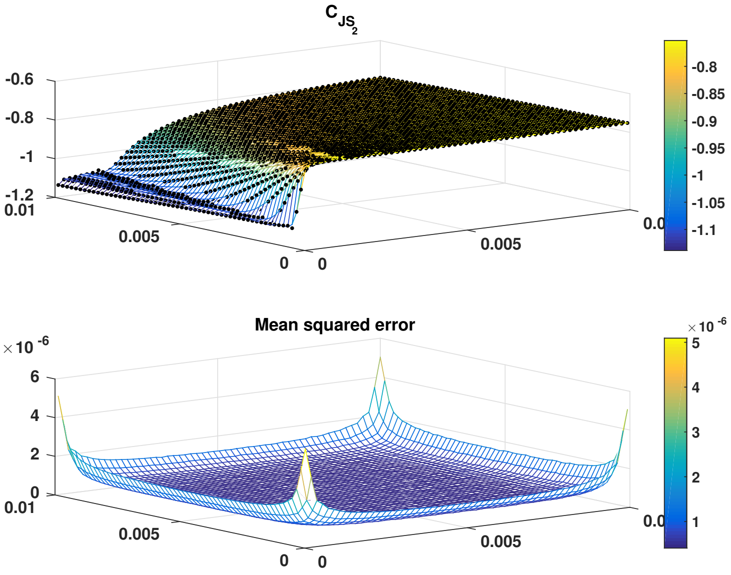

Figure 3.16: Kriging model of $\mathbf{C}_{i_2j}$ in θ and l at 45.5 Hz

tion. The 4D Pareto front was obtained using the DACE toolbox [Lophaven 2002]. The 3D view of the 4D Pareto front is shown in Figure 3.17.

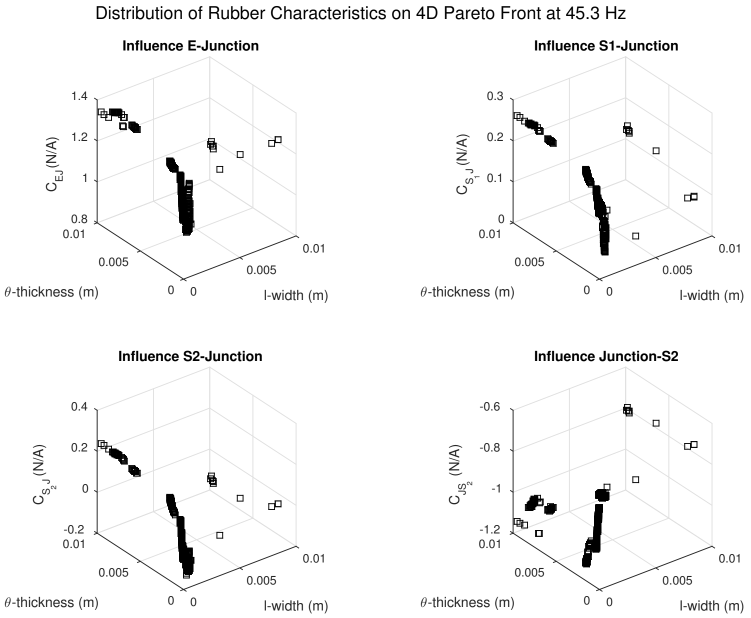

Figure 3.17: Distribution of each modal parameter on the 4D Pareto front for $\mathbf{C}_{je}$, $\mathbf{C}_{ji_1}$, $\mathbf{C}_{ji_2}$ and $\mathbf{C}_{i_2j}$ in function of rubber characteristics at at 45.5 Hz

The distribution of design variables corresponding to the 4D Pareto front is plotted in Figure 3.18. The coordinate data $[\theta,\ l]$ in these figures are the same as those that output $\mathbf{C}_{ej}$, $\mathbf{C}_{ji_1}$, $\mathbf{C}_{ji_2}$ and $\mathbf{C}_{i_2j}$ on the 3D Pareto front. It can be seen that the optima are located in several zones.

The average vibration amplitude on plate 2 computed with the proposed modal synthesis approach described in Chapter 1 is depicted in Figure 3.19. For the thickness and length varying from 0.1 mm to 10 mm and excitation frequency varying from 0 Hz to 50 Hz, the region for which the average forced response attains its minimum resides in the blue zone. This figure also shows that the forced response depends on the ratio of θ and l.

As stated above, Kriging approximations for the relevant modal parameters have been conducted prior to the optimization procedure. To verify whether the surrogate models are correct, the predictions output by the Kriging approximation and the true values given by computer experiment at untried design sites have been compared. The surrogate models of average amplitude of plate 2 appear to be well substantiated by the small mean squared errors, as shown in Figure 3.20.

By comparing Figure 3.19 and Figure 3.18, it is revealed that the optimum design by evaluating modal parameters locates in the same region as that obtained by the direct evaluation of transfer function. This supports the strategy of choosing

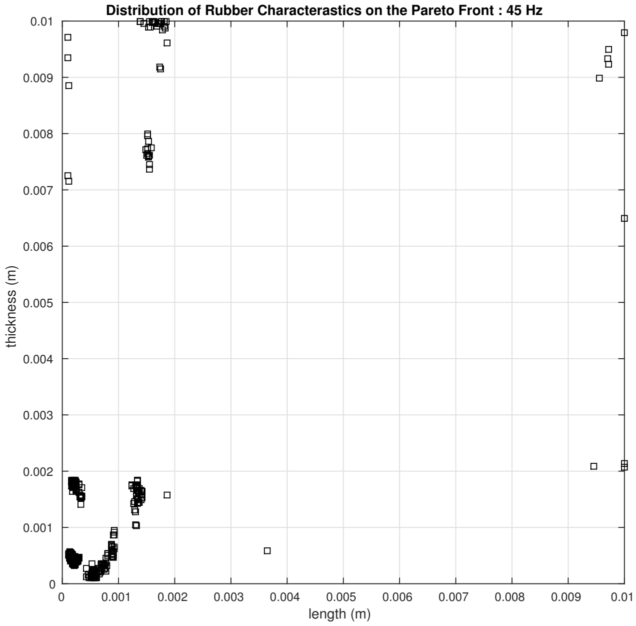

Figure 3.18: Distribution of θ and l on 4D Pareto front at 45.5 Hz

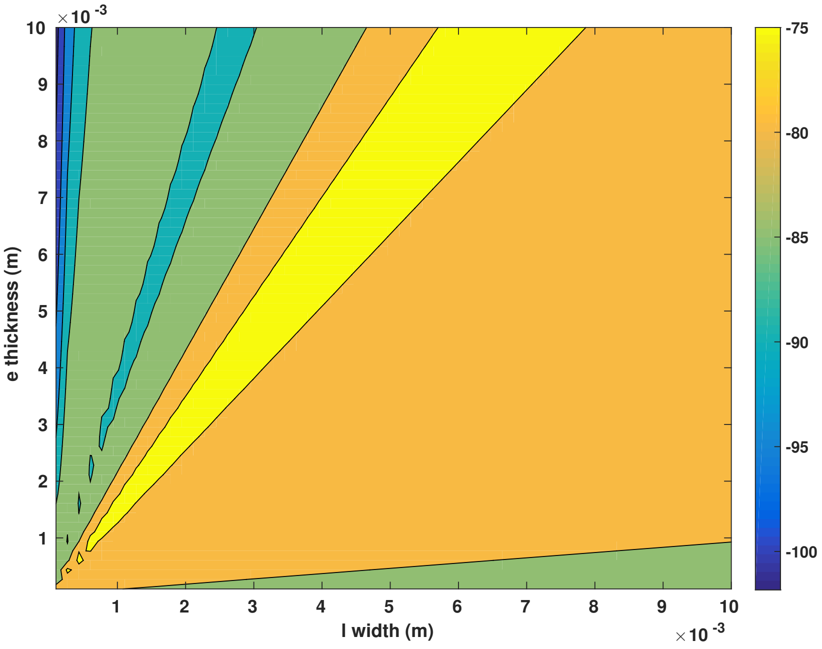

Figure 3.19: Distribution surface of the average amplitude of plate 2 in function of θ and l

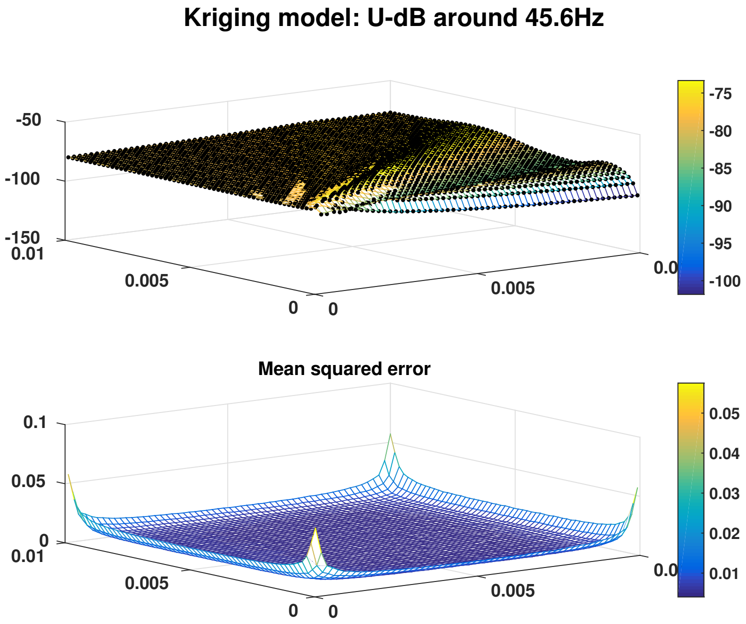

Figure 3.20: Surrogate model of the average amplitude of plate 2 in function of θ and l

modal parameters as objective functions for optimization. Two points in two zones on Figure 3.18 are chosen to compute average vibration amplitude on plate 2. In Figure 3.21, the vibration level obtained with these two points are compared with two arbitrary configuration, and found to be lower, which is in accordance with the optimization objective. It can be seen that the resonant frequency is shifted away from the excitation frequency for the two configurations from Pareto front, while that of the two arbitrary points not. That is the main reason that the average amplitude on plate 2 around 45.5 Hz of one is lower than that of another.

3.2.4 Conclusions

To summarize, we have presented herein the simulation results of an assembled plates system by employing the double modal synthesis presented in Chapter 1. First of all, the FE model of the assembled system was built. As a second step, an extended hybrid modal synthesis was then applied on the FE model. The quality of the reduced model was assured by examing its natural frequency, mode shapes and forced responses. Third, with this reduced model, modal parameters characterizing vibration transmission paths in the model, were deduced and then surrogated with Kriging approximations. The small mean squared errors at untried points ensure the quality of the surrogate models. A sensitivity analysis on the interface configuration was also conducted, and results showed that these modal parameters vary with θ and l. Lastly, the MOO procedure is accomplished with NSGA-II, and optimization

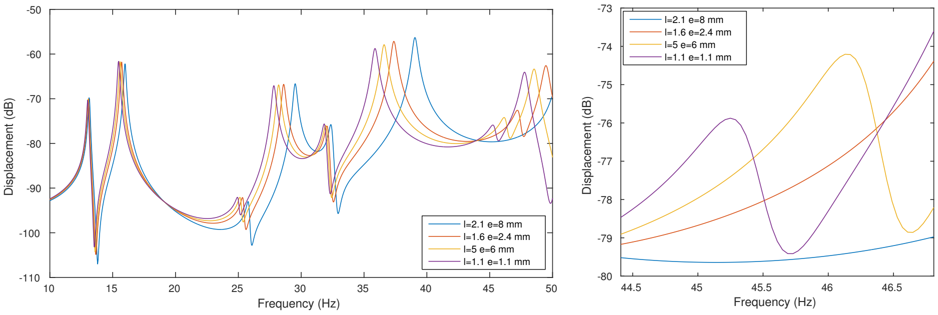

Figure 3.21: Comparison of average amplitude for excitation frequency around 45 Hz with different interface configuration- Arbitrary design site: $l = 5 \ mm, \theta = 6 \ mm$ and $l = 1.1 \ mm, \theta = 1.1 \ mm$(upper), Optimal design site: $l = 2.1 \ mm, \theta = 8 \ mm$ and $l = 1.6 \ mm, \theta = 2.4 \ mm$(lower). The right figure is an amplification of the left figure around 45.5 Hz

results are validated by analyzing the modal parameters. The localization of interface configurations in Pareto front suggests that the optimal vibration amplitude on plate 2 can be obtain with $\theta = 8 \ mm$ and $l = 2.1 \ mm$, which is in accordance with the results from a direct calculation of forced responses (-79.5 dB) by using FE model.

3.3 An assembled box filled with air

Simulation results of an assembled box filled with air are reported in this section. The aim is to show the efficiency of triple modal synthesis outlined in Chapter 2 to analyze coupled fluid-structure systems, as well as improving acoustic comfort in the cavity. The analysis is in analogous with that for assembled plates system in Section 3.2. Three modal parameters depending on the interface configuration are considered to be dominant for indicating the influence of external load on the pressure variations in the cavity: $\mathbf{C}_{aj}$, $\mathbf{C}_{ji_1}$ and $\mathbf{C}_{i_2 j}$.

The FE model contains a total of 4,810 DOFs, 900 elements in the cavity, 340 elements in S_1 and 220 elements in S_2, as shown in Figure 3.22. The model is excited with a harmonic excitation ($\mathbf{F}$) of $1,000 \ N$ at a frequency ω. The excitation is located at $x = 0.200 \ m$, $y = 0.189 \ m$ and $z = 0.650 \ m$, hence lying on S_1. Rayleigh damping has been integrated into the model. The damping ratios are: $\alpha = 2$, and $\beta = 5e^{-6}$.

Further details on the geometric dimension and material properties are provided in Table 3.6.

With a targeted frequency band ranging from 0 to 350 Hz, a convergence study on the FE mesh size has been performed, and 4 elements per wavelength are utilized for the mesh size, which provides a good compromise between accuracy and computation time.

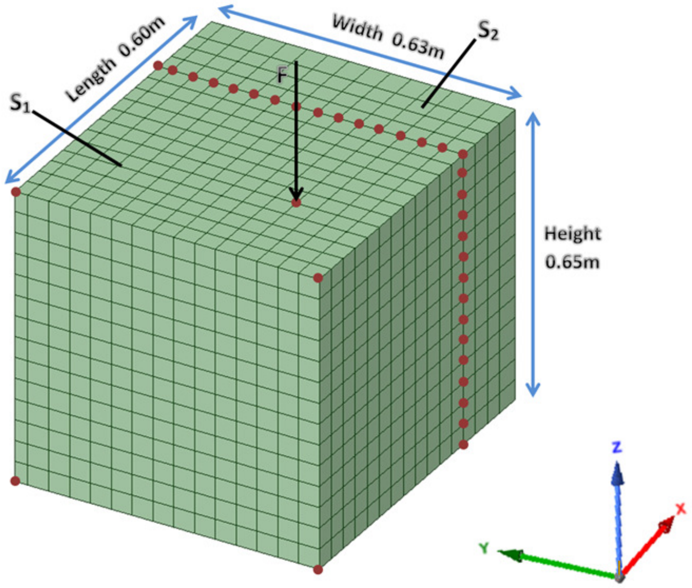

Figure 3.22: FE model with all DOFs retained

Table 3.6: Model characteristics

SubStructure	Physical quantity	Unit	Value
Plates	material		steel
	type		Kirchhoff
	thickness	mm	2
	Poisson's ratio		0.285
	density	kg/m^3	7800
	Young's modulus	Pa	2.10E+11
	Shear modulus	Pa	8.17E+11
Joint	thickness	mm	[0.1, 10]
	length	mm	[0.1, 10]
	Poisson's ratio		0.49
	Young's modulus	Pa	1.0E+08
	Shear modulus	Pa	3.4E+07
Cavity	material		air
	density	kg/m^3	1.225
	velocity	m/s	330
	dimension	m^3	$0.6 * 0.63 * 0.65$

3.3.1 Reduced model

Triple modal synthesis presented in Chapter 2.2 is employed so as to avoid the considerable computational cost. According to a convergence study of the reduction coefficient, $\alpha = 3$ is used for all types of retained modes, *i.e.* fixed interface modes, branch modes and acoustic modes. The quality analysis of the reduced model is conducted by evaluating the natural frequency of normal modes. The natural frequency error always turns out to be less than 1% up to 350 Hz, as shown in Figure 3.23. In addition, MAC values have been calculated to compare the reduced mode and exact mode shapes. The MAC values are in fact greater than 0.9 up to 350Hz, which confirms the quality of the reduced model.

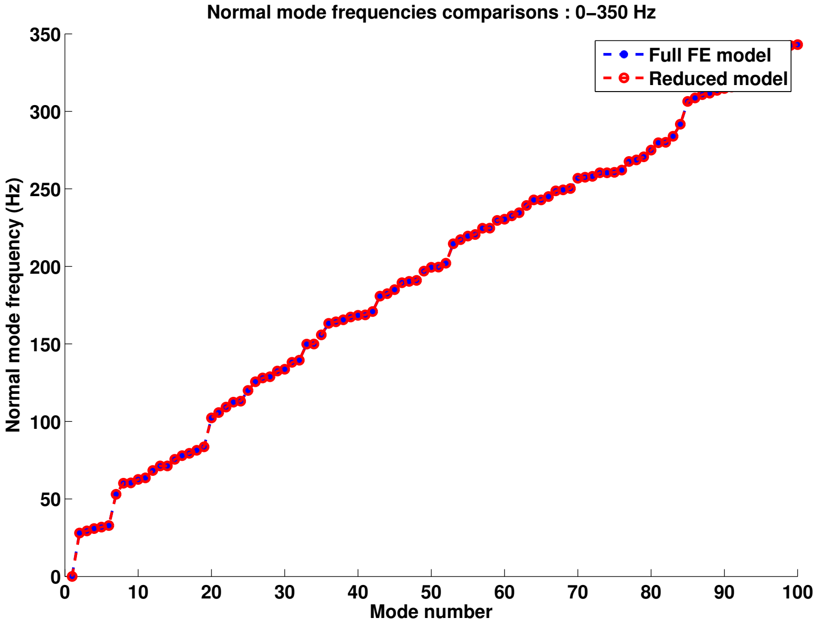

Figure 3.23: Comparison of normal modes frequencies of the full FE model and the reduced model

Figure 3.24 reveals the modal density of the reduced model, including the fixed interface modes, branch modes and acoustic modes. This depiction provides evidence of the need to disperse the modes. For example, when $\theta = 1\ mm$ and $l = 1\ mm$, the modal density study indicates that the branch mode and fixed interface mode of S_1 both occur at 242 Hz, which leads to violent pressure variations.

The coincidence of resonant modes can be avoided by adjusting the natural frequency of branch modes, which can be achieved by varying the interface configuration parameters θ and l. Figure 3.25 presents the variation range of branch mode frequency along with θ $[0.1\ mm, 10\ mm]$ and l $[0.1\ mm, 10\ mm]$. Figure 3.25 suggests that the natural frequency of branch modes is sensitive to both θ and l, which

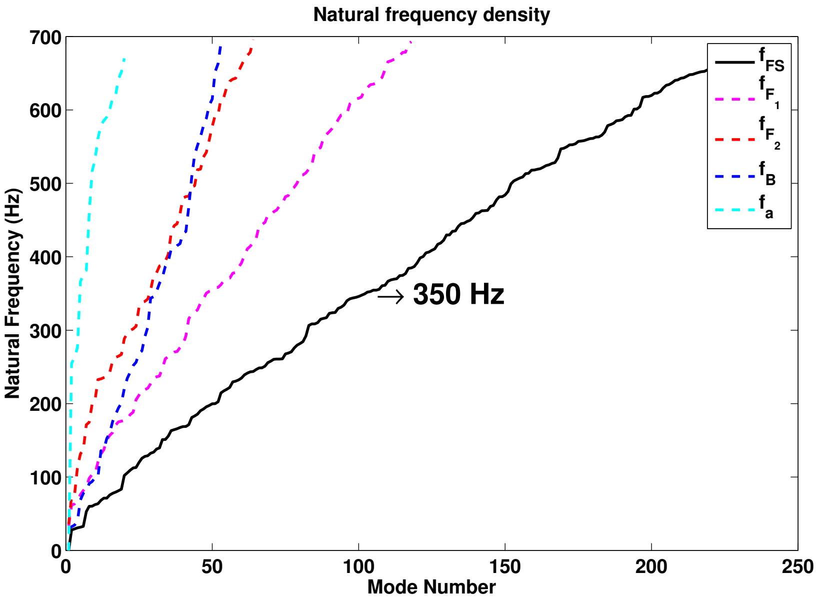

Figure 3.24: Normal mode frequency distribution of the reduced model with $\theta = 1mm$ and $l = 1\ mm$. f_{FS}: natural frequency of coupled fluid-structure model, f_{F_1} and f_{F_2}: natural frequency of S_1 and S_2 fixed-interface modes, f_B: natural frequency of branch modes, f_a: natural frequency of acoustic modes

confirms the fact that optimization of the dynamic behavior of vehicle structures can be attained by means of passive interface controls.

Table 3.7 compares the retained DOFs of the reduced model and the DOFs of the full FE model. It is shown that 90% of DOFs are truncated by applying the proposed modal synthesis. This finding implies a significant reduction in the simulation time for large-scale systems.

Table 3.7: Comparison of mode number retained in the full and reduced model

Model	Excitation	Branch Mode	S_1: Fixed Interface Mode	S_2: Fixed Interface Mode	Acoustic Mode	Total
FE	1	480	1913	1206	1210	4810
$\alpha = 3$	1	74	184	109	60	428

Simulations have been conducted on a server containing 32 Xeon (R) processors running at 2.9 GHz. Considering the $5,000$ linearly-spaced excitation frequencies from 0 to 350 Hz, the CPU time consumed when calculating average pressure variations in the cavity over this frequency band is compared for typical models: the full FE model, the reduced model obtained using Craig & Bampton method, the reduced model obtained with the double modal synthesis method, and lastly the

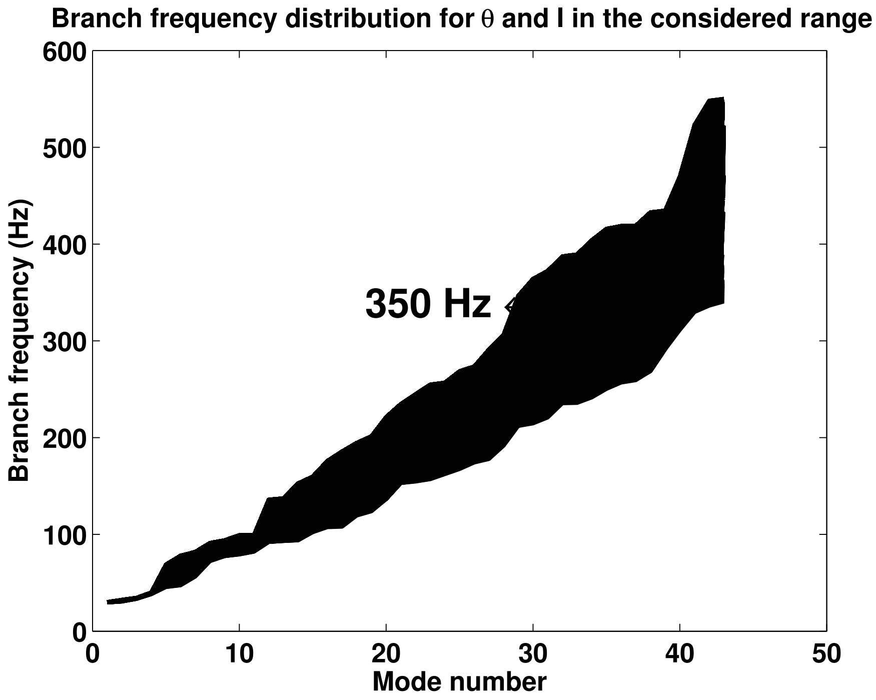

Figure 3.25: Distribution of branch modes in function of θ and l

reduced model obtained with the proposed modal synthesis method, as presented in Table 3.8. All reduction techniques serve to lower computation time, and several observations are worth discussing. The double modal synthesis consumes less time than the Craig & Bampton method by also condensing interface DOFs. Craig & Bampton, on the other hand, conserves all DOFs on the interface, which may be prohibitive in certain cases. The proposed modal synthesis method consumes a bit more time than the double modal synthesis method; this outcome is reasonable since it conserves all special region modes.

Table 3.8: CPU time comparison of different reduction techniques

Methods	FE (all DOFs retained)	Craig&Bampton Method	Double Modal Synthesis	Extensive Modal Synthesis
CPU time(s)	2989	276	75	81

3.3.2 Modal-based criteria and sensitivity analysis

In this section, the modal parameters deduced in Section 2.4 will be investigated. As revealed by their mathematical expressions, all these parameters are sensitive to the excitation frequency and reach their peaks when $\omega = {\omega_n}^k$. To validate this property, a simulation has been performed on a model with $\theta = 1\ mm$ and $l = 1\ mm$. It can be seen from Figures 3.26 through 3.29 that: $\mathbf{C}_{ae}$, $\mathbf{C}_{ai_1}$, $\mathbf{C}_{aj}$ and $\mathbf{C}_{ai_2}$ all reach their peaks when $\omega = {\omega_a}^k$; $\mathbf{C}_{i_1e}$ reaches its peak when $\omega = {\omega_{i_1}}^k$; $\mathbf{C}_{ji_1}$ reaches its peak when $\omega = {\omega_j}^k$; and $\mathbf{C}_{i_2j}$ reaches its peak when $\omega = {\omega_{i_2}}^k$. The levels of $\mathbf{C}_{ae}$, $\mathbf{C}_{ai_1}$, $\mathbf{C}_{aj}$ and $\mathbf{C}_{ai_2}$ are found to be higher than the level of the others as well. This finding can be explained by the modal participation coefficient $\tilde{\mathbf{G}}_n^k$: since the denominator m_a^k of $\tilde{\mathbf{G}}_a^k$ is much lower than m_B^k, $m_{i_1}^k$ and $m_{i_2}^k$. Consequently, the pressure variations related to these quantities may be more sensitive to the variation in interface configurations. This point may be useful when it comes to identifying the modes responsible for pressure variations inside the cavity.

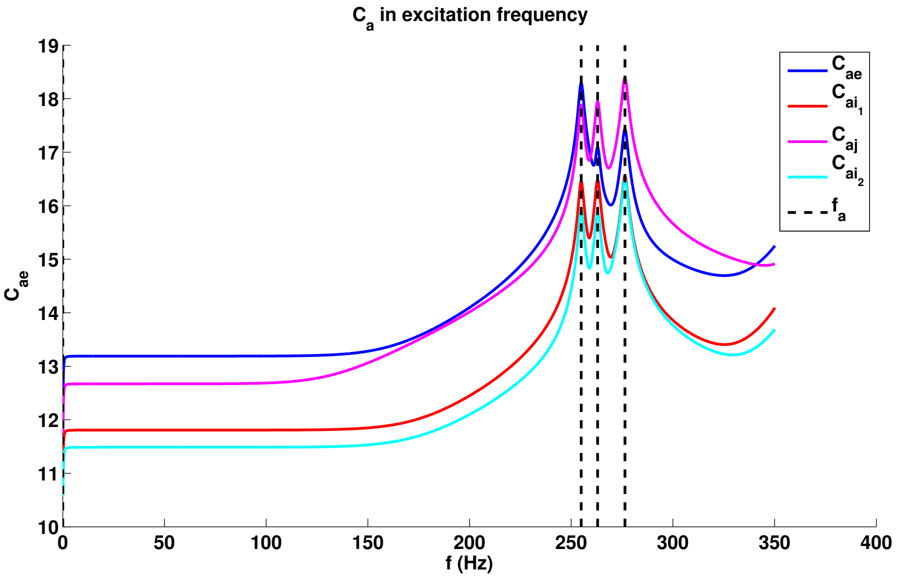

Figure 3.26: Pressure variations induced by the vibration of structure components

The same approach is applicable to the branch mode frequency shown in Figure 3.25, and a sensitivity analysis of interface configurations for the proposed criteria has been conducted. The range of variation is $\theta = [0.1\ mm, 10\ mm]$ and $l = [0.1\ mm, 10\ mm]$. The simulation results (Figs. 3.30 to 3.32) show that, among these seven terms, $\mathbf{C}_{aj}$, $\mathbf{C}_{ji_1}$ and $\mathbf{C}_{i_2j}$ change with the interface configuration, while the other four remain unchanged. This outcome is in accordance with the mathmatical expressions of the modal parameters, as outlined in Section 2.4. These figures show that these modal parameters depend on the ratio of θ and l. Moreover, it appears that $\mathbf{C}_{aj}$, $\mathbf{C}_{ji_1}$ and $\mathbf{C}_{i_2j}$ do not reach their minima at the same coordinate data. A compromise should thus be made among these three parameters.

Considering the noise transmission path, which starts from excitation, via S_1 and the interface, and ultimately arrives in the cavity, the relevant parameters along this path are: $\mathbf{C}_{ji_1}$ and $\mathbf{C}_{aj}$. The impacts of these criteria on the noise transmission path are not identical. As indicated in Table 3.9, $\mathbf{C}_{ji_1}$ is more sensitive to the variation

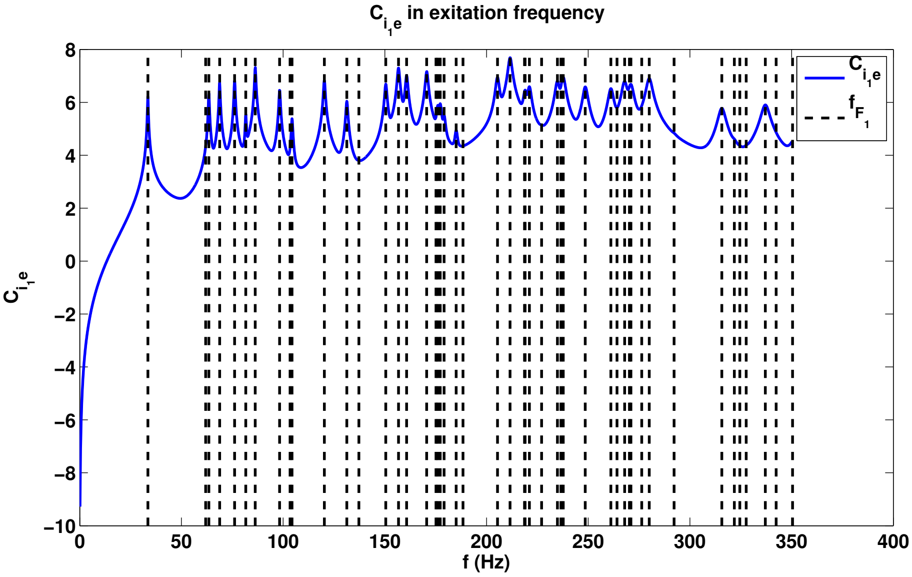

Figure 3.27: S_1 displacements induced by the displacements of the excitation nodes

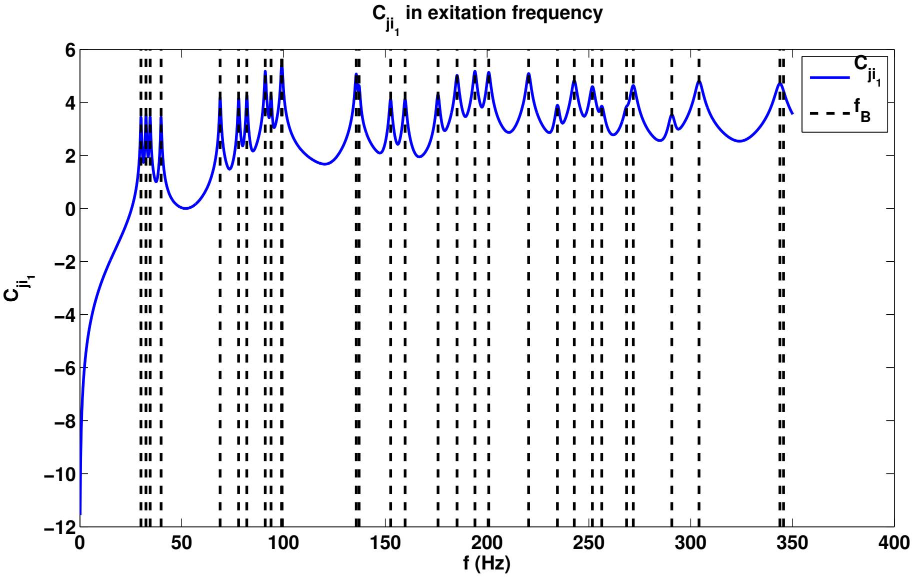

Figure 3.28: Interface displacements induced by the displacements of S_1 nodes

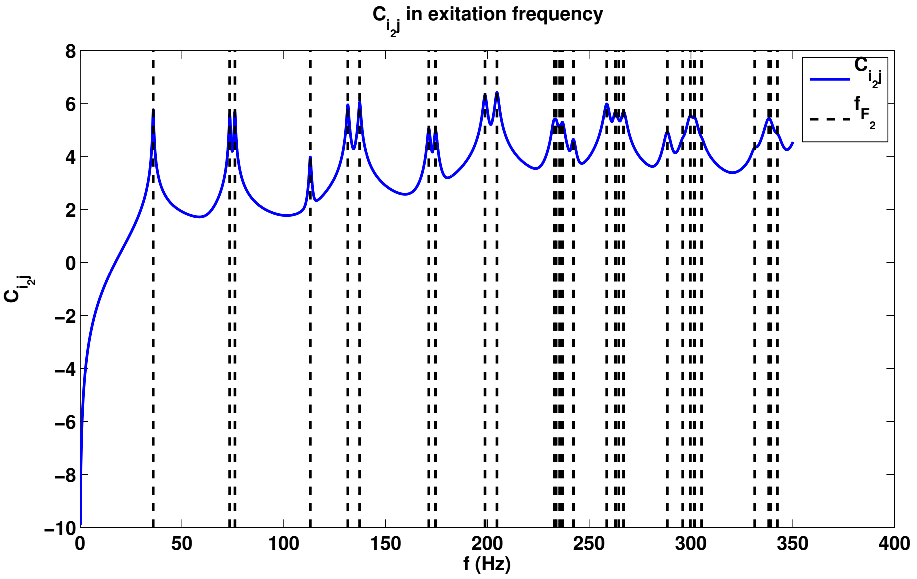

Figure 3.29: S_2 displacements induced by the displacements of the interface nodes

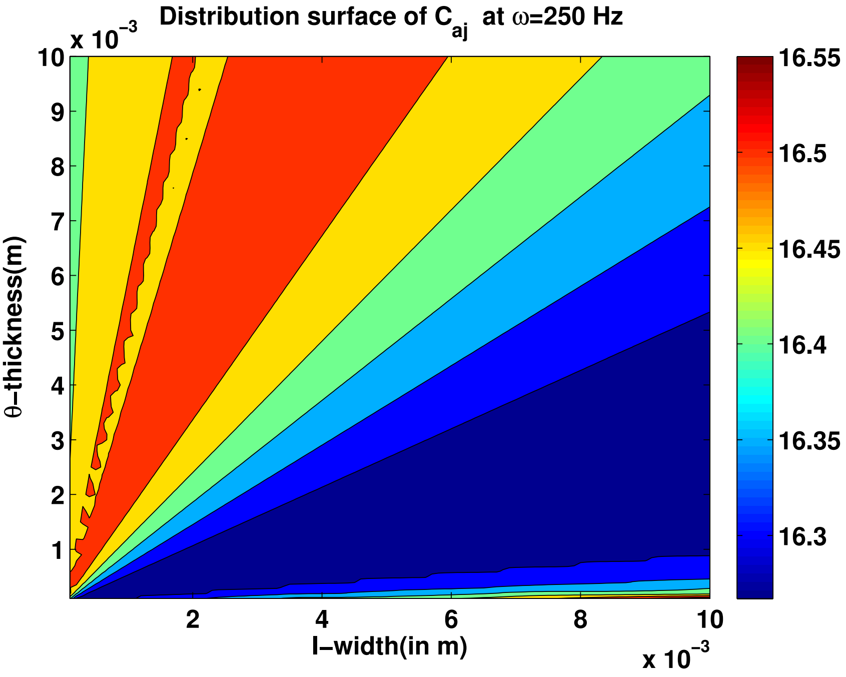

Figure 3.30: Value of $\mathbf{C}_{aj}$ in function of θ and l

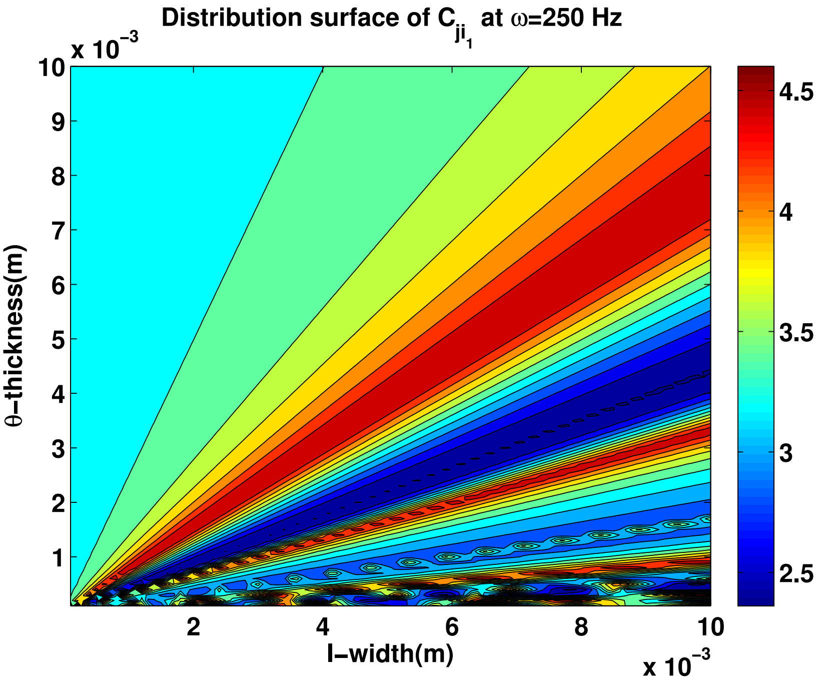

Figure 3.31: Value of $\mathbf{C}_{ji_1}$ in function of θ and l

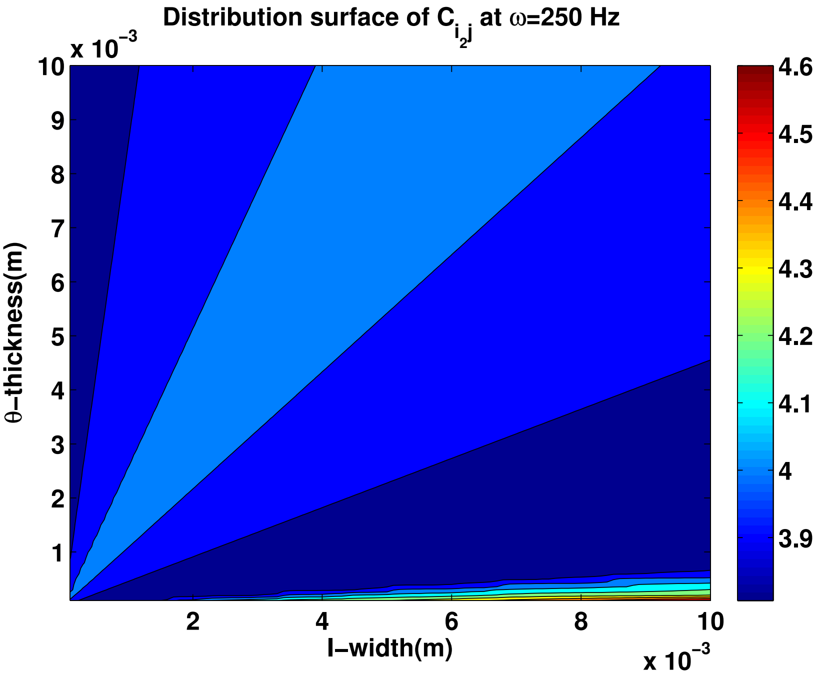

Figure 3.32: Value of $\mathbf{C}_{i_2j}$ in function of θ and l

in θ and l than $\mathbf{C}_{aj}$ and $\mathbf{C}_{i_2j}$; $\mathbf{C}_{aj}$ is greater than $\mathbf{C}_{i_2j}$ and $\mathbf{C}_{ji_1}$ in dimension; and it appears that the impact of $\mathbf{C}_{i_2j}$ always lies in the middle of $\mathbf{C}_{aj}$ and $\mathbf{C}_{ji_1}$. This finding can be explained by the fact that $\mathbf{C}_{i_2j}$ corresponds to the noise transmission path from the interface to S_2, which is less determinative for pressure variations in the cavity. $\mathbf{C}_n^m$ represents the average value of criteria $\mathbf{C}_n$ within the targeted frequency band.

To enable us to study the critical factors for pressure variations in the cavity, optimizations have been performed based on two groups of objective functions: $[\mathbf{C}_{aj}, \mathbf{C}_{i_2j}, \mathbf{C}_{ji_1}]$, and $[\mathbf{C}_{aj}, \mathbf{C}_{ji_1}]$.

Table 3.9: Sensibility of defined criteria to rubber properties

	C_{aj}	C_{ji_1}	C_{i_2j}
$[min - max]$	16.3 - 16.5	2.5 - 4.5	3.9 - 4.2
$\frac{max-min}{C_n^m}$	1.2%	57.1%	7.4%

3.3.3 Meta-models and Pareto optimal

As stated above, Kriging approximations for the relevant modal parameters have been conducted prior to the optimization procedure. 10,000 simulations were carried out in order to construct the data for Kriging interpolation. The range of design sites were set as follows: θ and l are to be equally distributed within a rectangular grid from 0.1 mm to 10 mm by means of applying Latin hypercube sampling. The combination of a zero-order polynomial regression model and a Gaussian correlation model has been tested to be robust and efficient when interpolating $\mathbf{C}_{aj}$, $\mathbf{C}_{ji_1}$ and $\mathbf{C}_{i_2j}$. To verify whether the surrogate models are correct, the predictions output by the Kriging approximation and the true values given by computer experiment at untried design sites have been compared. The surrogate models appear to be well substantiated by the small mean squared errors, as shown in Figures 3.33-3.35.

Optimizations were then conducted based on these surrogate models. The objective is to achieve Pareto optimal of $\mathbf{C}_{aj}$, $\mathbf{C}_{ji_1}$ and $\mathbf{C}_{i_2j}$ with θ and l as the design variables. The 3D Pareto front was obtained using the DACE toolbox [Lophaven 2002]. The 2D view of the 3D Pareto front is shown in Figures 3.36-3.38.

The distribution of design variables corresponding to the 3D Pareto front is plotted in Figure 3.39. The coordinate data $[\theta,\ l]$ in these figures are the same as those that output $\mathbf{C}_{aj}$, $\mathbf{C}_{ji_1}$ and $\mathbf{C}_{i_2j}$ on the 3D Pareto front. It can be seen that the optima are located in several zones. Figure 3.40 displays the surface of average pressure variations in the cavity. Note that the design parameters on the 3D Pareto front result in lower pressure variations, which supports the strategy of choosing modal parameters as objective functions for optimization.

From a modal point of view, the optima given in the 3D Pareto front are also

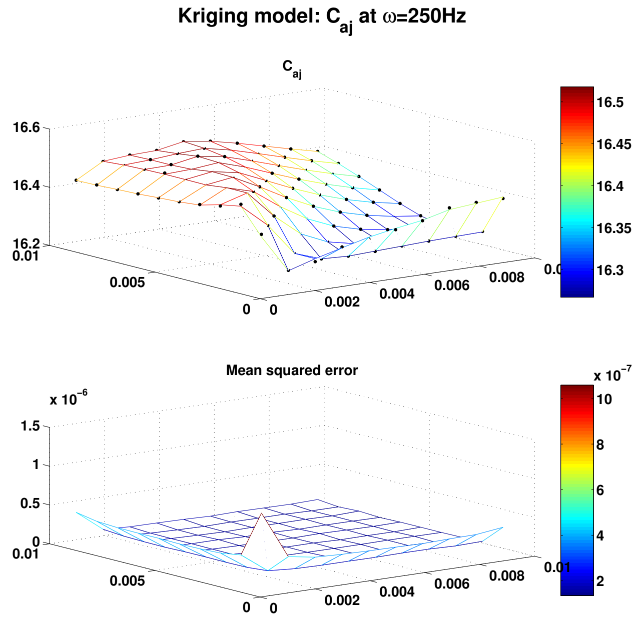

Kriging model: C_{aj} at ω=250Hz

Mean squared error

Figure 3.33: Kriging model of $\mathbf{C}_{aj}$ in θ and l at 250 Hz

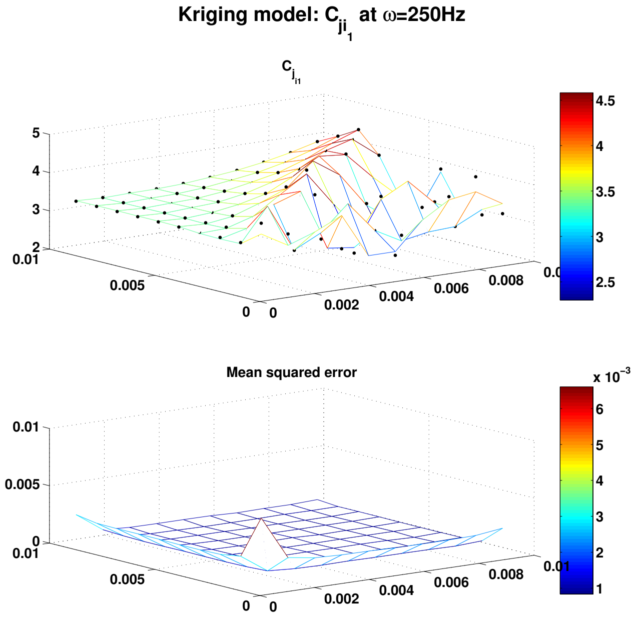

Kriging model: C_{ji_1} at ω=250Hz

Mean squared error

Figure 3.34: Kriging model of $\mathbf{C}_{ji_1}$ in θ and l at 250 Hz

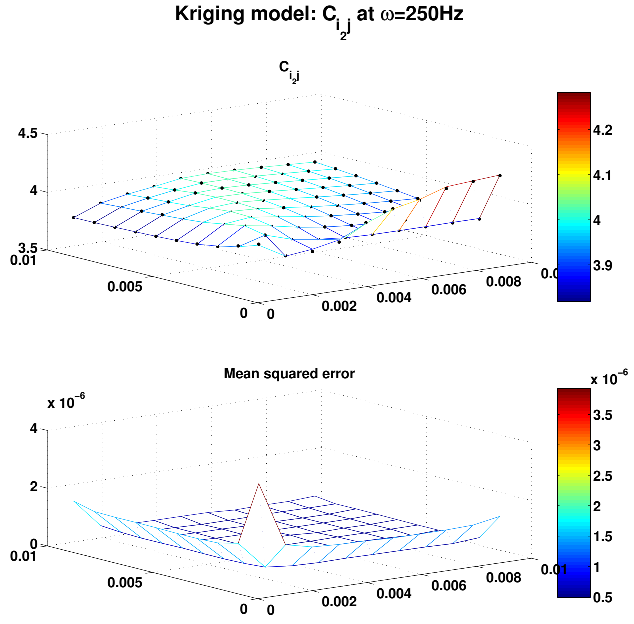

Figure 3.35: Kriging model of $\mathbf{C}_{i_2j}$ in θ and l at 250 Hz

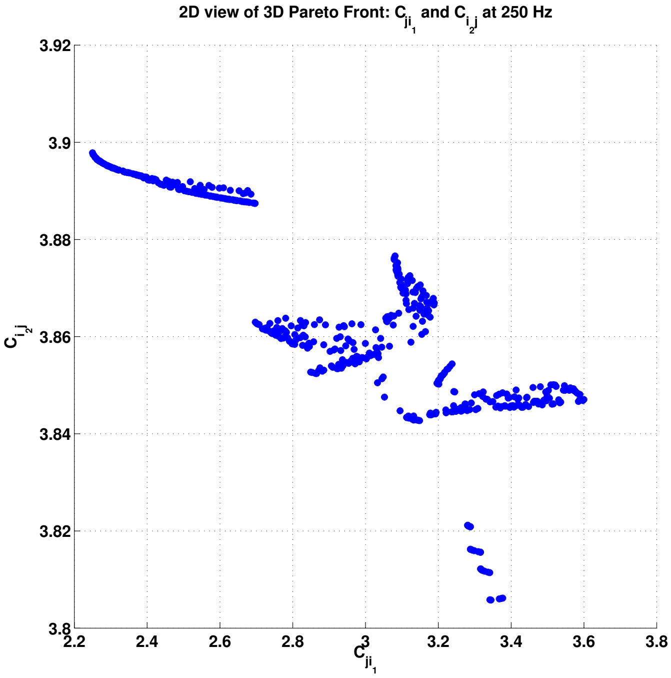

Figure 3.36: 2D view of 3D Pareto front for $\mathbf{C}_{ji_1}$ and $\mathbf{C}_{i_2j}$ in function of rubber characteristics

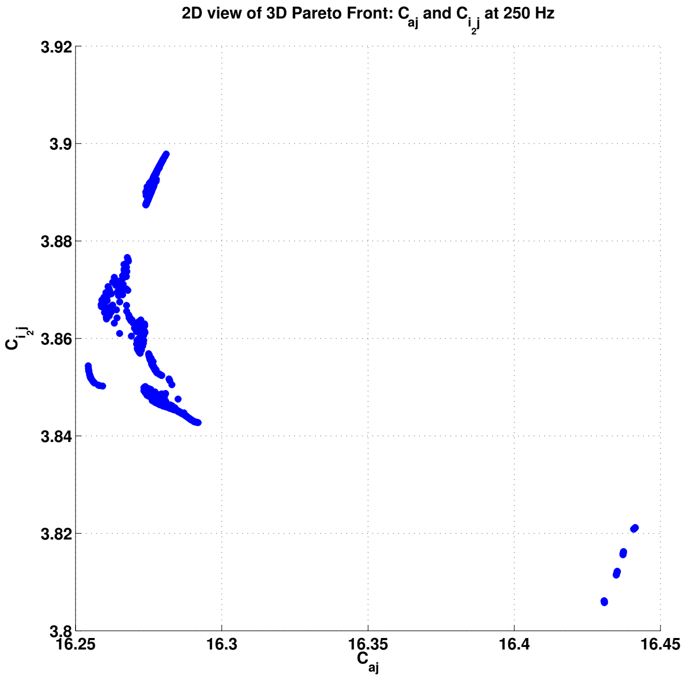

Figure 3.37: 2D view of 3D Pareto front for $\mathbf{C}_{aj}$ and $\mathbf{C}_{i_2j}$ in function of rubber characteristics

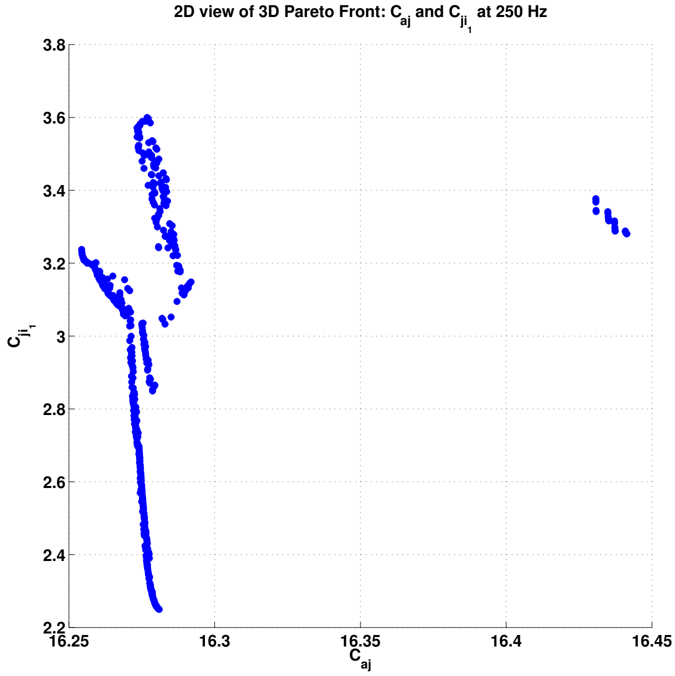

Figure 3.38: 2D view of 3D Pareto front for $\mathbf{C}_{aj}$ and $\mathbf{C}_{ji_1}$ in function of rubber characteristics

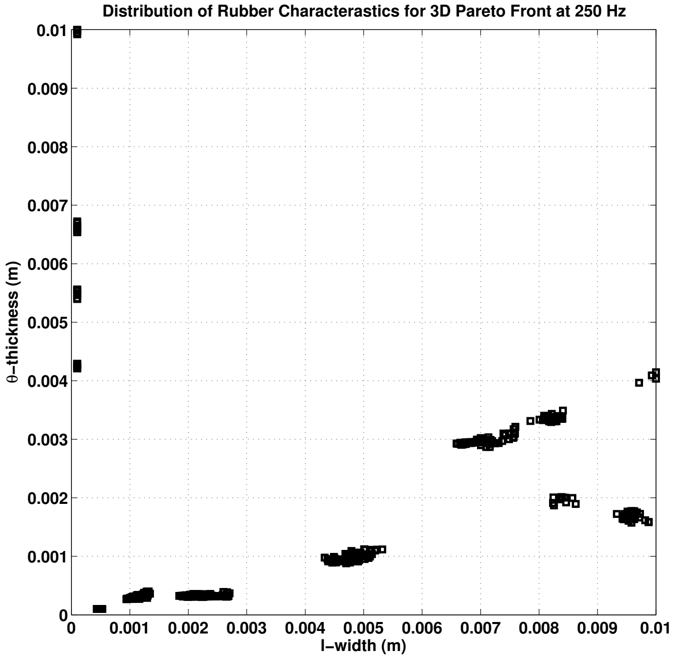

Figure 3.39: Distribution of θ and l in 3D Pareto front

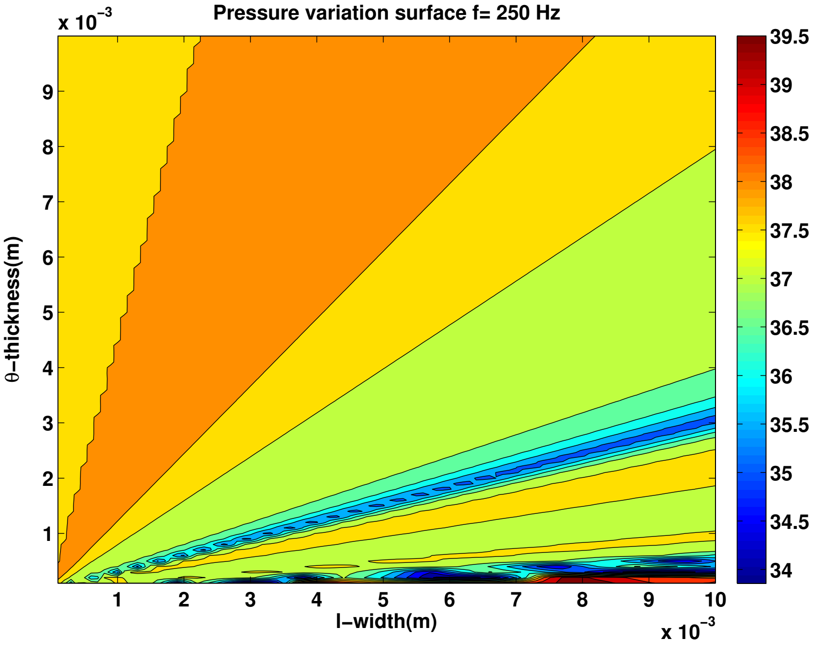

Figure 3.40: Distribution surface of the average pressure variations in function of θ and l

rational. The values of $\lambda_{aj}^{k}\tilde{\mathbf{G}}_{aj}^{k}$, $\lambda_{ji_1}^{k}\tilde{\mathbf{G}}_{ji_1}^{k}$, and $\lambda_{i_2j}^{k}\tilde{\mathbf{G}}_{i_2j}^{k}$ for all modes are pinpointed in Figure 3.41, which can be explained as follows: an arbitrary design site in the grid is chosen, and the corresponding results are plotted on the upper subfigure; an optimized design site on the Pareto front is chosen, and the corresponding results are plotted on the lower subfigure. The value of $\sum_{k=1}^{N}(\lambda_n^k\tilde{\mathbf{G}}_n^k)$ is marked by blue horizontal line. Figure 3.41 reveals that acoustic mode number 1, branch mode numbers 22 and 23, S_2 fixed interface mode numbers 15 and 16 are all responsible for the high noise level inside the cavity. It can also be observed that modal criteria on the bottom are smaller than those on top, which is in agreement with the optimization target.

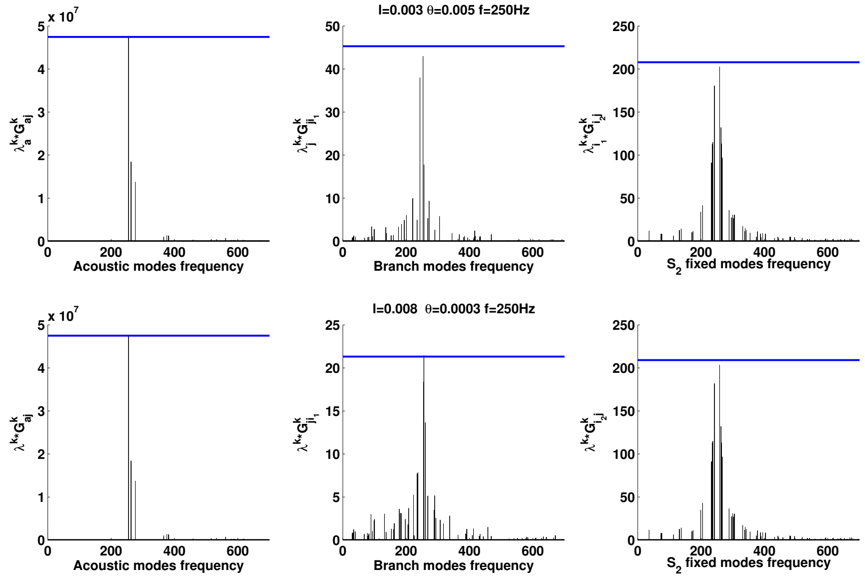

Figure 3.41: Comparison of modal parameters for an excitation frequency of 250 Hz - Arbitrary design site: $l = 3\ mm, \theta = 5\ mm$(upper), Optimal design site: $l = 8\ mm, \theta = 3\ mm$(lower).

Table 3.10 lists the average pressure variations within the cavity for four arbitrary sites within the design range, and two optimal sites on the Pareto front are evaluated using the reduced model. This matches well with the results given by modal criteria in Figure 3.41. Several observations can be forwarded. For $\theta = [0.1\ mm, 10\ mm]$ and $l = [0.1\ mm, 10\ mm]$, the maximum value of the average pressure variation in the cavity equals 42.9 dB, and the average value of the average pressure variation in the cavity is 38 dB. However, the maximum value of average pressure variation on the Pareto front is 38.4 dB, with the average value of average pressure variation on the Pareto front being 37.1 dB. Moreover, the Pareto front provides a minimum value of 35.8 dB.

Further study of the modal parameters has been carried out herein. Let's start

Table 3.10: Comparison of average pressure variations for different configurations

Reduced model at $\omega = 250$ Hz						
Group	1	2	3	4	5	6
Length (mm)	6.6	1.0	3.0	5.0	8.0	1.3
Thickness (mm)	0.1	4.3	5.0	3.0	3.0	0.4
Pressure Variation(dB)	39.3	38.6	38.3	37.5	36.8	35.9

by assuming that the problem can be simplified into a two-objective optimization of $\mathbf{C}_{aj}$ and $\mathbf{C}_{ji_1}$ with respect to θ and l. Then just like for the three-objective optimization problem, 500 populations and 150 generations are performed with the non-domination-based genetic algorithm on the two-objective optimization problem. The 2D Pareto front is shown in Figure 3.42, and the corresponding distribution of interface configurations is presented in Figure 3.43.

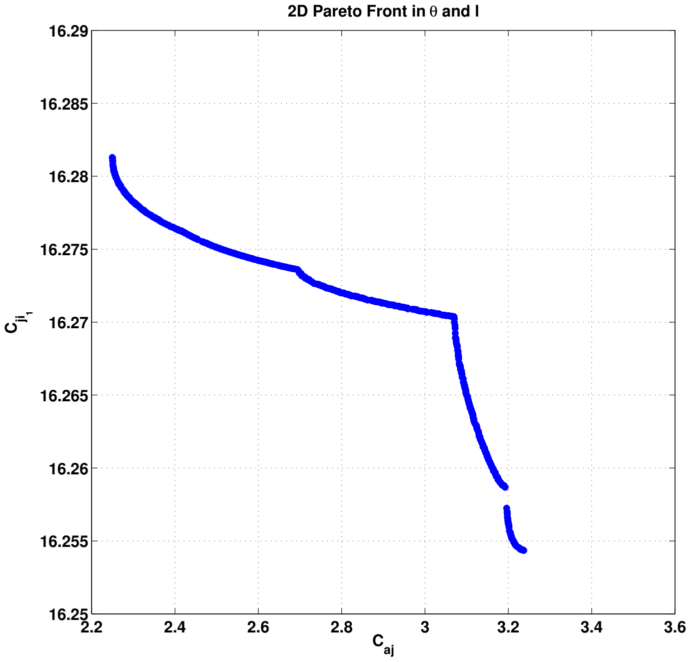

Figure 3.42: 2D Pareto front for $\mathbf{C}_{aj}$ and $\mathbf{C}_{ji_1}$

No significant difference is observed between the optimization results in Figures 3.43 and 3.39. In referring to Figure 3.40, the results from the two-objective optimization are even more suitable for this case.

3.3.4 Conclusions

To summarize, we have presented herein the simulation results of a coupled fluid-structure system by employing the strategy proposed in Chapter 2. First of all, the

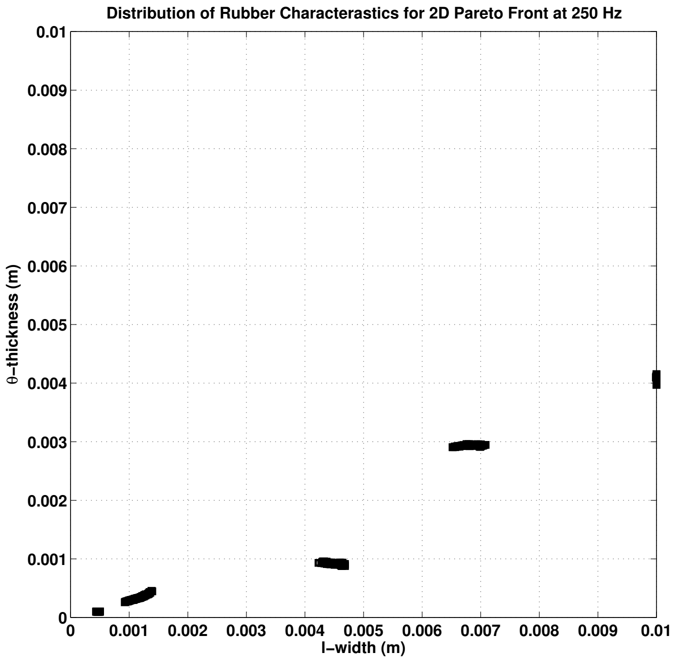

Figure 3.43: Distribution of θ and l in 2D Pareto front for $\mathbf{C}_{aj}$ and $\mathbf{C}_{ji_1}$

FE model of the coupled fluid-structure system was built. As a second step, an extended hybrid modal synthesis was then applied on the FE model. The quality of the reduced model was assured by the fact that the natural frequency error remained less than 1%, the MAC value greater than 0.9 up to 350 Hz and the good coincidence of forced responses. In the meantime, as an initial attempt at verifying whether global characteristics can be influenced by local modifications on the interface, a sensitivity analysis of the natural branch mode frequency was performed. Third, with this reduced model, $\mathbf{C}_{aj}$, $\mathbf{C}_{ji_1}$ and $\mathbf{C}_{i_2j}$, characterizing vibration transmission paths in the model, were investigated. Meta-models of these modal criteria were constructed with Kriging approximations. The small mean squared error at untried points ensured the quality of the surrogate models. A sensitivity analysis in respect to θ and l was conducted to show the influence of the interface configuration on modal criteria. Lastly, simulation results showed that average pressure variations in the cavity may vary from 42.9 dB to 35.8 dB for $\theta = [0.1\ mm, 10\ mm]$ and $l = [0.1\ mm, 10\ mm]$. The localization of interface configurations in both the 3D and 2D Pareto fronts suggests that a lower noise level can be found at: $\theta = 1.3\ mm$ and $l = 0.4\ mm$.

Part 1: Conclusions

A new strategy for reducing vibration level of the structure and raising acoustic comfort in the cavity is proposed in this part, through the use of passive interface controls.

The reduced model, based on an extensive hybrid modal synthesis, has been applied herein: double modal synthesis for assembled structures and triple modal synthesis for coupled fluid-structure system; this model converts the entire complex model into a simpler and smaller-sized one while maintaining sufficient information to describe system performance over the targeted frequency band. The branch modes were also observed to be sensitive to interface characteristics, which confirmed the feasibility of our strategy. Instead of regulating the characteristics of the entire system, the optimization of interface characteristics can also improve the system's dynamic behavior.

Modal-based criteria characterizing vibration transmission and noise transmission paths between substructures in the system have been derived to a further extent. These criteria depend on the excitation frequency, the natural frequency of the fixed interface modes, the branch modes and acoustic modes, and the modal participations. Modal parameters were found to depend on interface characteristics and can thus be employed in the optimization procedure. This strategy is based on the assumption that the dynamic behavior is dominated by the direct paths, which is similar to the statistical energy analysis.

The significant advantage of a mathematical model substituting for the analytical functions of the criteria lies in lowering the computational cost. The low mean square errors of these models justify the rationality of surrogate models. The optima selected by the non-domination-based genetic algorithm for MOO has been validated by comparing average vibration level of the reduced model and by analyzing the proposed modal criteria. The optima shown here represent better choices at these design sites for system's acoustic comfort and dynamic performance.

Part II

Optimization of passive interfaces for vibration control of nonlinear systems

Abstract: We have studied methods to optimize the dynamic behavior of an assembled structure and a coupled fluid-structure system in Chapters 1 and 2 in Part I. These systems were assumed to be linear, while the structures are more likely to be nonlinear in engineering. The linear modal synthesis is no longer sufficient to analyze these structures, and renders results biased. The theory of nonlinear modal analysis has witnessed significant developments due to requirements in analyzing large flexible structures that are in general nonlinear. A general method for analyzing nonlinear structures is presented in this Part. The proposed strategy is based on a generalized nonlinear modal superposition approach supplemented by a double modal synthesis strategy. The reduced nonlinear modes methodology combines nonlinear mode concept with reduction techniques. The modal parameters containing essential nonlinear information are determined and then employed to calculate the stationary responses of the nonlinear system subjected to various types of excitation. The advantages of the proposed nonlinear modal synthesis are mainly derived in three ways: 1) computational costs are considerably reduced when analyzing large assembled systems with local and weak nonlinearities; 2) the nonlinear modes can be used to analyze the same system under various external loads without having to reanalyze the entire system; and 3) the nonlinear effects can be investigated by a modal overview. The proposed strategy is applied to an assembled system composed of plates and nonlinear rubber interfaces.

The objective of Chapter 5 is to implemente nonlinear modal synthesis described in Chapter 4 to study the dynamic performance of assembled structures with dry friction. Both complex modes and real modes can be used in the synthesis, leading to a particular frictional damping term. A generalized Masing model is employed to describe the dry friction in the modal synthesis. The implementation of the nonlinear modal synthesis combined with the generalized Masing model yields a simple, fast and efficient numerical method to describe nonlinear performance of structures with dry friction. A simple two degrees of freedom example, a cantilevel beam model and an assembled plates system are used to show the efficiency and reliability of this method; passive control of normal force applied on contact point where dry friction occurs is conducted in the aim to optimize the dynamic behavior of assembled structures.

Part 2: Introduction

Numerical methods for analyzing nonlinear structures

In the context of engineering structural dynamics, systems are generally large-sized and of nonlinear nature. In order to solve the nonlinear problems, numerical time integration methods, such as the Newmark method and Runge-Kutta method, are often used [Ascher 1998]. These methods yield quite accurate results though appear to be time-consuming, especially when analyzing large nonlinear systems containing many degrees of freedom (DOFs).

To overcome this drawback, Rosenberg proposed a nonlinear normal mode (NNM) concept to study nonlinear systems [Rosenberg 1962]. His premise was that resonance occurs in the neighborhood of the normal mode vibration regardless of whether the system is linear or nonlinear; moreover, the response around the main resonance can be represented by this main resonant mode response. The NNMs concept has been further developed by various authors based on analytical aspects [Nayfeh 2007, Awrejcewicz 2012], numerical aspects [Hugo Ramon 2004, Kerschen 2009] and experimental aspects [Setio 1995, Ewins 2000, Gibert 2001, Peeters 2009, Ciambella 2015]. Based on this NNM concept, Szemplinska-Stupnicka [Szemplinska-Stupnicka 1980] legitimized a single nonlinear modal approach by solving the steady-state responses of nonlinear differential equations using approximate methods, *e.g.* the harmonic balance method, averaging method and asymptotic method [Nayfeh 1979]. In relying on this single nonlinear modal method, Jezequel and Lamarque have developed a nonlinear modal analysis (NLMA) method to describe the forced response of harmonically excited systems for a two-DOF system [Jézéquel 1991]. Furthermore, Setio et al. [Setio 1992] extended this NLMA method to express general transient responses as the algebraic addition of nonlinear modal responses of general systems.

These generalized nonlinear modal analysis methods are efficient in reducing the computation time when analyzing nonlinear systems relative to time integration methods, yet prove to be time-consuming since the iterations are being integrated into the numerical approaches. Reduction techniques are therefore required. A comprehensive review of reduction techniques is presented in [Touzé 2006, Lülf 2013]. In general, these methods are devoted to analyzing complex nonlinear phenomena. While set up for weak, large nonlinear systems, the nonlinear problem may be simplified under appropriate assumptions and lead to a faster algorithm.

To obtain a reduced-order model of industrial structures, the linear mode synthesis (LMS) theory has been developed into a powerful tool by various authors for analyzing mechanical systems as described in Part I. These techniques are all limited to the linear systems, while the nonlinear effect on global structural dynamics cannot be neglected in most cases and moreover linear assumptions in these cases may lead to considerable discrepancies. We propose herein to integrate reduction techniques with the nonlinear mode concept in studying the dynamic performance of assembled systems. Before calculating nonlinear normal modes, the reduction techniques are first applied to the nonlinear model in the case of free vibrations: physical displacements of the system are projected onto the generalized modal coordinates. A second reduction proceeds by selecting the dominant nonlinear normal modes obtained by solving the reduced nonlinear problem with numerical iteration methods.

Nonlinear models can subsequently be reduced by integrating reduction techniques analogous to those employed in the LMS method. It is worth noting that various reduction techniques exist for extending the NLMA theory; nonetheless, the chosen reduction technique must comply with the particular case study. A typical nonlinear industrial case consists of assembled structures containing nonlinearities located along interfaces between substructures. To analyze the nonlinear effects and calculate the steady-state responses of these systems under a constrained computation time, fast and efficient methods are needed. A discussion on all reduction techniques available has not been included herein, but special attention has been paid to Craig & Bampton reduction and double modal synthesis based on branch modes.

One objective of this thesis is to extend this nonlinear normal analysis method to study nonlinear behavior of large-size system; Reduction techniques are integrated with nonlinear mode concept to study the dynamic behavior of assembled systems in Chapter 4.

Vibration control by using dry friction dampers

The dynamic behavior of assembled structures, such as vehicles or large lightweight space structure, is significantly influenced by structural connections. Damping treatments need to be conducted on these structures to mitigate the vibration problems. In some aerodynamic applications, high temperatures and high rotation speeds prevent traditional damping treatments. In case that no special damping treatment is added to these structures, dry friction damping at bolted joints may be the most important damping source [Gaul 1997, Gaul 2008, Louis 1983].

Since dry friction devices are usually introduced to reduce resonant responses of the systems, the simulation of these friction devices appears to be very important to find the optimum parameters during the pre-design process.

For the simulation of mechanical systems with dry friction, the friction force model plays a fundamental role. The choice of friction model depends on the concrete usage of friction and many physical parameters characterizing the contact surface. Dry friction consists of two states: stick state and slide state. Various adapted models have been developed to describe friction phenomena in nonlinear dynamics [Geffen 2009]. The most basic friction model is the Coulomb model, which provides a threshold value for the friction force, above which motion would commence. Complex phenomena such as hysteresis, stick-slip and Stribeck effect can be exhibited by dry friction. To solve this problem, other dynamic models such as the Dahl's model, the LuGre model, the Leuven's model have been developed with velocity dependent functions and additional damping terms associated with micro- and macro- displacement [Piatkowski 2014]. It should be acknowledged that each model has its own distinctive pros and cons, while none of them can claim general validity.

In engineering applications concerned with dry friction, the hysteresis phenomenon is widely prevalent in nature. Various approaches and mathematical models [Bouc 1967, Duhem 1980, Krasnoselskii 1989] are available for the description of hysteresis. Masing rule is employed in this chapter to characterize the hysteresis behavior during the modal analysis. Masing's hypothesis [Masing 1926, Chiang 1999] is that the unloading and reloading branches of the steady-state hysteretic response of the system are geometrically similar to the initial-loading curve. Based on this assumption, nonlinear force induced by dry friction in steady-state can be calculated with the initial-loading curve.

Due to the geometry of the dry friction damping element, the friction force varies with the physical displacement of friction point along with stick-slip behavior of the system. In particular, the overall damping level as well as stick-slip motion amount dependent strongly on the displacement of friction point [Ferri 1996]. This renders the problem of nonlinear nature. To analyze these nonlinear structures in steady-state, time integration methods [Gavin 2014] such as Newmark method, Runge-Kutta method can provide quite accurate results, but appearing to be quite time-consuming, especially when analyzing large nonlinear systems containing numerous DOFs [Ascher 1998]. While industrial systems are in general of large-scale and their discrete models contain a great deal of DOFs. Geometry optimization of these nonlinear systems turns out to be impossible with time integration methods or traditional iterative methods. These methods may induce large discrepancies if time steps are not properly chosen. To fulfill the optimization in the pre-design process of industrial systems, fast and efficient numerical methods are required.

In relying on Masing's rule, dry friction models are integrated into nonlinear modal synthesis presented in Chapter 4 to study the nonlinear phenomena due to dry friction in Chapter 5.

Chapter 4

Extensions of nonlinear modal synthesis to analyze nonlinear systems

---

Contents

4.1 Introduction 87
4.2 Reference numerical method – Runge-Kutta 88
4.3 Theoretical basis of nonlinear modal analysis 89
  4.3.1 Nonlinear normal modes 89
  4.3.2 Nonlinear modal parameters 91
  4.3.3 Modal synthesis of forced responses 92
4.4 Reduced nonlinear modal synthesis 92
4.5 Case study of an assembled structure 96
  4.5.1 Truncation effects of higher-order nonlinear normal modes 98
  4.5.2 Truncation effects of internal modes and branch modes 98
  4.5.3 Analysis of nonlinear phenomena from a modal overview 107

4.1 Introduction

This chapter describes a simple and fast numerical procedure to study the steady-state responses of assembled structures with nonlinearities along continuous interfaces. The systems under consideration herein are large assembled systems, with slight damping and weak nonlinearity continuously located in connections between substructures, as shown in Figure 4.1.

The governing motion equation is expressed as Equation (4.1) [Nayfeh 1979]:

$$\mathbf{M}\ddot{\mathbf{u}} + \mathbf{D}\dot{\mathbf{u}} + \mathbf{K}\mathbf{u} + \tilde{\mathbf{f}}(\mathbf{u}) = \mathbf{F} \tag{4.1}$$

where $\mathbf{M}$ is the mass matrix, $\mathbf{D}$ the damping matrix, $\mathbf{K}$ the stiffness matrix, and $\mathbf{u}$ the array of unknown physical displacements. $\mathbf{F}$ is the force vector applied on the system. $\tilde{\mathbf{f}}(\mathbf{u})$ is the nonlinear restoring force, which depends on the unknown physical displacements and renders the system nonlinear nature.

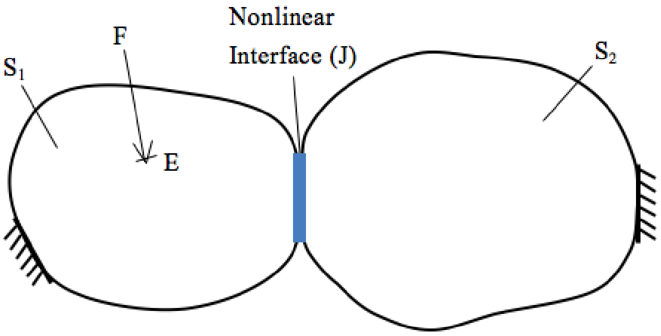

Figure 4.1: Substructures with nonlinear interfaces

4.2 Reference numerical method – Runge-Kutta

The Runge-Kutta methods are a family of implicit and explicit iterative methods, which includes the well-known routine called the Euler Methods, used in temporal discretization for the approximate solutions of ordinary differential equations. The most widely known member of the Runge-Kutta family is generally referred to as “RK4" or “classical Runge-Kutta method" [Hazewinkel 2001, Butcher 1987].

The approach is to rewritten the N second order differential equation in the following $2N$ first order differential equation by employing $(\mathbf{u}, \mathbf{v})$, where $\dot{\mathbf{u}} = \mathbf{v}$:

$$\begin{bmatrix} \dot{\mathbf{v}} \\ \dot{\mathbf{u}} \end{bmatrix} = \begin{bmatrix} \mathbf{M} & \mathbf{0} \\ \mathbf{0} & \mathbf{I} \end{bmatrix}^{-1} \begin{bmatrix} -\mathbf{D}\mathbf{v} - \mathbf{K}\mathbf{u} - \tilde{\mathbf{f}}(\mathbf{u}) + \mathbf{F}\cos(\omega t) \\ \mathbf{v} \end{bmatrix} \tag{4.2}$$

Defining a state vector $\mathbf{y}$, with $\mathbf{y}^T = [\mathbf{u}, \mathbf{v}]^T$, the problem is reformulated as follows:

$$\dot{\mathbf{y}} = f(t, \mathbf{y}) \tag{4.3}$$

where f is a given function of t and $\mathbf{y}$, representing the rate at which $\mathbf{y}$ changes. $\mathbf{y}$ is the unknown function of time t, where y_0 is the corresponding y-value at the initial time t_0, *i.e.*, $\mathbf{y}(t_0) = \mathbf{y}_0$.

The RK4 approximation of $\mathbf{y}(t_{n+1})$ is determined by the present value $\mathbf{y}(t_n)$ plus the weighted average of four increments. Defining is step-size $h > 0$, each increment is the product of h and an estimated slope specified by function f on the right-hand side of the differential equation.

$$\begin{aligned} \mathbf{y}_{n+1} &= \mathbf{y}_n + \tfrac{h}{6}\left(k_1 + 2k_2 + 2k_3 + k_4\right), \\ t_{n+1} &= t_n + h, \end{aligned} \tag{4.4}$$

Here k_1 is the increment based on the slope at the beginning of the interval, using y, which is also referred to Euler’s method; k_2 is the increment based on the slope at the midpoint of the interval, using $\mathbf{y} + \frac{h}{2}k_1$; k_3 is again the increment based on the slope at the midpoint, but now using $\mathbf{y} + \frac{h}{2}k_2$; k_4 is the increment based on the slope at the end of the interval, using $\mathbf{y} + hk_3$:

$$\begin{aligned} k_1 &= f(t_n, \mathbf{y}_n), \\ k_2 &= f(t_n + \tfrac{h}{2}, \mathbf{y}_n + \tfrac{h}{2}k_1), \\ k_3 &= f(t_n + \tfrac{h}{2}, \mathbf{y}_n + \tfrac{h}{2}k_2), \\ k_4 &= f(t_n + h, \mathbf{y}_n + hk_3). \end{aligned} \tag{4.5}$$

Runge-kutta method is among the most popular for solving nonlinear functions, providing a simple mechanism for iteratively converging to the solution with a severe step-size and a close initial guess [Butcher 1987]. Currently, there are no methods which can guarantee global convergence in a nonlinear problem, so the importance of estimating a proper step-size and initial guess can not be over-stressed, resulting in expensive high computational effort during the calculations.

4.3 Theoretical basis of nonlinear modal analysis

The nonlinear modal analysis (NLMA) entails decoupling Equation (4.1) with N uncoupled equations through the use of nonlinear normal modes (NNMs), as well as solving for eigensolutions to these uncoupled equations.

Notations analogous to those used in linear mode synthesis (LMS) introduced in chapter 1. Let's define $\tilde{\lambda}_j$ and $\tilde{\mathbf{\Phi}}_j$ as the eigenvector for a given modal amplitude $|q_j|$, respectively. According to [Setio 1992], when normal modes are slightly coupled, the forced responses of the nonlinear model can be expressed as Equation (4.6) by applying the Ritz-Galerkin method:

$$\mathbf{u}\cos(\omega t) \approx \sum_{j=1}^{N} \mathbf{u}_j \cos(\omega t) \approx \sum_{j=1}^{N_r} q_j \tilde{\mathbf{\Phi}}_j \cos(\omega t) \tag{4.6}$$

The nonlinear resonant frequencies $\tilde{\omega}_j$ and the nonlinear mode $\tilde{\mathbf{\Phi}}_j$ of the nonlinear system can be calculated by a standard eigenvalue solution for each equivalent stiffness value. Then modal amplitudes q_j corresponding to the nonlinear terms $\tilde{\omega}_j$ and $\tilde{\mathbf{\Phi}}_j$ can be obtained by:

$$q_j = \tilde{\mathbf{\Phi}}_j^{-1}\mathbf{u} \tag{4.7}$$

4.3.1 Nonlinear normal modes

By substituting Equation (4.6) into Equation (4.1), the nonlinear normal modes of the model become the eigensolutions to Equation (4.8). Distinct from the linear modal analysis, Equation (4.8) is a nonlinear problem and its eigensolutions depend on amplitude; moreover, they are solved by iterative numerical methods.

$$(-\tilde{\omega}_j^2\mathbf{M} + \mathbf{K})(q_j\tilde{\mathbf{\Phi}}_j) + \tilde{\mathbf{f}}(q_j\tilde{\mathbf{\Phi}}_j) = \mathbf{0} \tag{4.8}$$

Kryloff and Bogoliubov method is a method used in non-linear oscillation theory to study oscillatory processes. It is based on an averaging principle, *i.e.*, the exact differential equation of the motion is replaced by an averaged equation.[W.D. 1973] The principal approach of the method is to replace the nonlinear differential equation with a equivalent linear equation, for which the exact analytical formula for the solution is known [Caughey 1962, Setio 1992].

For the nonlinear second order differential equation of motion of the non-conservative nonlinear system with nonlinear function $\tilde{\mathbf{f}}(q_j\tilde{\mathbf{\Phi}}_j)$, the equivalent linear equation is:

$$(-\tilde{\omega}_j^2\mathbf{M}+\mathbf{K})(q_j\tilde{\mathbf{\Phi}}_j)+(\tilde{\omega}_j\tilde{\mathbf{D}}+\tilde{\mathbf{K}})(q_j\tilde{\mathbf{\Phi}}_j)=\mathbf{0} \tag{4.9}$$

where $\tilde{\mathbf{D}}$ and $\tilde{\mathbf{K}}$ are respectively the equivalent damping matrix and the equivalent stiffness matrix, characterizing the nonlinear effect of $\tilde{\mathbf{f}}(q_j\tilde{\mathbf{\Phi}}_j)$. These two matrices are determined by minimizing the difference ε between the nonlinear system and the equivalent linear system for every q_j:

$$\varepsilon(q_j)=\Big[(-\tilde{\omega}_j^2\mathbf{M}+\mathbf{K})(q_j\tilde{\mathbf{\Phi}}_j)+(i\tilde{\omega}_j\tilde{\mathbf{D}}+\tilde{\mathbf{K}})(q_j\tilde{\mathbf{\Phi}}_j)\Big]-\Big[(-\tilde{\omega}_j^2\mathbf{M}+\mathbf{K})(q_j\tilde{\mathbf{\Phi}}_j)+\tilde{\mathbf{f}}(q_j\tilde{\mathbf{\Phi}}_j)\Big] \tag{4.10}$$

Given that the nonlinear restoring force $\tilde{\mathbf{f}}(q_j\tilde{\mathbf{\Phi}}_j)$ has been integrated in the motion equation. Both the natural frequencies $\tilde{\omega}_j$ and modal shapes $\tilde{\mathbf{\Phi}}_j$ are of a nonlinear nature and depend on the modal amplitude q_j. For the sake of simplicity, this dependence on q_j has not been denoted herein nor in the following discussion.

The NNMs to Equation (4.1) are solved by minimizing the residue function ε according to the steps outlined below. The unknowns of this equation are: ($\tilde{\lambda}_j$, $\tilde{\mathbf{\Phi}}_j$), where $\tilde{\lambda}_j=\tilde{\omega}_j^2$. The linear modes ($\lambda_j$, $\mathbf{\Phi}_j$) are set as initial conditions for the nonlinear problem corresponding to q_j^0, where $\lambda_j=\omega_j^2$. The nonlinear normal modes of iteration k ($\tilde{\lambda}_j^k$, $\tilde{\mathbf{\Phi}}_j^k$) corresponding to q_j^k are set as initial conditions in order to calculate ($\tilde{\lambda}_j^{k+1}$, $\tilde{\mathbf{\Phi}}_j^{k+1}$) of the next iteration q_j^{k+1}.

Assuming the model dimension to be of size N, then $N+1$ unknowns are thus involved in the numerical approach to solve the nonlinear problem: 1 eigenvalue and N eigenvector components. A normalization condition should be imposed in this case to solve the problem. The normalization step can be conducted by either assigning 1 to a nonlinear eigenvector component, or normalizing the eigenvector with respect to the mass matrix. The normalization condition relative to the mass matrix is given by:

$$(\tilde{\mathbf{\Phi}}_i)^T\mathbf{M}\tilde{\mathbf{\Phi}}_i=1$$

It should be noted that the orthogonality relation is not satisfied for nonlinear modal shapes as a result of their dependence on modal amplitude:

$$(\tilde{\mathbf{\Phi}}_i)^T\mathbf{M}\tilde{\mathbf{\Phi}}_j\neq 0 \quad (i\neq j)$$

Special attention must be paid when normalizing the nonlinear eigenvector by setting a nonlinear eigenvector component at 1. For example, if the chosen component is not as highly sensitive to the modal amplitude as the other components, then small perturbations on the modal amplitude may lead to large variations in other eigenvector components. The solutions can thus diverge very quickly, and the incremental step used in Newton-Raphson iterations should be very small.

4.3.2 Nonlinear modal parameters

The nonlinear perturbation effect has been integrated into the nonlinear natural frequency and nonlinear modes, thus resulting in a nonlinear stiffness matrix:

$$\tilde{\lambda}_j = (\tilde{\mathbf{\Phi}}_j)^T \tilde{\mathbf{K}} \tilde{\mathbf{\Phi}}_j \tag{4.11}$$

where

$$(\tilde{\mathbf{\Phi}}_j)^T \tilde{\mathbf{K}} \tilde{\mathbf{\Phi}}_j q_j = (\tilde{\mathbf{\Phi}}_j)^T \mathbf{K} \tilde{\mathbf{\Phi}}_j q_j + (\tilde{\mathbf{\Phi}}_j)^T \tilde{\mathbf{f}}(q_j \tilde{\mathbf{\Phi}}_j) \tag{4.12}$$

The nonlinear modal mass is given by:

$$\tilde{\mu}_j = (\tilde{\mathbf{\Phi}}_j)^T \mathbf{M} \tilde{\mathbf{\Phi}}_j \tag{4.13}$$

Assuming that proportional damping $\mathbf{D}$ is considered for the system under consideration, the nonlinear modal damping is given by:

$$\tilde{d}_j = (\tilde{\mathbf{\Phi}}_j)^T \mathbf{D} \tilde{\mathbf{\Phi}}_j \tag{4.14}$$

and the nonlinear modal damping factor is given by:

$$\tilde{\xi}_j = \frac{1}{2} \frac{(\tilde{\mathbf{\Phi}}_j)^T \mathbf{D} \tilde{\mathbf{\Phi}}_j}{\tilde{\lambda}_j} \tag{4.15}$$

Once the nonlinear normal modes $\tilde{\mathbf{\Phi}}_j$ have been derived, they may be written as a linear combination of N_l linear modes. Instead of conserving the information about all components in the nonlinear mode vector, only N_l modal participation coefficients are stocked.

$$\tilde{\mathbf{\Phi}}_j = \sum_{k=1}^{N_l} \tilde{\beta}_{jk} \mathbf{\Phi}_k \tag{4.16}$$

where $\tilde{\beta}_{jk}$ denotes the participation of linear normal mode $\mathbf{\Phi}_k$ in the nonlinear mode j; also the normalization step is performed by exerting:

$$\tilde{\beta}_{jj} = 1, \quad (k = j)$$

The participation coefficient of the linear normal mode-k in the nonlinear normal mode-j is expressed by:

$$\tilde{\beta}_{jk} = (\mathbf{\Phi}_k)^T \mathbf{M} \tilde{\mathbf{\Phi}}_j \quad (j \neq k) \tag{4.17}$$

The impacts of higher-order linear normal modes on this nonlinear normal mode are thus being neglected when using this representation.

According to the normalization condition, the nonlinear modal mass equals 1. Moreover, as q approaches 0, the nonlinear effort converges to 0 and nonlinear mode shapes $\tilde{\mathbf{\Phi}}_j$ converge to the linear normal mode shapes $\mathbf{\Phi}_j$. Consequently, $\tilde{\beta}_{jk}$ turns out to be 0 for all $k \neq j$ and 1 for $k = j$.

We propose conserving the participation coefficients $\tilde{\beta}_{jk}$ and nonlinear eigenvalue $\tilde{\lambda}_j$ as a function of modal amplitude $|q_j|$. $\tilde{\omega}_j$ and $\tilde{\beta}_{jk}$ are then interpolated with respect to modal amplitude $|q_j|$. The interpolation models are subsequently used to calculate the forced responses in the following section.

4.3.3 Modal synthesis of forced responses

When the modes are slightly coupled, the nonlinear forced responses can be approximated from a superposition of the forced responses associated with single nonlinear normal mode. To obtain the forced responses of a single nonlinear normal mode, found by multiplying Equation (4.1) by $(\tilde{\mathbf{\Phi}}_j)^T$ according to Ritz's approximation method, the governing equation of the model subjected to harmonic excitations is as follows:

$$(\tilde{\mathbf{\Phi}}_j)^T \left(-\omega^2\mathbf{M} + i\mathbf{D} + \tilde{\mathbf{K}}\right) \tilde{\mathbf{\Phi}}_j q_j = (\tilde{\mathbf{\Phi}}_j)^T \mathbf{F} \tag{4.18}$$

The modal amplitude can be expressed as:

$$q_j = \frac{\tilde{f}_j(|q_j|)}{-\omega^2\tilde{\mu}_j(|q_j|) + i\tilde{d}_j(|q_j|) + \tilde{\omega}_j^2(|q_j|)} \tag{4.19}$$

where

$$\tilde{f}_j = (\tilde{\mathbf{\Phi}}_j)^T \mathbf{F} \tag{4.20}$$

Both space and time complexity of nonlinear problems render nonlinear system difficult to be solved. Herein we search for a simple and efficient method to evaluate slightly nonlinear systems, in which complex nonlinear phenomena such as internal resonances are not concerned. The coordinates of forced responses $\mathbf{u}$ are approximated by the a superposition of forced responses $\mathbf{u}_j$ corresponding to the single nonlinear mode-j:

$$\mathbf{u} \approx \sum_{j=1}^{N_r} \mathbf{u}_j \approx \sum_{j=1}^{N_r} q_j \tilde{\mathbf{\Phi}}_j \tag{4.21}$$

In this approach, the coupling between nonlinear modes is neglected.

The modal parameters, *i.e.* mode shapes, natural frequencies and damping ratios, can be deduced based on the reduced nonlinear normal modes and then interpolated as a function of their corresponding modal amplitudes. Analyzing these parameters yields a nonlinear modal overview, which is very useful to evaluate the dynamic performance of the system or to identify the modes responsible for nonlinear phenomena. Furthermore, by introducing these modal parameters, forced responses can then be computed by iterative numerical methods.

4.4 Reduced nonlinear modal synthesis

The above analysis has been based on the full FE model containing all N DOFs. Both the determination of nonlinear normal modes in Section 4.3.1 and the forced responses in Section 4.3.3 pertain to iterative procedures. If fewer variables were involved in the iterations, then the numerical computation process would be accelerated, thus leading to a significant savings in computational resources.

Transformation matrices, such as those with a reduced basis in the linear mode synthesis (LMS) theory, are employed herein to project physical coordinates onto the generalized modal coordinates in Equation (4.1) prior to the calculation of nonlinear modes. The single nonlinear modal analysis approach described in Section 4.3.1 is used according to the superposition of the single nonlinear normal mode responses, as indicated in Section 4.3.3. Lastly, the physical coordinates of the forced responses are obtained by using the mode shapes.

The nodes have been partitioned into both the master DOFs and the slave DOFs to facilitate the numerical protocol in $\mathbf{u}$, $\mathbf{M}$, $\mathbf{K}$, $\mathbf{D}$ and $\mathbf{F}$. Master DOFs are those on the interfaces containing nonlinearities that are conserved as physical DOFs, while slave DOFs are those in the model that would be projected onto the modal space. The numbers of master DOFs and slave DOFs are respectively denoted N_{J} and N_{S}.

In the following analysis, an initial reduction is carried out by truncating internal modes, referred to as Reduced Nonlinear Modal Synthesis based on Constraint modes and Internal modes (RNLMS-CI). A second reduction is applied on the boundary modes, called Reduced Nonlinear Modal Synthesis based on Branch modes and Internal modes (RNLMS-BI).

The RNLMS-CI method entails selecting the primary internal modes and all constraint modes: the physical displacements of slave DOFs are expressed as the addition of a static constraint modes matrix ($\boldsymbol{\Psi}_{\mathrm{SJ}}$) multiplied by the physical coordinates of master DOFs ($\mathbf{u}_J$), plus a reduced fixed interface modes matrix ($\boldsymbol{\Phi}_{\mathrm{II}}$) multiplied by the modal coordinates of slave DOFs ($\mathbf{q}_{\mathrm{I}}$). The selected fixed interface mode number is denoted N_{I}. In applying the reduced basis ($\mathbf{T}_{\mathrm{CI}}$) to transform physical coordinates into modal coordinates, we have:

$$\mathbf{u} = \begin{bmatrix} \mathbf{u}_{\mathrm{J}} \\ \mathbf{u}_{\mathrm{I}} \end{bmatrix} = \begin{bmatrix} \mathbf{T}_{\mathrm{C}} & \mathbf{T}_{\mathrm{F}} \end{bmatrix} \begin{bmatrix} \mathbf{u}_{\mathrm{J}} \\ \mathbf{q}_{\mathrm{I}} \end{bmatrix} \tag{4.22}$$

where

$$\mathbf{T}_{\mathrm{CI}} = \begin{bmatrix} \mathbf{T}_{\mathrm{C}} & \mathbf{T}_{\mathrm{F}} \end{bmatrix} \quad \mathbf{T}_{\mathrm{C}} = \begin{bmatrix} \mathbf{I}_{\mathrm{JJ}} \\ \boldsymbol{\Psi}_{\mathrm{SJ}} \end{bmatrix} \quad \mathbf{T}_{\mathrm{I}} = \begin{bmatrix} \mathbf{0} \\ \boldsymbol{\Phi}_{\mathrm{II}} \end{bmatrix} \quad \boldsymbol{\Psi}_{\mathrm{SJ}} = -\mathbf{K}_{\mathrm{SS}}^{-1}\mathbf{K}_{\mathrm{SJ}}$$

The fixed interface modes matrix $\boldsymbol{\Phi}_{\mathrm{II}}$ is formed by eigenvectors $\boldsymbol{\Phi}_{\mathrm{Ij}}$ to the following equation:

$$(-\omega_{\mathrm{Ij}}^2 \mathbf{M}_{\mathrm{SS}} + \mathbf{K}_{\mathrm{SS}})\boldsymbol{\Phi}_{\mathrm{Ij}} = \mathbf{0} \tag{4.23}$$

The above reduction basis serves to reduce internal DOFs, while boundary DOFs remain the same. Boundary DOFs can also be reduced by using a branch mode analysis described in Chapter 1: whereby branch modes are introduced to condense boundary modes on nonlinear interfaces. The master DOFs involving nonlinearities are thus also projected onto the modal space. The selected branch mode number is denoted N_{B}. Branch modes matrix $\mathbf{X}_{\mathrm{B}}$ is formed by eigenvectors $\mathbf{X}_{\mathrm{Bj}}$ to Equation (4.24):

$$(-\omega_{\mathrm{Bj}}^2 \mathbf{M}_{\mathrm{B}} + \widetilde{\mathbf{K}}_{\mathrm{B}})\mathbf{X}_{\mathrm{Bj}} = \mathbf{0} \tag{4.24}$$

where

$$\mathbf{M}_{\mathrm{B}} = (\mathbf{\Psi}_{\mathrm{B}})^T\mathbf{M}\mathbf{\Psi}_{\mathrm{B}}, \quad \mathbf{K}_{\mathrm{B}} = (\mathbf{\Psi}_{\mathrm{B}})^T\mathbf{K}\mathbf{\Psi}_{\mathrm{B}}, \quad \mathbf{\Psi}_{\mathrm{B}} = \begin{bmatrix} \mathbf{I}_{\mathrm{JJ}} \\ \mathbf{\Psi}_{\mathrm{SJ}} \end{bmatrix}$$

The transformation matrix $\mathbf{T}_{\mathrm{BF}}$ is applied as follows:

$$\mathbf{u} = \begin{bmatrix} \mathbf{u}_{\mathrm{J}} \\ \mathbf{u}_{\mathrm{I}} \end{bmatrix} = \begin{bmatrix} \mathbf{T}_{\mathrm{B}} & \mathbf{T}_{\mathrm{I}} \end{bmatrix} \begin{bmatrix} \mathbf{q}_{\mathrm{B}} \\ \mathbf{q}_{\mathrm{I}} \end{bmatrix} \tag{4.25}$$

where

$$\mathbf{T}_{\mathrm{BI}} = \begin{bmatrix} \mathbf{T}_{\mathrm{B}} & \mathbf{T}_{\mathrm{I}} \end{bmatrix} \quad \mathbf{T}_{\mathrm{B}} = \begin{bmatrix} \mathbf{X}_{\mathrm{B}} \\ \mathbf{\Psi}_{\mathrm{SJ}}\mathbf{X}_{\mathrm{B}} \end{bmatrix}$$

In the following analysis, the two transformation matrices $\mathbf{T}_{\mathrm{CF}}$ and $\mathbf{T}_{\mathrm{BF}}$ are denoted $\mathbf{T}_{\mathrm{r}}$ since a reduced basis is associated with both of them. Both $[\mathbf{q}_{\mathrm{C}};\mathbf{q}_{\mathrm{I}}]$ and $[\mathbf{q}_{\mathrm{B}};\mathbf{q}_{\mathrm{I}}]$ are denoted $\mathbf{q}_{\mathrm{r}}$. The reduced motion equation is expressed as:

$$(-\tilde{\omega}_{\mathrm{r}}^2\mathbf{M}_{\mathrm{r}} + i\mathbf{D}_{\mathrm{r}} + \mathbf{K}_{\mathrm{r}})\mathbf{q}_{\mathrm{r}} + (\mathbf{T}_{\mathrm{r}})^T\tilde{\mathbf{f}}(\mathbf{T}_{\mathrm{r}}\mathbf{q}_{\mathrm{r}}) = \mathbf{0} \tag{4.26}$$

where the reduced mass matrix, damping matrix and stiffness matrix are:

$$\mathbf{M}_{\mathrm{r}} = (\mathbf{T}_{\mathrm{r}})^T\mathbf{M}\mathbf{T}_{\mathrm{r}}, \quad \mathbf{D}_{\mathrm{r}} = (\mathbf{T}_{\mathrm{r}})^T\mathbf{D}\mathbf{T}_{\mathrm{r}}, \quad \mathbf{K}_{\mathrm{r}} = (\mathbf{T}_{\mathrm{r}})^T\mathbf{K}\mathbf{T}_{\mathrm{r}}$$

By applying Ritz's approximation based on a single nonlinear mode approach, the modal coordinates of forced responses are expressed by the superposition of the first N_r reduced nonlinear modes:

$$\mathbf{q}_{\mathrm{r}} \approx \sum_{j=1}^{N_r} \mathbf{q}_{\mathrm{rj}} \approx \sum_{j=1}^{N_r} q_j \tilde{\mathbf{\Phi}}_{\mathrm{rj}} \tag{4.27}$$

In this way, we've introduced the reduced nonlinear normal modes $(\tilde{\lambda}_{\mathrm{rj}}, \tilde{\mathbf{\Phi}}_{\mathrm{rj}})$, which are calculated using the same procedure as described in Section 4.3.1. The modal coordinates of forced responses are derived by the same rule presented in Section 4.3.3. The reduced nonlinear mode shapes $\mathbf{\Phi}_{\mathrm{r}}$ can be separated into two parts: $\mathbf{\Phi}_{\mathrm{rj}}^J$ and $\mathbf{\Phi}_{\mathrm{rJ}}^S$.

$$\tilde{\mathbf{\Phi}}_{\mathrm{rj}} = \begin{bmatrix} \mathbf{\Phi}_{\mathrm{rj}}^J \\ \mathbf{\Phi}_{\mathrm{rj}}^S \end{bmatrix}$$

Analyzing the components in $\mathbf{\Phi}_{\mathrm{rj}}^J$ allows studying the contributions of linear constraint modes or linear branch modes in the nonlinear mode -j; moreover, evaluating the components in $\mathbf{\Phi}_{\mathrm{rj}}^S$ yields the contributions of internal modes in the nonlinear mode -j. It should be observed that even though the nonlinearities are only located on the interface, the components representing fixed interface mode contributions also vary with q_j. This finding can be explained by the way in which the reduced basis has been integrated into the nonlinear problem: since $\mathbf{\Psi}_{\mathrm{SJ}}$ in RNLMS-CI or $\mathbf{\Psi}_{\mathrm{SJ}}\mathbf{X}_{\mathrm{B}}$ in RNLMS-BI is nonzero in the reduced basis, nonlinearity would be transmitted to the last N_{I} components in $\mathbf{\Phi}_{\mathrm{rj}}^{S}$ through the coupling term within the reduced mass matrix: $\mathbf{M}_{\mathrm{r}}$.

Let's note that only $N_{\mathrm{J}} + N_{\mathrm{I}}$ variables are involved in the iterations when deducing the eigenvectors of the reduced nonlinear problem with RNLMS-CI, instead of computing $N_{\mathrm{J}} + N_{\mathrm{S}}$ variables using the NLMA method. Furthermore, $N_{\mathrm{B}} + N_{\mathrm{I}}$ variables are part of the iterative process when employing the RNLMS-BI, rather than introducing $N_{\mathrm{J}} + N_{\mathrm{S}}$ variables into the nonlinear problem by applying the RNLMS-CI method. Let's also note that when $N_{\mathrm{B}} = N_{\mathrm{J}}$, the RNLMS-BI method is equivalent to the RNLMS-CI method. From the full model described in Section 4.3, when $N_{\mathrm{I}} = N_{\mathrm{S}}$, the RNLMS-CI method is equivalent to the NLMA method applied on the full model.

The advantage of this approach is that nonlinear normal modes can be computed once and for all types of external loading. They are independent of imposed loads and that frequency response can be computed with the modal parameters defined with nonlinear normal modes. When calculating frequency response with this method, the inversion of the matrices is a trivial algebraic inversion instead of complex inversion of matrix. This leads to a significant reduction in computation time.

The algorithm for calculating forced responses of the nonlinear model by the proposed reduced nonlinear modal synthesis approach is outlined as follows:

Step 1: Construct the Finite Element (FE) model of the nonlinear system with the help of Structural Dynamics Toolbox [Balmès 2009];

$$\mathbf{M}\ddot{\mathbf{u}} + \mathbf{D}\dot{\mathbf{u}} + \mathbf{K}\mathbf{u} + \tilde{\mathbf{f}}(\mathbf{u}) = \mathbf{F}\cos(\omega t + \varphi)$$

Step 2: Perform reductions on the full-order FE model, *e.g.* Craig & Bampton reduction technique, Branch mode analysis 1 or another reduction technique;

$$\mathbf{u} = \mathbf{T}_{\mathrm{r}}\mathbf{q}_{\mathrm{r}}$$

Step 3: Compute the reduced nonlinear modes $(\tilde{\lambda}_{\mathrm{rj}}, \tilde{\mathbf{\Phi}}_{\mathrm{rj}})$ of the reduced model by implementing Kryloff and Bogoliubov's equivalent linearization method with the Matlab solver;

$$(-\tilde{\omega}_{\mathrm{rj}}^{2}\mathbf{M}_{\mathrm{r}} + i\mathbf{D}_{\mathrm{r}} + \mathbf{K}_{\mathrm{r}})q_j\tilde{\mathbf{\Phi}}_{\mathrm{rj}} + (\mathbf{T}_{\mathrm{r}})^T\tilde{\mathbf{f}}(\mathbf{T}_{\mathrm{r}}q_j\tilde{\mathbf{\Phi}}_{\mathrm{rj}}) = \mathbf{0}$$

Step 4: Extract nonlinear modal parameters $\tilde{\mu}_{rj}$, $\tilde{d}_{rj}$, $\tilde{\omega}_{rj}$, and $\tilde{f}_{rj}$ from the reduced nonlinear modes;

$$\tilde{\mu}_{\mathrm{rj}} = (\tilde{\mathbf{\Phi}}_{\mathrm{rj}})^T\mathbf{M}_{\mathrm{r}}\tilde{\mathbf{\Phi}}_{\mathrm{rj}} \quad \tilde{d}_{\mathrm{rj}} = (\tilde{\mathbf{\Phi}}_{\mathrm{rj}})^T\mathbf{D}_{\mathrm{r}}\tilde{\mathbf{\Phi}}_{\mathrm{rj}} \quad \tilde{f}_{\mathrm{rj}} = (\tilde{\mathbf{\Phi}}_{\mathrm{rj}})^T\mathbf{F}$$

Step 5: Interpolate the extracted modal parameters as a function of modal amplitude;

Step 6: Compute the generalized modal coordinates $\mathbf{q}_{\mathrm{rj}}$ of the steady-state response of each nonlinear mode by using the interpolated functions in Step 5 along with the Matlab solver.

$$\mathbf{q}_{\mathrm{rj}} = q_{\mathrm{j}}\tilde{\mathbf{\Phi}}_{\mathrm{rj}} \qquad q_{\mathrm{j}} = \frac{\tilde{f}_j(|q_j|)}{-\omega^2\tilde{\mu}_j(|q_j|) + i\tilde{d}_j(|q_j|) + \tilde{\omega}_j^2(|q_j|)}$$

Step 7: Project the generalized modal coordinates of steady-state responses of the reduced model onto the physical space with the reduced basis used in Step 2.

$$\mathbf{u}_{\mathrm{j}} = \mathbf{T}_{\mathrm{r}}\mathbf{q}_{\mathrm{rj}}$$

Step 8: Superimpose the physical coordinates of steady-state responses of the selected nonlinear modes; the steady-state responses of the nonlinear model are then obtained.

$$\mathbf{u} \approx \sum_{j=1}^{N_r} \mathbf{u}_{\mathrm{j}}$$

4.5 Case study of an assembled structure

For a description and validation of the proposed strategy, the same model used in Section 3.2 has been investigated, while the rubber layer padding on the interfaces are nonlinear. We remind readers the model contains two Kirchhoff plates and one rubber layer interface, as shown in Figure 4.2. Plate 1 on the left side is denoted by S_1: its length a_1 is 0.66 m, the width $b_1 = 0.6$ m and the thickness e is 0.002 m; Plate 2 on the right is denoted by S_2: its length a_2 is 0.44 m, the width $b_2 = 0.6$ m and thickness $e = 0.002$ m; The rubber layer interface is denoted by J: the rubber material is padded on both the top and bottom of plates so as to ensure the connections between S_1 and S_2, with a thickness (θ) of 0.002 m and a width (l) of 0.003 m. The thickness and width variation of the rubber layer acts upon the change in its stiffness value. Figure 4.3 shows the details of this rubber layer model.

The model is excited with a tire balance type loading [Agnieszka 2005]: $\mathbf{F} = m\omega^2 R\cos\omega t$ at a frequency ω, with $m = 6$ g, and $R = 4$ cm. The excitation is located at $x = 0.44$ m and $y = 0.2$ m, hence lying on S_1. The investigated excitation frequency band is [3, 50] Hz. Structural hysteresis damping has been integrated into the model, with a damping ratio of 0.02 on the nonlinear interface J, and 0.01 on the plates S_1 and S_2.

The finite element (FE) model has been built with a Structural Dynamics Toolbox (SDTools) [Balmès 2009], as shown in Figure 4.4. To compute the forced responses of the FE model, Runge-Kutta's reference time integration method uses a considerable amount of time. As a compromise between the accuracy of the reduced model and the computation time, 4 elements per wavelength were utilized for the mesh size. The entire model contains 72 DOFs and 15 elements, of which 9 are in

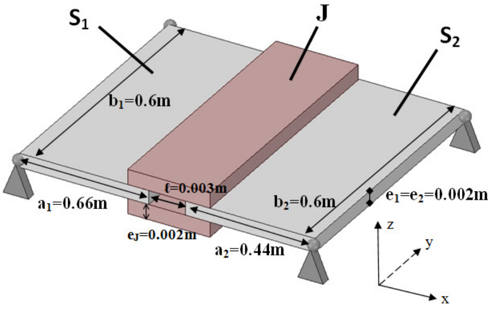

Figure 4.2: Assembled system composed of Kirchoff plates and nonlinear rubber layer interface

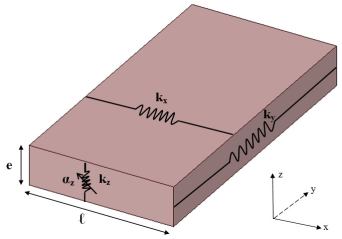

Figure 4.3: Rubber layer model

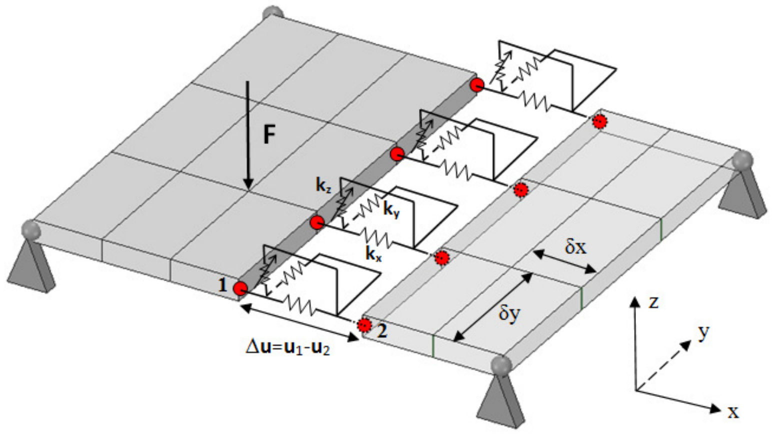

Figure 4.4: Assembled system composed of Kirchoff plates and nonlinear rubber layer interface

plate 1 on the left (*i.e.* $S_1 : a = 0.66\ m,\ b = 0.6\ m,\ e = 0.002\ m$), 6 in plate 2 on the right (*i.e.* $S_2 : a = 0.44\ m,\ b = 0.6\ m,\ e = 0.002\ m$), and 4 elements in the joints on the interface ($J : e = 0.002\ m,\ l = 0.003\ m$).

Nonlinearities are continuously distributed along the interface. The nonlinear restoring forces are assumed to lie in the translation direction of z. Cubic nonlinearity is one of the most popular means to describe the nonlinear effect on the dynamic behavior of the system, as revealed in many works [Sangriyadi 1990, Nayfeh 1992, Jiang 2005]. The nonlinearities included herein are Duffing oscillators in the form of a cubic nonlinear restoring force that depends on the relative displacement between nodes on the interface. The cubic nonlinearity ratio is denoted α, and the nonlinear restoring force is given by:

$$\tilde{\mathrm{f}}(\mathrm{u}) = \alpha \Delta \mathrm{u}^3 \tag{4.28}$$

It should be mentioned that other nonlinear forces having analytical expressions can also be investigated by using the method presented in Chapter 4.3, herein Duffing oscillator is taken as example. The geometry and material properties are the same as the description for assembled plates in Table 3.2 in Chapter 3, except that a nonlinear coefficient of 0.9 is added to describe the nonlinear behavior of interfaces.

4.5.1 Truncation effects of higher-order nonlinear normal modes

By applying this nonlinear modal analysis on the full FE model, steady-state responses of the model within the targeted frequency band (*i.e.* [3, 50] Hz) can be compared to those output by the classical Runge-Kutta method. Given their spatial limitations, responses in the z direction of the excitation point will be analyzed herein. Moreover, stable responses are examined since instable branches are not available using time integration method.

A sensitivity analysis of the forced responses to the nonlinear mode reduction coefficient has been performed here for $r_c = 1$, $r_c = 1.5$, $r_c = 2$ and $r_c = 4$ (Figure 4.5). That's to say, the nonlinear normal modes of the built-up model are retained up to $r_c * 100$ Hz. The forced response curves corresponding to the excitation frequency sweeping across the targeted frequency band from 3 Hz to 50 Hz are marked in solid lines, while those as the excitation frequency sweeps across the targeted band from 50 down to 3 Hz in the reverse direction are plotted in dotted lines. It can be observed that $r_c = 2$ appears to suffice for the study of dynamic behavior up to 50 Hz, since the response curves obtained by the NLMA method with $r_c = 2$ show only small differences with respect to the response curves given by $r_c = 4$.

A reduction coefficient of $r_c = 2$ for nonlinear normal modes has thus been assigned to construct the forced responses. Figure 4.6 compares the response curves obtained by superimposing the steady-state responses of the first 18 single nonlinear modes with those obtained by the classical Runge-Kutta's method. Two curves were generated for each method: as the excitation frequency sweeps across the targeted frequency band from 3 Hz up to 50 Hz, and as this excitation frequency sweeps across the targeted band from 50 down to 3 Hz in the opposite direction. The amplitude of steady-state responses is plotted on the upper subfigure, and the phase is indicated on the lower subfigure. These results demonstrate the effectiveness and accuracy of the nonlinear modal analysis method.

4.5.2 Truncation effects of internal modes and branch modes

Before applying the reduced nonlinear modal synthesis to the nonlinear model, a convergence study of forced responses to the reduction coefficient corresponding to component modes has been conducted on the linear model with LMS. Setting $r_c = 2$ as the reduction coefficient for all types of component modes, *i.e.* constraint modes, branch modes and internal modes, a quality analysis of the reduced model is evaluated as follows: The normal mode frequencies for the free vibration-reduced

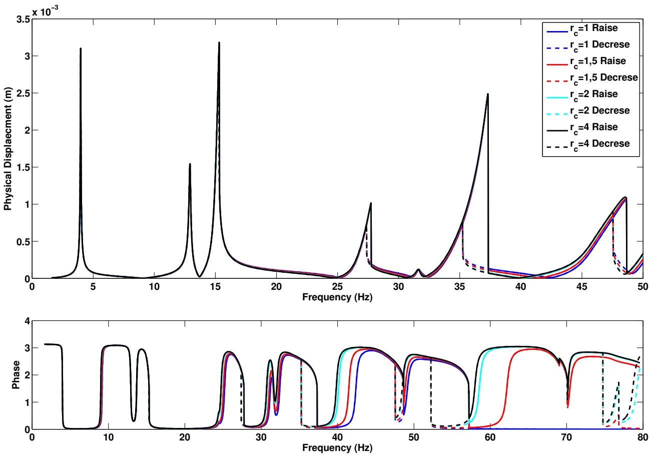

Figure 4.5: Comparison of the forced responses obtained by NLMA method applied on the full FE model, corresponding to different r_c. r_c corresponds to the reduction coefficient on nonlinear modes. Results corresponding to $r_c = 1$, $r_c = 1.5$, $r_c = 2$ and $r_c = 4$ are compared herein.

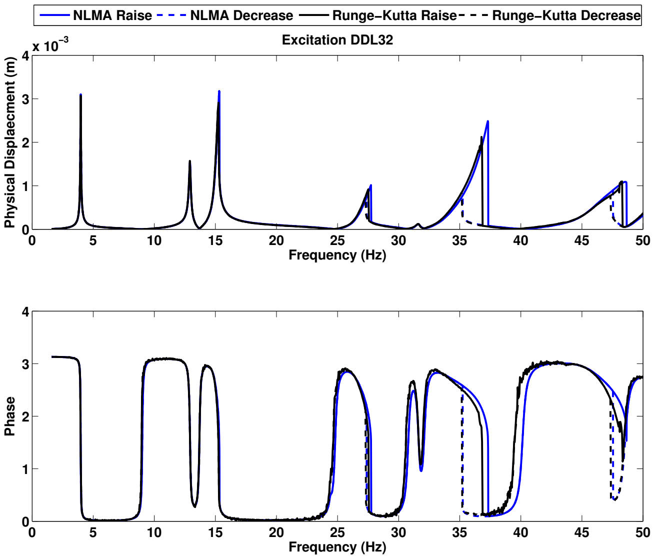

Figure 4.6: Comparison of the forced responses obtained by nonlinear modal analysis corresponding to $r_c = 2$ and those obtained by RungeKutta method

Table 4.1: Comparison of natural frequency of the full FE and reduced model

Mode number	1	2	3	4	5	6	7	8	9
NLMA (Hz)	3.97	12.91	15.06	24.42	26.73	31.50	34.04	43.36	46.24
RNLMS-CI (Hz)	3.97	12.91	15.06	24.43	26.75	31.59	34.14	43.47	46.45
RNLMS-BI (Hz)	3.97	12.91	15.06	24.44	26.76	31.64	34.16	43.64	46.51

model are compared with those of the full FE model. The natural frequency error is negligible up to 50 Hz, as displayed in Table 4.1. The modal assurance criterion (MAC) is also calculated in order to compare the reduced mode shapes and the exact mode shapes, with the MAC value being greater than 0.95 up to 50 Hz.

Based on these simulation results with LMS, a reduced nonlinear modal synthesis has been performed with $r_c = 2$ for all mode types involved in the transformation matrix T_r used in the following analysis. Note that a higher r_c value may be selected in cases when a more accurate reduced model is needed. The reduction effect of internal modes and branch modes on the forced responses will be presented in the next section.

By using the RNLMS-CI method, both the constraint modes and internal modes are included in the transformation matrix. The reduction step is performed by condensing internal DOFs. Figure 4.7 depicts the forced responses at the excitation point corresponding to various reduction coefficients: this figure 4.7 indicates good convergence of these responses around resonant frequencies when the selected internal mode number varies between 1 and 6, which has also revealed a reduction effect of the internal modes. It appears that $r_c = 2$ suffices for studying the dynamic performance of a nonlinear system up to 50 Hz. No higher-order internal modes need to be selected since the forced responses remain the same when more internal modes are conserved with a reduction coefficient greater than 2.

By employing the reduced nonlinear modal synthesis with constraint modes and internal modes (RNLMS-CI), the forced responses at four points of the model are calculated and compared to results obtained by the Runge-Kutta's method, *i.e.*: an excitation point in Figure 4.8, a randomly selected point on J in Figure 4.9, a randomly selected point on S_1 in Figure 4.10, and a randomly selected point on S_2 in Figure 4.11. All these figures show response curves that closely match the reference method.

A further reduction is performed on the boundary DOFs using the reduced basis combined with branch modes and internal modes in the nonlinear modal synthesis (RNLMS-BI). To study the truncation effect of branch modes on the forced responses, stationary responses at the excitation point are plotted in Figure 4.12. The reduced model investigated herein corresponds to $r_c = 1$, $r_c = 2$, $r_c = 4$, no reduction for branch modes and $r_c = 2$ for internal modes. When observing the response curves around 27 Hz, it appears that a reduced model with $r_c = 4$ for

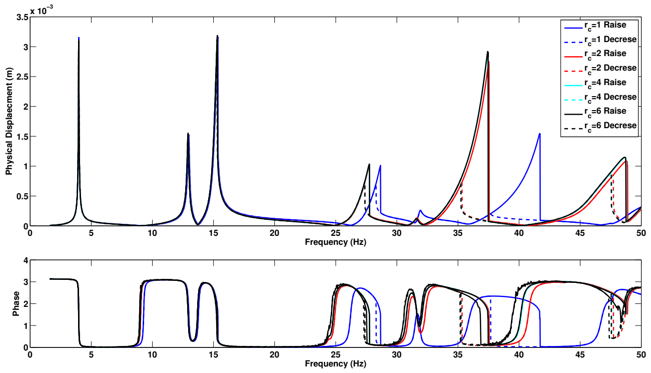

Figure 4.7: Comparison of the forced responses obtained by RNLMS-CI method corresponding to different r_c. r_c corresponds to the reduction coefficient on internal modes. Results corresponding to $r_c = 1$, $r_c = 2$, $r_c = 4$ and $r_c = 6$ are shown herein

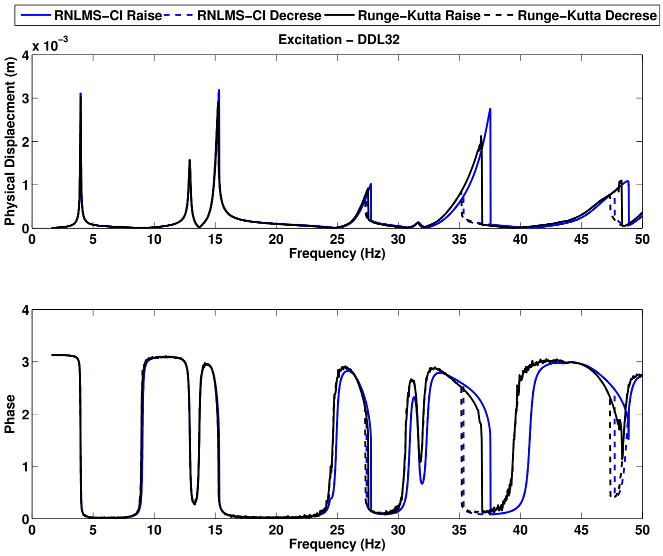

Figure 4.8: Comparison of the forced responses on excitation point obtained by Constraint NLMS method with $r_c = 2$ and by RungeKutta method

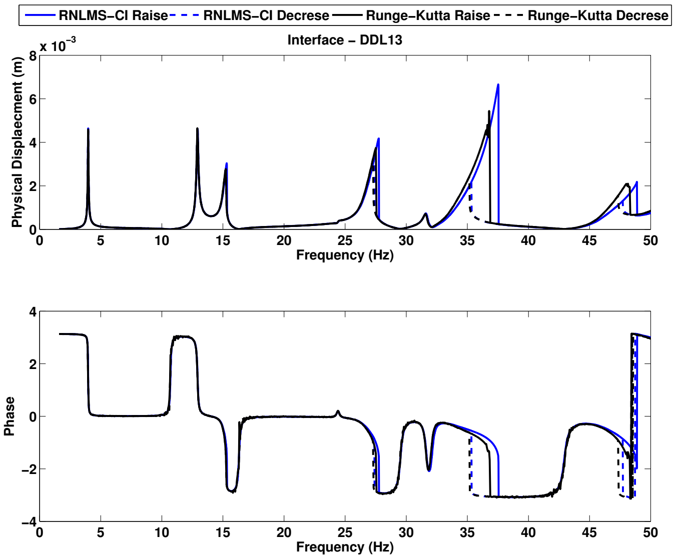

Figure 4.9: Comparison of the forced responses on an arbitrary point of J obtained by Constraint NLMS method with $r_c = 2$ and by RungeKutta method

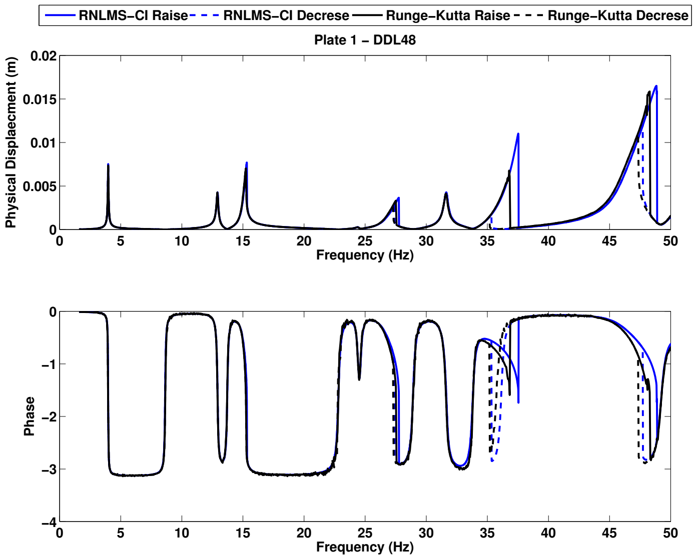

Figure 4.10: Comparison of the forced responses on an arbitrary point of S_1 obtained by Constraint NLMS method with $r_c = 2$ and by RungeKutta method

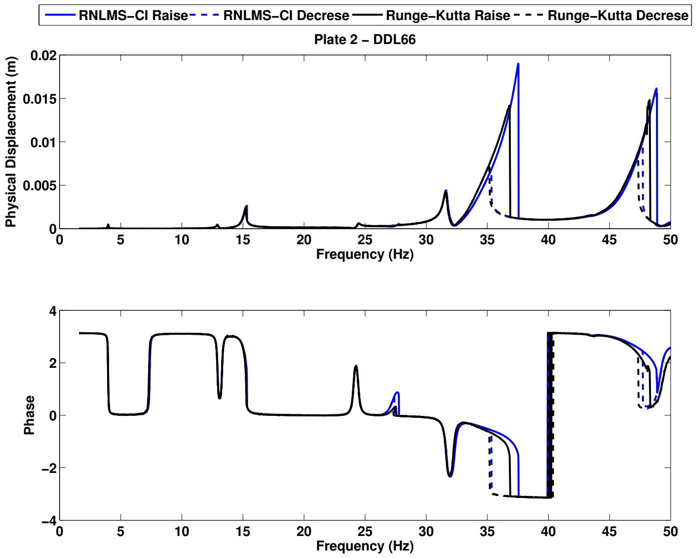

Figure 4.11: Comparison of the forced responses on an arbitrary point of S_2 obtained by Constraint NLMS method with $r_c = 2$ and by RungeKutta method

branch modes provides sufficient accuracy to study the stationary responses.

The truncation effect of internal modes on the forced responses of the reduced model has also been analyzed when setting $r_c = 4$ for branch modes. Stationary responses at the excitation point corresponding to $r_c = 2$, $r_c = 4$ and $r_c = 6$ for internal modes are compared in Figure 4.13. It appears that the reduced model with $r_c = 2$ for internal modes provides adequate accuracy to study the stationary responses.

The forced responses are observed to be more sensitive to the selected branch mode number than to the internal mode number, which can be explained by the fact that branch modes are associated with the nonlinear interface behavior.

The amplitude and phase of physical displacement in the z direction for the 4 points obtained by RNLMS-BI with $r_c = 4$ for branch modes and $r_c = 2$ for internal modes are compared to those obtained using Runge-Kutta's reference method: the excitation point (Figure 4.14), a randomly selected point on J (Figure 4.15), a randomly selected point on S_1 (Figure 4.16), and a randomly selected point on S_2 (Figure 4.17). These figures all suggest fairly good match between response curves obtained with the RNLMS-BI method and the temporal integration reference method, which proves the efficiency of the RNLMS-BI method.

Whenever the amplitude reaches a peak on the upper subfigure, there is violent phase changes occur on the lower subfigure. In another finding, the model shows an obvious nonlinear performance when resonance is encountered, *i.e.* around 27 Hz, 36 Hz and 48 Hz. The response curve inflection leads to multivalued amplitudes and hence a "jump" phenomenon, which is actually a consequence of nonlinearities

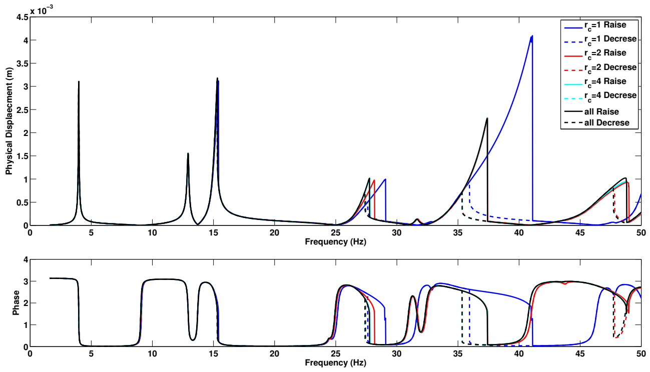

Figure 4.12: Comparison of the forced responses obtained by RNLMS-BI method corresponding to different r_c. r_c corresponds to the reduction coefficient on branch modes. Results corresponding to $r_c = 1$, $r_c = 2$, $r_c = 4$ and no truncation are shown herein

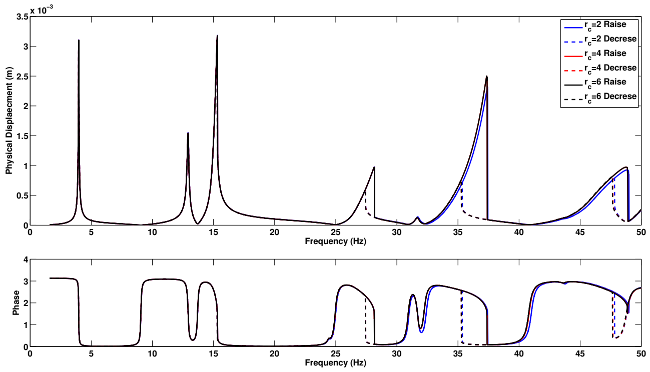

Figure 4.13: Comparison of the forced responses obtained by RNLMS-BI method corresponding to different r_c. r_c corresponds to the reduction coefficient on internal modes. Results corresponding to $r_c = 2$, $r_c = 4$, and $r_c = 6$ are shown herein

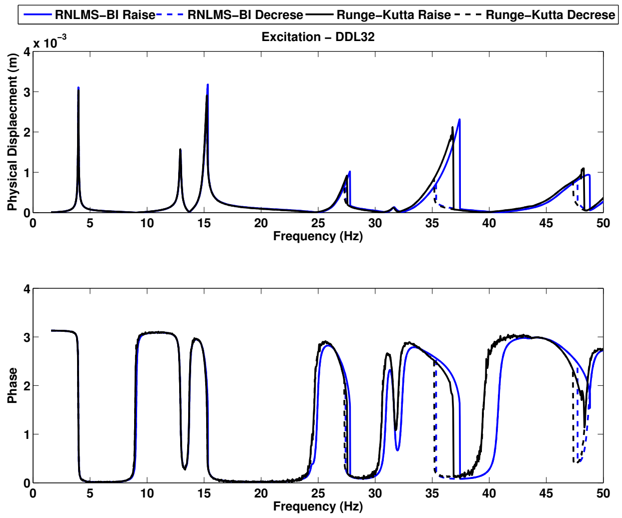

Figure 4.14: Comparison of the forced responses on excitation point obtained by Branch NLMS method with $r_c = 2$ for internal modes and with $r_c = 2$ for branch modes and by RungeKutta method

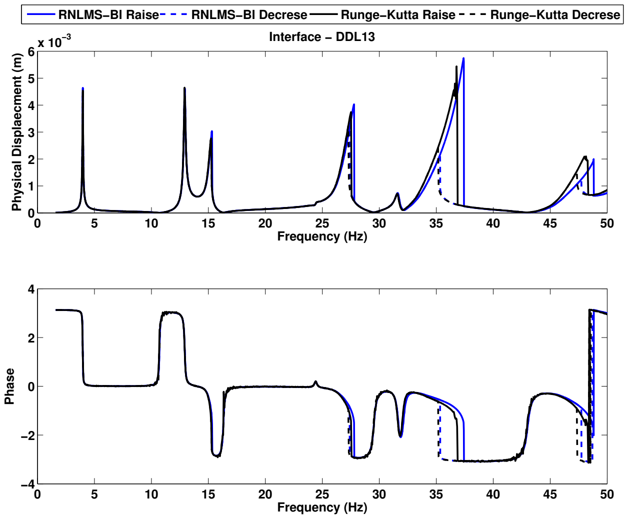

Figure 4.15: Comparison of the forced responses on an arbitrary point of J obtained by Branch NLMS method with $r_c = 2$ for internal modes and with $r_c = 2$ for branch modes and by RungeKutta method

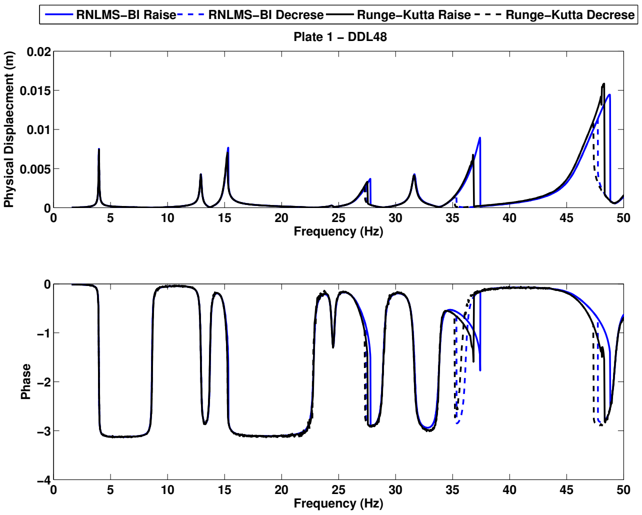

Figure 4.16: Comparison of the forced responses on an arbitrary point of S_1 obtained by Branch NLMS method with $r_c = 2$ for internal modes and with $r_c = 2$ for branch modes and by RungeKutta method

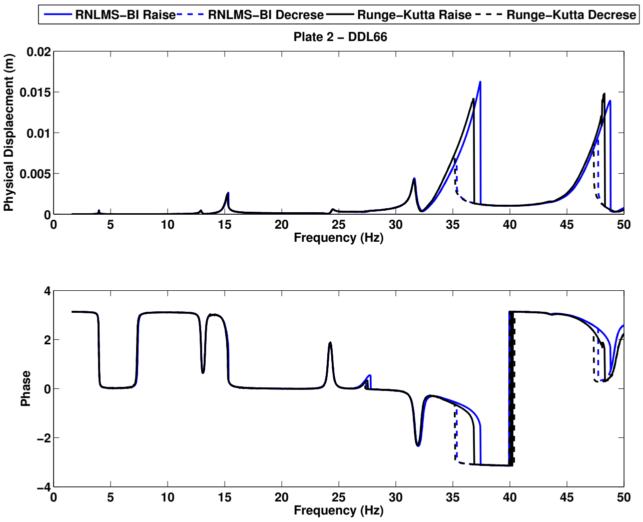

Figure 4.17: Comparison of the forced responses on an arbitrary point of S_2 obtained by Branch NLMS method with $r_c = 2$ for internal modes and with $r_c = 2$ for branch modes and by RungeKutta method

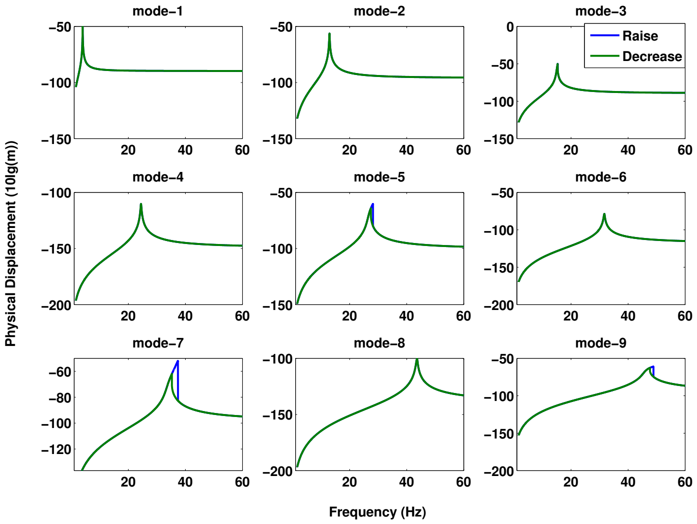

Figure 4.18: Forced responses of the nine first nonlinear modes

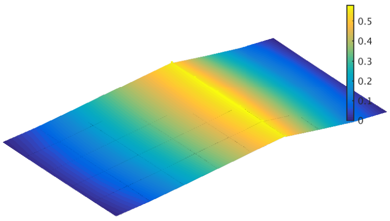

Figure 4.19: mode 1 around 6 Hz

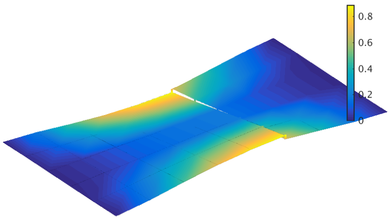

Figure 4.20: mode 2 around 6 Hz

located along the joints.

4.5.3 Analysis of nonlinear phenomena from a modal overview

Figure 4.18 displays the forced responses of the first 9 nonlinear modes. It is observed that mode 1 around 4 Hz and mode 2 around 13 Hz are nearly linear, while mode 7 around 36 Hz and mode 9 around 48 Hz show a relatively strong nonlinear performance.

By observing the linear modes shapes of the system (Figures 4.19, 4.20, 4.21, 4.22), the deformations on the nonlinear interface are not evident for mode 1 and 2, while become large when passing to mode 7 and 9. Since nonlinearities are located on the interface, the amplitude of interface reveals the nonlinear influence on the system's dynamic performance. The color defined herein is proportional to motion norm.

Furthermore, analyzing nonlinear modes provides a modal overview of the dynamic performance of the nonlinear system. Figure 4.23 reveals how nonlinear

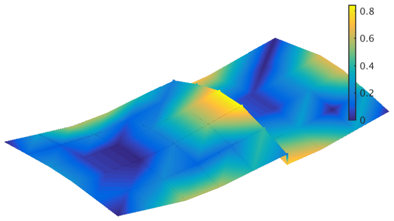

Figure 4.21: mode 7 around 6 Hz

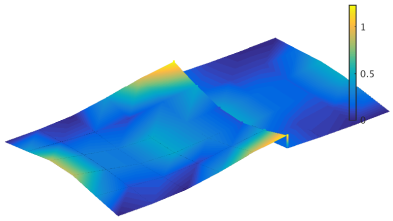

Figure 4.22: mode 9 around 46 Hz

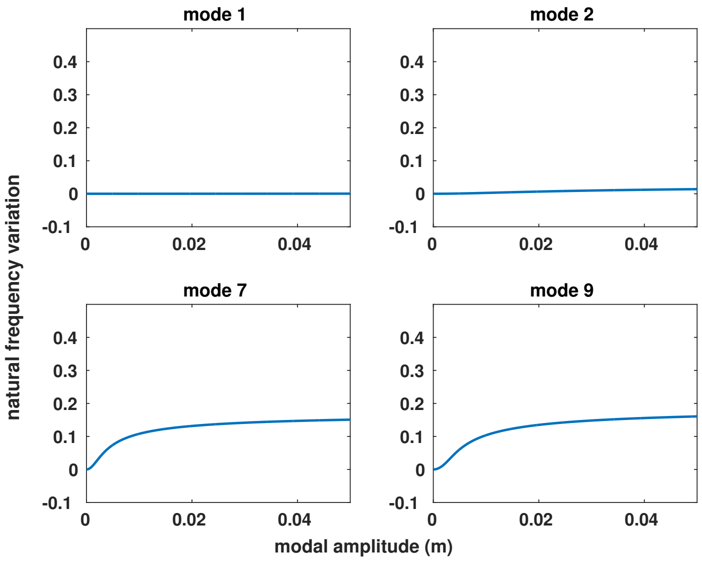

Figure 4.23: Nonlinear normal mode frequency variation in function of the modal amplitude for nonlinear modes-$1, 2, 7, 9$

natural frequency varies with its modal amplitude. It is seen that nonlinear natural frequencies all stem from the natural frequencies of the linear model, without a Duffing oscillator, and ultimately approximate the model's linear natural frequencies when the nodes on the interface connecting each substructures are clamped to each other.

The variation in modal damping ratios as a function of modal amplitude is also plotted in Figure 4.24. This variation tends to be nearly reciprocal to that of nonlinear natural frequencies, which can be explained by the mathematical expression of the modal damping ratio in Equation (4.15).

The participation of linear normal modes in reduced nonlinear modes 1, 2, 7 and 8 ($\tilde{\beta}_{k1}$, $\tilde{\beta}_{k2}$, $\tilde{\beta}_{k7}$, $\tilde{\beta}_{k8}$ where $k = 1, ..., 18$) is captured in Figure 4.25. The participation of the corresponding linear mode in the nonlinear mode always equals 1, which is in agreement with the assumption that $\tilde{\beta}^{\mathrm{r}}_{jj} = 1$.

Figures 4.23, 4.24 and 4.25 explain the dynamic performance shown in Fig-

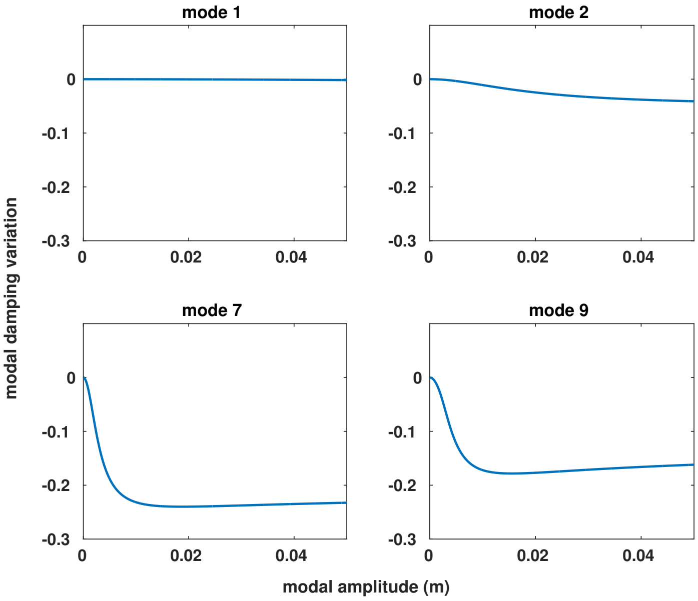

Figure 4.24: Damping ratio variation in function of the modal amplitude for nonlinear modes-1, 2, 7, 9

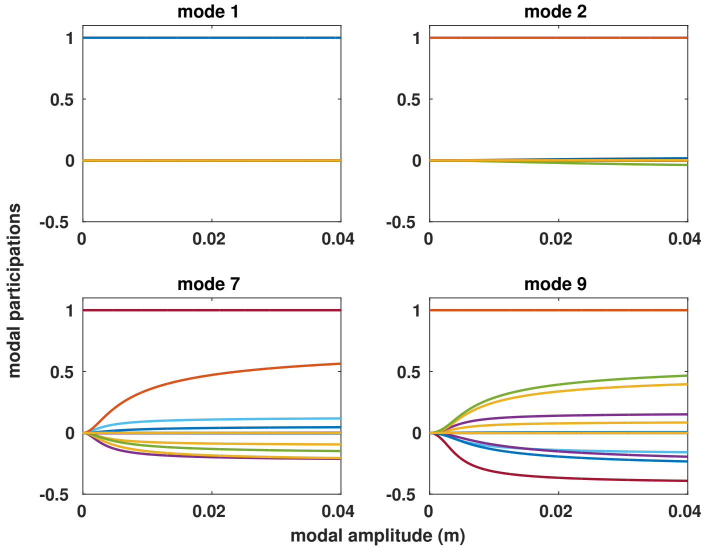

Figure 4.25: Modal participations of linear normal modes in function of the modal amplitude for nonlinear modes-1, 2, 7, 9

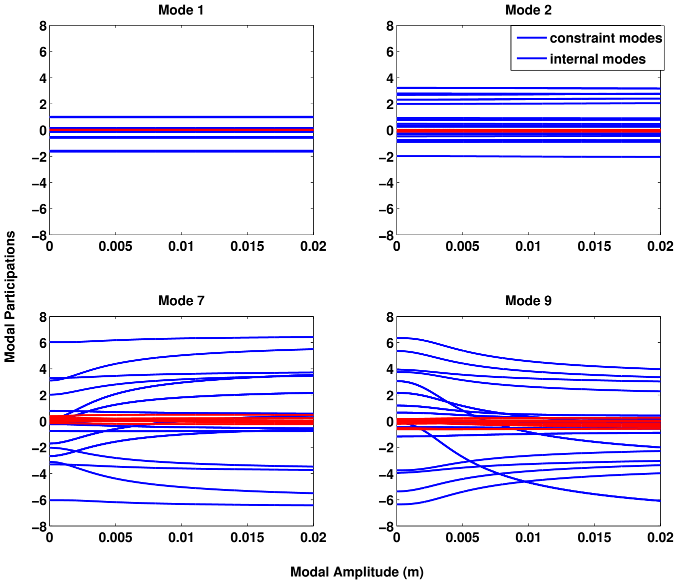

Figure 4.26: Variation of modal components versus their corresponding modal amplitude for nonlinear modes-$1, 2, 7, 9$ obtained with reduced constraint NLMS strategy

ure 4.6, *i.e.* mode 1 around 4 Hz and mode 2 around 13 Hz are nearly linear, while mode 7 around 36 Hz and mode 9 around 48 Hz exhibit a relatively strong nonlinear behavior. The natural frequency, damping factor and linear mode participation parameters do not vary with modal amplitude for modes 1 and 2, while those for modes 7 and 8 vary substantially.

Furthermore, with a transformation matrix composed of constraint modes and fixed interface modes, another modal overview can be derived on the nonlinear behavior. Similar to the above analysis, modes 1, 2, 7 and 9 have been investigated. Figure 4.26 shows the variation trends of components in the reduced nonlinear modes *vs.* the modal amplitude. These components pertain to internal modes and are marked by red lines, while those representing constraint modes are marked in blue in Figure 4.26. Nonlinear modes vary with constraint mode components, yet they do not vary considerably with internal modes components. It can be concluded that constraint modes are responsible for the model's nonlinear performance.

To summarize, the reduced nonlinear modal synthesis methods are proven to be accurate and efficient in analyzing assembled systems with nonlinearities continuously located at interfaces between substructures. For this assembled system composed of Kirchhoff plates and a nonlinear rubber layer, 50% of DOFs are truncated by applying the RNLMS-CI method and, furthermore, 67% of DOFs are truncated by applying the RNLMS-BI method, as indicated in Table 4.2. Simulations have been conducted on a server containing 32 Xeon (R) processors running at 2.9 GHz. Considering the $10,000$ linearly-spaced modal amplitudes from 0 to 1, the CPU time consumed in computing one nonlinear mode is: $6,394\ s$ when employing the NLMA method on the full FE model, $4,098\ s$ when applying reduced nonlinear modal synthesis with constraint modes and internal modes on the reduced model, and $2,636\ s$ when using reduced nonlinear modal synthesis with branch modes and internal modes on the reduced model.

All reduction techniques serve to reduce computation time, with the branch mode analysis providing even more savings since branch modes are also truncated compared to Craig & Bampton method. This finding may be especially valuable for analyzing large assembled systems, since DOFs on the interfaces represent the majority of DOFs and demonstrates considerable computation time savings whenever the proposed RNLMS approaches are applied to study large assembled systems. Moreover, there is no need to recompute the nonlinear modes for different excitations, and forced response of the system can be calculated by using the interpolated models of modal parameters that characterize the system behavior. Both analytical and numerical synthesis methods of forced responses are presented. Jump phenomena are observed when the nonlinear systems are concerned with Duffing nonlinearities, and unstable regions are thus identified by using modal synthesis method by sweeping across the interested frequency range in two directions.

Table 4.2: Comparison of retained modes number and CPU time

Method	Branch Modes number	S_1 Internal Modes number	S_2 Internal Modes number	Total modes number	CPU time(s)
full FE	24	30	18	72	6 394
RNLMS-CI	24	7	5	36	4 098
RNLMS-CB	10	7	5	24	2 636

Chapter 5

Structures involving dry friction

Contents

5.1 Friction models 113
5.1.1 Static friction models 114
5.1.2 Dynamic friction models 115
5.1.3 Masing models by the use of restoring force 117
5.2 Generalized Masing model 119
5.3 Reference numerical methods 124
5.3.1 Theory of Newmark-β method 124
5.3.2 Theory of Harmonic Balance method 127
5.4 Theory of nonlinear modal analysis 129
5.4.1 Frictional damping by using real modal synthesis 130
5.4.2 Frictional damping by using complex modal synthesis 132
5.5 Case study of 2 DOFs mass-stiffness model 133
5.5.1 Time history of responses by using Newmark-β method . . . 134
5.5.2 Steady-state responses by using nonlinear modal synthesis method 137
5.5.3 Modal overview based on nonlinear modal synthesis method . 140
5.6 Case study of a cantilever beam 144
5.6.1 Time history of responses by using Newmark-β method . . . 144
5.6.2 Analysis based on nonlinear modal synthesis method 145
5.7 Case study of the assembled plates 148
5.7.1 Time responses by using Newmark-β method 149
5.7.2 Analysis based on nonlinear modal synthesis method 151

5.1 Friction models

In this section, we will present different phenomenological and rheological models, which can be used to predict friction phenomena that are linked with pertinent hypotheses or measurements. Various rheological models are discussed, including static model depending solely on the velocity, dynamic models introducing an extra state to describe the average deflection of the asperities and physics-based models.

5.1.1 Static friction models

Coulomb, viscous and Stribeck model

The most ubiquitous model in the modeling and simulation literature is Coulomb friction. [Andersson 2006] The Coulomb, the viscous and the Stribeck model form the basic elements of friction. The friction force including all these three effects is [Geffen 2009]:

$$F_f(v) = F_c(v) + F_v(v) + F_s(v) \tag{5.1}$$

The friction force given by the Coulomb model is $F_c = \mu F_n \mathrm{sign}(v)$, with F_n the normal force, μ the friction coefficient, and v the relative velocity of the moving object.

The viscous friction force is linear with respect to the velocity: $F_v(v) = \sigma_v v$, with σ_v the viscous friction coefficient.

The Stribeck friction describes the negatively sloped characteristics taking place at low velocities, *i.e.* the friction decreases with increasing velocity for a certain velocity regime. It is realized by varying the friction coefficient to interpret the start-up of lubrication mechanism. Herein it is kept in the general form $F_s(v)$ as a describing function of velocity.

When the velocity crosses $v = 0$ line, the model comes across numerical instabilities. A switch model [Drincic 2012] can be applied to enhance the friction model with the elastic part.

The Switching model

The Switch model is a technique that smooth out the discontinuous dynamics around the discontinuity $v = 0$. It consists of two separate models for the stiction phase and for the sliding phase.

For the stiction phase, it is simply modeled as a spring element, with σ_0 the micro stiffness and x the displacement:

$$F_f(x) = \sigma_0 x \tag{5.2}$$

For the sliding phase, it is modeled by the Coulomb viscous friction and the Stribeck curve with frictional lag. This model attempts to capture the dynamics of friction by introducing a time delay, which only affects the friction in sliding phase and oversimplifies it. The expression is given by:

$$\begin{aligned} F_f\left(\dot{x}, t\right) &= \left(F_c + F_v|\dot{x}| + F_{s,a} + F_s \frac{1}{1+\left(\frac{\dot{x}(t-\tau_L)}{\dot{x}_s}\right)^2} \right) \mathrm{sign}(\dot{x}) \\ F_s &= (F_{s,\infty} - F_{s,a}) \frac{t_2}{t_2+\gamma}) \end{aligned} \tag{5.3}$$

where F_s is the magnitude of the Stribeck friction, $F_{s,a}$ is the magnitude of the Stribeck friction at the end of the previous sliding period, $F_{s,\infty}$ the magnitude of the Stribeck friction after a long time at rest (with a slow application of force), $\dot{x}_s$ is the characteristic velocity of the Stribeck friction, τ_L is the time constant of frictional memory, γ is the temporal parameter of the rising static friction, and t_2 is the time at zero velocity.

However, when a tangential load is applied to the contact, elastic-plastic deformations and slip occur over the contact patch, which affects the frictional behavior. In these cases a friction coefficient value needs to be determined. The static models do not describe friction accurately enough for some applications that operate near zero velocity. Even with the switch model, the transition between the phases is not well described. In these situations, dynamic models requiring a more complex model with more parameters are necessary.

5.1.2 Dynamic friction models

Among these dynamic models, the Dahl model, the LuGre model, the Leuven integrated model and generalized Maxwell slip model are presented herein [Piatkowski 2014, Al-Bender 2010].

The Dahl model

In the Dahl model, the friction is a function of both velocity and displacement. The friction behavior is analyzed by analogy the stress-strain property for materials. When small displacements occur, the force is modeled by a spring-like elastic material behavior; while when displacements are larger, a plastic deformation resulting in a permanent displacement is taken into account. An empirical expression is used for this model:

$$\frac{dF_f(x)}{dx} = \sigma \left| 1 - \frac{F_f}{F_c} \mathrm{sign}(\dot{x}) \right|^n \mathrm{sign} \left(1 - \frac{F_f}{F_c} \mathrm{sign}(\dot{x}) \right) \tag{5.4}$$

where σ is the stiffness parameter at equilibrium point $F_f = 0\ N$, n is a material dependent parameter, *i.e.*, n is chosen between 0 and 1 for brittle materials and superior to 1 for more ductile like materials.

Dahl's model is able to model pre-displacement and hysteresis in a dynamic model, but it is unable to capture many other phenomena like the Stribeck effect and the ability to predict stick-slip motion.

The LuGre model

The LuGre model is based on Dahl's model, but else is able to describe both pre-sliding and sliding regime and the transition between them. A state variable $z = F_f/\sigma_0$ is involved in LuGre model to represent the internal friction mechanism. Besides, the constant F_c is replaced with a velocity-dependent function $g(v)$ and two more terms are added: an additional damping σ_1 associated with micro displacement and a memoryless velocity-dependent term $f(v)$ associated with macro damping.

$$\begin{aligned} F_f &= \sigma_0 z + \sigma_1 \dot{z} + \sigma_2 v \\ \dot{z} &= v\left(1 - \alpha(v,z)\operatorname{sign}(v)\frac{z}{z_{ss}(v)}\right) \end{aligned} \tag{5.5}$$

The modified LuGre model

Although the LuGre model is able to capture almost all known friction phenomena it still lacks the ability to describe hysteresis with nonlocal memory and undesired position drift occurred in simulations. These issue's are solved in the Leuven model, but at the cost of numerical and implementation problems. With two modifications a discontinuity issue and the implementation problem are solved in the modified Leuven model. LuGre model by including pre-sliding hysteresis with nonlocal memory. This type of hysteresis occurs for non-periodic pre-sliding and is an improvement for the model's accuracy with respect to reality. The state variable z represents the average deformation of the asperities of the contacting surfaces. The friction force and state equation are stated as:

$$\begin{aligned} F_f &= F_h(z) + \sigma_1 \frac{dz}{dt} + \sigma_2 v \\ \frac{dz}{dt} &= v\left(1 - \operatorname{sign}\left(\frac{F_d(z)}{S(v) - F_b}\right)\cdot\left|\frac{F_d(z)}{S(v) - F_b}\right|^n\right) \\ S(v) &= \operatorname{sign}(v)\left(F_c + (F_s - F_c)\, e^{-(|v|/v_s)^{\delta}}\right) \end{aligned} \tag{5.6}$$

where σ_1 is the micro-viscous damping coefficient, σ_2 is the viscous damping coefficient, $F_h(z)$ is a hysteresis friction force consisting of two parts: F_b at the beginning of a transition curve and $F_d(z)$ the current transition curve, n is a coefficient determining the transition curve shape, and $S(v)$ is a function that models the constant velocity behavior.

Notwithstanding, when the state variable z is reset to zero, discontinuity in the friction force can occur. To overcome this problem, a modified Leuven model was established by replacing the argument $F_d(z)/(S(v) - F_b(z))$ with $F_h(z)/S(v)$ and the hysteresis force function with the Maxwell slip model. The new state equation becomes:

$$\frac{dz}{dt} = v\left(1 - \operatorname{sign}\left(\frac{F_h(z)}{S(v)}\right)\cdot\left|\frac{F_h(z)}{S(v)}\right|^n\right) \tag{5.7}$$

The Maxwell model

The Maxwell-slip model with N masses and N springs using discrete stick-slip elements assumes an empirical friction coefficient and limiting friction force. The hysteresis force is thus a superposition of N Coulomb forces. Each mass is associated with a displacement dead band x_i, below which the mass does not move, and above which the mass moves with the same velocity as the common termination point. Hence, k_i is the minimum spring force needed to move the mass m_i. Once the mass m_i begins to move, the spring force remains at $k_i * x_i$ for all velocities of the mass. Hence, each mass-spring combination in the Maxwell-slip model is subjected to an equivalent Coulomb friction force steady state sliding property. The hysteresis force is equal to the sum of hysteresis forces of each element.

$$F_h(k) = \sum_{i=1}^{N} F_i \tag{5.8}$$

The Coulomb law at slip is replaced by a rate-state law: $F_i = K_i(z - \zeta_i)$ for $(z - \zeta_i) < W_i/k_i$ and $F_i = \mathrm{sign}(z - \zeta_i)W_i$ otherwise.

When combining with physics of the problem and imposing sliding dynamics onto the slip phase of the Maxwell-slip implementation of the hysteresis, the model turns to be a Generalized Maxwell-slip friction model.

The Physics-based model

Physics-based friction models study essential aspects of interface chemistry, mechanics and material properties, and develop a global behavior of friction from the local physics. Simulations normally consist of a large amount of asperities to acquire a decent representation. One of the major limitations of physics-based friction models is the difficulty in developing a bottom-up multi-scale model for macro-scale contacts. Although the physics-based models are capable of capturing all friction-induced phenomena that are observed so far, the computational recourses required by these models prevent its application for analyzing complex structures and are not considered herein.

5.1.3 Masing models by the use of restoring force

Rheological models and restoring force models are the two main categories widely used in mechanical engineering to predict those components behavior. The former provide damping and stiffness parameters, while the latter provide a restoring force to be introduced in the second member of the equations[Bastien 2006]. By combining these two categories together, a generalized Masing model can be developed.

The main difficulty in the representation of dry friction force resides in the calculation of the tangential contact force around zero. There exist various possibilities for the mathematical representation of the restoring force in hysteresis damping.

For hysteresis damping govern by Masing rules, one possibility is to replace $sign(v)$ with $atan(v)$ in Coulomb model (see Figure 5.1), which prevents the discontinuity around zero:

$$F_c = \mu F_n atan(v) \tag{5.9}$$

Another example is shown in the work of [Gaul 2008], a generalized Coulomb friction with contact stiffness govern by the Masing evolution rule is:

$$\dot{F}_f = k_T v \frac{1}{2} \left\{1 - \mathrm{sgn}\left(F_f^2 - F_C^2\right) - \mathrm{sgn}(vF_f)\left[1 + \mathrm{sgn}\left(F_f^2 - F_C^2\right)\right]\right\} \tag{5.10}$$

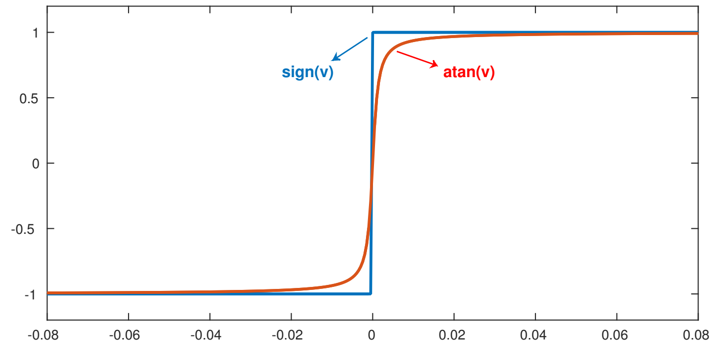

Figure 5.1: Difference of Coulomb model around zero with $sign(v)$ and $atan(v)$, x axis represents the velocity, y axis represents the dry friction force

The other possibility is to model the restoring force by differential equation. In the work of [Clavel 2001], it is modeled by an ordinary differential equation:

$$\dot{F_d}(t) = -1/e * |v(t)| * F_d(t) + f/e * v(t) \tag{5.11}$$

where e and f are two unknown parameters with dimensions of distance and force, respectively.

Moreover, inspired by Iwan type friction elements that describe contact in terms of discrete contact points and spring elements, at least three parameters should be provided to describe the restoring force with a mathematical smooth function. Several requirements should be satisfied: when no relative displacement at the contact node occurs, the friction force is zero; when the relative displacement tends to infinity, the friction force tends to its maximal value f_m; the slop of the curve at the beginning is a constant; the slop of the curve when the displacement tends to infinity is also a constant. Based on these rules, here are two mathematical models available for the calculation of restoring force of tangential contact:

$$f(x) = f_m \left(1 - e^{\left(-\frac{x}{\varepsilon} - \frac{x^3}{\alpha}\right)}\right) \tag{5.12}$$

$$f(x) = f_m(\beta_1 + (1-\beta_1)e^{-\beta_2 x^p}), \quad \beta_2 \geq 0 \tag{5.13}$$

Considering that these dynamic models are in general more difficult to implement and identify, and also computationally expensive, polynomial representation for restoring force is often adopted.

$$f(x) = \sum_{i=1}^{n} a_i x^n \tag{5.14}$$

where n is the degree of the polynomial.

Moreover, the polynomial is more natural and easy to handle for the implementation in the numerical frame. Polynomial representation (5.14) is found to be quicker than the others (5.12) and (5.13). In experimental measurements, the most general smooth function is possibly the polynomial function, with the polynomial coefficients being determined by physical constraints.

5.2 Generalized Masing model

In order to obtain a general representation of friction phenomena in engineering, a turbomachinary blade with properly designed interfaces is taken as example [Chatelet 2008]. Dry friction on the interface can provide displacement and velocity dependent damping. Two forces are observed: a pressure force that is normal to the frictional interface and an in-plane restoring force that opposes transverse displacement of the damping node. One simple model is a bilinear damper device. When these devices are put in parallel, abundant friction phenomena can be observed and this model yields a general dry friction model. The friction model can be obtained by curve fitting based on the least squares method with experimental data.

Various dry friction models can be extended to a generalized Masing model by applying Masing's rule. Polynomial is employed in representing the restoring force in hysteresis loop, thanks to its simplicity in numerical computation aspect, and its capability for the description of abundant phenomena. For example, stiction, Stribeck effect, and pre-sliding displacement can all be taken into account by selecting properly polynomial coefficients of the polynomial.

Many mathematical models have been proposed for the description of rate independent hysteresis. Among them the Masing model seems quite appropriate, because it allows a very convenient analysis of the behaviour along any loading path. Masing model is originally proposed for cyclically stabilized hysteretic behavior [Masing 1926]. In its general form the Masing model is obtained from the continuous limit of a discrete spring-friction model and it can be presented in two equivalent forms based respectively on a parallel or serial model.

For constructing the Masing model, two basic components are involved: A constitutive equation, which introduces the initial elastic stiffness and the universal evolution equations, which are independent of the special mode. The universal rule completed by the constitutive equation yields to the hysteresis loop. This is in fact the whole spirit of the Masing model which allows the finite treatment of a continuous spectrum of internal variables. [Fourgers 1989]

The hysteresis loop is illustrated on a cyclic strain path between x_m and $-x_m$. The first loading starts from the virgin state $x = 0$, and the state evolution under increasing strain up to x_m is given by the rule of constrained translation $F_0(x)$ (see Figure 5.2). The stiffness spectrum is obtained by its initial slope. The unloading behavior with decreasing x from x_m to $-x_m$ will be described in terms of the variation of F_{nl} from point A, passing by point B, and attaining point C. The unloading curve (solid lines in Figure 5.2) is deduced from the first loading curve by an homothety of ratio 2. Again the state evolution directly follows from the rule

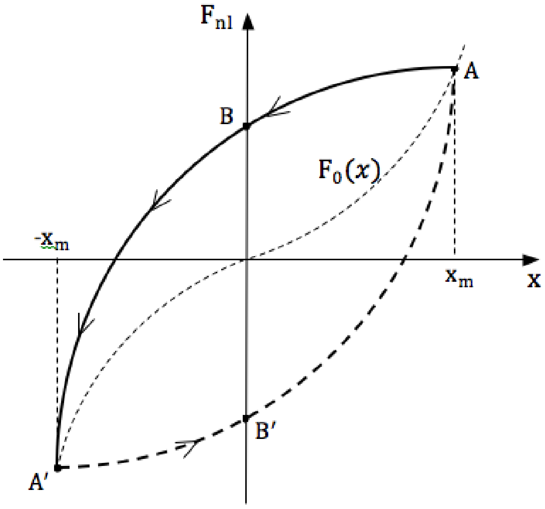

Figure 5.2: lumped-parameter system with dry friction modeled by one damper

of constrained translation. While for the reloading, an entirely symmetric situation is encountered (dashed lines in Figure 5.2), allowing the construction of the entire hysteresis loop. The Masing's rule for the whole hysteresis loop is described by Equation (5.45).

$$\begin{aligned} f_{m_1}(x) &= 2f\left(\frac{x+x_m}{2}\right) - f_m \quad x \in \text{lower branch - 1, 2} \\ f_{m_2}(x) &= -2f\left(\frac{-x+x_m}{2}\right) + f_m \quad x \in \text{upper branch - 3, 4} \end{aligned} \tag{5.15}$$

The stabilized loop can be thus obtained at the first cycle. The friction-displacement curve obtained in this way is called first loading curve. By using this first loading curve, the harmonic components of dry friction force over one steady-state period can be determined. This single bilinear hysteresis element is often used to model friction damping in systems, due to the computation costs and the simplicity in calibrating of damped model against experimental data. The drawback of this model is that it cannot capture the full richness of the frequency response with more complicated friction phenomena [Berger 2002].

Masing model with one bilinear element

The dry friction model presented herein is inspired by elasto-plastic bilinear element [Argatov 2011]: the static stiffness k_t, friction coefficient μ_d and normal force N applied on the contact. The general lumped-parameter system is illustrated by Figure 5.3.

The kinematic state is related to a static stiffness k_t, a kinetic stiffness k_d, a kinetic coefficient μ_d and a certain value for the force at which slip occurs x_d (the

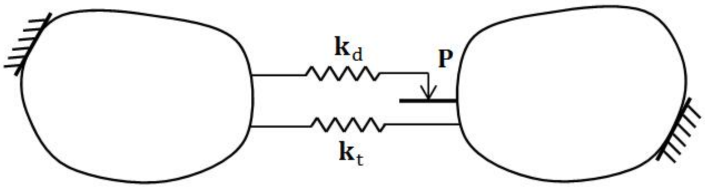

Figure 5.3: lumped-parameter system with dry friction modeled by one damper

threshold). The corresponding friction law reads:

$$f = \begin{cases} (k_d + k_t)x & x \in [0, x_d] \\ k_t x + k_d x_d & x \in [x_d, +\infty] \end{cases} \tag{5.16}$$

By employing the Masing's rule depicted in Equation (5.45), the hysteresis loop of this bilinear model is shown in Figure 5.4.

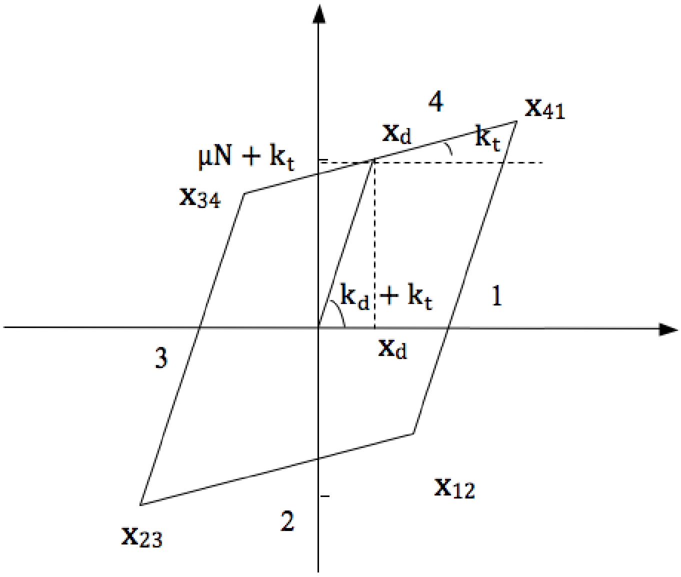

Figure 5.4: The hysteresis loop of the bilinear model

Masing model with three bilinear elements

Before getting down to a generalized Masing model, we introduce here a transitional friction model with three bilinear elements. When three macro-slip bilinear elements are set in parallel (see Figure 5.5), the friction model reproduces friction forces at three critical displacements. The friction law is expressed as Equation

(5.17).

$$
f = \begin{cases} (k_{d_1} + k_{d_2} + k_{d_3} + k_t)x & x \in [0, x_{d_1}] \\ (k_{d_2} + k_{d_3} + k_t)x + k_{d_1}x_{d_1} & x \in [x_{d_1}, x_{d_2}] \\ (k_{d_3} + k_t)x + k_{d_1}x_{d_1} + k_{d_2}x_{d_2} & x \in [x_{d_2}, x_{d_3}] \\ k_t x + k_{d_1}x_{d_1} + k_{d_2}x_{d_2} + k_{d_3}x_{d_3} & x \in [x_{d_3}, +\infty] \end{cases} \tag{5.17}
$$

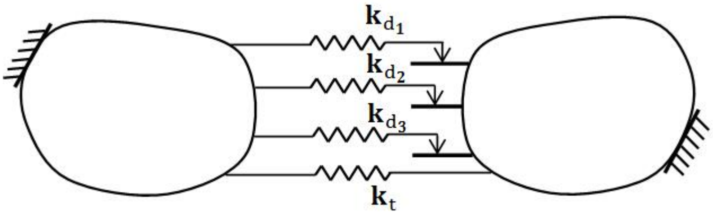

Figure 5.5: lumped-parameter system with dry friction modeled by three dampers in parallel

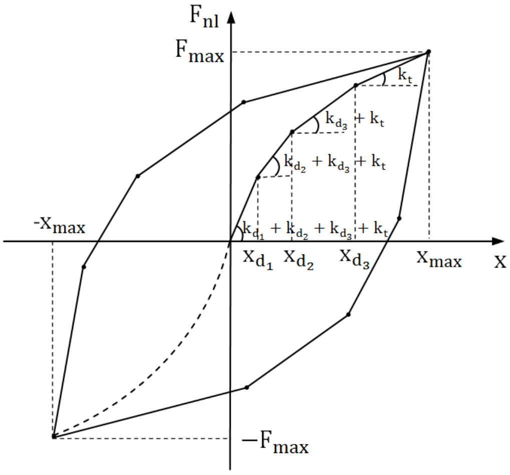

Figure 5.6: The hysteresis loop of the three bilinear dampers in parallel

The first loading curve corresponding to this expression is shown in Figure 5.6. The bilinear hysteretic element is found to act like a “soft spring". The first loading curve given by the friction model formed by three dampers are observed to be smoother compared to that of one damper.

Masing model with an inifity of bilinear elements

We propose to describe any type of friction element with an extended hysteresis model, *i.e.*, an infinity of macro-slip dampers are set in parallel (see Figure 5.7) to model the dry friction, which comes to the generalized Maxwell model [Al-Bender 2010]. The physics behind this model can be understood by imagining friction as a contact scenario involving a large population of interacting asperities subject to such phenomenological mechanisms. Therefore, the hysteresis losses take place as soon as the first slip occurs. The hysteresis loop obtained at contact point is usually used to determine the nonlinear force transmitted along the contact surface as accurately as possible.

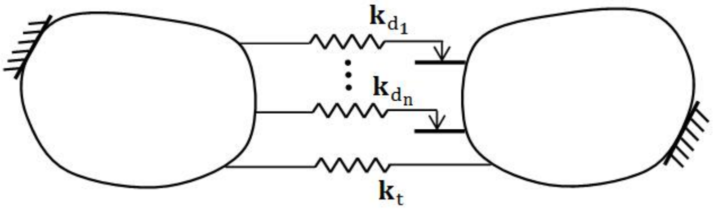

Figure 5.7: lumped-parameter system with dry friction modeled by an infinity of dampers in parallel

Each element contains two characterizing parameters, the damper stiffness k_{dn} and the threshold force f_{nln}. These elements are assembled together in parallel to represent the nonlinear force, which is very useful in representing nonlinear frictional phenomena for forced response predictions; because it captures qualitatively realistic physical behaviors with these lumped elements. The first dampers slip after some initial transient oscillations and, successively, other dampers slip after the first dampers. Substantial stick-slip can be observed providing two fundamental functionality simultaneously: frictional energy dissipation due to slip-state of some damping elements - tuned absorber; resonant response amplitude reduction due to stick-state of other damping elements-damper.

Herein the dry friction behavior in this case can be approximated by an interpolation function of physical displacement coordinates; its hysteresis loop is then deduced by Masing rules - referred to as “generalized Masing model". For example, the dry friction law of this model can be approximated by a polynomial function Equation (5.18). The coefficients would be determined by the experiments.

As an example, a_1 is determined by the initial slope (the complete stick state), a_2 represents the curvature of the loading curve, a_3 and a_4 are calculated with the static stiffness and the threshold of the dry friction elements (threshold of slip state). The damping force is described by:

$$f = \begin{cases} P(x) = a_1 x + a_2 x^3 + a_3 x^5 + a_4 x^7 \quad x \in [0, x_p] \\ P(x_p) + k_t(x - x_p) \quad x \in [x_p, +\infty] \end{cases} \tag{5.18}$$

More specifically, supposing n dampers are set in parallel to interpolate the generalized Masing model:

$$(x_0, f_{d0}), (x_2, f_{d2}) \cdots (x_j, f_{dj}) \cdots (x_k, f_{dk})$$

The threshold of each damper is determined by a ratio $r_i \in [0, 1]$:

$$x_1 = r_1 x_g, x_2 = r_2 x_g \cdots x_j = r_j x_g \cdots x_n = r_n x_g \tag{5.19}$$

where the maximum threshold of all bilinear dampers is:

$$x_g = \frac{\mu_d N}{n} \tag{5.20}$$

In consequence, the nonlinear force f_i corresponds to each threshold value x_i are given as follows:

$$\begin{aligned}
f_1 &= x_1\left(k_t + (k_{d_1} + k_{d_2} + \cdots + k_{d_n})\right)\\
f_2 &= x_2\left(k_t + (k_{d_2} + \cdots + k_{d_n})\right) + k_{d_1}x_1\\
&\vdots\\
f_i &= x_i\left(k_t + \sum_{j=i}^{n} k_{d_j}\right) + \sum_{j=1}^{i-1} k_{d_j}x_j \qquad (5.21)\\
&\vdots\\
f_n &= x_n k_t + \sum_{j=1}^{n} k_{d_j}x_j
\end{aligned}$$

The following relationship can be deduce by analogy:

$$f_{i+1} - f_i = (x_{i+1} - x_i)\left(k_t + \sum_{j=i+1}^{n} k_{d_j}\right) \tag{5.22}$$

Based on the given data set, the interpolation polynomial in the Lagrange form is defined by:

$$L(x) := \sum_{j=0}^{k} f_{dj} l_j(x) \tag{5.23}$$

where

$$l_j(x) := \prod_{\substack{0\le m\le k\\ m\neq j}} \frac{x - x_m}{x_j - x_m} = \frac{(x-x_0)}{(x_j-x_0)}\cdots\frac{(x-x_{j-1})}{(x_j-x_{j-1})}\frac{(x-x_{j+1})}{(x_j-x_{j+1})}\cdots\frac{(x-x_k)}{(x_j-x_k)} \tag{5.24}$$

Equation (5.18) shows that dry friction force applied on the system varies in a continuous form, which avoids damper “lock up". The first loading curve is found to be a smooth curve as shown in Figure 5.8.

5.3 Reference numerical methods

5.3.1 Theory of Newmark-β method

Newmark-β method is a time integration method employed to solve differential equations. It is widely used in numerical evaluation of the dynamic response in FE

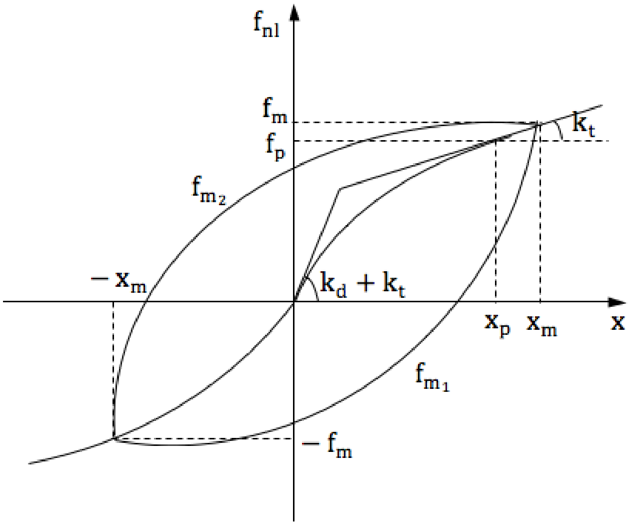

Figure 5.8: The hysteresis loop of an infinity of dampers in parallel

analysis. In Newmark-β method, relationships between displacement and velocity are defined by using the extended mean value theorem.

$$\dot{u}_{t+\Delta t} = \dot{u}_t + (1-\gamma)\ddot{u}_t \Delta t + \gamma \ddot{u}_{t+\Delta t} \Delta t \tag{5.25}$$

$$u_{t+\Delta t} = u_t + \dot{u}_t \Delta t + (\frac{1}{2} - \beta)\ddot{u}_t \Delta t^2 + \beta \ddot{u}_{t+\Delta t} \Delta t^2 \tag{5.26}$$

The relations above are implicit, because $\ddot{u}_{t+\Delta t}$ needs to be determined in order to find $\dot{u}_{t+\Delta t}$ and $u_{t+\Delta t}$, but $\ddot{u}_{t+\Delta t}$ can not be found without knowing $\dot{u}_{t+\Delta t}$ and $u_{t+\Delta t}$. Implicit methods involve the solution of a set of nonlinear algebraic equations at each time step. The advantage is that they are unconditionally stable. Transforming Equation (5.26), the acceleration is:

$$\ddot{u}_{t+\Delta t} = \frac{1}{\beta \Delta t^2}\left(u_{t+\Delta t} - u_t\right) - \frac{1}{\beta \Delta t}\dot{u}_t - \left(\frac{1}{2\beta} - 1\right)\ddot{u}_t \tag{5.27}$$

Substituting Equation (5.27) in Equation (5.25), we get the velocity at instant $t+\Delta t$:

$$\dot{u}_{t+\Delta t} = \frac{\gamma}{\beta \Delta t}\left(u_{t+\Delta t} - u_t\right) + \left(1 - \frac{\gamma}{\beta}\right)\dot{u}_t + \left(1 - \frac{\gamma}{2\beta}\right)\Delta t \ddot{u}_t \tag{5.28}$$

Since the displacement, velocity and acceleration all satisfy the motion equation Equation (5.29), we can obtain the following relationship Equation (5.30) to calculate the displacement at instant $t + \Delta t$ by substituting Equations (5.27) and (5.28) into Equation (5.29):

$$M\ddot{u}_{t+\Delta t} + C\dot{u}_{t+\Delta t} + Ku_{t+\Delta t} = Q_{t+\Delta t} \tag{5.29}$$

$$\hat{K}u_{t+\Delta t} = \hat{Q}_{t+\Delta t} \tag{5.30}$$

$\hat{Q}_{t+\Delta t}$ is the effective loading at instant $t + \Delta t$.

$$\begin{aligned} \hat{Q}_{t+\Delta t} = Q_{t+\Delta t} + M \left[\frac{1}{\beta \Delta t^2} u_t + \frac{1}{\beta \Delta t} \dot{u}_t + \left(\frac{1}{2\beta} - 1 \right) \ddot{u}_t \right] \\ + C \left[\frac{\gamma}{\beta \Delta t} u_t + \left(\frac{\gamma}{\beta} - 1 \right) \dot{u}_t + \left(\frac{\gamma}{2\beta} - 1 \right) \Delta t \ddot{u}_t \right] \end{aligned} \tag{5.31}$$

The equivalent stiffness $\hat{K}$ is:

$$\hat{K} = K + \frac{1}{\beta \Delta t^2} M + \frac{\gamma}{\beta \Delta t} C \tag{5.32}$$

To calculate forced response of the discrete model with Newmark-β method, the algorithm is outlined as follows:
Step 1: Construct the model and form the stiffness, mass and damping matrix;
Step 2: Initialize u_t, $\dot{u}_t$ and compute $\ddot{u}_t$;
Step 3: Choose an appropriate time step Δt, Newmark parameter β and γ and deduce the following constants used in integration:

$$c_1 = \frac{\gamma}{\beta \Delta t}, \quad c_2 = \frac{1}{\beta \Delta t}, \quad c_3 = \frac{1}{2\beta} - 1, \quad c_4 = \frac{\gamma}{\beta} - 1,$$

$$c_5 = \Delta t \left(\frac{\gamma}{2\beta} - 1 \right), \quad c_6 = \Delta t (1 - \gamma), \quad c_7 = \gamma \Delta t;$$

Step 4: Form the equivalent stiffness matrix:

$$\hat{K} = K + c_0 M + c_1 C;$$

Step 5: Calculate the loading:

$$\hat{Q}_{t+\Delta t} = Q_{t+\Delta t} + M \left(c_0 u_t + c_2 \dot{u}_t + c_3 \ddot{u}_t \right) + C \left(c_1 u_t + c_4 \dot{u}_t + c_5 \ddot{u}_t \right);$$

Step 6: Compute the displacement at instant $t + \Delta t$: $\hat{K} u_{t+\Delta t} = \hat{Q}_{t+\Delta t}$;
Step 7: Deduce the velocity and acceleration at instant $t + \Delta t$ using the following relationship:

$$\ddot{u}_{t+\Delta t} = c_0 \left(u_{t+\Delta t} - u_t \right) - c_2 \dot{u}_t - c_3 \ddot{u}_t,$$

$$\dot{u}_{t+\Delta t} = \dot{u}_t + c_6 \ddot{u}_t + c_7 \ddot{u}_{t+\Delta t}.$$

Step 8: Take the last stable periods of the displacement time history and extract the first harmonic response.

$\gamma = 0.5$, and $\beta = 0.25$ yields the “constant average acceleration method". In using Newmark-β method, the damper kinematic states depend on instantaneous velocity and force conditions, which need to be evaluated at each time step, especially the sign of the damper velocity. In order to get accurate response, the integration time step should be chosen appropriately.

5.3.2 Theory of Harmonic Balance method

Among all methods in the frequency domain, the Harmonic Balance Method (HBM), also known as the Fourier-Galerkin method, is introduced by Nayfeh and Mook to study the dynamics of periodically excited systems with friction damping [Nayfeh 1979]. The Fourier coefficients become the new unknowns of the problem through an approximation of the periodic signals. The nonlinear problem can be solved with a Newton-like iterative method. The accuracy of the response depends on the retained harmonic or Fourier orders.

The governing equation of the discrete model is given by Equation (5.33), where the friction force is introduced in the first member of the governing equation, which reads:

$$\mathbf{M}\ddot{\mathbf{u}} + \mathbf{D}\dot{\mathbf{u}} + \mathbf{K}\mathbf{u} = \mathbf{F} + \mathbf{f}_{nl}(\mathbf{u}, \dot{\mathbf{u}}, t) \tag{5.33}$$

where $\mathbf{M}$ is the mass matrix, $\mathbf{D}$ the damping matrix, $\mathbf{K}$ the stiffness matrix, and $\mathbf{u}$ the array of the unknown physical displacements. $\mathbf{F}$ is the force vector applied on the system. $\mathbf{f}_{nl}(\mathbf{u}, \dot{\mathbf{u}}, t)$ is the nonlinear friction force, which depends on the unknown physical displacement and velocity.

By using the HBM, the time-dependent variables in the nonlinear equation are expressed in terms of truncated Fourrier series [Laxalde 2007].

$$\begin{aligned}
\mathbf{u}(t) &= \mathbf{u}^0 + \sum_{n=1}^{N_h} \{\mathbf{u}^{n,c} cos(n\omega t) + \mathbf{u}^{n,s} sin(n\omega t)\} \\
\mathbf{f}_{nl}(t) &= \mathbf{f}_{nl}^0 + \sum_{n=1}^{N_h} \left\{\mathbf{f}_{nl}^{n,c} cos(n\omega t) + \mathbf{f}_{nl}^{n,s} sin(n\omega t)\right\} \\
\mathbf{F}(t) &= \mathbf{F}^0 + \sum_{n=1}^{N_h} \{\mathbf{F}^{n,c} cos(n\omega t) + \mathbf{F}^{n,s} sin(n\omega t)\}
\end{aligned} \tag{5.34}$$

By using Galerkin procedure, the motion equation in the frequency domain can be written as follows with the balanced Fourrier components:

$$\boldsymbol{\Lambda}\mathbf{u} = \mathbf{F} + \mathbf{f}_{nl} \tag{5.35}$$

The new unknowns of the motion equation are the Fourier components $\mathbf{u}^{n,c}$, and $\mathbf{u}^{n,s}$. The Fourier components $\mathbf{F}^{n,c}$, and $\mathbf{F}^{n,s}$ of the external force are derived by using Discrete Fourier Transformation (DFT). The Fourier components $\mathbf{f}_{nl}^{n,c}$, and $\mathbf{f}_{nl}^{n,s}$ of the nonlinear forces $\mathbf{f}_{nl}$ are deduced with Alternating Frequency Time (AFT) method [Cameron 2007, Lin 2016], which is illustrated in Figure 5.9. The AFT method starts from the harmonic components of the response $\mathbf{u}^{n,c}$ and $\mathbf{u}^{n,s}$, which are predicted by a given iteration of Newton-like method. The associated displacement and velocity in the time domain is expressed by using Inverse Discrete Fourier Transform (IDFT) procedure. The nonlinear force in the time domain is then deduced in relying on the dry friction law. Lastly the harmonic components of the nonlinear force in the frequency-domain are given by using Discrete Fourier Transform (DFT).

$$\begin{aligned}\mathbf{u} &= \left[\mathbf{u}^0, \mathbf{u}^{1,c}, \mathbf{u}^{1,s}, \ldots, \mathbf{u}^{N_h,s}\right]^T \\ \mathbf{f}_{nl} &= \left[\mathbf{f}_{nl}^0, \mathbf{f}_{nl}^{1,c}, \mathbf{f}_{nl}^{1,s}, \ldots, \mathbf{f}_{nl}^{N_h,s}\right]^T \\ \mathbf{F} &= \left[\mathbf{F}^0, \mathbf{F}^{1,c}, \mathbf{F}^{1,s}, \ldots, \mathbf{F}^{N_h,s}\right]^T\end{aligned} \tag{5.36}$$

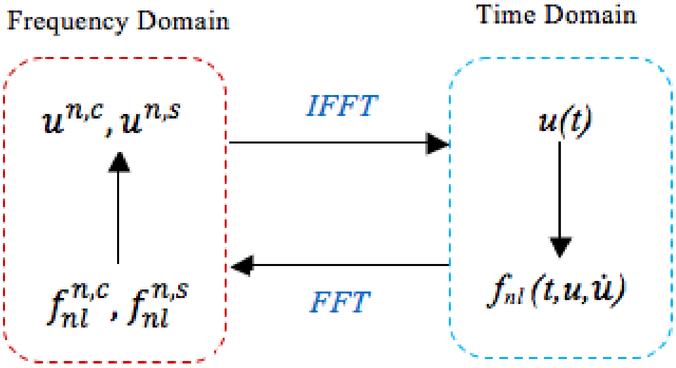

Figure 5.9: Illustration of Alternating Frequency Time process [Lin 2016]

The matrix Λ is block-diagonal, with

$$\begin{aligned}\mathbf{\Lambda} &= \mathrm{diag}(\mathbf{K}, \mathbf{\Lambda}_1, \cdots, \mathbf{\Lambda}_{N_h}) \\ \mathbf{\Lambda}_k &= \begin{pmatrix} -(k\omega)^2\mathbf{M} + \mathbf{K} & k\omega\mathbf{C} \\ -k\omega\mathbf{C} & -(k\omega)^2\mathbf{M} + \mathbf{K}\end{pmatrix}\end{aligned} \tag{5.37}$$

The resulting nonlinear equations are solved using a modified Broyden's method [Broyden 1965], which greatly enhances the robustness and efficiency of the procedure [Lin 2016].

Moreover, in order to get an accuracy and stable response to describe complex nonlinear phenomena, marks turning and bifurcation points, [Von Groll 2001] developed a numerical algorithm based on HBM, permits following a solution branch over varying system parameters via arc-length continuation [Nayfeh 2007].

Equation (5.35) is transformed into finding the root of the following equivalent equation:

$$\varepsilon(\mathbf{u}, \omega) = \mathbf{\Lambda}\mathbf{u} - \mathbf{F} - \mathbf{f}_{nl} = 0 \tag{5.38}$$

The idea of arc-length continuation method is to choose a continuation parameter along the arc-length of a solution branch, p_c, so that $\omega = \omega(p_c)$ and $u = u(p_c)$. From equation (5.38), we have:

$$F_u \frac{du}{dp_c} + F_\omega \frac{d\omega}{dp_c} = [F_u \; F_\omega] \begin{pmatrix} u' \\ \omega' \end{pmatrix} = 0 \tag{5.39}$$

The root (ω, u) to equation (5.38) is found by conducting a normalization with respect to p_c so that the tangent vector $[u'; \omega']^T$ has unit length:

$$\left(\frac{du}{dp_c} \right)^2 + \left(\frac{d\omega}{dp_c} \right)^2 = 1 \tag{5.40}$$

Responses obtained with this method is more accurate while more computational expensive. Since our research focuses on the numerical efficiency, modal synthesis method retaining the first harmonic is used to evaluate the dynamic performance of the system in the following.

5.4 Theory of nonlinear modal analysis

Time integration method such as Newmark-β provides quite accurate results as well as transient responses; HBM is one of the most popular numerical methods in analyzing nonlinear systems involving dry friction and the accuracy of the obtained responses depends on the harmonic orders kept back in the analysis. Since we are interested in the optimization of nonlinear systems with dry friction, more efficiency numerical methods are required.

In this section, extensions of nonlinear modal synthesis are conducted to study structures featuring hysteresis dry friction. A general formulation integrating friction force is developed by combing modal synthesis method and Masing's rule. Two analysis techniques are compared: real modal synthesis and complex modal synthesis. The first technique consists in using real modes in modal synthesis; the friction damping is obtained by evaluating the ratio of energy dissipation and maximum energy per cycle. The second technique pertains to the use of complex modes; the friction damping is obtained by calculating the ratio of eigenvalue's imaginary and real part. Compared to real modal synthesis, the complex modal synthesis method has involved the friction damping in the resulting set of nonlinear equations to be solved. This allows the extraction of nonlinear properties of the dry friction damper without having to recalculate the energy dissipation. The nonlinear modal synthesis provides nonlinear modes, the forced responses in steady-state can thus be computed without having to recalculate the nonlinear modes. Frictional impact phenomena and steady-state responses are analyzed by using the nonlinear modal parameters extracted from the proposed method.

Modal synthesis method, which permits numerical efficiency to calculate steady-state responses, is used to evaluate the dynamic performance of the system in the following.

The friction model proposed herein is composed of two parts, the static stiffness and the kinetic stiffness. $\mathbf{f}_{nl}(\mathbf{u}, \dot{\mathbf{u}}, t)$ can be split into two terms: one a dissipative term and the other a spring term. The first term shows the damping capacity, and that the second term implies the shifting of the spring term that changes the naturel frequencies of the system.

In general, the slip at the interface is a result of dynamic magnification around the resonances [Guillen 1999]. It is therefore justifiable that one single mode of vibration is involved to investigate the dynamic performance of the system in case of slip. Nonlinear modal synthesis and modal synthesis of forced responses described in 4 can thus be applied to obtain the nonlinear modal shape, nonlinear frequency and modal parameters depending on modal amplitude corresponding to Equation (5.33).

The nonlinear modal analysis (NLMA) entails decoupling Equation (5.33) with N uncoupled equations through the use of nonlinear normal modes (NNMs), as well as solving for eigensolutions to these uncoupled equations. $\tilde{\lambda}_j$ and $\tilde{\mathbf{\Phi}}_j$ are defined as the eigenvector for a given modal amplitude q_j, respectively. The forced responses of the nonlinear model can be expressed as Equation (5.41) by applying the Ritz-Galerkin method:

$$\mathbf{u} \approx \sum_{j=1}^{N} \mathbf{u}_j \approx \sum_{j=1}^{N_r} q_j \tilde{\mathbf{\Phi}}_j \tag{5.41}$$

In relying on the nonlinear modal synthesis presented in Chapter 4, the nonlinear mode shapes $\tilde{\mathbf{\Phi}}_j$ and the eigenvalue $\tilde{\lambda}_j$ to the characterizing equation of the nonlinear model Equation (5.42) can be computed by numerical calculations corresponding to each modal amplitude q:

$$(-\tilde{\lambda}_j \mathbf{M} + \mathbf{K})(q_j \tilde{\mathbf{\Phi}}_j) + \mathbf{f}_{nl}(q_j, \tilde{\mathbf{\Phi}}_j) = \mathbf{0} \tag{5.42}$$

The algorithm to compute nonlinear modes and forced responses of the nonlinear model involving dry friction is illustrated in Figure 5.10

The main difficulty with this model involving dry friction is the treatment of dry friction force and the calculation of damping induced by dry friction force in the nonlinear modal synthesis approach. Two modal synthesis methods can be used to study the dynamic behavior of the system, *i.e.*, by employing either real modes or complex modes. The main difference between these two methods lies in the operation of dry friction and the determination of frictional damping. Both these two approaches support modal overview on the frictional damping phenomena, by analyzing modal parameters of the nonlinear modes.

5.4.1 Frictional damping by using real modal synthesis

When applying real modal synthesis to the model, the dissipative anti-phase component part of the friction force is neglected (the dissipative effect) when computing eigen-solutions to Equation (5.33). However, the in-phase effect of the friction force (the tuning absorber) is integrated in $\tilde{\lambda}_j$.

The maximum elastic energy E_{mj} for mode j is defined by:

$$E_{mj} = \frac{1}{2} \lambda_j q_j^2 \tag{5.43}$$

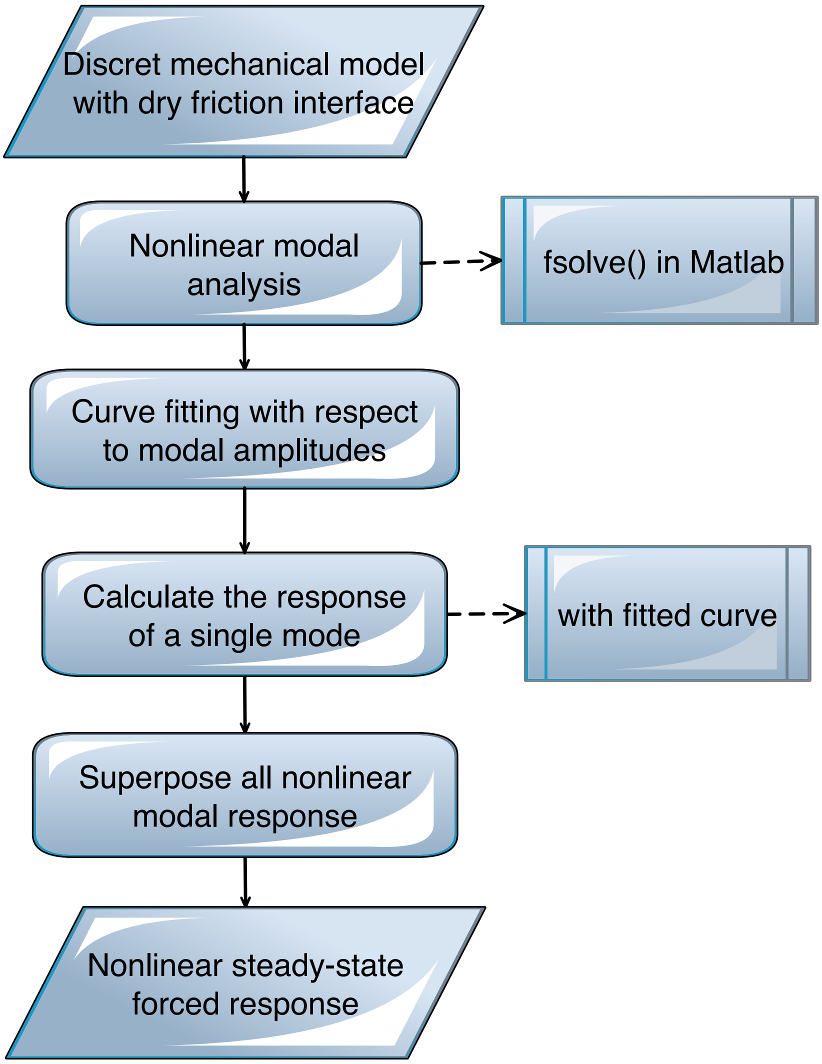
Discret mechanical model
with dry friction interface
Nonlinear modal
analysis
fsolve() in Matlab
Curve fitting with respect
to modal amplitudes
Calculate the response
of a single mode
with fitted curve
Superpose all nonlinear
modal response
Nonlinear steady-state
forced response

Figure 5.10: Algorithm for the computation of forced responses of mechanical model involving dry friction

where λ_j is the eigenvalue to the characterizing equation, and q_j is the modal amplitude of the nonlinear mode j.

The displacement for one cycle with frequency ω_j is:

$$x_t = q_j \tilde{\mathbf{\Phi}}_j \cos(\omega_j t) \tag{5.44}$$

The dry friction force f is determined by the friction law mentioned in Chapter 5.2, either bilinear (see Equation (5.16)) or polynomial(see Equation (5.18)) *etc.*.

Using Masing's rule, the friction force on one stabilized cycle is obtained with the hysteresis loop:

$$\begin{aligned} f_{m_1}(x) &= 2f\left(\frac{x+x_m}{2}\right) - f_m \quad x \in \text{lower branch - 1, 2} \\ f_{m_2}(x) &= -2f\left(\frac{-x+x_m}{2}\right) + f_m \quad x \in \text{upper branch - 3, 4} \end{aligned} \tag{5.45}$$

The dissipated energy per cycle of the FE model is expressed as:

$$dE_j = \sum_{i=2}^{N_t} \frac{1}{2}\left(f_{nl}(i) + f_{nl}(i-1)\right)\left(x_t(i) - x_t(i-1)\right) \tag{5.46}$$

where N_t is the sampling number over one stabilized period of friction-displacement curve.

The frictional damping factor is afterwards determined by calculating the ratio between the dissipated energy by the slip per cycle and the maximum elastic energy:

$$\eta_j = \frac{1}{2\pi}\frac{dE_j}{E_{mj}} \tag{5.47}$$

5.4.2 Frictional damping by using complex modal synthesis

By analogue, the nonlinear modal synthesis presented in Chapter 4 is used to obtain the nonlinear mode shapes $\tilde{\mathbf{\Phi}}_j$ and the eigenvalue $\tilde{\lambda}_j$. However, when employing the complex modal analysis, the eigen-frequency and eigen-vector are both in complex form, that is, composed by both real component and imaginary component. The interaction of damping between the two masses is taken into account by using this method. According to the normalization and orthogonal condition, the nonlinear modal mass is 1 in real modal synthesis. while the nonlinear modal mass is no longer 1 in this complex modal synthesis, but a complex value.

The nonlinear normal mode and natural frequency are written by:

$$\tilde{\lambda}_j = \tilde{\lambda}_j^c + i\tilde{\lambda}_j^s \tag{5.48}$$

$$\tilde{\mathbf{\Phi}}_j = \tilde{\mathbf{\Phi}}_j^c + i\tilde{\mathbf{\Phi}}_j^s \tag{5.49}$$

By using this approach, the dynamics of the structure is also described by nonlinear modal parameters. The dissipative effect of friction force is involved in the deduction of the eigen-solutions. Since f_{nl} can be divided into two terms: the first term (imaginary part) showing the damping capacity; the second term (real part) implying the shifting of the spring term that changes the naturel frequencies of the system:

$$\mathbf{f}_{nl} = \mathbf{f}_{nl}^{c} + i\mathbf{f}_{nl}^{s} \tag{5.50}$$

The relationship between the friction force and damper motion in steady state is governed strictly by the first loading curve. The real part and imaginary part of the dry friction force are deduced by taking the first harmonic when transforming the first loading curve from time domain to frequency domain. This procedure explains why the first loading curve is highlighted in Section 5.2.

Using the complex modal formulation, the frictional damping factor is determined directly by the ratio between $\tilde{\lambda}_j^s$ and $\tilde{\lambda}_j^c$, but not by calculating energy dissipation compared to the real modal synthesis.

$$\eta_j = -\frac{\tilde{\lambda}_j^s}{\tilde{\lambda}_j^c} \tag{5.51}$$

It should be mentioned that complex modal synthesis will be more stable and accurate compared to real modal synthesis in case that strong and complex damping are involved in the structure, which is not considered here. Because damping factor is included in the computation of nonlinear modes in complex modal synthesis. While in real modal synthesis, energy dissipation in one cycle is used to deduce frictional damping, while the dissipative terms are not integrated in the computation of eigen-solutions.

Once the nonlinear mode shapes, nonlinear modal frequency, modal parameters are determined, and frictional damping are calculated, forced responses of the system can also be computed in relying on the modal synthesis approach presented in Chapter 4.3.3.

5.5 Case study of 2 DOFs mass-stiffness model

In this section, a simple 2 DOFs mass-stiffness model described in Section 5.5 is studied for the illustration of the proposed methodology and the validation purpose as well. Transient responses are given by Newmark-β integration method in Section 5.5.1, and the steady-state responses and modal parameters are investigated in with the proposed method in Section 5.4. Simulation results are discussed for the Masing model with one bilinear element and the generalized Masing model with an infinity of bilinear elements.

For the description and validation of the proposed strategy using the generalized Masing model, the dynamic behavior of a simple 2-DOFs system is investigated. The mass on the left is clamped to the wall and the right side is connected to dry friction element. The system is excited by a tire balance type loading on $m_1 = 1\ kg$ [Agnieszka 2005]: $\mathbf{F} = m\omega^2 R \cos\omega t$ at a frequency ω, with $m = 6\ g$, $R = 4\ cm$.

The investigated excitation frequency band is [8, 70] Hz. Friction damping elements are connected to $m_2 = 1\ kg$. A slight viscous structural damping is integrated into the model, with a damping ratio of 0.0005 proportional to the stiffness matrix ($k_1 = 600\ N/m,\ k_2 = 400\ N/m$). The aforementioned nonlinear modal synthesis based on real modes and complex modes in Chapter 5.4 are both applied to analyze the dynamic performance of the system. Newmark's method is used to get the reference response curves.

Two types of Masing model are discussed in the following: the Masing model with one bilinear element as shown in Figure 5.11; and the Masing model with n dampers set in parallel to model the dry friction with $n = 10$, which is depicted in Figure 5.12.

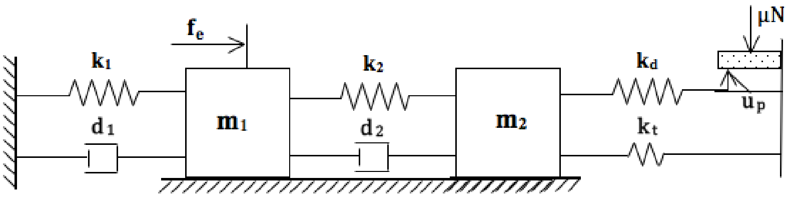

Figure 5.11: 2-DOF model with dry friction modeled by one damper

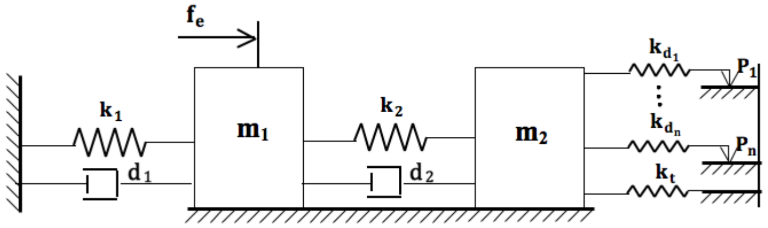

Figure 5.12: 2-DOF model with dry friction modeled by an infinity of dampers in parellel

5.5.1 Time history of responses by using Newmark-β method

When the dry friction damper is modeled by a bilinear model with $k_0 = 1/2000 * k_2$, $k_d = 1/20 * k_2$ and $\mu_d = 0.5$, temporal histories of the displacement and friction force can be obtained by using Newmark-β method ($\beta = 0.25$ and $\gamma = 0.5$). The whole transient period can be observed with Newmark-β time integration method, while it takes time to obtain the stabilized results.

For a normal force $N = 5\ N$, the damping point displacement, friction force and displacement-friction curve are depicted in Figures 5.13, 5.15 and 5.17 respectively. These curves tend to be stable with a sufficient fine time step for integration. Their corresponding steady-state curves are shown in Figures 5.14, 5.16 and 5.18. Figure 5.16 shows that slip occurs when large amplitude displacement of damping point takes place. The dissipated energy induced by the slip in one period is represented by the enclosed surface shown in Figure 5.18.

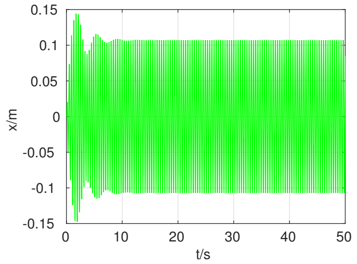

Figure 5.13: Time history of m_2 displacement obtained with Newmark-β method when $N = 5$ N

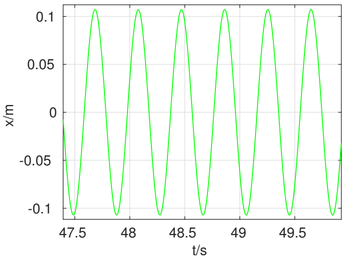

Figure 5.14: Stabilized displacement of m_2 obtained with Newmark-β method when $N = 5$ N

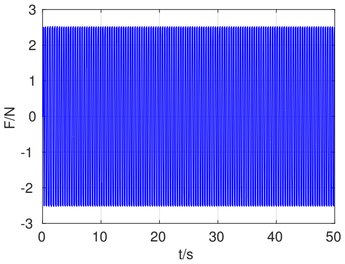

Figure 5.15: Time history of friction force obtained with Newmark-β method when $N = 5$ N

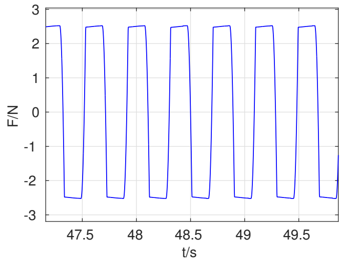

Figure 5.16: Stabilized friction force obtained with Newmark-β method when $N = 5$ N

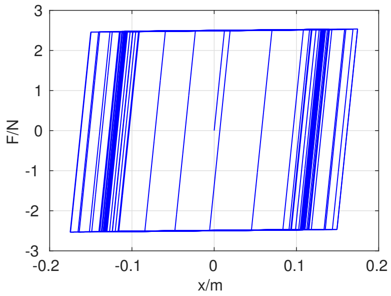

Figure 5.17: Time history of loading curve obtained with Newmark-β method when $N = 5$ N

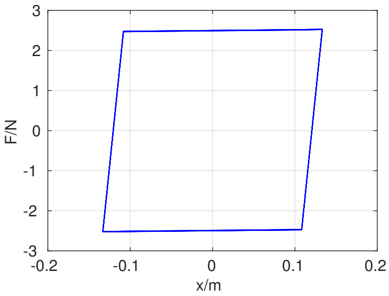

Figure 5.18: Stabilized first loading curve obtained with Newmark-β method when $N = 5$ N

Applying the Newmark-β time integration method, the stabilized curves of damper's displacement, the friction force and hysteresis loop are displayed in Figure 5.19 for the bilinear model, and in Figure 5.20 for the polynomial model.

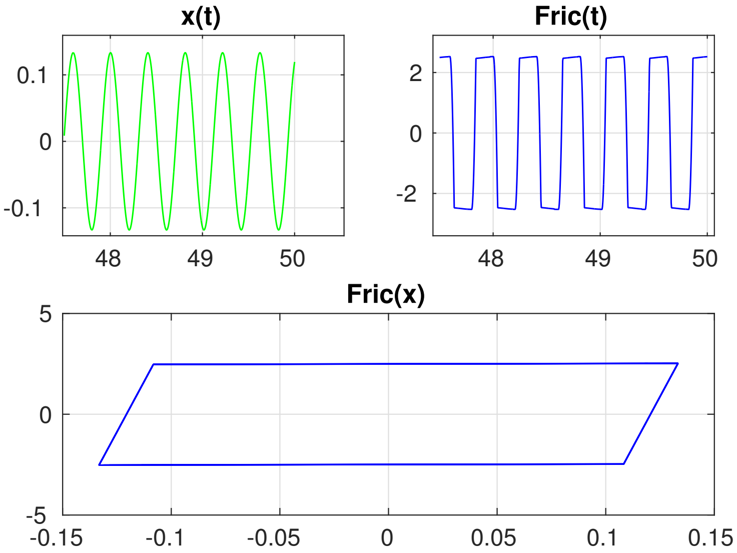

Figure 5.19: Bilinear Masing: Stabilized m_2 displacement, frictional force and hysteresis loop obtained with Newmark-β method in case that $N = 5\ N$

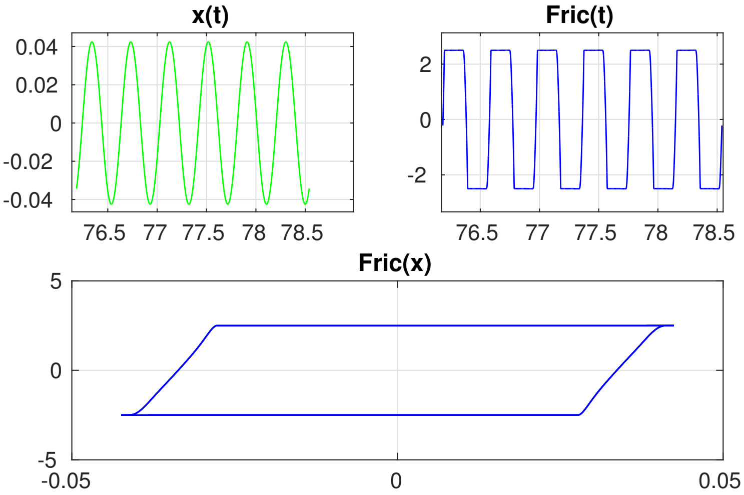

Figure 5.20: Polynomial Masing: Stabilized m_2 displacement, frictional force and hysteresis loop obtained with Newmark-β method in case that $N = 5\ N$

As one can see, when the normal load and the nonlinear friction coefficient are fixed, these two models give different stabilized curves. For the bilinear damper model, the amplitude of m_2 displacement is 0.125 m; while 0.052 for the polynomial model. As for the friction-displacement loading curve: the slope of the virgin curve is constant for the bilinear model; while it varies for the polynomial Masing model, which is reasonable since the derivation of the polynomial in function of m_2 displacement is no longer a constant. We can get better damping effect by properly selecting polynomial coefficients, which will be discussed later.

5.5.2 Steady-state responses by using nonlinear modal synthesis method

The emphasis in the present study is on qualitative trends in the dynamic behavior of the generic system. By using modal synthesis is employed to study the steady-state response with the aforementioned values of normal loads, the responses of m_1 and m_2 obtained with real modal synthesis (reported in plus marks), complex modal synthesis (reported in asterisk marks) are compared to that obtained with HBM method (reported in dotted lines) and Newmark-β method (reported in solid lines), as depicted in Figure 5.21 for m_1 and Figure 5.22 for m_2 ($N = 35\ N$). All these figures show response curves that closely match the reference methods, which reveals that nonlinear modal synthesis method is applicable to the calculation of the forced response of the system without sacrificing the accuracy of the results, especially considering the complexity of the nonlinear effect being synthesized. Once again the tuning effect and the damping effect corresponding to different normal loads are revealed herein.

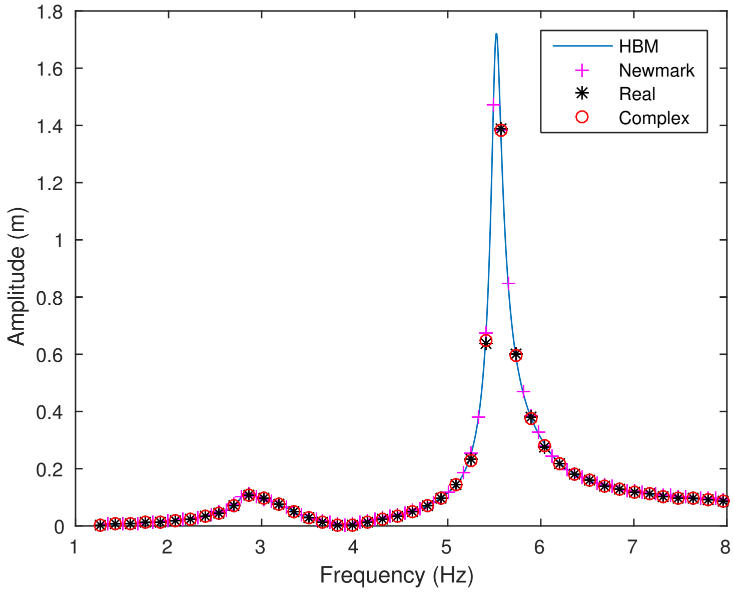

Figure 5.21: Comparison of forced response of m_1 obtained with real modal synthesis, complex modal synthesis, Harmonic balance and Newmark methods for $N = 35\ N$

The influence of normal loads on the dynamic performance of the system is

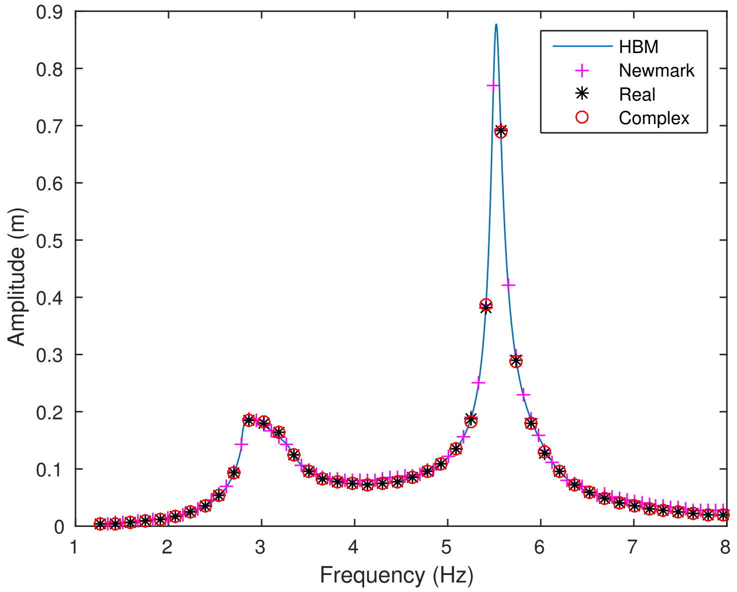

Figure 5.22: Comparison of forced response of m_2 obtained with real modal synthesis, complex modal synthesis, Harmonic balance and Newmark methods for $N = 35\ N$

analyzed herein. When the damper model is a simple bilinear model, the steady state frequency response of m_1 and m_2 corresponding to six normal loads ($N = 0, 5, 15, 25, 35,$ and $85\ N$) are plotted in Figures 5.23 and 5.24 by using complex modal synthesis. As one can see, the variation of normal load affects the resonant peak level and resonant frequency value: All these figures have revealed the damping effect around the resonance and damper tuning effect of dry friction, that is, the resonant frequency is dislocated or becomes greater when the normal force increases; In the meanwhile, the damping level varies with the normal load level. The optimal normal load that allows a maximal frictional damping in the neighborhood of the first resonance is around 20 N; the optimal normal load that allows a maximal frictional damping in the neighborhood of the second resonance is around 150 N, as that can be seen in Figures 5.23 and 5.24.

When 10 dampers are set in parellel, the dry friction force is approximated by The same conclusion can be obtained when the dry friction model is modeled by an infinity of bilinear dampers (*i.e.* the friction policy is approximated by a polynomial function). The frequency response curves obtained with aforementioned normal load values are shown in Figures 5.25 and 5.26. The optimal normal load that allows a maximal frictional damping in the neighborhood of the first resonance is also around 20 N.

Another interesting finding about the hysteresis damping model combined by an infinity parallel damping elements is related to the coefficients of the polynomial. The polynomial is used to represent the restoring force introduced in the motion

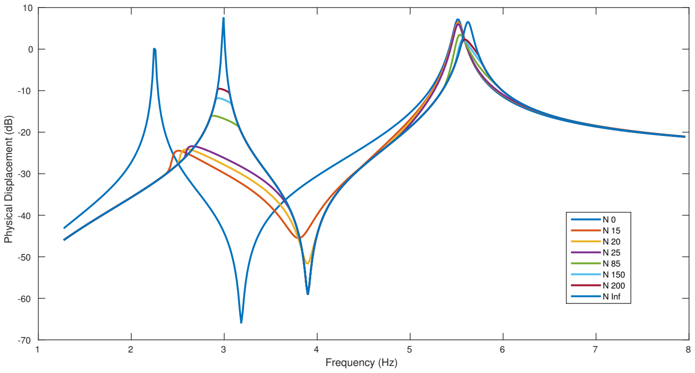

Figure 5.23: Forced response of m_1 corresponding to different normal load level of bilinear model. N denotes the normal load, *e.g.*, $N = 15$ N represents that the normal load applied on the dry friction contact point is 15 N

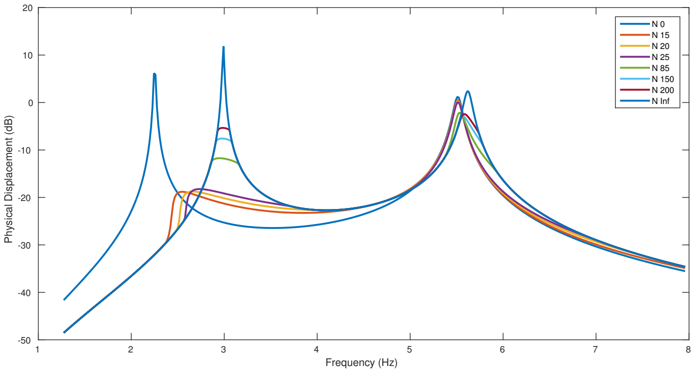

Figure 5.24: Forced response of m_2 corresponding to different normal load level of bilinear model

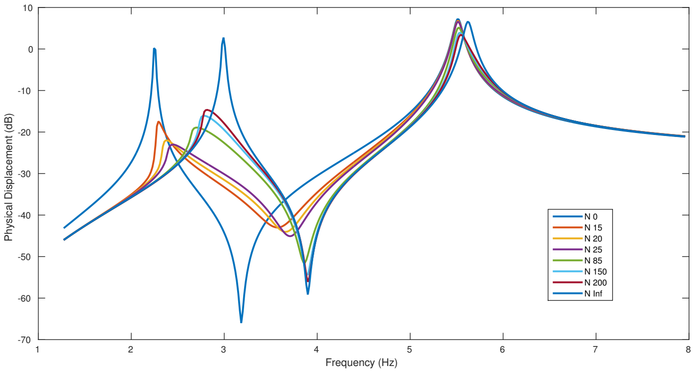

Figure 5.25: Forced response of m_1 corresponding to different normal load level when the 10 bilinear model are set in parallel

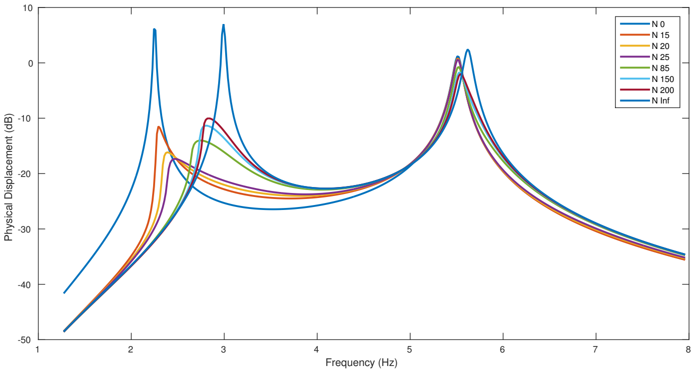

Figure 5.26: Forced response of m_2 corresponding to different normal load level when 10 bilinear model are set in parallel

equation. The polynomial coefficients are determined by the rheological model. Their values are thus revealed by the design parameters of the dampers in the model. Herein we have explored the influence of the distribution of r_i associated to each damper. The normal load is fixed: $N = 5\ N$; the dry frictional coefficient is constant $\mu_d = 0.5$; and the threshold for complete slipping state is $x_g = 0.0125\ m$.

When r_i varies in the defined range for each bilinear hysteresis damper, the damping effect and tuning effect are compared in using complex modal synthesis. Forced responses of m_1 and m_2 corresponding to different threshold values of each damper are displayed in Figures 5.27. These results imply that there exists a very substantial stick-slip design region for physically reasonable values of damper stiffness. This also indicates that even in parameter ranges yielding substantial stick-slip, an optimal distribution of r_i exists. The optimization of dry friction damping effect can be investigated by employing techniques presented in Chapter 3, an optimal r_i distribution can be obtained by using an elitist multi-objective genetic algorithm, which is not performed in this thesis.

5.5.3 Modal overview based on nonlinear modal synthesis method

Further insight into the qualitative nature of the dynamic response is gained by looking at the equivalent natural frequency and modal damping ratio. Figures 5.28 and 5.29 display the variation of natural frequency and modal damping factor in terms of modal amplitudes for the two modes, corresponding to different normal load values. It is seen that nonlinear natural frequencies all stem from the linear natural frequencies of the underlying system with dynamic stiffness and ultimately approximate the linear natural frequencies of the system without the dynamic stiffness. The low level modal amplitude corresponds to the case in which the system features a crack, and the high level modal amplitude conforms to the case in which the corresponding nonlinear boundary conditions are ignored. The evolution of the modal damping factor exhibits a maximum, which accounts for an optimum non-

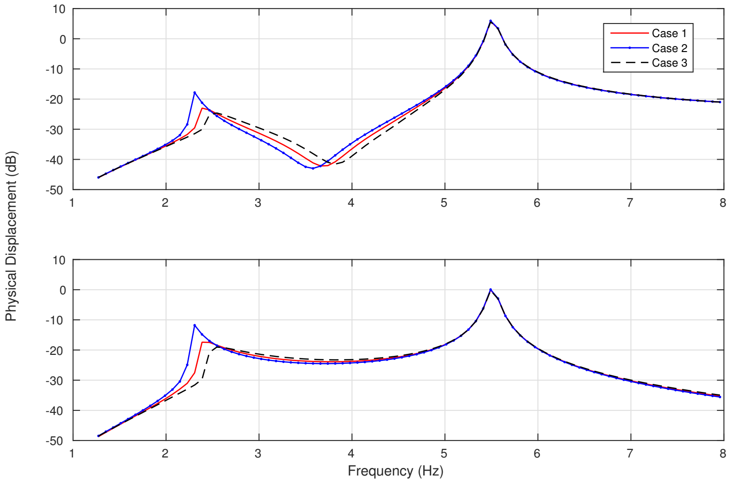

Figure 5.27: Forced responses in function of frequency corresponding to different design of polynomial Masing model when $N = 15\ N$ and $x_g = 0.0375\ m$ are constant

linear damping arising from the friction element. It should be mentioned that the maximum modal damping does not depend on the normal load, that is, when the value of normal load changes, the value of maximum modal damping remains the same. This can be explained by the reasoning in Annexes D. Notwithstanding, the modal amplitude corresponding to maximum modal damping varies with normal load.

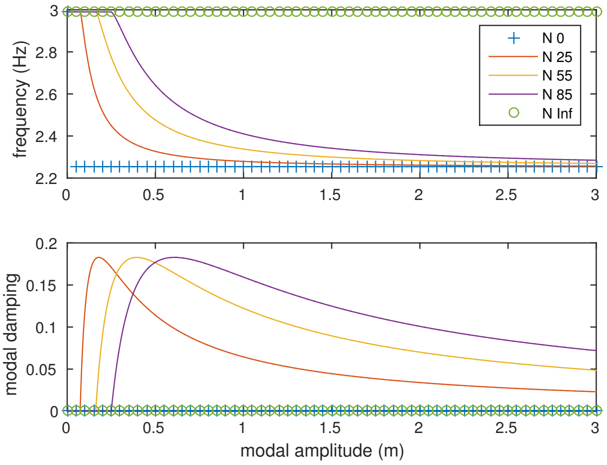

Figure 5.28: Evolution of natural frequency and modal damping factor *vs.* modal amplitude, corresponding to different normal load level, using bilinear model

When the dry friction model is modeled by an infinity of bilinear dampers, the variation of modal parameters vs. modal amplitude are indicated in Figure 5.30 for

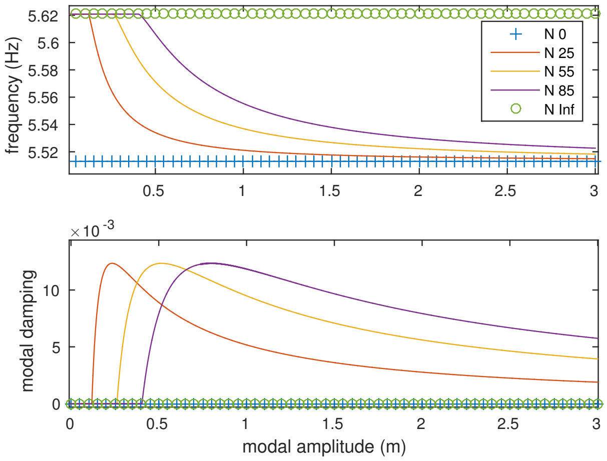

Figure 5.29: Evolution of natural frequency and modal damping factor *vs.* modal amplitude, corresponding to different normal load level, using bilinear model

the first mode and Figure 5.31 for the second mode.

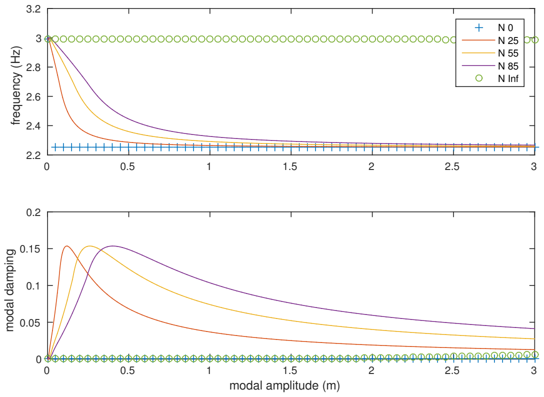

Figure 5.30: Evolution of natural frequency and modal damping factor *vs.* modal amplitude, corresponding to different normal load level, using generalized Masing model

If we compare Figures 5.28, 5.29 and Figures 5.30, 5.31, the difference between bilinear model and generalized Masing model is that the variation of natural frequency and modal damping occurs immediately and continuously when slip takes place. For example, both the modal frequency and the modal damping in Figures 5.28 and 5.29 initiate their variations when modal amplitude attains a certain value; while the change of modal frequency and modal damping in Figures 5.30 and 5.31 take place as soon as the modal amplitude differing 0.

The curve of modal amplitude q in function of excitation frequency ω is called

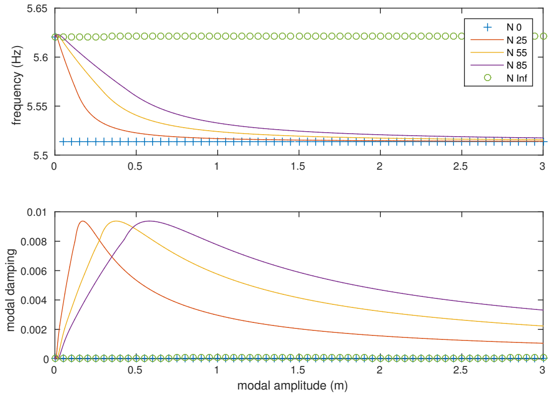

Figure 5.31: Evolution of natural frequency and modal damping factor *vs.* modal amplitude, corresponding to different normal load level, using generalized Masing model

“backbone curve". The “backbone curve" provide a valuable description of the system dynamics that may allow for characterizing and quantifying nonlinearities in the system. For a bilinear model, the synthesized forced responses corresponding to different external load level are plotted in Figure 5.32 nearby the first resonance and Figure 5.33 around the second resonance. The backbone curves are predicted by nonlinear modes (reported in dashed lines). It can be observed that the pic-values of forced responses follow the backbone curves.

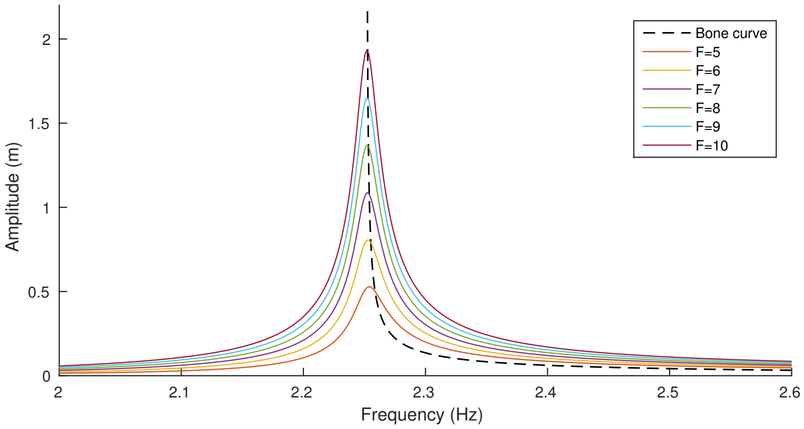

Figure 5.32: Synthesized forced response corresponding to different external loads *vs.* Backbone curve for mode 1

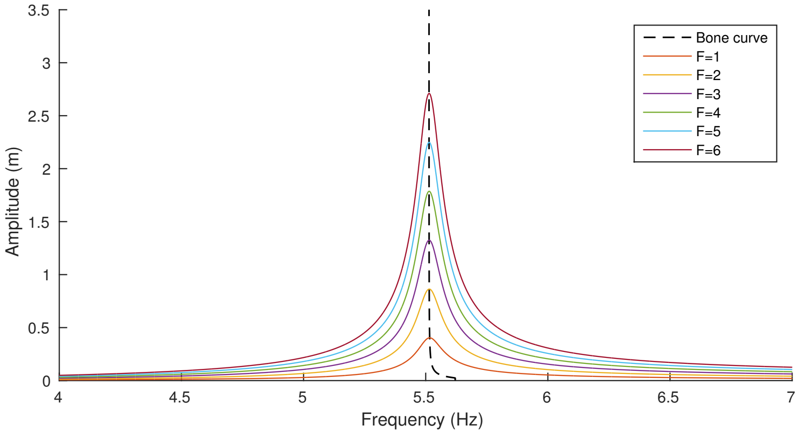

Figure 5.33: Synthesized forced response corresponding to different external loads *vs*. Backbone curve for mode 2

5.6 Case study of a cantilever beam

Simulations on a cantilever beam have also been conducted. The length of the beam is 5 m. An external sinusoidal excitation is applied on $x = 2$ m in the opposite direction of y. A Rayleigh type damping is integrated in the structure, with $\alpha = 1$ and $\beta = 3 * 10^{-4}$. The translation in z direction and rotations around x and y axis are neglected. The left end is clamped to the wall; the right end is simply supported and linked to a torsional spring, as illustrated in Figure 5.34. The movement of the right end in θ_z yields to the dry friction law of a bilinear Masing model.

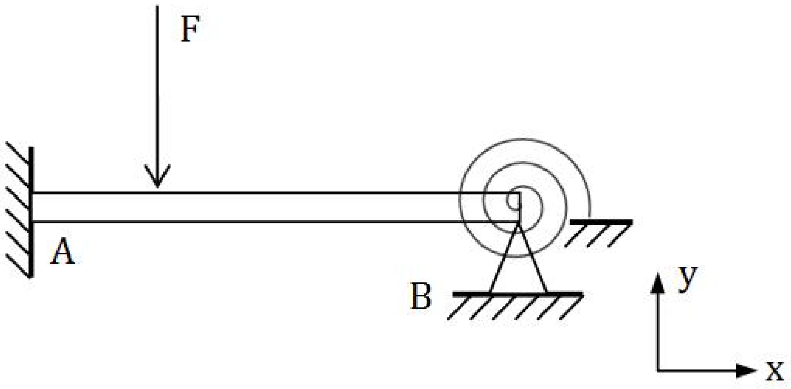

Figure 5.34: Beam model

5.6.1 Time history of responses by using Newmark-β method

By using Newmark time integration method, time histories as well as stable responses can be obtained. For an external sinusoidal force with an amplitude of

10 N, a normal force of $N = 10$ N on the friction contact point. The temporal responses and the stable responses of the DOF linked to torsional spring are plotted in Figures 5.35 and 5.36. The time history and steady-state of friction force are shown in Figures 5.37 and 5.38. It can be seen that the responses are stabilized after a while, and both stick and slip states occurred. Similarly, the time history and stable figures of displacement-friction force curves are depicted in Figures 5.17 and 5.18. The enclosed surface represents the dissipated energy by the friction force.

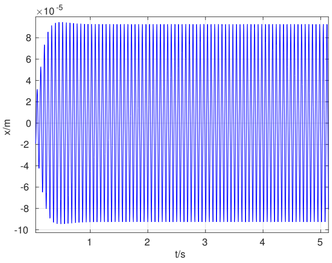

Figure 5.35: Time history of displacement obtained with Newmark-β method when $N = 10$ N

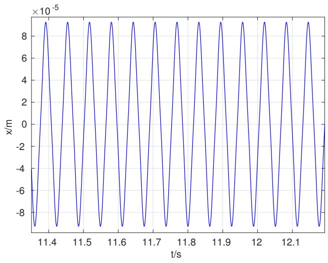

Figure 5.36: Stabilized displacement obtained with Newmark-β method when $N = 10$ N

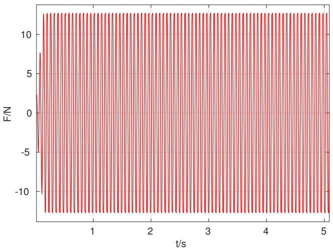

Figure 5.37: Time history of friction force obtained with Newmark-β method when $N = 10$ N

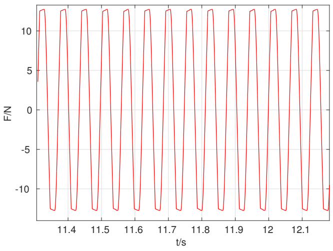

Figure 5.38: Stabilized friction force obtained with Newmark-β method when $N = 10$ N

5.6.2 Analysis based on nonlinear modal synthesis method

A comparative study of forced responses is conducted by using Newmark-β method, HBM method retaining the first harmonic and nonlinear modal synthesis method based on real modes. For an amplitude of external sinusoidal load equals to 10 N and normal load applied on the friction point equals to 10 N, the forced responses of the excitation node and friction point are given in Figure 5.41 and Figure 5.42, respectively. The responses obtained with HBM method are reported in blue solid lines, Newmark-β method are given in asterisk marks and real modal synthesis are marked by black circles. All these figures show that the response curve closely match with each another, which reveals that nonlinear modal synthesis method can be used to calculate forced response of the system without sacrificing the accuracy

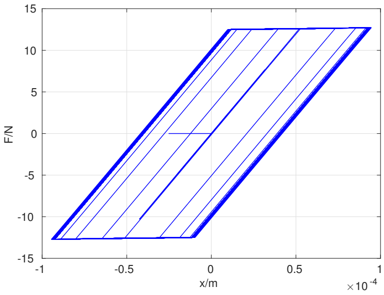

Figure 5.39: Time history of loading curve obtained with Newmark-β method when $N = 10$ N

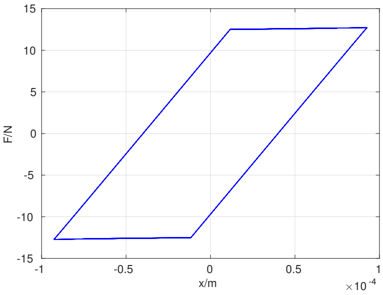

Figure 5.40: Stabilized first loading curve obtained with Newmark-β method when $N = 10$ N

of the results, especially considering the complexity of the nonlinear effect being synthesized.

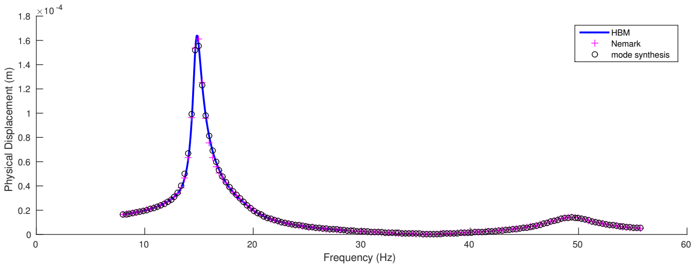

Figure 5.41: Comparison of forced response of excitation point obtained with complex modal synthesis, Harmonic balance and Newmark methods for $N = 10$ N

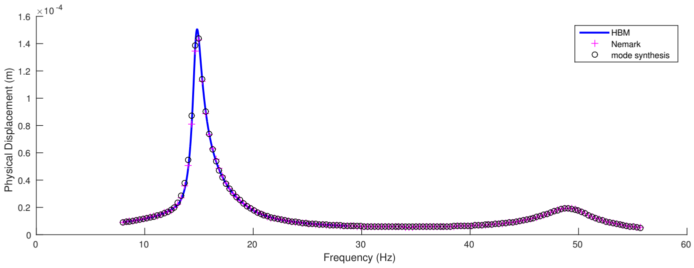

Figure 5.42: Comparison of forced response of friction point obtained with complex modal synthesis, Harmonic balance and Newmark methods for $N = 10$ N

Since nonlinear modal synthesis method is proven to be efficiency, it can be employed to identify the optimal normal load applied on the contact point for an optimal frictional damping. When observing forced responses around the first resonance, response curves corresponding to different normal loads ($N = 5, 10, 18, 25, 30,$ and 35 N) are plotted in Figures 5.43 and 5.44 by using modal synthesis method. As one can see, the variation of normal load affects the resonant peak level and resonant frequency value: All these figures have revealed the damping effect around the resonance and damper tuning effect of dry friction, that is, the resonant frequency is dislocated or becomes greater when the normal force increases; In the meanwhile, the damping level varies with the normal load level. The optimal normal load, which allows a maximal frictional damping in the neighborhood of the first resonance, is around 20 N.

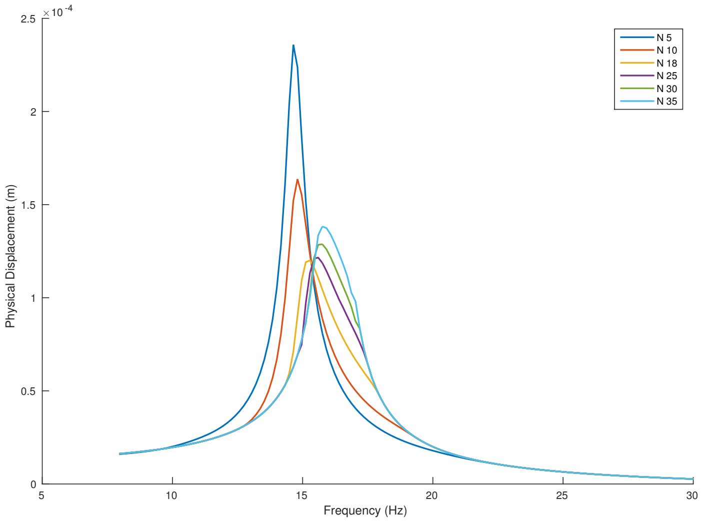

Figure 5.43: Forced response of excitation point corresponding to different normal load level of bilinear model

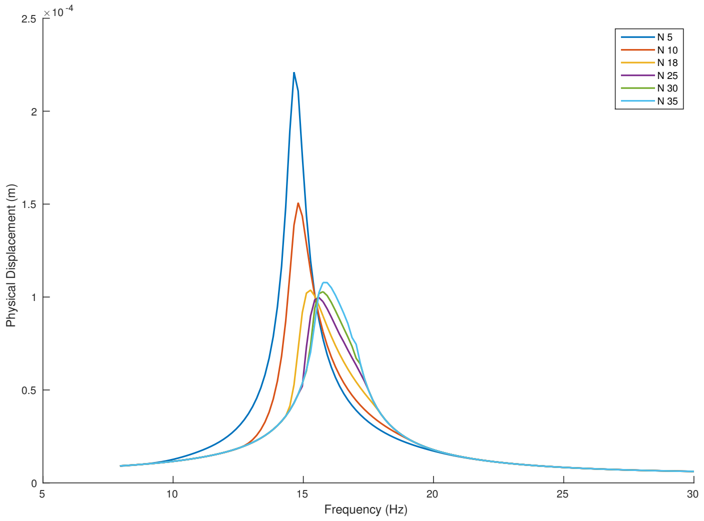

Figure 5.44: Forced response of friction point corresponding to different normal load level of bilinear model

Further insight into the qualitative nature of the dynamic response is gained by looking at the equivalent natural frequency and modal damping ratio. Figures 5.45 display the variation of natural frequency and modal damping factor in terms of modal amplitudes for the first mode, corresponding to different normal load values on the friction point. It can be seen that nonlinear natural frequencies all stem from the linear natural frequencies of the underlying system with dynamic stiffness (16.3 Hz) and ultimately approximate the linear natural frequencies of the system without the dynamic stiffness (14.7 Hz). The low level modal amplitude corresponds to the case in which the system features a crack, and the high level modal amplitude conforms to the case in which the corresponding nonlinear boundary conditions are ignored. The evolution of the modal damping factor exhibits a maximum, which accounts for an optimum nonlinear damping arising from the friction element. It should be mentioned that the maximum modal damping does not depend on the normal load, that is, when the value of normal load changes, the value of maximum modal damping (0.065) remains the same. This can be explained by the reasoning in Annexes D. Notwithstanding, the modal amplitude corresponding to maximum modal damping varies with the normal load.

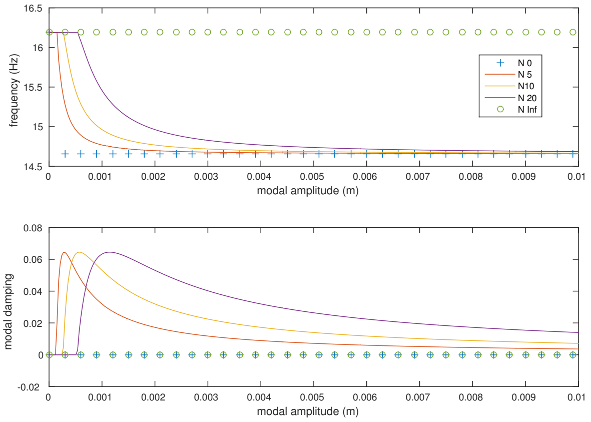

Figure 5.45: Evolution of natural frequency and modal damping factor *vs.* modal amplitude, corresponding to different normal load level, using bilinear model

5.7 Case study of the assembled plates

Simulations on an assembled plates model have also been conducted. The same model used in Section 3.2 and 4.5 has been investigated. Rubber layers are bonded on the interfaces between the substructures. We remind readers the model contains two Kirchhoff plates and one rubber layer interface. Plate 1 on the left side is denoted by S_1: its length a_1 is 0.66 m, the width $b_1 = 0.6$ m and the thickness e is 0.002 m; Plate 2 on the right is denoted by S_2: its length a_2 is 0.44 m, the width

$b_2 = 0.6\ m$ and thickness $e = 0.002\ m$; The rubber material is padded on both the top and bottom of plates so as to ensure the connections between S_1 and S_2, with a thickness (θ) of $0.002\ m$ and a width (l) of $0.003\ m$. The thickness and width variation of the rubber layer acts upon the change in its stiffness value. The model is excited with a tire balance type loading [Agnieszka 2005]: $\mathbf{F} = m\omega^2 R \cos \omega t$ at a frequency ω, with $m = 6\ g$, and $R = 4\ cm$. The excitation is located at $x = 0.44\ m$ and $y = 0.2\ m$, hence lying on S_1. Structural hysteresis damping has been integrated into the model, with a damping ratio of 0.02. Dry friction devices are continuously distributed along the interface, acting as tortional forces between S_1 and S_2. The nonlinear frictional forces are assumed to lie in the tortional direction of θ_y. The relative displacement between S_1 and S_2 in θ_y direction yields to the dry friction law of a bilinear Masing model, and the dry friction damper is modeled by a bilinear model with $k_d = 50$, $k_t = 1/100 * k_d$ and $\mu_d = 0.5$. Figure 4.3 shows the FE model of this system.

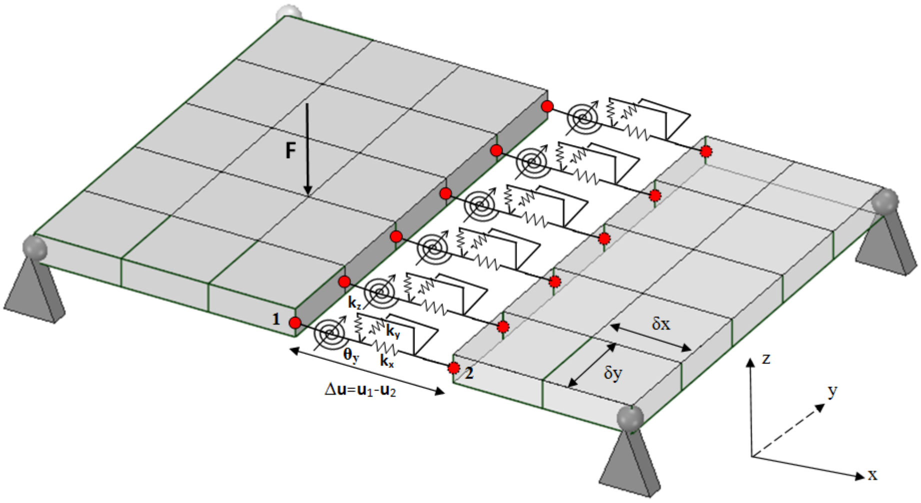

Figure 5.46: FE model of the plate

5.7.1 Time responses by using Newmark-β method

By using Newmark time integration method, time histories as well as stable responses can be obtained. The value of normal forces applied on the dry friction contacts along the interface is $N = 0.01\ N$. The stablized responses of one DOF linked to its torsional spring is plotted in Figure 5.47. The steady-state figure of the friction force of one device is shown in Figure 5.48. It can be seen that both stick and slip states occurred. The stablized displacement-friction force curves is also depicted in Figure 5.49. The enclosed surface represents the dissipated energy by the friction force.

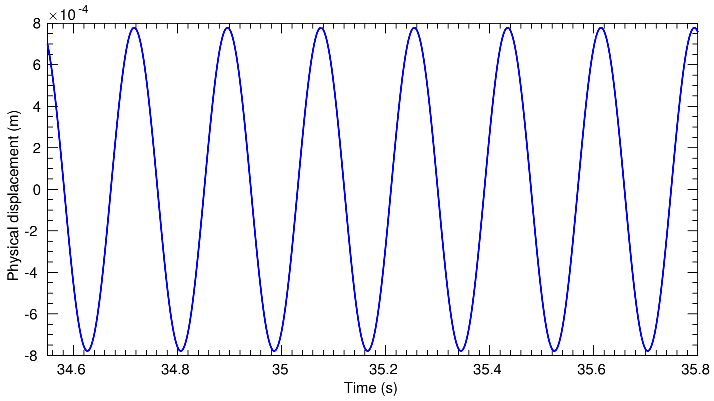

Figure 5.47: Stabilized displacement obtained with Newmark-β method ($N = 0.01\ N$)

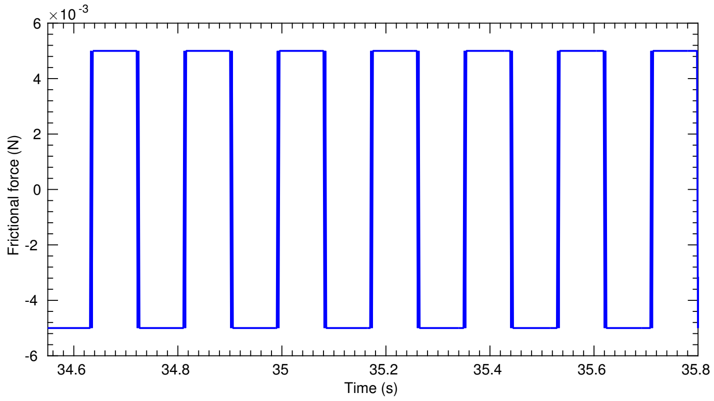

Figure 5.48: Stabilized friction force obtained with Newmark-β method ($N = 0.01\ N$)

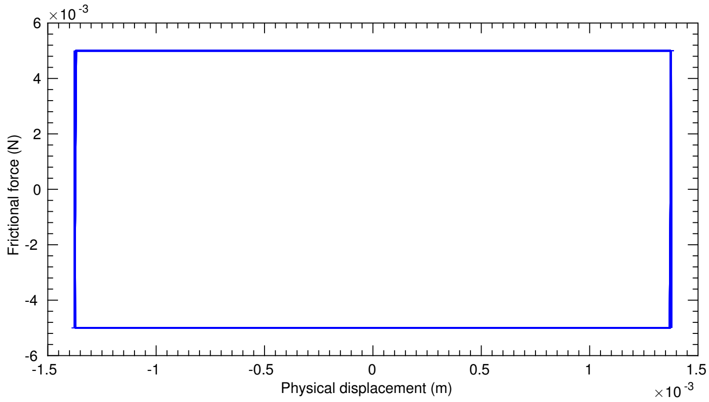

Figure 5.49: Stabilized loading curve obtained with Newmark-β method ($N = 0.01\ N$)

5.7.2 Analysis based on nonlinear modal synthesis method

A comparative study of forced responses is conducted by using Newmark-β method, HBM method retaining the first three harmonics, HBM method retaining the first harmonic and nonlinear modal synthesis method based on real modes and complex modes. For an amplitude of external sinusoidal load equals to 0.25 N and normal load applied on the friction point equals to 0.01 N, the forced responses of the excitation node is given in Figure 5.50. The response obtained with Newmark-β method is shown in black solid line, HBM method retaining the first three harmonics in blue solid line, HBM method retaining the first three harmonics in magenta solid line, modal synthesis based on real modes in plus marks and modal synthesis based on complex modes by red asterisk marks. No significant difference is observed between the HBM method retaining the first three harmonics and only the first harmonic. This figure also reveals that the response curves given by these methods closely match with each another, which shows that nonlinear modal synthesis method can be used to calculate forced response of the system without sacrificing the accuracy of the results, especially considering the complexity of the nonlinear effect being synthesized.

Since nonlinear modal synthesis method is proven to be efficiency, it can be employed to identify the optimal normal load applied on the contact point for an optimal frictional damping. When observing forced responses around the first resonance, response curves corresponding to different normal loads ($N = 0, 0.02, 0.05, 0.1, 0.3,$ and 30 N) is plotted in Figure 5.51 by using modal synthesis method. As one can see, the variation of normal load affects the resonant peak level and resonant frequency value: All these figures have revealed the damping effect around the resonance and damper tuning effect of dry friction, that is, the resonant frequency is dislocated or becomes greater when the normal force increases; In the meanwhile, the damping level varies with the normal load level. The optimal normal load, which allows a

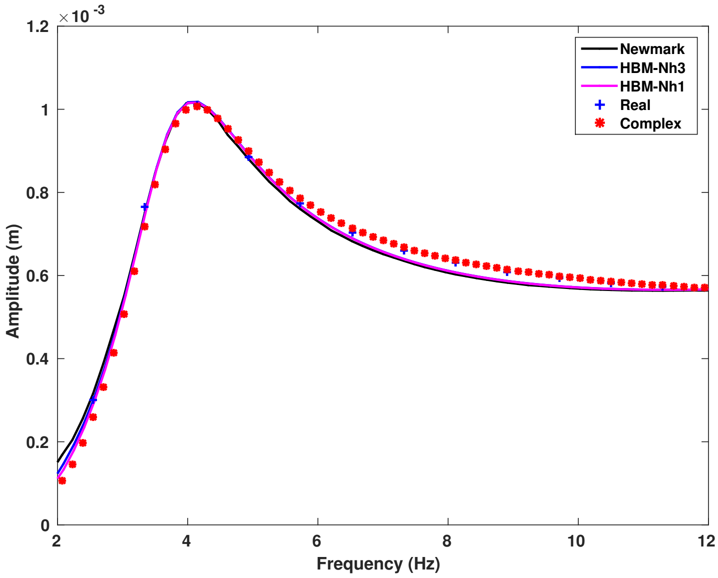

Figure 5.50: Comparison of forced response of excitation point obtained with real modal synthesis, complex modal synthesis, Harmonic balance-3 harmonics, Harmonic balance-1harmonic and Newmark methods for $N = 0.01\ N$

maximal frictional damping in the neighborhood of the first resonance, is around 0.05 N.

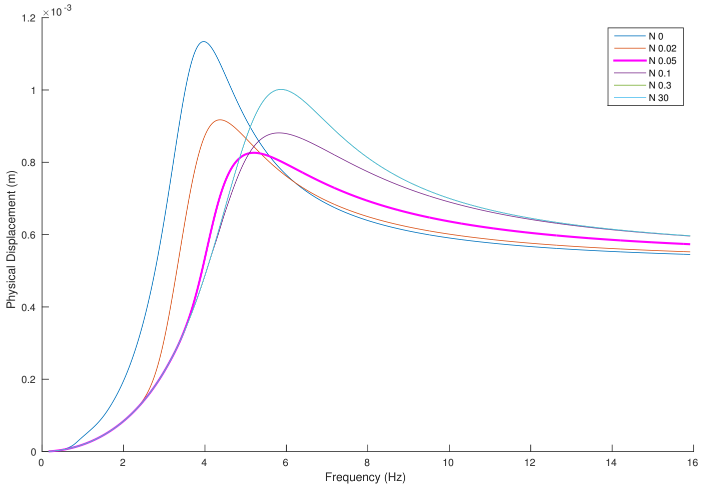

Figure 5.51: Forced response of excitation point corresponding to different normal load level of the plate. N denotes the normal load applied on the dry friction contact

Further insight into the qualitative nature of the dynamic response is gained by looking at the equivalent natural frequency and modal damping ratio. Figures 5.52

display the variation of natural frequency and modal damping factor in terms of modal amplitudes for the first mode, corresponding to different normal load values on the friction point. It can be seen that nonlinear natural frequencies all stem from the linear natural frequencies of the underlying system with dynamic stiffness (5.4 Hz) and ultimately approximate the linear natural frequencies of the system without the dynamic stiffness (3.7 Hz). The low level modal amplitude corresponds to the case in which the system features a crack, and the high level modal amplitude conforms to the case in which the corresponding nonlinear boundary conditions are ignored. The evolution of the modal damping factor exhibits a maximum, which accounts for an optimum nonlinear damping arising from the friction element. It should be mentioned that the maximum modal damping does not depend on the normal load, that is, when the value of normal load changes, the value of maximum modal damping (0.25) remains the same. This can be explained by the reasoning in Annexes D. Notwithstanding, the modal amplitude corresponding to maximum modal damping varies with the normal load.

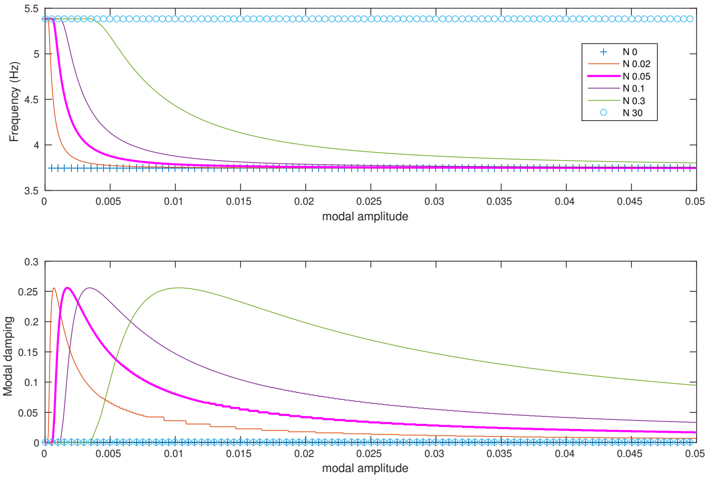

Figure 5.52: Evolution of natural frequency and modal damping factor *vs.* modal amplitude, corresponding to different normal load level, using bilinear model

To sum up, steady-state responses obtained with modal synthesis method is in accordance with that with Newmark-β time integration method and HBM. Modal parameters in function of modal amplitude, including natural frequency and modal damping are also available. The efficiency and the speed of the method allow one to study the optimal normal load that should be applied on the friction damper.

Part 2: Conclusions

In Chapter 4, we proposed a nonlinear modal synthesis approach for analyzing assembled nonlinear systems. The nonlinear mode concept is combined with reduction techniques. Reduced nonlinear modal synthesis is developed by employing constraint modes or branch modes. Nonlinear mode shapes and nonlinear modal parameters are obtained by using the proposed reduced nonlinear modal synthesis. Steady-state forced responses were approximated by selected nonlinear modes based on a single nonlinear mode approach. The numerical results of an assembled system have proven the efficiency of this derived strategy. This model has been reduced to a smaller size while maintaining sufficient information to describe model performance over the targeted frequency band. A significant advantage of the reduced nonlinear modal synthesis lies in its computation time savings. The truncation effects of internal modes and branch modes were subsequently investigated. Furthermore these extended approaches provide a modal overview to analyze the nonlinear behavior of the system. Based on the reduced nonlinear modal synthesis, forced responses of harmonic excitation can be easily calculated and the application on an assembled plates system show that evident instable regions are detected when excitation frequency are nearby 36 Hz or 48 Hz for the interested frequency range under 50 Hz.

In Chapter 5, we've presented a simple and efficient modal synthesis method to analyze the dynamic behavior of a nonlinear system integrating dry friction. Passive control of system vibration is conducted by regulating normal load applied on the frictional surface. A generalized Masing model for describing dry friction model is implemented in the nonlinear modal synthesis approach that is described in Chapter 4. This generalized model based on Masing rules can describe rich nonlinear phenomena with the polynomial coefficients determined by physical-based constraints. Both real nonlinear modal synthesis and complex nonlinear modal synthesis have been carried out and gave satisfying results. While it should be noted that when analyzing more complicated nonlinear structures, real nonlinear modal synthesis may come with difficulty in calculating nonlinear damping factor, since the damping factor is not integrated in the modal synthesis approach. The proposed method has been applied to a two DOFs system and a cantilever beam for purpose of illustration and validation. The optimal normal load for the two DOFs system is 20 N around the first resonance, that for the cantilevel beam is 25 N in the neighborhood of the first resonance, and that for the assembled plates system is 0.05 N. All these examples have proven the efficiency of the presented methodology.

The proposed reduced nonlinear modal synthesis is applicable to optimizing weakly nonlinear systems in the pre-design process.

Conclusions and perspectives

General conclusions

In this thesis, hybrid modal synthesis methods are developed to study the dynamic characteristics of assembled systems, including linear systems, nonlinear systems and coupled fluid-structure systems. The methods are then applied to design the passive interfaces in assembled structures so as to reduce the vibration and noise. Specifically, the main contributions and finds are listed below.

The extension of double modal synthesis method. The method can be used to analyze assembled structures with huge interface degrees of freedom. There are two stages of condensation: the first one is on the internal DOFs; and the second one is related to branch mode which further reduces the number of interface DOFs. The reduction basis then consists of the branch modes, the excitation modes and the constraint modes. This double modal synthesis method is further extended to study coupled fluid-structure systems by using a third modal reduction on the fluid DOFs. In the presented examples, the CPU time for the forced responses is reduced by 80% when double modal synthesis is applied; The CPU time for the forced responses of a coupled fluid-structure system is saved by 97%, since only 428 modes of the overall 4810 modes are retained. In the meanwhile, the results still have good agreements with the full finite element model.

The study of modal parameters. As the mid-stage results, these parameters can be extracted from the aforementioned modal synthesis process. The main advantage is that computing these modal parameters are faster than the forced response. Moreover, they also have physical meanings: modal parameters described in Chapter 1 indicate vibration transmission between substructures in the system and those in Chapter 2 characterize noise transmissions in the system. The vibration or noise transmission between substructures can thus be quantified by these parameters.

The proposal of a numerical scheme for the optimization process. The aim of the optimization process is searching for a best design of the interface damper in order to reduce the vibration and noise level of the assembled structure. The modal parameters are regarded as objective functions. Meta-models based on Kriging approximations as well as an elitist non-dominated sorting genetic algorithm are employed to solve this multi-objective problem. Two examples are given for validation purposes: the first one is an assembled plates system and the second one is coupled fluid-structure system. We show that the CPU time of evaluating surrogate models is reduced by 0.01 % while the accuracy is maintained. The best configurations for both examples are found and validated by the forced response results.

The extensions of modal synthesis for analyzing nonlinear system. To extend modal synthesis for nonlinear systems, the nonlinear mode concept is introduced. The computing of nonlinear modes of the system is accelerated by using reduction techniques similar with the linear version. However, different from those linear modes, these nonlinear modes may depend on their modal amplitudes. Nonlinear modal parameters characterizing dynamic performance of nonlinear systems are deduced from nonlinear modal synthesis approach, and they are further interpolated in function of their modal amplitudes. The application on an assembled nonlinear system shows that the CPU time of computing nonlinear modes is reduced by 67% using reduced models instead of the full finite element model. The accuracy of the numerical results is verified by the analytical solutions.

The optimization of nonlinear systems based on nonlinear modal synthesis using dry friction dampers. The extended nonlinear modal synthesis method is then applied to analyze the dry friction systems. Both complex modes and real modes are used in the synthesis to calculate the frictional damping. By applying this numerical scheme on two degrees of freedom system and a cantilever beam, steady-state responses obtained by the proposed modal synthesis method show quite good agreement with those obtained by multi-harmonic balance method and Newmark method. Optimization of the system is then executed by regulating the normal load applied on frictional contact.

Future work

Application on real industrial models. This thesis is in collaboration with PSA group, a straightforward direction for the future work is to apply the proposed numerical schemes on finite element models of PSA. The passive interface control strategies, including padding rubber layer and adding dry friction dampers, have shown their efficiency in studying academic models. Since these strategies are easy for implementation, it's worthwhile to employ this strategy to analyze large-size industrial models with more realistic rubber layer model. It will also be interesting to apply friction dampers on interfaces between substructures of more complex models.

Optimization design of interfaces in the nonlinear systems. In our work, we manage to control the vibration of linear systems by padding rubber layers on interfaces. It is natural to think about extending this strategy to nonlinear systems. Since the analysis of nonlinear systems requires more time for their dependence on modal amplitude and other complexities, we propose to conduct the optimization in two steps: a first control of system vibration by adding dry friction dampers with an appropriate normal load; a second optimization of the dynamic performance of the nonlinear system by padding viscoelastic rubber layers on the interfaces between substructures.

Active control of nonlinear systems. The optimal normal load applied on the frictional contact for a certain frequency range is found by employing nonlinear modal synthesis method, while the optimal normal load depends on the external excitation force and the excitation frequency. When the interested frequency range is wide, active control by tuning normal load in accordance with interested frequency can be used. Since the dynamic behavior of the system in resonant condition is dominated by its main resonant mode, Independent Modal Space Control (I.M.S.C.) seems to be prominent in performing the active control mode by mode. Moreover, active or semi-active devices can be conceived so as to improve the dynamic performance. We propose to research a system that allows for real-time control of friction forces at interfacial bonding sites by using piezo-electric materials.

Experimental validations. All the numerical schemes proposed in this thesis need to be experimentally validated so as to confirm our understanding. It seems to be prominent to pad rubber layers on interfaces between substructures and examine the vibration attenuation of doing so. It will also be interesting to optimize the localization of rubber layers in the global system. We can also measure the instable excitation range of nonlinear systems experimentally by observing the temporal response. Experimental validation of dry friction dampers are also expected.

Publications during the thesis

International Journals

- **X.R. Huang**, L. Jézéquel, S. Besset, L. Li, O. Sauvage, Nonlinear modal synthesis for analyzing structures with dry friction using generalized Masing model, Computational Mechanics, under review.
- **X.R. Huang**, L. Jézéquel, Jiuzhou Liu, Lin Li, A comparative study of numerical methods for analyzing structures with dry friction, International Journal of Computational Methods, under review.
- Jiuzhou Liu, Lin Li, **X.R. Huang**, L. Jézéquel, Dynamic characteristics of the blisk with synchronized switch damping based on negative capacitor, Mechanical Systems and Signal Processing, under review.
- **X.R. Huang**, L. Jézéquel, S. Besset, L. Li, Optimization of the dynamic behavior of vehicle structures by means of passive interface controls, Journal of Vibration and Control.
- **X.R. Huang**, S. Besset, L. Jézéquel, L. Li, Improving the acoustic comfort of vehicle structures by padding rubber layer on interfaces, Noise Control Engineering Journal.

International Conferences

- **X.R. Huang**, L. Jézéquel, S. Besset, L. Li, O. Sauvage, Double modal synthesis method applied in analyzing large-size nonlinear systems, 27th International Conference on Noise and Vibration Engineering, Leuven, Belgium, 2016.
- **X.R. Huang**, S. Besset, L. Jézéquel, L. Li, Improving the acoustic comfort of vehicle structures by padding rubber layer on interfaces, 43rd International Congress on Noise Control Engineering, San Francisco, United States, 2015.
- **X.R. Huang**, L. Jézéquel, S. Besset, L. Li, O. Sauvage, Analysis of dynamic behavior of assembled structures based on hybrid modal synthesis, 8ème Colloquium for the research collaboration of Beihang-GEC, Marseille, France, 2015.
- **X.R. Huang**, L. Jézéquel, S. Besset, L. Li, O. Sauvage, Optimizaion of the dynamic behavior of vehicle structures by means of passive interface controls, « Vibro-Acoustic-Tribology » OpenLAB DongFeng-PSA, Wuhan, China, 2014.

National/ Regional Conferences

- **X.R. Huang**, A. Gatt, S. Besset, Synthèse modale généralisée, Summer Colloquium of LTDS, Saint-Étienne, France, 2016.
- **X.R. Huang**, L. Jézéquel, S. Besset, L. Li, O. Sauvage, Synthèse modale non-linéaire Pour l'analyse des systèmes complexes, 13e Congrès Français d'Acoustique et le 20e colloque VIbrations, SHocks and NOise, CFA2016, le Mans, France, 2016.
- **X.R. Huang**, S. Besset, L. Jézéquel, L. Li, O. Sauvage, Optimization of interface characteristics in a coupled fluid-structure system for vibroacoustic comfort, French mechanic conference, CFM2015, Lyon, France, 2015.
- **X.R. Huang**, L. Jézéquel, S. Besset, L. Li, Extended modal synthesis in studying the dynamic behavior of vehicle structures, Colloquium of young researchers of LTDS, Lyon, France, 2014.
- **X.R. Huang**, L. Jézéquel, S. Besset, L. Li, O. Sauvage, Optimization of the dynamic behavior of vehicle structures by means of passive and active interface controls, Colloquium of PhD. Students Inter Écoles Centrales, Lyon, France, 2013.

Appendix A

Kriging approximations

The theoretical aspects of Kriging approximations are briefly introduced in two steps as follows: the first step consists of construction of interpolation models; the second is about the prediction of intermediate values.

In order to construct surrogates models, a set of m design sites $S = [s_1 \, ... \, s_m]$ and responses $Y = [y_1 \, ... \, y_m]$ are given by computer experiments, which are assumed to satisfy the following conditions:

$$\begin{aligned} &\mu\left[S_{:,j}\right] = 0, \quad V\left[S_{:,j}, S_{:,j}\right] = 1, \quad j = 1, \, ... \, , \, n, \\ &\mu\left[Y_{:,j}\right] = 0, \quad V\left[Y_{:,j}, Y_{:,j}\right] = 1, \quad j = 1, \, ... \, , \, q, \end{aligned} \tag{A.1}$$

where μ represents the mean and V denotes the covariance.

By the use of a regression model $\mathcal{F}$ and a stochastic process, $\hat{y}$ is adopted to express the deterministic response $y(x)$:

$$\hat{y}_l(x) = \mathcal{F}\left(\beta_{:,l}, x\right) + z_l(x), \quad l = 1, \, ... \, , \, q. \tag{A.2}$$

The regression model is realized by the use of a linear combination of p chosen functionsf_j, and $\beta_{k,l}$ are regression parameters:

$$\begin{aligned} \mathcal{F}\left(\beta_{:,l}, x\right) &= \beta_{1,l} f_1(x) + \cdots + \beta_{p,l} f_p(x) \\ &= \left[f_1(x) \cdots f_p(x)\right] \beta_{:,l} \\ &= f(x)^T \beta_{:,l} \end{aligned} \tag{A.3}$$

The stochastic process is assumed to have mean zero and covariance between $z(w)$ and $z(x)$:

$$E\left[z_l(w) z_l(x)\right] = \sigma_l^2 \mathcal{R}(\theta, w, x), \quad l = 1, \, ... \, , \, q \tag{A.4}$$

where σ_l^2 is the process variance for the lth compnent of the response and $\mathcal{R}(\theta, w, x)$ is the correlation model with parameters θ.

The true value of the response is written as:

$$y_l(x) = \mathcal{F}\left(\beta_{:,l}, x\right) + \alpha\left(\beta_{:,l}, x\right), \tag{A.5}$$

By proper choice of β, the approximation error α would behave like white noise in the region of interest.

The prediction on untried sites is carried out based on the expansion of the deduced models above: correlation models $F = \left[f(s_1) \, \cdots \, f(s_m)\right]^T$ and stochastic models $R_{ij} = [\mathcal{R}(\theta, s_1, s_m)]^T$. The stochastic-process correlations models at an untried point x is:

$$r(x) = [\mathcal{R}(\theta, s_1, x) \ \cdots \ \mathcal{R}(\theta, s_m, x)]^T \tag{A.6}$$

In considering a linear predictor $\hat{y}(x) = c^T Y$, the error is:

$$\begin{aligned}\hat{y}(x) - y(x) &= c^T (F\beta + Z) - \left(f(x)^T \beta + z\right) \\ &= c^T Z - z + \left(F^T c - f(x)\right)^T \beta,\end{aligned} \tag{A.7}$$

Under the condition that the predictor is unbiased, *i.e.* $F^T c - f(x) = 0$, the mean squared error of the predictor is:

$$\begin{aligned}\varphi(x) &= E\left[(\hat{y}(x) - y(x))^2\right] \\ &= E\left[\left(c^T Z - z\right)^2\right] \\ &= E\left[z^2 + c^T Z Z^T c - 2c^T Z z\right] \\ &= \sigma^2 \left(1 + c^T R c - 2c^T r\right).\end{aligned} \tag{A.8}$$

The Lagrangian function subject to the unbiased constraint gives:

$$L(c, \lambda) = \sigma^2 \left(1 + c^T R c - 2c^T r\right) - \lambda^T \left(F^T c - f\right) \tag{A.9}$$

The minimization of φ with respect to c requires the derivation of Lagrangian function to be zero. Then λ and c satisfy:

$$\begin{aligned}\tilde{\lambda} &= \left(F^T R^{-1} F\right)^{-1} \left(F^T R^{-1} r - f\right), \\ c &= R^{-1} \left(r - F\tilde{\lambda}\right). \\ \tilde{\lambda} &= -\frac{\lambda}{2\sigma^2}\end{aligned} \tag{A.10}$$

The approximate value of the response is thus:

$$\begin{aligned}\hat{y}(x) &= r^T R^{-1} Y - \left(F^T R^{-1} r - f\right)^T \beta^* \\ &= f^T \beta^* + r^T R^{-1} (Y - F\beta^*) \\ &= f(x)^T \beta^* + r(x)^T \gamma^*.\end{aligned} \tag{A.11}$$

where the generalized least squares solution with respect to R for the regression problem is

$$\beta^* = (F^T R^{-1} F)^{-1} F^T R^{-1} Y \tag{A.12}$$

where γ^* is computed via the residuals:

$$R\gamma^* = Y - F\beta^* \tag{A.13}$$

With probabilistic tools, the mean squared error of the predictor is expressed by:

$$\begin{aligned}
\varphi(x) &= \sigma^2 \left(1 + c^T \left(Rc - 2r\right)\right) \\
&= \sigma^2 \left(1 + \left(F\tilde{\lambda} - r\right)^T R^{-1} \left(F\tilde{\lambda} + r\right)\right) \\
&= \sigma^2 \left(1 + \tilde{\lambda}^T F^T R^{-1} F\tilde{\lambda} - r^T R^{-1} r\right) \\
&= \sigma^2 \left(1 + u^T \left(F^T R^{-1} F\right)^{-1} u - r^T R^{-1} r\right).
\end{aligned} \tag{A.14}$$

where $\sigma^2 = \frac{1}{m}(Y - F\beta^*)^T R^{-1}(Y - F\beta^*)$ and $u = F^T R^{-1} r - f$ with the maximum likelihood estimate method.

It should be noted that β^* and γ^* are fixed for a fixed set of design sits. We only need to compute $f(x)$ and $r(x)$ for every new x and add up $f(x)^T\beta^*$ and $r(x)^T\gamma^*$.

The construction of Kriging models relies on three aspects: the experimental design, the regression model and the correlation model. 1) For the experimental design, it is important to select the inputs at which to run the deterministic simulation in order to reduce the statistical uncertainty of the computed prediction. Algorithms with space filling properties are needed to produce deterministic designs, such as rectangular grid and Latin hypercube sampling strategy. 2) For the regression model, the toolbox provides regression models with polynomials of orders 0, 1 and 2. 3) For the correlation model, the toolbox is equipped with 7 correlation functions: the exponential, the general exponential (which have both shapes depending on the parameter: Gaussian and exponential), the Gaussian, the cubic, the linear, the spline and the spherical function. The choice of correlation function should in accordance with the underlying phenomenon, for example: if the underlying phenomenon is continuously differentiable, Gaussian, cubic or the spline function should be chosen since the correlation function would likely show a parabolic behavior near the origin; while exponential, general exponential, linear or spherical behaves better for phenomena showing a linear behavior near the origin.

Further details about the Kriging approximation can be found in the DACE toolbox by [Lophaven 2002].

APPENDIX B

An elitist multi-objective genetic algorithm

The theoretical aspects concerned in this method are briefly presented in the following.

The initialized population is sorted based on non-domination by the use of the information about the set that an individual dominate (S_p) and number of individuals that dominate the individual (n_p).

Once the non-dominated sort is complete the crowding distance is assigned. The boundary values for each individual are assigned infinite distance with $I(d_1) = \infty$ and $I(d_n) = \infty$. The basic idea behind the crowing distance is finding the euclidian distance between each individual in a front based on their m objectives in the m dimensional hyper space. So for the k_{th} individual, we have:

$$I(d_k) = I(d_k) + \frac{I(k+1).m - I(k-1).m}{f_m^{max} - f_m^{min}} \tag{B.1}$$

After that the individuals are sorted based on non-domination and with crowding distance assigned, the selection is carried out with a crowded-comparison-operator using a binary tournament selection. The genetic algorithm employed Simulated Binary Crossover operator for crossover and polynomial mutation[Deb 1994]. The simulated binary crossover is given by:

$$\begin{aligned} c_{1,k} &= \frac{1}{2}\left[(1-\beta_k)p_{1,k} + (1+\beta_k)p_{2,k}\right] \\ c_{2,k} &= \frac{1}{2}\left[(1+\beta_k)p_{1,k} + (1-\beta_k)p_{2,k}\right] \end{aligned} \tag{B.2}$$

$c_{i,k}$ is the i_{th} child with k_{th} component, $p_{i,k}$ is the selected parent and β_k (≥ 0) is a sample from a random generated number having the density:

$$\begin{aligned} p(\beta) &= \frac{1}{2}(\eta_c + 1)\beta^{\eta_c}, \quad \text{if } 0 \leq \beta \leq 1 \\ p(\beta) &= \frac{1}{2}(\eta_c + 1)\frac{1}{\beta^{\eta_c+2}}, \quad \text{if } \beta > 1 \end{aligned} \tag{B.3}$$

The distribution is obtained from a uniformly sampled random number u between 0 and 1.

$$\begin{aligned} \beta(u) &= (2u)^{\frac{1}{\eta+1}} \\ \beta(u) &= \frac{1}{[2(1-u)]^{\frac{1}{\eta+1}}} \end{aligned} \tag{B.4}$$

η_c is the distribution index for crossover, which decides how well spread the children will be from their parents.

Defining p_k the parent with p_k^u being the upper bound and p_k^l the lower bound, the child c_k is:

$$c_k = p_k + (p_k^u - p_k^l)\delta_k \tag{B.5}$$

δ_k is small variation which is calculated from a polynomial distribution by using

$$\begin{aligned} \delta_k &= (2r_k)^{\frac{1}{\eta m+1}} - 1, \quad \text{if } r_k < 0.5 \\ \delta_k &= 1 - [2(1-r_k)]^{\frac{1}{\eta m+1}}, \quad \text{if } r_k \geq 0.5 \end{aligned} \tag{B.6}$$

r_k is an uniformly sampled random number between 0 and1; η_m is mutation distribution index.

The offspring population is afterwards combined with the current generation population and selection is performed to set the individuals of the next generation.

Further details about the fast, elitist multi-objective genetic algorithm can be found in the NSGA-II toolbox by [Seshadri 2006].

Appendix C

Discussion on nonlinear branch modal synthesis

Since the nonlinearities are located at the interfaces between substructures and other parts are assumed to be linear, naturally we consider decomposing nonlinear modes by nonlinear branch modes (condensation of interface DOFs) and linear fixed interfaces modes (condensation of internal DOFs of substructures).

This idea is attractive since less variables (N_B) are involved in the nonlinear problem in place of $N_r = N_B + N_I$ with branch modes. This method is referred as nonlinear branch modal synthesis and the problem is formulated as follows:

The solutions to nonlinear branch mode-j are solved by the use of a residu function according to Kryloff and Bogoliubov's equivalent linearization method:

$$\varepsilon(q_j) = \left[(-\tilde{\lambda}_B^j \mathbf{M}_B + \tilde{\lambda}_B^j)(q_j \tilde{\mathbf{\Phi}}_B^j)\right] - \left[(-\tilde{\lambda}_B^j \mathbf{M}_B + \mathbf{K}_B)(q_j \tilde{\mathbf{\Phi}}_B^j) + \mathbf{\Psi}_{\mathrm{B}} \tilde{\mathbf{f}}(q_j \tilde{\mathbf{\Phi}}_B^j)\right] \tag{C.1}$$

where

$$\mathbf{M}_{\mathrm{B}} = (\mathbf{\Psi}_{\mathrm{B}})^T \mathbf{M} \mathbf{\Psi}_{\mathrm{B}}, \quad \mathbf{K}_{\mathrm{B}} = (\mathbf{\Psi}_{\mathrm{B}})^T \mathbf{K} \mathbf{\Psi}_{\mathrm{B}}, \quad \mathbf{\Psi}_{\mathrm{B}} = \begin{bmatrix} \mathbf{I}_{\mathrm{JJ}} \\ \mathbf{\Psi}_{\mathrm{SJ}} \end{bmatrix}$$

The calculation here is is similar to that for nonlinear modes described in Section 4.3.1, except that herein we compute nonlinear branch modes.

Since nonlinearities only make appearance in interface DOFs, the nonlinear force is simplified with the transformation matrix $\mathbf{T}_{\mathrm{BI}}$ as follows:

$$\tilde{\mathrm{f}}(\mathrm{u}) = \alpha \Delta \mathrm{u}^3 \quad = \frac{3}{4} \alpha \Delta (\mathbf{T}_{\mathrm{BI}} \mathbf{q}_{\mathrm{BI}})^3 = \frac{3}{4} \alpha \begin{bmatrix} \Delta (\tilde{\mathbf{\Phi}}_B \mathbf{q}_{\mathrm{B}})^3 \\ 0 \end{bmatrix} \tag{C.2}$$

where

$$\mathbf{u} = \mathbf{T}_{\mathrm{BI}} \mathbf{q}_{\mathrm{BI}}$$

$$\mathbf{T}_{\mathrm{BI}} = \begin{bmatrix} \mathbf{T}_{\mathrm{B}} & \mathbf{T}_{\mathrm{I}} \end{bmatrix} \quad \mathbf{T}_{\mathrm{B}} = \begin{bmatrix} \mathbf{X}_{\mathrm{B}} \\ \mathbf{\Psi}_{\mathrm{SJ}} \mathbf{X}_{\mathrm{B}} \end{bmatrix} \quad \mathbf{q}_{\mathrm{BI}} = \begin{bmatrix} \mathbf{q}_{\mathrm{B}} \\ \mathbf{q}_{\mathrm{I}} \end{bmatrix}$$

The solution to the residu function contains $N_B + 1$ variables with $\tilde{\lambda}_B^j = (\tilde{\omega}_B^j)^2$:

$$\tilde{\mathbf{X}}_B^j = \begin{pmatrix} \tilde{\lambda}_B^j \\ \tilde{\mathbf{\Phi}}_B^j \end{pmatrix} \tag{C.3}$$

By analogy, the nonlinear branch modes are solved by minimizing the residue function ε according to the steps outlined in Section 4.3. The difference is that the linear branch modes (λ_B^j, $\mathbf{\Phi}_B^j$) are set as initial conditions for this nonlinear problem. Likewise, the nonlinear branch mode can also be written by a linear combination of linear branch modes with nonlinear coefficients depending on the modal amplitude:

$$\tilde{\mathbf{\Phi}}_B^j = \sum_{k=1}^{N_B} \tilde{\beta}_{jk} \mathbf{\Phi}_B^j, \quad (\tilde{\beta}_{jj} = 1) \tag{C.4}$$

The matrix of nonlinear branch modes is formed by the retained modes:

$$\tilde{\mathbf{\Phi}}_B = \left[\begin{array}{cccc} \tilde{\mathbf{\Phi}}_B^1 & \tilde{\mathbf{\Phi}}_B^2 & \cdots & \tilde{\mathbf{\Phi}}_B^{N_B} \end{array} \right] \tag{C.5}$$

The motion equation of the system subjected to a harmonic excitation force F at frequency ω is:

$$\tilde{\mathbf{T}}^T \left(-\tilde{\omega}^2 \mathbf{M} + i\mathbf{C} + \mathbf{K}\right) \tilde{\mathbf{T}} q + \tilde{\mathbf{T}}^T \frac{3}{4} \alpha \Delta (\tilde{\mathbf{T}} q)^3 = \tilde{\mathbf{T}}^T \mathbf{F} \tag{C.6}$$

with

$$\mathbf{M} = \left[\begin{array}{cc} \mathbf{M}_{JJ} & \mathbf{M}_{JS} \\ \mathbf{M}_{SJ} & \mathbf{M}_{SS} \end{array} \right] \quad \mathbf{C} = \left[\begin{array}{cc} \mathbf{C}_{JJ} & \mathbf{C}_{JS} \\ \mathbf{C}_{SJ} & \mathbf{C}_{SS} \end{array} \right] \quad \mathbf{K} = \left[\begin{array}{cc} \mathbf{K}_{JJ} & \mathbf{K}_{JS} \\ \mathbf{K}_{SJ} & \mathbf{K}_{SS} \end{array} \right]$$

The transformation matrix is also nonlinear due to $\tilde{\mathbf{\Phi}}_B$:

$$\tilde{\mathbf{T}} = \left[\begin{array}{cc} \mathbf{I}_{JJ} \tilde{\mathbf{\Phi}}_B & \mathbf{0} \\ -\mathbf{K}_{SS}^{-1} \mathbf{K}_{SJ} \tilde{\mathbf{\Phi}}_B & \mathbf{\Phi}_S \end{array} \right] \tag{C.7}$$

The transformed matrix turn out to be:

$$\mathbf{T}^T \mathbf{M} \mathbf{T} = \left[\begin{array}{cc} \widetilde{\bar{\mathbf{M}}}_{JJ} & \widetilde{\bar{\mathbf{M}}}_{JS} \\ \widetilde{\bar{\mathbf{M}}}_{SJ} & \widetilde{\bar{\mathbf{M}}}_{SS} \end{array} \right] \quad \mathbf{T}^T \mathbf{K} \mathbf{T} = \left[\begin{array}{cc} \tilde{\bar{\mathbf{K}}}_{JJ} & \tilde{\bar{\mathbf{K}}}_{JS} \\ \tilde{\bar{\mathbf{K}}}_{SJ} & \tilde{\bar{\mathbf{K}}}_{SS} \end{array} \right] \quad \mathbf{T}^T \mathbf{C} \mathbf{T} = \left[\begin{array}{cc} \tilde{\bar{\mathbf{C}}}_{JJ} & \tilde{\bar{\mathbf{C}}}_{JS} \\ \tilde{\bar{\mathbf{C}}}_{SJ} & \tilde{\bar{\mathbf{C}}}_{SS} \end{array} \right]$$

$$\mathbf{T}^T \mathbf{f}_{nl} = \left[\begin{array}{c} \widetilde{\bar{\mathbf{f}}}_{nl} \\ 0 \end{array} \right] \quad (\mathbf{T}^T) \mathbf{F} = \left[\begin{array}{c} \tilde{\bar{\mathbf{F}}}_J \\ \bar{\mathbf{F}}_S \end{array} \right]$$

with

$$\begin{aligned} \widetilde{\bar{\mathbf{M}}}_{JJ} &= \left(\tilde{\mathbf{\Phi}}_B\right)^T (\mathbf{M}_{JJ} + \mathbf{D}_{SJ}^T \mathbf{M}_{SJ} + \mathbf{M}_{JS} \mathbf{D}_{SJ} + \mathbf{D}_{SJ}^T \mathbf{M}_{SS} \mathbf{D}_{SJ}) \tilde{\mathbf{\Phi}}_B \\ \widetilde{\bar{\mathbf{M}}}_{JS} &= \left(\tilde{\mathbf{\Phi}}_B\right)^T (\mathbf{M}_{JS} + \mathbf{D}_{SJ}^T \mathbf{M}_{SS}) \mathbf{\Phi}_S \\ \widetilde{\bar{\mathbf{M}}}_{SJ} &= (\mathbf{\Phi}_S)^T (\mathbf{M}_{SJ} + \mathbf{M}_{SS} \mathbf{D}_{SJ}) \tilde{\mathbf{\Phi}}_B \\ \widetilde{\bar{\mathbf{M}}}_{SS} &= (\mathbf{\Phi}_S)^T \mathbf{M}_{SS} \mathbf{\Phi}_S \\ \mathbf{D}_{SJ} &= -\mathbf{K}_{SS}^{-1} \mathbf{K}_{SJ} \end{aligned} \tag{C.8}$$

Further reduction can be applied by seperating the reduced matrixes into two parts (branch modes and internal modes) when calculating forced responses of the system. By developing the second part of Equation C.6, we get:

$$\left[-\omega^2 \widetilde{\bar{\mathbf{M}}}_{SJ} q_J + i\omega \tilde{\bar{\mathbf{H}}}_{SJ} q_J + \tilde{\bar{\mathbf{K}}}_{SJ} q_J\right] + \left[-\omega^2 \bar{\mathbf{M}}_{SS} q_S + i\omega \bar{\mathbf{H}}_{SS} q_S + \bar{\mathbf{K}}_{SS} q_S\right] = \bar{\mathbf{F}}_S \tag{C.9}$$

The generalized coordinates q_S can be replaced by:

$$q_S = (\bar{\mathbf{E}}_{SS}(\omega))^{-1} (\mathbf{F}_S - \tilde{\bar{\mathbf{E}}}_{SJ}(\omega) q_J) \tag{C.10}$$

with

$$\begin{aligned}\bar{\mathbf{E}}_{SJ} &= -\omega^2\widetilde{\bar{\mathbf{M}}}_{SJ} + i\omega\tilde{\bar{\bar{\mathbf{H}}}}_{SJ} + \tilde{\bar{\bar{\mathbf{K}}}}_{SJ} \\ \bar{\mathbf{E}}_{SS} &= -\omega^2\bar{\mathbf{M}}_{SS} + i\omega\bar{\mathbf{H}}_{SS} + \bar{\mathbf{K}}_{SS}\end{aligned} \tag{C.11}$$

By developing the first part of Equation C.6:

$$\left[-\omega^2\widetilde{\bar{\mathbf{M}}}_{JJ} + i\tilde{\bar{\bar{\mathbf{H}}}}_{JJ} + \tilde{\bar{\bar{\mathbf{K}}}}_{JJ}\right] q_J + \left[-\omega^2\widetilde{\bar{\mathbf{M}}}_{JS} + i\tilde{\bar{\bar{\mathbf{H}}}}_{JS} + \tilde{\bar{\bar{\mathbf{K}}}}_{JS}\right] q_S + \tilde{\bar{\bar{\mathbf{f}}}}_{nl} = \tilde{\bar{\bar{\mathbf{F}}}}_J \tag{C.12}$$

with

$$\begin{aligned}\tilde{\bar{\bar{\mathbf{E}}}}_{JJ}(\omega) &= -\omega^2\widetilde{\bar{\mathbf{M}}}_{JJ} + i\tilde{\bar{\bar{\mathbf{H}}}}_{JJ} + \tilde{\bar{\bar{\mathbf{K}}}}_{JJ} \\ \tilde{\bar{\bar{\mathbf{E}}}}_{JS}(\omega) &= -\omega^2\widetilde{\bar{\mathbf{M}}}_{JS} + i\tilde{\bar{\bar{\mathbf{H}}}}_{JS} + \tilde{\bar{\bar{\mathbf{K}}}}_{JS}\end{aligned} \tag{C.13}$$

In replacing C.10 in this equation, the problem turns out to be solving q_J to the following equation:

$$\tilde{\bar{\bar{\mathbf{E}}}}_{JJ}(\omega)q_J + \tilde{\bar{\bar{\mathbf{E}}}}_{JS}(\omega)(\tilde{\bar{\bar{\mathbf{E}}}}_{SS}(\omega))^{-1}(\bar{\mathbf{F}}_S - \tilde{\bar{\bar{\mathbf{E}}}}_{SJ}(\omega)q_J) + \tilde{\bar{\bar{\mathbf{f}}}}_{nl} = \tilde{\bar{\bar{\mathbf{F}}}}_J \tag{C.14}$$

The reasoning seems to be persuasive, while the simulation results are not satisfying. This can be explained from both theoretical and physical aspects.

From the theoretical point of view, a logic hole is checked out. The nonlinear branch modes represent global system performance while remain component modes, thus the dependancy of eigenvectors on q could not be employed during the calculation of generalized coordinates q_J of the system as that in Section 4.3.1. Because q is the modal amplitude of the global mode, while the relationship established in $\tilde{\mathbf{\Phi}}$ and q is for branch mode. The generalized coordinates of branch mode can be solved by projecting the physical coordinates on modal space with constraint mode matrix $\mathbf{T}_B$. q_J is thus the solution to Equation C.15. However, q_S remains unknown. These variables can be approximated as linear, but the approximations turn out to be quite coarse and dangerous since nonlinear phenomena show their complexity and interaction with each other.

$$(\tilde{\mathbf{T}}_B)^T\left(-\omega^2\mathbf{M} + i\mathbf{C} + \tilde{\mathbf{K}}\right)\tilde{\mathbf{T}}_B q_J = \tilde{\mathbf{T}}_B^T\mathbf{F} \tag{C.15}$$

From the physical aspect, nonlinear phenomenon can not be decomposed into nonlinear part and linear part. Once nonlinearity takes place, the whole system is influenced. Thus the idea about nonlinear branch modes and linear internal modes is biased, and internal modes are also nonlinear when combined with nonlinear branch modes.

APPENDIX D

Analysis of nonlinear modal damping ratio

The objective of this study is to analyze the modal damping ratio of dry friction devices. The nonlinear state is a transition state between linear state of the system when the friction contact is set free and linear state of the system when the friction contact is encastered. We are thus thinking about representing the nonlinear state by using the free linear state and encastered linear state with an appropriate mathematical expression.

For the sake of simplicity, substructures connected by this damping device are denoted M_1 and M_2 respectively, as shown in Figure D.1. The dry friction device is a hysteresis damper with stiffness shifting effect, thus expressed by: $k^* = e(1 + i\beta)$. The analysis is carried out by the residu approach described in [Jézéquel 1990]: the residu stiffness attached to M_1 and M_2 are denoted k_1 and k_2, which represent the influence of initial structure on the global system by the encastered DOF; the modal displacements X_1 and X_2 are supposed to be not influenced by the addition of the damping device.

The equivalent stiffness of this model (see Figure D.2) with two stiffness in series is:

$$k = \frac{k_1 * k_2}{k_1 + k_2} \tag{D.1}$$

Suppose that the initial structure (before the addition of the friction device) is subjected to hysteresis damping, the complex eigenvalue is expressed by:

$$\lambda_1 = -\tilde{\omega}_1^2(1 + i\eta_1) \tag{D.2}$$

where $\tilde{\omega}_1$ is the natural frequency and η_1 is the hysteresis damping for one mode. According to [Jézéquel 1990], the equivalent impedance is written by:

$$\lambda_1 = -\tilde{\omega}_1^2(1 + i\eta_1) \tag{D.3}$$

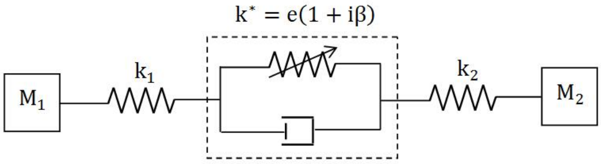

Figure D.1: Rheological model of assembled structures

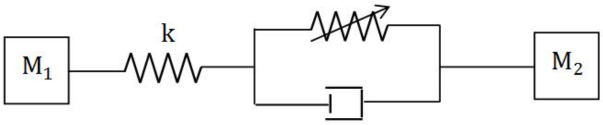

Figure D.2: Equilavent rheological model of assembled structures

where

$$a = \frac{k\left[\chi + 1 + \beta^2\right]}{(\chi+1)^2 + \beta^2} \quad b = \frac{k\chi\beta}{(\chi+1)^2+\beta^2} \quad \chi = \frac{k}{e} \tag{D.4}$$

The eigenvalue of the new model after the addition of this damping device turns to be:

$$\lambda = \lambda_1 - Z_{eq}\left(X_2 - X_1\right)^2 = -\tilde{\omega}_1^2(1+i\eta_1) - (a+ib)\left(X_2 - X_1\right)^2 \tag{D.5}$$

The natural frequency is:

$$\tilde{\omega}^2 = -Re(\lambda) = \tilde{\omega}_1^2 + a\left(X_2 - X_1\right)^2 \tag{D.6}$$

and the hysteresis damping factor is:

$$\eta = \frac{Im(\lambda)}{Re(\lambda)} = \frac{\tilde{\omega}_1^2\eta_1 + b\left(X_2 - X_1\right)^2}{\tilde{\omega}_1^2 + a\left(X_2 - X_1\right)^2} \tag{D.7}$$

when the system is extremely damped, *i.e.* $e \to +\infty$, the real part of the equivalent impedance tends to k. According to equation, The natural frequency of the encastered system is:

$$\tilde{\omega}_\infty^2 \approx \tilde{\omega}_1^2 + k\left(X_2 - X_1\right)^2 \tag{D.8}$$

Conversly, the residu stiffness can be expressed by:

$$k \approx \frac{\tilde{\omega}_\infty^2 - \tilde{\omega}_1^2}{\left(X_2 - X_1\right)^2} \tag{D.9}$$

In replacing Equation D.4, D.5 and D.9 in Equation D.6, we get:

$$\tilde{\omega}^2 \approx \frac{\left[\chi + 1 + \beta^2\right]\tilde{\omega}_\infty^2 + (\chi+1)\chi\tilde{\omega}_1^2}{(\chi+1)^2 + \beta^2} \tag{D.10}$$

In replacing Equation D.4 and D.9 in Equation D.7, the damping factor is expressed by:

$$\eta \approx \frac{\beta\chi(\tilde{\omega}_\infty^2 - \tilde{\omega}_1^2) + \left[(\chi+1)^2 + \beta^2\right]\tilde{\omega}_1^2\eta_1}{\left[\chi + 1 + \beta^2\right]\tilde{\omega}_\infty^2 + (\chi+1)\chi\tilde{\omega}_1^2} \tag{D.11}$$

In the following the maximum of the damping ratio is investigated and the objective function is denoted $f(\chi) = \frac{u(\chi)}{v(\chi)}$. The maximum is attained when

$$f'(\chi) = \frac{u'(\chi)v(\chi) - u(\chi)v'(\chi)}{v^2(\chi)} = 0 \tag{D.12}$$

In replacing these notations in the expression of damping factor, we have:

$$\begin{aligned} f(\chi) &= \eta(\chi) \\ v(\chi) &= (\chi+1)(\tilde{\omega}_\infty^2+\tilde{\omega}_1^2)+\beta^2\tilde{\omega}_\infty^2 \\ u(\chi) &= \left[\chi+1+\beta^2\right]\tilde{\omega}_\infty^2+(\chi+1)\tilde{\omega}_1^2 \end{aligned} \tag{D.13}$$

and

$$\begin{aligned} v'(\chi) &= \tilde{\omega}_\infty^2+\tilde{\omega}_1^2 \\ u'(\chi) &= \beta(\tilde{\omega}_\infty^2-\tilde{\omega}_1^2)+2(\chi+1)\tilde{\omega}_1^2\eta_1 \end{aligned} \tag{D.14}$$

By making $u'(\chi)v(\chi)-u(\chi)v'(\chi)=0$, a maximal damping factor is obtained:

$$\boxed{\eta^{opt} \approx \frac{\beta\chi_{opt}(\tilde{\omega}_\infty^2-\tilde{\omega}_1^2)+\left[(\chi_{opt}+1)^2+\beta^2\right]\tilde{\omega}_1^2\eta_1}{[\chi_{opt}+1+\beta^2]\,\tilde{\omega}_\infty^2+(\chi_{opt}+1)\chi_{opt}\tilde{\omega}_1^2}} \tag{D.15}$$

with

$$\chi_{opt} = \frac{1+\beta^2+\sqrt{\mu(1+\beta^2)(\beta\eta_1+\mu\alpha+1-\alpha)}}{\mu-1} \tag{D.16}$$

where

$$\begin{cases} \mu = \dfrac{\beta}{\eta_1} \\ \alpha = \dfrac{\tilde{\omega}_\infty^2}{\tilde{\omega}_1^2} \end{cases} \tag{D.17}$$

It's revealed from the expression of Equation (D.15) that the optimal value of modal damping is not substantially influenced by the applied normal force value.

Bibliography

[Aarts 1992] Ronald Aarts. *Comparison of some loudness measures for loudspeaker listening tests*. AES: Journal of the Audio Engineering Society, vol. 40, no. 3, pages 142–146, 1992. (Cited on page 33.)

[Agnieszka 2005] Muszynska Agnieszka. Rotordynamics. CRC Press, 2005. (Cited on pages 96, 133 and 149.)

[Al-Bender 2010] Farid Al-Bender. *Fundamentals of Friction Modelling*. ASPE Spring Topical Meeting on Control of Precision Systems, pages 117–122, 2010. (Cited on pages 115 and 122.)

[Andersson 2006] Soren Andersson and Stefan Soderberg, Andersorklund. *Friction models for sliding dry, boundary and mixed lubricated contacts*. Tribology International, vol. 40, no. 4, pages 580–587, 2006. (Cited on page 114.)

[Argatov 2011] Ivan I. Argatov and Eric A. Butcher. *On the Iwan models for lap-type bolted joints*. International Journal of Non-Linear Mechanics, vol. 46, no. 2, pages 347–356, 2011. (Cited on page 120.)

[Ascher 1998] U.M. Ascher and L.R. Petzold. Computer Methods for Ordinary Differential Equations and Differential-Algebraic Equations. 1998. (Cited on pages 83 and 85.)

[Avitabile 1990] P. Avitabile, J. O'Callahan and F. Pechinsky. *Understanding Structural Dynamic Modification Truncation*. In 8th International Modal Analysis Conference, Orlando, FL, February 1990. (Cited on page 6.)

[Avitabile 2000] Peter Avitabile. *TUTORIAL NOTES : Structural Dynamics and experimental modal analysis*. Technical report, University of Massachusetts Lowell, 2000. (Cited on page 11.)

[Avitabile 2003] P. Avitabile. *Twenty years of structural dynamic modification-a review*. Journal of Sound and Vibration, vol. 37, no. January, pages 14–25, 2003. (Cited on page 7.)

[Awrejcewicz 2012] J. Awrejcewicz, IV. Andrianov and LI Manevitch. Asymptotic Approaches in Nonlinear Dynamics: New Trends and Applications. Springer Berlin / Heidelberg, 2012. (Cited on page 83.)

[Balmès 2009] Etienne Balmès. *Structural dynamics toolbox*. Technical report, 2009. (Cited on pages 95 and 96.)

[Bastien 2006] J Bastien, G Michon, L Manin, R Dufour and Valeo Electrical Systems. *Rheological and restoring force models regarding belt tensioner dymamic behavior : prediction & experiment* . 2006. (Cited on page 117.)

[Berger 2002] Ej Berger. *Friction modeling for dynamic system simulation.* Applied Mechanics Reviews, vol. 55, no. 6, page 535, 2002. (Cited on page 120.)

[Berger 2003] Elliott H Berger. The noise manual. Aiha, 2003. (Cited on page 33.)

[Besselink 2013] B Besselink, U Tabak, A. Lutowska, N. Van De Wouw, H. Nijmeijer, D. J. Rixen, M. E. Hochstenbach and W. H A Schilders. *A comparison of model reduction techniques from structural dynamics, numerical mathematics and systems and control*, 2013. (Cited on page 5.)

[Besset 2008a] Sébastien Besset and L. Jézéquel. *Vibroacoustical Analysis Based on a Multimodal Strategy: Triple Modal Synthesis.* Journal of Vibration and Acoustics, vol. 130, no. 3, page 031009, 2008. (Cited on pages 5 and 6.)

[Besset 2008b] Sébastien Besset and Louis Jézéquel. *Dynamic Substructuring Based on a Double Modal Analysis.* Journal of Vibration and Acoustics, vol. 130, no. 1, page 011008, 2008. (Cited on page 5.)

[Besset 2011] Sébastien Besset and Louis Jézéquel. *Optimization of the Dynamic Behaviour of Complex Structures Based on a Multimodal Strategy.* Numerical Analysis-Theory and Application, 2011. (Cited on pages 31 and 32.)

[Bouc 1967] R. Bouc. *Forced vibration of mechanical systems with hysteresis.* In Proceedings of Fourth Conference ICNO, pages 2601–2608, Prague, 1967. (Cited on page 85.)

[Brizard 2012] Denis Brizard, Sébastien Besset, Louis Jézéquel and Bernard Troclet. *Determinantal method for locally modified structures. Application to the vibration damping of a space launcher.* Computational Mechanics Journal, vol. 50, pages 631–644, 2012. (Cited on pages 5, 14 and 15.)

[Broyden 1965] C. G. Broyden. *A Class of Methods for Solving Nonlinear Simultaneous Equations.* volume 19, pages 577–593, 1965. (Cited on page 128.)

[Butcher 1987] J.C. Butcher. The numerical analysis of ordinary differential equations. Runge-Kutta and general linear methods. Wiley, 1 édition, 1987. (Cited on pages 88 and 89.)

[Cameron 2007] T. M. Cameron and J. H. Griffin. *An alternating frequency/time domain method for calculating the steady-state response of nonlinear dynamic systems.* Journal of Applied Mechanics, vol. 56, pages 149–154, 2007. (Cited on page 127.)

[Caughey 1962] T. K. Caughey. *Equivalent Linearization Techniques.* The Journal of the Acoustical Society of America, vol. 34, no. 12, page 2001, 1962. (Cited on page 90.)

[Chatelet 2008] E. Chatelet, G. Michon, L. Manin and G. Jacquet. *Stick/slip phenomena in dynamics: Choice of contact model. Numerical predictions & experiments.* Mechanism and Machine Theory, vol. 43, no. 10, pages 1211–1224, 2008. (Cited on page 119.)

[Chen 2006] Hua-Peng Chen. *Efficient methods for determining modal parameters of dynamic structures with large modifications.* Journal of Sound and Vibration, vol. 298, no. 1-2, pages 462–470, 2006. (Cited on page 6.)

[Chiang 1999] Dar-Yun Chiang. *The generalized Masing models for deteriorating hysteresis and cyclic plasticity.* Applied Mathematical Modelling, vol. 23, pages 847–863, 1999. (Cited on page 85.)

[Ciambella 2015] J. Ciambella and F. Vestroni. *The use of modal curvatures for damage localizationin beam-type structures.* Journal of Sound and Vibration, vol. 340, pages 126–137, 2015. (Cited on page 83.)

[Clavel 2001] A. Clavel, M. Sorine and Q. Zhang. *Modeling and identification of a leaf spring system.* In Third IFAC Workshop on Advances in Automotive Control, Karlsruhe, Germany, 2001. (Cited on page 118.)

[Craig 1966] R. R. Craig. *Coupling of substructures for dynamic analyses: an overview.* AIAA Journal, vol. 6, no. 7, pages 1313–1319, 1966. (Cited on page 14.)

[Craig 1968] R-R. Craig and M C C Bampton. *Coupling of Substructures for Dynamics Analyses.* AIAA Journal, vol. 6, no. 7, page 1313, 1968. (Cited on page 5.)

[Cruz 2011] Carlos Cruz, Juan R. González and David A. Pelta. *Optimization in dynamic environments: A survey on problems, methods and measures.* Soft Computing Journal, vol. 15, pages 1427–1448, 2011. (Cited on pages 7 and 8.)

[Deb 1994] Kalyanmoy Deb and Ram Bhushan Agrawal. *Simulated Binary Crossover for Continuous Search Space.* Complex Systems, vol. 9, pages 1–34, 1994. (Cited on pages 43 and 167.)

[Deb 2002] Kalyanmoy Deb, Amrit Pratap, Sameer Agarwal and T. Meyarivan. *A fast and elitist multiobjective genetic algorithm: NSGA-II.* IEEE Transactions on Evolutionary Computation, vol. 6, no. 2, pages 182–197, 2002. (Cited on pages 9 and 43.)

[Drincic 2012] Bojana Drincic. *Mechanical Models of Friction That Exhibit Hysteresis, Stick-Slip, and the Stribeck Effect.* PhD thesis, University of Michigan, 2012. (Cited on page 114.)

[Duhem 1980] P.M.M. Duhem. The Evolution of Mechanics. 1980. (Cited on pages 7 and 85.)

[Ewins 2000] D.J. Ewins. Modal Testing: Theory, Practice and Application. 2000. (Cited on page 83.)

[Ferri 1996] W. E. Whiteman Ferri and al. *Displacement-Dependent Dry Friction Damping of a Beam-Like Structure*. Journal of Sound and Vibration, vol. 198, pages 313–329, 1996. (Cited on page 85.)

[Forrester 2009] Alexander I.J. Forrester and Andy J. Keane. *Recent advances in surrogate-based optimization*. Progress in Aerospace Sciences, vol. 45, no. 1-3, pages 50–79, 2009. (Cited on page 9.)

[Fourgers 1989] R Fourgers and F Sodoroff. *The evolutive masing model and its application to cyclic plasticity and aging*. Nuclear Engineering and Design, vol. 114, pages 273–284, 1989. (Cited on page 119.)

[FRANK 2007] FAHY FRANK and GARDONIO PAOLO. Sound and Structural Vibration. Elsevier, Oxford, 2 édition, 2007. (Cited on page 47.)

[Gaul 1997] L. Gaul and J. Lenz. *Nonlinear dynamics of structures assembled by bolted joints*. Acta Mechanica, vol. 125, pages 169–181, 1997. (Cited on page 84.)

[Gaul 2008] L Gaul, J Roseira and J Becker. *Structural Damping with Friction Beams*. Shock and Vibration, vol. 15, no. 3-4, pages 291–298, 2008. (Cited on pages 84 and 117.)

[Gavin 2014] Henri P Gavin. *Numerical Integration in Structural Dynamics*. Technical report, Department of Civil & Environmental Engineering, Duke University, 2014. (Cited on page 85.)

[Geffen 2009] V Van Geffen. *A study of friction models and friction Compensation*. A study of friction models and friction Compensation, pages 1–24, 2009. (Cited on pages 84 and 114.)

[Gibert 2001] Claude Gibert. *Analyse modale nonlineaire experimentale*. PhD thesis, Ecole centrale de Lyon, 2001. (Cited on page 83.)

[Gladwell 1964] G. M. L. Gladwell. *Branch Mode Analysis of Vibrating Systems*. Journal of Sound and Vibration, vol. 1, no. 1, pages 41–59, 1964. (Cited on page 5.)

[Gobbi 2006] M. Gobbi, I. Haque, P. Papalambros and G. Mastinu. *A Critical Review of Optimization Methods for Road Vehicles Design*. American Institute of Aeronautics and Astronautics, no. September, pages 1–14, 2006. (Cited on pages 7 and 8.)

[Guillen 1999] J Guillen and C Pierre. *An efficient hybrid frequency-time domain method for the dynamics of large-scale dry-friction damped structural systems*. In IUTAM Symposium on Unilateral Multibody Contacts, volume 72, pages 169–178, 1999. (Cited on page 130.)

[Hazewinkel 2001] ed. Hazewinkel Michiel. Runge-Kutta method. Encyclopedia of Mathematics, Springer, 1 édition, 2001. (Cited on page 88.)

[Henderson 2006] Shane G. Henderson and Barry L. Nelson. Handbooks in Operations Research and Management Science: Simulation. North-Holland, Amsterdam, The Netherlands, 2006. (Cited on page 9.)

[Huang 2016] Xingrong Huang, Louis Jézéquel, Sebastien Besset and Lin Li. *Optimization of the dynamic behavior of vehicle structures by means of passive interface controls.* Journal of vibration and Control, 2016. (Cited on page 5.)

[Hugo Ramon 2004] Elizalde Siller Hugo Ramon. *Non-Linear Modal Analysis Methods for Engineering.* PhD thesis, Imperial College London, 2004. (Cited on page 83.)

[Hurty 1960] W.C. Hurty. *Vibrations of structural systems by component mode synthesis.* ASCE Journal of the Engineering Dynamics Division, vol. 1, pages 581–601, 1960. (Cited on page 5.)

[Hurty 1971] Walter C. Hurty, Jon D. Collins and Gary C. Hart. *Dynamic analysis of large structures by modal synthesis techniques.* Special Issue on Structural Dynamics, vol. 1, no. 4, pages 535–563, 1971. (Cited on page 5.)

[Imbert 1979] J.F. Imbert. Analyse des structures par Elements Finis. Ecole Nationale de l'Aéronautique et de l'Espace, 1979. (Cited on page 32.)

[James 1943] Hubert M. James and Eugene Guth. *Theory of the elastic properties of rubber.* Journal of Chemical Physics, vol. 11, no. 10, page 455, 1943. (Cited on page 47.)

[Jézéquel 1990] L. Jézéquel. *Procedure to reduce the effects of modal truncation in Eigensolution Reanalysis.* AIAA Journal, vol. 28, no. 5, pages 896–902, 1990. (Cited on page 173.)

[Jézéquel 1991] L Jézéquel and C Lamarque. *Analysis of non-linear dynamical systems by the normal form theory.* Journal of Sound and Vibration, vol. 149, no. 3, pages 429–459, 1991. (Cited on page 83.)

[Jézéquel 1994a] L. Jézéquel and H.D. Setio. *Component Modal Synthesis Methods Based on Hybrid Models, Part I: Theory of Hybrid Models and Modal Truncation Methods.* ASME. J. Appl. Mech., pages 100–108, 1994. (Cited on pages 5, 6 and 13.)

[Jezequel 1994b] L. Jezequel and H.D. Setio. *Component Modal Synthesis Methods Based on Hybrid Models, Part II: Numerical Tests and Experimental Identification of Hybrid Models.* Journal of Applied Mechanics, vol. 1, pages 100–108, 1994. (Cited on page 5.)

[Jiang 2005] D. Jiang, C. Pierre and S. W. Shaw. *Nonlinear normal modes for vibratory systems under harmonic excitation.* Journal of Sound and Vibration, vol. 288, no. 4-5, pages 791–812, 2005. (Cited on page 97.)

[Jin 2001] Ruichen Jin, Wei Chen and Timothy W Simpson. *Comparative Studies of Metamodeling Techniques Under Multiple Modeling Criteria.* Structural and Multidisciplinary Optimization, vol. 23, no. 1, pages 1–13, 2001. (Cited on page 9.)

[Kerschen 2009] G. Kerschen, M. Peeters, J. C. Golinval and a. F. Vakakis. *Nonlinear normal modes, Part I: A useful framework for the structural dynamicist.* Mechanical Systems and Signal Processing, vol. 23, pages 170–194, 2009. (Cited on page 83.)

[Klerk 2008] D. De Klerk, Daniel J. Rixen and S. N. Voormeeren. *General Framework for Dynamic Substructuring: History, Review and Classification of Techniques.* AIAA Journal, vol. 46, no. 5, pages 1169–1181, 2008. (Cited on page 5.)

[Krasnoselskii 1989] M.A. Krasnoselskii and A.V. Pokrovskii. Systems with Hysteresis. New York, 1989. (Cited on page 85.)

[Krige 1951] D.G Krige. *A statistical approach to some mine valuations and allied problems at the Witwatersrand.* PhD thesis, University of Witwatersrand, 1951. (Cited on page 42.)

[Laxalde 2007] D. Laxalde, F. Thouverez, J. J. Sinou and J. P. Lombard. *Qualitative analysis of forced response of blisks with friction ring dampers.* European Journal of Mechanics, A/Solids, vol. 26, no. 4, pages 676–687, 2007. (Cited on page 127.)

[Lemerle 1994] P. Lemerle. *Optimisation des structures selon des critères imposes par la discretion.* PhD thesis, Ecole Centrale de Lyon, 1994. (Cited on page 6.)

[Lin 2016] LI Lin and LIU Jiu-zhou. *Analysis of damping effect of dry friction damped structural system under wideband multi-harmonic excitation.* Journal of Aerospace Power, vol. 31, 2016. (Cited on pages xvi, 127 and 128.)

[Lophaven 2002] S. N. Lophaven, Jacob Sondergaard and Hans Bruun Nielsen. *Kriging Toolbox.* Technical report, 2002. (Cited on pages 42, 57, 69 and 165.)

[Louis 1983] Jézéquel Louis. *Structural Damping by Slip in Joints.* ASME. J. Vib., Acoust., vol. 105, 1983. (Cited on page 84.)

[Lülf 2013] Fritz Adrian Lülf, Duc-Minh Tran and Roger Ohayon. *Reduced bases for nonlinear structural dynamic systems: A comparative study.* Journal of Sound and Vibration, vol. 332, no. 15, pages 3897–3921, jul 2013. (Cited on page 83.)

[Marler 2004] R T Marler and J S Arora. *Survey of multi-objective optimization methods for engineering*, 2004. (Cited on page 9.)

[Masing 1926] G. Masing. *Eigenspannungen und Verfestigung beim Messing*. In Proceedings of the Second International Congress of Applied Mechanics, pages 332–335, Prague, 1926. (Cited on pages 85 and 119.)

[Másson 1990] Egill Másson and Yih-Jeou Wang. *Introduction to computation and learning in artificial neural networks*. European Journal of Operational Research, vol. 47, no. 1, pages 1–28, 1990. (Cited on page 9.)

[Millard 2006] F. Millard and Jr. PhD Beatty. Principles of Engineering Mechanics, volume 33. Springer, 2006. (Cited on page 12.)

[Nayfeh 1979] A.H. Nayfeh and D.T. Mook. Nonlinear oscillations. 1979. (Cited on pages 83, 87 and 127.)

[Nayfeh 1992] A.H. Nayfeh and J.F. Nayfeh. *On methods for continuous systems with quadratic and cubic nonlinearities*. Nonlinear Dynamics, vol. 3, pages 145–162, 1992. (Cited on page 97.)

[Nayfeh 2007] Ali H. Nayfeh and Balakumar Balachandran. Applied Nonlinear Dynamics: Analytical, Computational, and Experimental Methods. 2007. (Cited on pages 83 and 128.)

[Ohayon 2014] R. Ohayon and C. Soize. *Clarification about component mode synthesis methods for substructures with physical flexible interfaces*. International Journal of Aeronautical and Space Sciences, vol. 15, no. 2, pages 113–122, 2014. (Cited on page 5.)

[Peeters 2009] M. Peeters, R. Viguié, G. Sérandour, G. Kerschen and J. C. Golinval. *Nonlinear normal modes, Part II: Toward a practical computation using numerical continuation techniques*. Mechanical Systems and Signal Processing, vol. 23, pages 195–216, 2009. (Cited on page 83.)

[Piatkowski 2014] T. Piatkowski. *Dahl and LuGre dynamic friction models - The analysis of selected properties*. Mechanism and Machine Theory, vol. 73, pages 91–100, 2014. (Cited on pages 85 and 115.)

[Puel 2013] Guillaume Puel, Béatrice Bourgeteau and Denis Aubry. *Parameter identification of nonlinear time-dependent rubber bushings models towards their integration in multibody simulations of a vehicle chassis*. Mechanical Systems and Signal Processing, vol. 36, no. 2, pages 354–369, 2013. (Cited on page 7.)

[Ren 2009] Yuan Ren and Guangchen Bai. *Comparison of Neural Network and Kriging Method for Creating Simulation-Optimization Metamodels*. 2009 Eighth IEEE International Conference on Dependable, Autonomic and Secure Computing, no. 1, pages 815–821, 2009. (Cited on page 9.)

[Rosenberg 1962] R.M. Rosenberg. *The Normal Modes of Nonlinear n-Degree-of-Freedom Systems.* ASME, 1962. (Cited on page 83.)

[Ruzika 2005] S. Ruzika and M. M. Wiecek. *Approximation methods in multiobjective programming.* Journal of Optimization Theory and Applications, vol. 126, no. 3, pages 473–501, 2005. (Cited on page 9.)

[Sangriyadi 1990] S. Sangriyadi. *Nonlinear modal analysis.* PhD thesis, Ecole Centrale de Lyon, 1990. (Cited on page 97.)

[Seshadri 2006] Aravind Seshadri. *A fast elitist multiobjective genetic algorithm: NSGA-II ToolBox.* Technical report, 2006. (Cited on pages 42, 43 and 168.)

[Setio 1992] S Setio, H D Setio and L Jezequel. *Modal Analysis of Nonlinear Multi-Degree-of-Freedom Structure.* The International Journal of Analytical and Experimental Modal Analysis, vol. 7, no. 0, pages 75–93, 1992. (Cited on pages 83, 89 and 90.)

[Setio 1995] H D Setio, S Setio and L Jezequel. *A method of non-linear modal identification from frequency response tests.* Journal of Sound and Vibration, vol. 182, pages 336–341, 1995. (Cited on page 83.)

[Szemplinska-Stupnicka 1980] W. Szemplinska-Stupnicka. *The resonant vibration of homogeneous non-linear systems.* International Journal of Non-Linear Mechanics, vol. 15, no. 4-5, pages 407–415, 1980. (Cited on page 83.)

[Touzé 2006] C. Touzé and M. Amabili. *Nonlinear normal modes for damped geometrically nonlinear systems: Application to reduced-order modelling of harmonically forced structures.* Journal of Sound and Vibration, vol. 298, pages 958–981, 2006. (Cited on page 83.)

[Vermot 2010] Guillaume Vermot, Jean-Philippe Bianchi and Etienne Balmes. *Using component modes in a system design process.* IMAC XXXII A Conference and Exposition on Structural Dynamics, pages 1–9, 2010. (Cited on page 5.)

[Von Groll 2001] Gotz. Von Groll and David J. Ewins. *The harmonic balance method with arc-length continuation in rotor/stator contact problems.* Journal of Sound and Vibration, vol. 241, no. 2, pages 223–233, 2001. (Cited on page 128.)

[W.D. 1973] Iwan W.D. *A generalization of the concept of equivalent linearization.* International Journal of Non-Linear Mechanics, vol. 8, no. 3, pages 279–287, 1973. (Cited on page 90.)

[W.Kwon 1997] Young W.Kwon and Hyochoong Bang. The Finite Element Method using Matlab. CRC Press, Boca Raton London NewYork Washington,D.C., 1997. (Cited on page 12.)